Measurement of some radiative properties of solar absorber materials

Thesis

MEASUREMENT OF SOME RADIATIVE PROPERTIES OF SOLAR ABSORBER MATERIALS

A thesis submitted to the Open University

for the Degree

of

Doctor of Philosophy

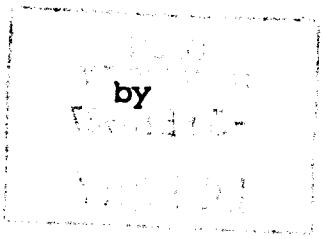

by

AJIT AMAL DE SILVA B.Sc.(Hons)

OCTOBER

1986

Department of Physics

The Open University

Milton Keynes.

IMAGING SERVICES NORTH
Boston Spa, Wetherby
West Yorkshire, LS23 7BQ
www.bl.uk

CONTAINS PULLOUT

ABSTRACT

This work describes,

(i) the designing and building of two sets of apparatus, namely a Liquid Nitrogen Cooled Directional Emissometer and a Laser-source Spectral Bidirectional Reflectometer

(ii) measurements using the above apparatus on Solar selective absorber (Maxorb, Cusorb, Skysorb, Solarcoat-100), non-selective absorber (Nextel, Solarcoat-50) and metal (Al, Cu and brass) samples.

The emissometer incorporates liquid nitrogen cooling of the sample chamber thus reducing the error due to emission from the surroundings and extending the working range of sample temperature down to about 273 K. This instrument also uses a beam chopper with a phase sensitive detection system, and a Golay-cell detector. The overall error in the emittance values measured is estimated to be ± 5%.

Using the emissometer all the samples in (ii) above were studied. The directional emittance behaviour of the metals and the non-selective absorbers agree well with theoretical predictions and with measurements made by other workers. In the case of the solar selective absorbers however, a peak in the directional emittance at 20°-30° reported by Hutchins (1979) is not seen in any of the present measurements. It is

suggested that the $\epsilon/\epsilon'(0°)$ vs. $\epsilon'(0°)$ plot can be used in comparing the emittance properties of solar selective absorbers with their substrate metals.

The bidirectional reflectometer incorporates a novel device for mounting, positioning and orienting both the sample and the detector (Sample and Detector Assembly - SDA). The relatively small dimensions of this device compared with that of other bidirectional reflectometers reported makes it convenient to use and also allows it to be housed within a light-tight enclosure that minimizes problems with stray light. Extensive measurements have been made using laser sources at λ = 633 nm and λ = 1152 nm on the same set of samples of solar absorbers (selective and non-selective) studied with the emissometer.

Comparison of the bidirectional reflectance characteristics of the solar selective absorbers shows marked differences between the materials. However certain features common to 'specularly' reflecting materials and others common to 'diffusely' reflecting materials have been identified. Materials like Cusorb and Solarcoat-100 show a combination of these. Some of these features are discussed in terms of the surface microstructure data obtained using a scanning electron microscope and a conventional stylus type instrument.

STATEMENT OF ORIGINALITY

All work described in this thesis, other than that accredited for, is the candidate's own original work. This research project was originated by the candidate and his supervisor and was not a continuation, nor related to any previous project at the Open University. Thus all non commercial equipment used was designed and commissioned by the candidate. The only exception to the above is the mechanical design of the SDA, which was originally by the candidate's supervisor, but subsequently modified by the candidate.

ACKNOWLEDGEMENTS

First and foremost I would like to thank Dr.Barrie W.Jones for overall supervision of the project. His helpful advice at all stages of the work, including constructive criticism and suggestions to the first draft of this thesis is gratefully acknowledged. Thanks are offered also to my present group leader Dr.Keith A.Hodgkinson of the Open University for providing me with some of the time needed to write-up this thesis.

I am grateful to the Open University for a maintainence grant and for other funding.

Much of the construction of apparatus was carried out by Mr. Bill Thomas to whom thanks are due. I take this opportunity also to thank all members of the Physics Department and especially the other technical staff, and the secretarial staff.

Thanks are also offered to Mr.Ian Norman and Mr.Richard Black of the Materials Science Department of the Open University for the SEM work and for preparing Aluminium substrates. I am also grateful to Mr.Colin Dougherty of Rank-Taylor-Hobson Ltd., Leicester for the surface roughness measurements.

Most of the present measurements were made on samples kindly sent to me by the following companies. Many thanks.

1) INCO Selective Surfaces Ltd., Birmingham

2) ZUEL Corporation, USA

3) 3M Company, USA

Finally I would like to thank Mrs.Pam Berry for her skillful word processing of this manuscript.

Apologies are due to anyone accidentally omitted from the above list to whom thanks are due.

DEDICATION

This work is dedicated to my parents, and to my wife Shreeni and sons Muditha and Dinuka, whose indirect contribution to this project is difficult to put into words.

CONTENTS

CHAPTER 3 DIRECTIONAL EMITTANCE WORK

LIST OF SYMBOLS

		UNITS
a	surface area	m^2.
a_0	projected sample area	m^2.
A	surface area	m^2.
B	electrical bandwidth	Hz
C1,C2	constants	
c	specific heat capacity	$J\ kg^{-1}K^{-1}$.
D	detectivity	W^{-1}.
d	optical density	
E	radiant power incident on the Golay Cell	W
e	emissive power	
F	view factor, Heat removal factor	
f	some function, electrical frequency	Hz
G	voltage gain (of the ratiometer)	
H	hemispherical space (see description for $\int_H$)	
h	constant	
I,i	intensity (of radiation)	$Wm^{-2}\mu m^{-1}sr^{-1}$.
i	electric current	A
K	the 'Solar Constant'	$W\ m^{-2}$.
k	constant, imaginary part of refractive index	
L	function of sample temperature	W
l	distance, length	m
m	mass	kg
n	real part of refractive index	
Q	radiant energy per unit time per unit area	Wm^{-2}.
q	radiant energy per unit time (radiant power)	W
R	voltage responsivity	VW^{-1}.
r	distance, length	m

S	spectrum of solar radiation	
T	temperature	K
t	time	
U	overall heat loss coefficient	$Wm^{-2}K^{-1}$.
V	signal voltage reading displayed on the DVM	V
v	voltage	V
Y	function of absorptance (of the absorber plate)	
Z	time constant	s
α	absorptance, phase angle	
β	angular frequency	rad s^{-1}.
γ	angle	
Δ	a small interval, error	
δ	small interval, error	
ϵ	emittance	
η	efficiency	
θ	polar angle	
ρ	reflectance	
σ	Stefan-Boltzmann constant standard deviation	
Φ	azimuthal angle	
τ	transmittance	
λ	wavelength	μm
μ	10^{-6}	
Ω	field of view	sr
ω	solid angle	sr
$\int_H$	integration over all directions in the 'hemispherical space' above the surface area concerned.	

Superscripts

'	directional quantity
"	bidirectional quantity
*	specific (detectivity)
**	background independent-specific (detectivity)

Subscripts

A	collector A
a	absorber, absorbed
a_0	projected sample area
B	collector B
bb	blackbody
c	cover plate (of solar collector)
d	detector
d1,d2	at differential element d1 or d2, pertaining to detectors 1 and 2
e	emitted, emission
FPC	flat plate collector
I	total input
i	incident, incidence
ℓ	lost
m	integer, mirror
N	noise
n	normal
o	ambient
PSD	phase sensitive detector
p	parallel

R	reference, reference sample, Removal
r	reflected, reflection, reference sample
S	signal
s	absorber sample
w	sample chamber wall
λ	spectral
ω	pertaining to a solid angle

CHAPTER 1 INTRODUCTION

1.1 Background

Over the last decade photothermal conversion of solar energy has been shown to be a practical and an attractive means of supplying a portion of the energy needs of a community depending on its geographical location. This refers in particular to the space and water heating requirements. Large scale adoption of this technology however depends on social, political and economic factors (Jones and Oreszczyn, 1981). At the present time, much work remains to be done in improving the materials and techniques employed, in order that the energy conversion costs may be further reduced.

1.2 Aims and Objectives of the present project

The broad aim of this project is to contribute to the field of radiative property measurement of photothermal solar absorber materials. The radiative properties concerned are absorptance, emittance and reflectance. Each of these properties are however functions of wavelength, temperature and geometrical configuration of measurement. The latter refers to the directions of the incident and/or exitant beams, usually specified in terms of 'polar' and 'azimuthal' angles, and their solid angular extents. Experimental data on the variation of the above radiative properties with the

geometrical configuration of measurement are relatively rare. Nevertheless this information is of importance to workers in the following areas of study.

1) Accurate calculations of overall absorptance and/or emittance of a given solar collector, subject to a given set of operating conditions (e.g. direction/s of incident solar radiation - both direct and diffuse components; absorber and ambient temperatures).

2) Detailed analysis of radiation exchange processes within a given solar collector geometry, especially in computer modelling.

3) Research and development work on solar absorber materials.

A specific aim of the present project is, therefore, to obtain experimental data on the directional variation of some important radiative properties, in several commercial solar absorber materials. The particular measurements to be made are the following:

(i) spectral bidirectional reflectance at 633nm and 1152nm wavelengths

(ii) total directional emittance at a sample temperature around 100°C.

In (i) above, 633nm is roughly at the centre of the solar spectrum and 1152nm is approximately twice this value. Measurements at these wavelengths will therefore give values typical for solar radiation.

The equipment necessary to carry out the above measurements is not commercially available and therefore needs to be specially designed. This is generally true for most 'directional' measurements and is one of the main reasons for the scarcity of these data. Hence the other main aim of this project is to design and develop equipment that will allow the above measurements to be made to a sufficiently high degree of accuracy, with the least amount of complexity and expense.

Thus the objectives can be stated as follows.

I Design and build a total directional emittance apparatus that has a sample operating temperature range of 0 - 200°C. A liquid nitrogen cooled sample chamber and a beam chopper are to be incorporated.

II Design and build a spectral bidiretional reflectance apparatus incorporating two He-Ne lasers (633,1152nm) as radiation sources. A relatively simple, compact and novel device is to be used for setting the angles of incidence and detection.

III Obtain experimental data (i.e. total directional emittance and spectral bidirectional reflectance) using the above equipment on several commercial solar absorber materials.

IV Compare these data with any in the literature, and perform general analysis.

1.3 Solar Absorbers

The main component of any photothermal collector is the photothermal conversion element, usually referred to as the 'absorber'. This consists of material that is a good absorber of solar radiation (Figure (1.11)) usually on a metallic substrate in the form of a flat plate or a tube. Figure 1.2 shows a number of different collector configurations and the form of absorbers used in them. The absorber material itself may be a paint applied on to the surface of the substrate, or, a surface layer formed on the substrate by a chemical, chemical vapour deposition, oxidation, vacuum evaporation or other process. Some absorber materials are also manufactured in the form of a coated foil with an adhesive backing allowing easy attachment to a substrate.

The capability of the absorber to convert incident solar

radiation into useful heat sets an upper limit to the performance of any solar collector. A parameter often used in the analysis of collector performance is the 'instantaneous' efficiency, η. This is defined as (Duffie and Beckman (1980)),

$$\eta = \frac{q_{useful}}{q_i} \tag{1.1}$$

where q_{useful} is the rate at which useful heat is produced and q_i is the total power incident on top of the collector cover. Considering, for example, the case of a 'flat-plate collector' (FPC) in the steady state, the useful heat production rate q_{FPC} is given by equation 1.2.

$$q_{FPC} = F_R \left[q_i \tau_c \alpha_a - UA(T_{inlet} - T_0)\right] \tag{1.2}$$

Here F_R is the heat removal factor (see later), τ_c is the transmittance of the cover plate, α_a is the absorptance of the absorber plate, U is the overall heat loss coefficient, A is the area of the absorber plate, T_{inlet} is the temperature of the working fluid at the inlet to the collector and T_0 is the ambient temperature.

Using this in Eq.1.1, the instantaneous efficiency of a flat-plate collector η_{FPC} is obtained as shown in Eq.1.3, where $Q_i = q_i/A$.

$$\eta_{FPC} = F_R\left[\tau_c \alpha_a - \frac{U\,(T_{inlet} - T_0)}{Q_i}\right] \tag{1.3}$$

In Eq.1.2, $q_i \tau_c \alpha_a$ represents the incident power photo-

thermally converted while the second term within the square brackets refers to the total heat loss from the collector. This method of specifying the heat loss and therefore the efficiency as a function of the inlet fluid temperature (IFT) is convenient in most flat plate collector work as the latter is usually known or is easily determined. However the whole of the collector is not normally at the IFT and temperature variations exist across the collector, mainly between a) the inlet and the outlet b) the absorber surface and the working fluid. The heat removal factor F_R (< 1) is therefore a correction for the above. F_R is also defined as the ratio between the actual value of η and the value if the whole collector were at T_{inlet}.

For a given collector under constant irradiance (both in magnitude and direction), $q_i \tau_c \alpha_a$ is constant, and with constant ambient conditions U is also approximately constant. Additionally, for a given mass flow rate (of the working fluid) F_R is also approximately constant. Under these circumstances the curve of η vs $(T_{inlet} - T_0)/Q_i$, represented by Eq.1.3, is linear and provides a useful approximation to the performance of a flat plate collector.

Equation 1.3 however neglects the multiple reflections that always occur to some extent between absorber and the cover plate. This effect can be accommodated by modifying Eq.1.3 as follows:

$$\eta_{FPC} = F_R \left[f(\tau_c, \alpha_a) - \frac{U\,(T_{inlet} - T_0)}{Q_i} \right] \qquad (1.4)$$

where $f(\tau_c, \alpha_a)$ is a function that increases as τ_c increases and as α_a decreases.

From Eq.1.4 it is clear that the larger the α_a, the greater the efficiency. It is also clear that η increases with decreasing U. The absorber material, of course, mainly determines α_a, but it also affects the value of U. This is mainly because the thermal emittance (ϵ_a) of the absorber is an important determinant of the radiative heat loss from the collector. Thus it is seen that α_a and ϵ_a are the two most important radiative properties determining the performance of a solar absorber material.

1.4 α_a and ϵ_a : spectral considerations

The appropriate absorptance for the characterisation of solar absorber materials is that which is determined by the absorption of solar radiation. This is calculated as the weighted average of spectral absorptance of the material at solar wavelengths. However the spectral composition of solar radiation at the earth's surface varies with the optical path length travelled through the atmosphere (Fig. 1.3). This is because atmospheric attenuation due to absorption and scattering is more pronounced at certain wavelengths than others. A method of standardising solar radiation spectra has therefore been established by specifying an air mass

number. This is defined as the ratio of the optical path length travelled by the flux to that travelled by flux incident at sea level from a zenithal direction, at standard atmospheric pressure, turbidity, ozone level and humidity (Robinson 1966). Strictly therefore, every solar absorptance value α_a should refer to the particular solar spectrum used as the weighting function.

The emittance appropriate for the characterisation of a solar absorber material is that which determines the emission from it at a temperature approximately equal to that achieved when used within the collector. This temperature, when heat is being extracted by the working fluid, is unlikely to exceed 650 K in all but a very few collector types (Call, 1978).

Fig. 1.4 compares the spectral emission of a blackbody between the temperatures 300 K and 700 K with the air mass - 0 (AMO) solar spectrum. This shows that the blackbody radiation for this temperature range, lying predominantly in the range 2.5 μm to 20 μm which shall be named thermal wavelengths (extending to longer wavelengths at lower temperatures) , is well separated from most of the solar wavelengths (0.25 - 2.5 μm). It is therefore possible for a solar absorber material to have the desirable feature of having a high solar absorptance (α_{solar}) and a low thermal emittance ($\epsilon_{thermal}$). Such absorbers are called solar selective absorbers. (Tabor 1955, Agnihotri 1981, Koltun 1981). Were there no such separation in wavelength between

the solar and thermal radiations, α_a and ϵ_a would in many cases be approximately equal (section 2.3.6). In most commonly available black absorbing materials (e.g. paints) spectral absorptance is generally high and changes little between solar and thermal wavelengths. These therefore have a high solar absorptance and a high thermal emittance and are called non selective absorbers.

For both selective and non selective absorbers α_a and ϵ_a changes not only with wavelength but also with the direction of measurement. This is an important consideration in developing high efficiency solar collectors and in research and development work on new solar absorber materials, and has provided the main impetus for the work described in this investigation.

1.5 Directional Variation of α_{solar} and $\epsilon_{thermal}$.

Directional dependance of α and ϵ is usually given in terms of the polar angle θ and the azimuthal angle Φ, defining a direction in the hemispherical space above the sample with respect to a point on the surface (see Fig. 1.5). The polar angle θ is measured from the direction normal to the sample surface while the reference direction for Φ may be chosen arbitrarily (e.g. a sample edge or a striation on the surface).

In measuring the directional absorptance, and the directional

emittance, for many surfaces, it is the variations in θ that are the more marked. Hence for most practical work the values of $\alpha'(\theta)$ and $\epsilon'(\theta)$, averaged over Φ, suffice. However in determining these averages (appropriate for the given application) a knowledge of $\alpha'(\theta,\Phi)$ and $\epsilon'(\theta,\Phi)$ distributions is invaluable. This is because the appropriate averages for $\alpha'(\theta,\Phi)$ and $\epsilon'(\theta,\Phi)$ depend not only on the directional distributions themselves, but also on the collector geometry, distribution of incident radiation and a number of other factors.

Fig. 1.6 shows the calculated variation of spectral absorptance with incident angle θ (Hunter, 1965) for an ideal dielectric material with optical constants n = 1.3 and k = 0.3, typical of solar absorber materials (Seraphin, 1976). In the case of real solar absorber materials however this characteristic is modified due to the

a) departure of composition from that of an ideal dielectric
b) method of fabrication
c) texture of the sample surface.

The composition of solar absorber materials may vary from 'black paints' consisting of absorbing or scattering particles suspended in a binder solution, to various oxidised metals, and 'metal blacks' composed of combinations of oxides and other compounds of the metal to multilayer interference stacks. The absorption characteristic of the latter is

particularly sensitive to direction of incidence as the path difference causing the interference changes with the polar angle (Seraphin 1976). Factor c) above becomes important in the case of selective absorbers using the 'wavefront discrimination' technique (Tabor 1955). From these considerations it is to be expected that the directional absorptance of solar absorber materials would vary differently with the direction of incidence from that of ideal materials (an example of which is given in Fig.1.6), particularly at the larger angles of incidence.

The optimum choice of an absorber for a given application must depend on the suitability of the directional characteristic. Mainly in the case of 'non-tracking' collectors the polar angle of incidence of some or all of the flux on the absorber can be large depending on the geometry and orientation of collector, time of day and the presence of a diffuse component. For example the flat plate collector is used positioned horizontally, vertically or inclined. In addition it may or may not have reflectors placed adjacently to increase the incident flux density. The diffuse component of flux arises from both atmospheric and ground scattering. Therefore for these type of collectors material with a high absorptance extending to larger angles of incidence should be used.

Amongst the other factors determining the appropriate directionally averaged α_{solar} in a given application is the

bidirectional reflectance distribution $\rho''_{solar}(\theta_i, \Phi_i, \theta_r, \Phi_r)$ of the absorber material. This is an important characteristic of a surface that determines the directional distribution of the reflected radiation, for any given incident direction (section 2.3.5). ρ''_{solar} data of the absorber material together with the ρ''_{solar} data of the cover material would allow a highly accurate determination of the fraction of radiation reflected off the absorber, that will be redirected towards it. The dependence of this redirected component on the ρ''_{solar} distribution of the absorber is easily seen in the two extreme cases considered below.

Two flat plate collectors A and B (Fig. 1.7) have the following specifications. The absorbers in both A and B have the $\alpha'_{solar}(\theta, \Phi)$ constant over all Φ and their $\rho''_{solar}(\theta_i, \Phi_i, \theta_r, \Phi_r)$ characteristics are independent of Φ_i and Φ_r. For any given polar angle of incidence θ, both absorbers have the same value of $\alpha'_{solar}(\theta)$. The absorber in A reflects the non-absorbed fraction of the incident flux $Q_{i,A}$ perfectly specularly. The absorber in B reflects perfectly diffusely. Both collectors have single covers of the same material whose directional transmittance characteristic within solar wavelengths is as shown in Fig. 1.8. For most common materials (e.g. glass, Acrylic, polycarbonate) this changes little with the azimuthal angle Φ.

The situation when both collectors are subject to highly directional irradiation at a polar angle of incidence θ_i is

shown in Fig. 1.7. In collector A, the reflected flux $q_{r,A}$ (usually 5-20% of $q_{i,A}$) is incident highly directionally on the cover plate, with the same polar angle of incidence. It is seen from Fig. 1.8, that for values of θ up to about 50°, most of $q_{r,A}$ would escape from the collector and only a small fraction reflected back. In collector B the reflected flux $q_{r,B}$ is highly diffuse. Hence a significant fraction of this is incident on the cover plate at relatively large polar angles of incidence and therefore reflected back towards the absorber.

Real absorber materials however are neither perfectly specular nor perfectly diffuse. It has even been observed that for certain materials the direction of the reflection peak is much different from that of a specular reflection (Torrance and Sparrow 1966). In general each absorber material has a unique spectral bidirectional reflectance distribution depending on the bulk properties (e.g. complex index of refraction) and the surface microstructure. Therefore measured data on ρ''_{solar} of the absorber material is seen to be of much value in establishing an accurate average of α'_{solar} in a given application. α'_{solar} data obtained from direct measurements (e.g. by using an integrating sphere) may also be used for this purpose. In this case however, the interaction with the collector cover plate is less well defined because ρ''_{solar} is unknown.

The importance of bidirectional reflectance data in radiative

transfer calculations is in fact even more fundamental. The reason for this is that for any opaque material all radiometric quantities, including directional absorptance, may be derived from measurements of $\rho''(\lambda, \theta_i, \Phi_i, \theta_r, \Phi_r)$. The derivations of $\alpha'_{solar}(\theta,\Phi)$ and $\epsilon'_{solar}(\theta,\Phi)$ are shown in section 2.5.

Just as the appropriate directionally averaged value of α'_{solar} in a given application depends on the factors discussed earlier, the appropriate directionally averaged $\epsilon'_{thermal}$ for the absorber, which helps to determine the radiative heat loss, is dependent on the following factors, in addition to the $\epsilon'_{thermal}(\theta,\Phi)$ distribution of the absorber material itself.

a) collector geometry

b) $\rho''_{thermal}$ of cover/s and of absorber

c) $\epsilon'_{thermal}$ of cover/s

b) above is particularly important in the case of a collector using a 'heat mirror' type of selective cover material. The latter has high transmittance at solar wavelengths and high reflectance at thermal wavelengths (Meinel and Meinel 1977). Factor c) however is only important at relatively high operating temperatures when the cover temperature may not be much closer to the ambient than the absorber temperature.

The most use of ρ_λ'' and ϵ_λ' data on solar absorber materials is made in the following areas of study.

a) modelling and detailed studies of solar collectors. [Jones and Oreszczyn, 1986]

b) detailed studies of reflectance and emittance in the development of new absorber materials.

Yoshida (1978) has analysed the peformance of a (infinitely planar) flat plate collector system consisting of a 'heat mirror' type cover assumed to be a perfectly specular reflector, and an absorber that is neither perfectly diffuse nor perfectly specular and therefore characterised by its bidirectional reflectance distribution function.
Assuming perfect heat transfer and negligible conduction and convection losses, the instantaneous efficiency of this collector (Fig. 1.9) for near normal irradiation is given as

$$\eta = \frac{Q}{Q_I}$$

where

$$Q = Q_a - Q_r + Q_e$$

and $$Q_I = K \int_0^\infty S_m(\lambda)\, d\lambda$$

$S_m(\lambda)$ being the Air Mass m solar spectrum.

Q_a, Q_r and Q_e have been derived as

$$Q_a = H\int_0^\infty S_m(\lambda)\ \tau_c(\theta=0°,\lambda)\ \Big[\alpha_a(\theta=0°,\lambda) + \sum_{n=1}^{\infty}\frac{1}{\pi}\int_H \rho''_a\ (\lambda,\theta_i,\Phi_i,0°,0°)$$

$$\times\ \rho'_c(\lambda,\theta_i,\Phi_i)\ Y_{n-1}(\lambda,\theta_i,\Phi_i)\cos\ \theta_i d\omega_i\Big]\ d\lambda$$

$$Q_r = \int_0^\infty e_{bb}(\lambda,T_a)\Big[\frac{1}{\pi}\int_H \epsilon'_a(\lambda,\theta,\Phi)\ \cos\ \theta\ d\omega\ \Big]\ d\lambda$$

$$Q_e = \int_0^\infty e_{bb}(\lambda,T_a)\Big[\sum_{n=1}^{\infty}\frac{1}{\pi}\int_H \epsilon'_a(\lambda,\theta_i,\Phi_i)\ \rho'_c\ (\lambda,\theta_i,\Phi_i)$$

$$\times\ Y_{n-1}(\lambda,\theta_i,\Phi_i)\ \cos\ \theta_i d\omega_i\Big]\ d\lambda$$

where,

$$Y_n(\lambda,\theta_i,\Phi_i) = \frac{1}{\pi}\int_H \rho''_a(\lambda,\theta_i,\Phi_i,\theta_r,\Phi_r)\ \rho'_c\ (\lambda,\theta_r,\Phi_r)$$

$$\times\ Y_{n-1}(\lambda,\theta_r,\Phi_r)\ \cos\ \theta_r\ d\omega_r$$

$$Y_0(\lambda,\theta_i,\Phi_i) = \alpha_a(\lambda,\theta_i,\Phi_i)$$

and,

n takes up integer values.

When modelling collectors with more complex geometries Monte - Carlo type computer simulations may be carried out. [Gray amd Muller 1974, Schrieder 1964]. In this method all

radiation is treated as a flow of individual packets of energy. The path of each incident solar energy packet and each emitted thermal energy packet is followed until it is totally absorbed or expelled out of the system. This procedure is repeated for a very large number of energy packets. The outcome of each interaction between an energy packet and a surface is determined by a reflection emission probability distribution over θ, Φ. The former is derived from experimental data on $\alpha(\theta,\Phi)$ and $\epsilon(\theta,\Phi)$, or even more accurately from ρ''_{solar} and $\rho''_{thermal}$ data on materials used in the collector. However a common complaint by workers in this field is the lack of relevant data on most materials, compelling various simplifying assumptions to be made, some of which are listed below.

a) perfectly diffuse (reflecting and emitting) surface
b) perfectly diffuse reflected component + a specular component
c) perfectly specular surface
d) independence of α, ρ and ϵ on Φ.

Finally note that ρ''_λ and ϵ'_λ data are also used extensively in

1) modelling of the reflection and emission processes in materials. (Green, 1983)
2) modelling and analysis of light baffles and the stray light rejection in optical systems [SPIE vols.257, 362, 384, 511].

CHAPTER 2 THEORETICAL BACKGROUND

2.1 Nomenclature

The nomenclature used in this work with regard to the various radiometric quantities is very close to that adopted by Siegel and Howell (1981). (Much of the theory in this chapter is also based on the above.) The main departure is that regarding the use of the endings "ance" and "ivity". Here the recommendation by the National Bureau of Standards (US) has been followed (Nicodemus 1978). This reserves the use of "ivity" for describing a radiometric property of an optically smooth sample with an uncontaminated surface. The ending "ance" is used when referring to the result of a measurement on a particular sample where there is normally a need to specify the condition of the surface, such as surface roughness parameters, contaminations etc.

2.2 Radiometric characterisation of Opaque Materials

The present work is mainly concerned with materials that are highly opaque to radiation at solar and thermal wavelengths. Total opacity of all samples investigated is guaranteed by the metallic substrate on which the solar absorbing layer is formed. (The only exception to this was in the case of measuring the directional emittance of glass. However the 4 mm thickness of the sample was sufficient for it to be

assumed that any thermal radiation from the heater block transmitted through the sample was negligible in comparison with its own emission at the temperature of measurement.)

Some common definitions of the basic radiometric quantitites characterising opaque materials are given below.

$$\text{absorptance } (\alpha) = \frac{\text{radiant power absorbed}}{\text{radiant power incident on sample}}$$

$$\text{reflectance } (\rho) = \frac{\text{radiant power reflected}}{\text{radiant power incident on sample}}$$

$$\text{emittance } (\epsilon) = \frac{\text{radiant power emitted}}{\text{radiant power emitted by a blackbody of equal sample area at the same temperature.}}$$

A blackbody is defined as an ideal body that allows <u>all</u> incident radiation to pass into it (i.e. no reflected energy), and absorbs internally <u>all</u> the incident radiation (i.e. no transmitted energy), at all wavelengths, at all angles of incidence and at all polarisations (Siegel and Howell 1981).

The above definitions of absorptance reflectance and emittance are however seen to be rather ambiguous when looked at more closely taking into account the various parameters involved in the measurement procedure. This is examined in the following sections and the use of 'descriptors', indicating the experimental conditions imposed on the

measurement, is discussed. More precise definitions of the basic radiometric quantities are presented in section 2.2.2.

2.2.1 Descriptors for α, ρ and ϵ

The result of any measurement of absorptance, reflectance or emittance is affected by conditions imposed on the measurement procedure. Therefore, strictly, every reference to these measurements should be accompanied by an explicit statement of these conditions or at least by 'descriptors' indicating the imposed conditions. The latter may be grouped into the following areas

1) wavelength
2) geometrical configuration of measurement
3) temperature
4) polarization.

2.2.1.1 Wavelength Description

Some absorptance, reflectance and emittance measurements are carried out using radiation at only one wavelength. This is usually done by using a quasi-monochromatic source (e.g. a laser, discharge lamp etc.) or a monochromator in the measurement apparatus. Such measurements are referred to by the descriptor 'SPECTRAL'.

For some applications absorptance, reflectance or emittance data involving radiation within only a certain band of

wavelengths is required. Examples are the OPTICAL (0.4-0.75μm), the SOLAR (0.3-2.5μm) and the THERMAL (2.5-60 μm) bands. These measurements are normally carried out with either the source or the detector having a 'band' response (e.g. blackbody type sources at various temperatures, semiconductor detectors PbS, doped Ge), or by using spectral filters in the measurement system. The appropriate descriptor in each case is the same as the name given to the wavelength band.

Whenever a measurement is made involving radiation of all the wavelengths emitted by the source the descriptor used is TOTAL. Examples are the total - emittance of a sample at a given temperature, and the total - reflectance of a sample with a radiation source of known spectral composition.

2.2.1.2 Geometrical configuration of Measurement.

A complete specification of the geometrical configuration of measurement involves the solid angular extent as well as the directions of the radiations incident on, and/or, exitent from the sample. A direction in the hemispherical space above a planar sample is defined by the polar angle θ, ($0° < \theta < 90°$), and the azimuthal angle Φ ($0° < \Phi < 360°$) (section 1.4). The solid angular extent of a beam may vary from 0 to 2π steradians.

Most descriptors used to indicate the geometrical

configuration of of measurement however only indicate the solid angular extent of the beams in a semi-quantitative way. For example (see Fig. 2.1),

"DIRECTIONAL" relates to an infinitesimal solid angle $d\omega$

"CONICAL" relates to a finite solid angle ω where

$$0 < \omega < 2\pi \text{ steradians (sr).}$$

"HEMISPHERICAL" relates to a solid angle of 2π sr.

The only descriptor indicating directionality as well is "NORMAL". This refers to an ideal geometrial configuration where the beam concerned is confined within a solid angle of infinitesimal extent, around a direction normal to the sample surface.

When referring to emittance or absorptance measurements only a single descriptor is necessary to denote respectively the exitent or the incident beams. With reflectance measurements however two descriptors are needed to indicate both the incident and the exitent beams. Table 2.1 shows the notation for the various different types of absorptance, emittance and reflectance measurements.

2.2.1.3 Temperature

The descriptor used here is the sample temperature appropriate to the measurement. In the case of reflection (from non-dispersive materials) it is only the sample surface

that is involved and therefore it is this temperature that should be quoted. In emittance and absorptance measurements however, the incident or the exitent radiation interacts with a volume element of the material the extent of which depends on the value of the extinction coefficient. In the special case of metals the high value of the extinction coefficient limits the interaction to a thin surface layer. In general this is not the case and most solar absorber surfaces are of a particulate (dispersive) nature. Therefore determining the appropriate temperature is difficult due to the uncertainty in the extent of the participating layer and various temperature gradients present. (Harrison 1963). Hence in specifying sample temperature it is essential to state how this was measured.

2.2.1.4 Polarization

The relevant information in this area is the state of polarization of the detected radiation (i.e. reflected off, or emitted by the sample) and/or the incident radiation. Incident radiation is usually either polarized parallel or perpendicular to the plane of incidence, or unpolarized. Radiation detection is usually done either regardless of the state of polarization (i.e. equal sensitivity at all polarizations), or selectively, letting through only a plane polarized beam into the detector.

In the present work radiation incident on the sample was

polarized to a negligible extent at all times (see Appendix 2) and detection of radiation was always independent of the state of polarization. Thus polarization dependent behaviour is not invesigated and this dependence is totally neglected in all definitions of absorptance, emittance and reflectance in the following sections.

2.2.2 Definitions of the Basic Unaveraged Radiometric Quantities

Neglecting any polarization effects, the basic unaveraged quantities for measuring absorptance, emittance and reflectance of an opaque material are, respectively,

spectral directional absorptance - $\alpha'_\lambda(\lambda,\theta,\Phi,T)$
spectral directional emittance - $\epsilon'_\lambda(\lambda,\theta,\Phi,T)$
spectral bidirectional reflectance - $\rho''_\lambda(\lambda,\theta_i,\Phi_i,\theta_r,\Phi_r,T)$

the redundance in notation here is worth pointing out. Both the superscripts ', " and the functional notation $(\ldots,\theta,\Phi,\ldots)$ indicate directionality while the subscript λ and $(\ldots,\lambda,\ldots)$ indicate a spectral quantity. This system of notation however is adopted for the sake of consistency. The rule followed is that the superscripts and the subscripts shall be used at all times to indicate a directional, bidirectional or a spectral quantity irrespective of whether the functional notation is used.

In all the following definitions in this section, isothermal homogeneous samples are assumed.

Spectral Directional Absorptance: $\alpha'_\lambda(\lambda,\theta,\Phi,T)$ is defined as THE FRACTION of the radiant energy incident on the sample at a temperature T, within an elemental solid angle $d\omega$ centred around the direction (θ,Φ), within a small wavelength interval $d\lambda$ centred around the wavelength λ, THAT IS ABSORBED by the sample.

Spectral Directional Emittance: $\epsilon'_\lambda(\lambda,\theta,\Phi,T)$ is defined as the ratio BETWEEN the radiant energy emitted by the sample at a temperature T, per unit elemental solid angle centred around the direction (θ,Φ), per unit small wavelength interval centred around the wavelength λ, per unit area of sample, per unit time AND the radiant energy emitted by an equal area of blackbody under identical conditions.

Spectral Bidirectional Reflectance: $\rho''_\lambda(\lambda,\theta_i,\Phi_i,\theta_r,\Phi_r,T)$ is defined as the FRACTION of radiant energy incident on the sample at temperature T, within an elemental solid angle $d\omega$ centred around the direction (θ_i,Φ_i), within a small wavelength interval $d\lambda$ centred around the wavelength λ, THAT IS REFLECTED per <u>unit</u> elemental solid angle centred around the direction (θ_r,Φ_r) per unit 'projected-area' in the direction (θ_r,Φ_r). See Fig.2.2

An alternate set of definitions for the above quantities, in terms of incident, reflected and emitted <u>intensities</u>, are given in Siegel and Howell (1981).

Incident, reflected or emitted intensity (I) is defined as the radiant energy, respectively incident on, reflected by, or emitted by the sample " per unit elemental solid angle centred around the direction (θ,Φ), per unit elemental projected sample surface area, per unit elemental wavelength interval, per unit time."

2.2.3 Derivation of Spectrally Averaged Quantities

Using the three basic spectral quantities defined above, or indeed using any spectral radiometric quantity, the corresponding spectrally averaged total quantity is derived by integrating over all wavelengths. Of particular interest is the derivation of the total directional emittance from spectral directional emittance as the latter is the quantity that is measured using the present emissometer. This is shown in Eq.2.1.

$$\epsilon'(\theta,\Phi,T) = \frac{\int_0^\infty \epsilon'_\lambda(\lambda,\theta,\Phi,T) I'_{\lambda,bb}(\lambda,T)d\lambda}{\int_0^\infty I'_{\lambda,bb}(\lambda,T)d\lambda}$$

and using the Stefan-Boltzmann law (Section 2.3.5),

$$\epsilon'(\theta,\Phi,T) = \frac{\pi}{\sigma T^4} \int_0^\infty \epsilon'_\lambda(\lambda,\theta,\Phi,T) I'_{\lambda,bb}(\lambda,T)d\lambda \qquad (2.1)$$

2.2.4 Derivation of Spatially Averaged Quantities

In general, when a directional radiometric quantity is integrated over a specific region ($\Delta\omega$) of the solid angular space above the sample surface (ie. by integrating over a certain range of the variables θ and Φ) the corresponding conical quantity is obtained. The most commonly used spatially averaged quantity however is the hemispherical quantity where the solid angle of the beam is 2π steradians.

The spectral hemispherical absorptance and emittance are derived respectively from the spectral directional absorptance and emittance as shown in equations 2.2 - 2.3.a. The corresponding total quantities are obtained in a similar way.

$$\alpha_\lambda(\lambda,T) = \frac{\int_H \alpha'_\lambda(\lambda,\theta,\Phi,T)\ I_{\lambda,i}(\lambda,\theta,\Phi)\ \cos\theta\ d\omega}{\int_H I_{\lambda,i}(\lambda,\theta,\Phi)\ \cos\theta\ d\omega}$$

however when $I_{\lambda,i}$ is independent of (θ,Φ),

$$\alpha_\lambda(\lambda,T) = \frac{1}{\pi}\int_H \alpha'_\lambda(\lambda,\theta,\Phi,T)\ \cos\theta\ d\omega \qquad (2.2)$$

similarly, but with no restrictions,

$$\epsilon_\lambda(\lambda,T) = \frac{1}{\pi}\int_H \epsilon'_\lambda(\lambda,\theta,\Phi,T)\ \cos\theta\ d\omega \qquad (2.3.a)$$

and

$$\epsilon(T) = \frac{1}{\pi} \int_H \epsilon'(\theta,\Phi,T) \cos\theta \, d\omega \qquad (2.3.b)$$

Derivation of $\epsilon(T)$ from $\epsilon'(\theta,T)$ data

This may be done as shown below if ϵ' is assumed to be independent of Φ. Then, using Eq.2.3.b,

$$\epsilon(T) = \frac{1}{\pi} \int_H \epsilon'(\theta,\Phi,T) \cos\theta \, d\omega$$

however, $\qquad d\omega = 2\pi \sin\theta \, d\theta$

therefore,

$$\epsilon(T) = \int_0^{\pi/2} \epsilon'(\theta,T) \sin 2\theta \, d\theta \qquad (2.3.c)$$

The spectral bidirectional reflectance ρ''_λ, can be integrated over the hemisphere with respect to either the reflected or the incident directions, yielding respectively, the spectral directional-hemispherical and the spectral hemispherical-directional reflectances as shown in equations 2.4 - 2.5.

$$\rho'_\lambda(\lambda,\theta_i\Phi_i,T) = \int_H \rho''_\lambda(\lambda,\theta_i,\Phi_i,\theta_r,\Phi_r,T)\cos\theta_r d\omega_r \qquad (2.4)$$

$$\rho'_\lambda(\lambda,\theta_r,\Phi_r,T) = \frac{\int_H \rho''_\lambda(\lambda,\theta_i,\Phi_i,\theta_r,\Phi_r,T) I'_i(\lambda,\theta_i,\Phi_i)\cos\theta_i d\omega_i}{\frac{1}{\pi}\int_H I'_i(\lambda,\theta_i,\Phi_i)\cos\theta_i d\omega_i} \qquad (2.5)$$

where $I_i^{\prime}(\lambda,\theta,\Phi)$ is the spectral directional incident intensity. This is defined as the radiant energy incident on the sample per unit 'projected area' (see Fig. 2.3), per unit elemental solid angle $d\omega_i$ centred around the direction (θ_i,Φ_i), per unit small wavelength interval $d\lambda$ centred around the wavelength λ, per unit time. If however $I_i^{\prime}$ is uniform over all incident directions, eq. 2.5 reduces to,

$$\rho_\lambda^{\prime}(\lambda,\theta_r\Phi_r,T) = \int_H \rho_\lambda^{\prime\prime}(\lambda,\theta_i,\Phi_i,\theta_r,\Phi_r,T)\cos\theta_i d\omega_i \qquad (2.6)$$

Also when $I_i^{\prime}$ is independent of (θ_i,Φ_i) spectral hemispherical directional reflectance becomes equal to the spectral directional hemispherical reflectance via the Helmholtz Reciprocity principle (Section 2.3). Either of these quantities may be integrated again over the hemisphere to yield the spectral bihemispherical reflectancce as shown in equations 2.7 and 2.8.

$$\rho_\lambda(\lambda,T) = \frac{\int_H \rho_\lambda^{\prime\prime}(\lambda,\theta_i,\Phi_i,T)\ I_i^{\prime}(\lambda,\theta_i,\Phi_i)\cos\theta_i d\omega_i}{\int_H I_i(\lambda,\theta_i,\Phi_i)\cos\theta_i\, d\omega_i} \qquad (2.7)$$

If $I_i^{\prime}$ is independent of θ and φ, then

$$\rho_\lambda(\lambda,T) = \frac{1}{\pi}\int_H \rho_\lambda^{\prime}(\lambda,\theta_r,\Phi_r,T)\cos\theta_r d\omega_r \qquad (2.8)$$

Similar arguments would apply to the derivation of the corresponding <u>total</u> quantities.

2.3 Radiation Laws and Principles

A useful concept in radiometry called the emissive power (e) of a surface shall first be introduced. This measures the emission from a unit area of the sample surface and enables most of the radiation laws to be stated in terms of it quite succinctly. The basic unaveraged quantity measuring emissive power is defined below.

The spectral directional emissive power e'_λ is defined as the radiant energy emitted by a sample at temperature T per unit sample surface area, per unit elemental solid angle $d\omega$ centred around the direction (θ,Φ), per unit small wavelength interval $d\lambda$ centred around the wavelength λ, per unit time.

It is possible for all emittance quantities to be redefined as ratios between the corresponding emissive powers and the emissive power of a blackbody of the same temperature. This is done in the case of spectral directional emittance as shown in Eq.2.9.

$$\epsilon'_\lambda(\lambda,\theta,\Phi,T) = \frac{e'_\lambda(\lambda,\theta,\Phi,T)}{e'_{\lambda,bb}(\lambda,\theta,T)} \qquad (2.9)$$

2.3.1 Lambert's Cosine Law of Diffuse Emission

This states, that for a blackbody,

$$e'_{\lambda,bb}(\lambda,\theta,T) = e'_{\lambda,bb}(\lambda,0°,T)\cos\theta \qquad (2.10)$$

where $e'_{\lambda,bb}(\lambda,0°,T)$ is the spectral normal emissive power of the blackbody. Any surface that shows similar directional emittance behaviour is called a 'Lambertian emitter' or a perfectly diffuse emitter. Thus a blackbody also serves as an ideal standard for comparing diffusely emitting surfaces.

It may also be shown that for a Lambertian emitter,

$$e_{\lambda}(\lambda,T) = \pi \cdot e'_{\lambda}(\lambda,0°,T) \qquad (2.11)$$

where $e_{\lambda}(\lambda,T)$ is the spectral hemispherical emissive power.

2.3.2 Lambert's Cosine Law of Diffuse Reflection

This was proposed by Lambert (1760) on the basis of observations that a white wall illuminated by sunlight appears equally bright at all directions of observation. He assumed, therefore, that such a surface behaves as though itself were radiating independently of the direction of observation. Therefore in the case of a Lambertian reflector;

$$\rho''_{\lambda}\ (\lambda,\theta_i,\Phi_i,\theta_r,\Phi_r,T) \;=\; \rho''_{\lambda}\ (\lambda,\theta_i,\Phi_i,0°,0°,T) \qquad (2.12)$$

2.3.3 Planck's Law

Planck (1901) derived the spectral distribution of blackbody hemispherical emissive power in a vacuum. This is shown in Eq.2.13 as a function of wavelength.

$$e_{\lambda,bb} = \frac{2\pi\ C_1}{\lambda^5\left[\ e^{C_2/\lambda T} - 1\right]} \qquad (2.13)$$

where $C_1 = 0.59544\ 10^{-16}\ \dot{W}m^2$.

$C_2 = 14388\ \mu m.K$

2.3.4 Wien's Displacement Law

The variation with temperature of the wavelength at which there is a peak in the Planckian distribution is given by this law, as shown in equation 2.14.

$$\lambda_{max} \cdot T = C_3 \qquad (2.14)$$

where $C_3 = 2897.8\ \mu m.K$

2.3.5 Stefan-Boltzmann Law

The total hemispherical emissive power of a black surface in a vacuum is given by this law as,

$$e_{bb} = \sigma T^4 \qquad (2.15)$$

where $\sigma = 5.6696\ 10^{-8}\ W\ m^{-2}K^{-4}$.

2.3.6 Kirchoff's Law

The physical processes of absorption and emission of radiation are closely related. Kirchoff's law enables extremely useful relations to be derived between absorptance and the corresponding emittance quantities. This law in it's most general form is as shown in Eq.2.16.

$$\alpha'_{\lambda}(\lambda,\theta,\Phi,T) = \epsilon'_{\lambda}(\lambda,\theta,\Phi,T) \qquad (2.16)$$

The relationship between the various spectrally and/or spatially averaged quantities however is only valid when certain restrictive conditions are satisfied. These are listed in Table 2.2.

2.3.7 Helmholtz Reciprocity Principle

'The loss in flux density which an infinitely narrow bundle of rays of definite wavelength and state of polarization undergoes on its path through any medium by way of reflection, refraction and absorption is exactly equal to the loss in flux density suffered by an infinitely narrow bundle of the same wavelength and polarization pursuing an exactly opposite path.'

This statement of the reciprocity principle by Helmholtz (1909) leads to a number of very useful relations between

certain reflectance quantities which are listed in Table 2.3 together with the necessary restrictive conditions.

2.4 Geometrical Configuration Factor (GCF)

The geometrical configuration factor between two given surfaces is a concept often used in radiation exchange calculations. Although strictly defined in terms of surfaces that are perfectly black, it provides a useful means for carrying out approximate calculations with surfaces that are either nearly black or highly diffuse and consequently where it is often possible to ignore the effects of multiple reflections.

In the case of radiation exchange between two perfectly black surfaces, 1 and 2, the geometrical configuration factor F_{12} is defined as follows.

$$F_{12} = \frac{\text{flux emitted by surface 1 that is intercepted by surface 2}}{\text{total flux emitted by surface 1}}$$

GCF, as the name implies, depends only on the geometrical configuration and not on the radiative properties of the surfaces involved. Even when one of the surfaces is not black, GCF can be used to yield accurate results, as shown below.

Consider the situation in Fig.2.4, showing radiation exchange

between two elemental areas dA_1 and dA_2 on the surfaces 1 and 2. Surface 2 is perfectly black. Surface 1 has greybody characteristics and is diffuse over the directions within the solid angle determined by the extreme rays of the type BC and AD with a total directional emittance of $\epsilon_1'(\theta,\Phi)$. In this situation the flux received by dA_2 (from dA_1), $d^2q_{d1\to d2}$, can be written as;

$$d^2q_{d1\to d2} = I_1' \, d\omega_1 \, dA_1 \cos\theta_1$$

where I_1' is the intensity of emission from dA_1 towards dA_2, $d\omega_1$ the solid angle subtended by dA_2 at dA_1 and θ, the angle between the normal to dA_2 and the line joining the centres of dA_1 and dA_2.

As far as dA_2 is concerned dA_1 is a greybody. Therefore,

$$I_1' = \epsilon_1'\sigma T_1^4/\pi$$

$$\text{thus, } d^2q_{d1\to d2} = \left[\frac{\epsilon_1'\sigma T_1^4}{\pi}\right] d\omega_1 \, dA_1 \cos\theta_1$$

$$\text{also, from Fig. 2.4, } \quad d\omega_1 dA_1 \cos\theta_1 = d\omega_2 dA_2 \cos\theta_2$$

$$\text{and therefore, } \quad d^2q_{d1\to d2} = \left[\frac{\epsilon_1' \, \sigma T_1^4}{\pi}\right] d\omega_2 dA_2 \cos\theta_2$$

These relationships are frequently used in Appendix 1.

2.5 Derivation of Absorptance and Emittance of opaque materials from Reflectance Measurements

It is common practice to calculate absorptance quantities from reflectance data. Emittance quantities on the other hand are either measured directly, as in the present work, or are derived from reflectance data.

The derivation of both absorptance and emittance from reflectance data is carried out using the law of conservation of energy. The latter leads to the following useful relations between either absorptance or emittance, and reflectance. Transmittance is not relevant here because the present work is concerned only with opaque materials.

2.5.1 Relations between absorptance and reflectance quantities for opaque materials

The following apply without restriction,

$$\alpha'(\theta,\Phi,T) + \rho'(\theta_i,\Phi_i,T) = 1 \qquad (2.17)$$

$$\alpha'_\lambda(\lambda,\theta,\Phi,T) + \rho'_\lambda(\lambda,\theta_i,\Phi_i,T) = 1 \qquad (2.18)$$

$$\alpha(T) + \rho(T) = 1 \qquad (2.19)$$

$$\alpha_\lambda(\lambda,T) + \rho_\lambda(\lambda,T) = 1 \qquad (2.20)$$

Here $\rho'(\theta_i,\Phi_i,T)$ and $\rho'_\lambda(\lambda,\theta_i,\Phi_i,T)$ are <u>directional hemispherical</u> reflectances. Under certain conditions (see Table 2.3) these can be replaced by the <u>hemispherical directional</u> reflectances, $\rho'(\theta_r,\Phi_r,T)$, $\rho'_\lambda(\lambda,\theta_r,\Phi_r,T)$.

In addition, if the sample is assumed to be perfectly specular i.e. if,

$$\theta_r = \theta_i$$

$$\Phi_r = \Phi_i + 180$$

$$d\omega_r = d\omega_i$$

the following relations (Eqns.2.21 and 2.22) also hold.

$$\alpha'(\theta_i,\Phi_i,T) + \rho''(\theta_i,\Phi_i,\theta_r,\Phi_r,T) \cos\theta_r d\omega_r = 1 \qquad (2.21)$$

$$\alpha'_\lambda(\lambda,\theta_i,\Phi_i,T) + \rho''_\lambda(\lambda,\theta_i,\Phi_i,\theta_r,\Phi_r,T) \cos\theta_r d\omega_r = 1 \qquad (2.22)$$

As the numerical value of ρ''_λ is unchanged by exchanging the incident and reflected radiations, because of reciprocity, either quantity may be used in Eq.2.22. In the case of ρ'' in Eq.2.21 however, this may be done under certain restrictions (see Table 2.3).

2.5.2 Relations between emittance and reflectance quantities for opaque materials

These are derived by substituting emittance for absorptance in Eqns.2.17 - 2.22 using Kirchoff's law, as shown in Eqns.2.23 - 2.28. It is important to note that the latter equations (2.23-2.28) are valid only when the associated restrictive conditions in Table 2.2 are satisfied.

$$\epsilon'(\theta,\Phi,T) + \rho'(\theta_i,\Phi_i,T) = 1 \qquad (2.23)$$

$$\epsilon'_\lambda(\lambda,\theta,\Phi,T) + \rho'_\lambda(\lambda,\theta_i,\Phi_i,T) = 1 \qquad (2.24)$$

if the sample is assumed to be perfectly specular, (see Section 2.5.1)

$$\epsilon'(\theta_i,\Phi_i,T) + \rho''(\theta_i,\Phi_i,\theta_r,\Phi_r,T) \cos\theta_r d\omega_r = 1 \qquad (2.25)$$

$$\epsilon'_\lambda(\lambda,\theta_i,\Phi_i,T) + \rho''_\lambda(\lambda,\theta_i,\Phi_i,\theta_r,\Phi_r,T) \cos\theta_r d\omega_r = 1 \qquad (2.26)$$

When the sample is illuminated uniformly from directions over the hemispherical space i.e. when I'_i is independent of θ_i,Φ_i (see also Table 2.2),

$$\epsilon(T) + \rho(T) = 1 \qquad (2.27)$$

$$\epsilon_\lambda(\lambda,T) + \rho_\lambda(\lambda,T) = 1 \qquad (2.28)$$

As in the previous section, 'reciprocally equivalent' reflectance quantities may be used in Eqns.2.25 - 2.28, under restrictions listed in Table 2.3.

2.5.3 Derivation of Solar Absorptance and Thermal Emittance from spectral bidirectional reflectance data for opaque materials

Spectral bidirectional reflectance values are first integrated according to Eqns.2.4 or 2.5 to yield the spectral directional reflectance, ρ'_λ (the latter refers to either directional hemispherical or hemispherical directional). ρ'_λ may then be integrated again as shown in Eqns.2.7 and 2.8 to obtain spectral bihemispherical reflectance, ρ_λ. These values of ρ'_λ and ρ_λ when substituted respectively into Eqns.2.18 and 2.20 yield respectively the spectral directional absorptance, α'_λ and the spectral hemispherical

absorptance, α_λ. Similarly when the ρ'_λ and ρ_λ values are substituted into Eqns.2.24 and 2.28, the spectral directional emittance, ϵ'_λ and the spectral hemispherical emittance, ϵ_λ are obtained under the restrictions in Table 2.2.

In general, the α'_λ, α_λ, ϵ'_λ and ϵ_λ values derived above may be integrated over all wavelengths to yield respectively, α', α, ϵ' and ϵ. However when this is done over the solar and thermal spectral bands, as shown in Eqns.2.29 - 2.32, the directional and hemispherical solar absorptances and the directional and hemispherical thermal emittances are obtained.

$$\alpha'_{solar} = \frac{\int_{solar} \alpha'_\lambda(\lambda,\theta,\Phi,T) \cdot S_m(\lambda)\, d\lambda}{\int_{solar} S_m(\lambda)\, d\lambda} \qquad (2.29)$$

$$\alpha_{solar} = \frac{\int_{solar} \alpha_\lambda(\lambda,T) \cdot S_m(\lambda)\, d\lambda}{\int_{solar} S_m(\lambda)\, d\lambda} \qquad (2.30)$$

$$\epsilon'_{thermal} = \frac{\int_{thermal} \epsilon'_\lambda(\lambda,\theta,\Phi,T) \cdot e'_{bb}(\lambda,\theta,T))\, d\lambda}{\int_{thermal} e'_{bb}(\lambda,\theta,T)\, d\lambda} \qquad (2.31)$$

$$\epsilon_{thermal} = \frac{\int_{thermal} \epsilon_\lambda(\lambda,T) \cdot e_{bb}(\lambda,T)\, d\lambda}{\int_{thermal} e_{bb}(\lambda,T)\, d\lambda} \qquad (2.32)$$

CHAPTER 3 DIRECTIONAL EMITTANCE WORK

3.1 Brief Survey of Emissometric Techniques

Instrumentation and techniques employed in measuring thermal emittance of materials may be grouped as shown in Fig. 3.1.

The calorimetric steady state method is generally considered to be the most accurate (Millard and Streed, 1967). In this method a sample heated electrically, is placed within a chamber whose walls have a high absorptance to thermal radiation and are also cooled to reduce thermal emission. Heat loss from the sample, other than by means of radiation, is minimised by evacuating the chamber and also by suspending the sample using thin wires. Under thermal steady state conditions, the power input to the heater and the sample temperature are measured. Then, with a knowledge of the surface area of the sample, the 'total hemispherical emittance' can be calculated using Eq.3.1.

$$q_{heater} = v_{heater} \times i_{heater} = \sigma \epsilon_s T_s^4 A_s + q_\ell - q_a \qquad (3.1)$$

q_ℓ and q_a in Eq.3.1, denoting respectively the non-radiative losses and the sample absorption, are made negligibly small and/or calibrated out. The main advantage with this method

is that the power input to sample can be determined accurately and also easily controlled. However the length of time needed for a measurement to be carried out restricts its use only to occasions where a high accuracy is required. As with all calorimetric methods only the hemispherical total emittance may be measured.

The calorimetric transient method differs from the above in that the system is allowed to reach a steady state and then the heat input to the sample is stopped. The sample temperature is continuously recorded using for example a chart recorder. By determining the rate of change of sample temperature at a given temperature and knowing the heat capacity (mc) and surface area of sample (A_s) the hemispherical total emittance is calculated using Eq.3.2 (Butler and Inn, 1963).

$$mc \frac{dT_s}{dt} = A_s \epsilon_s \sigma T_s^4 + q_l - q_a \qquad (3.2)$$

This method, although not requiring the input power to be known and therefore enabling any form of sample heating to be used (e.g. radiative), is only useful as seen above, with samples whose heat capacity is either known or easily determined.

The radiometric indirect method is essentially the measurement of the directional reflectance at thermal wavelengths of a sample positioned either within a heated cavity or within a hemispherical, ellipsiodal or paraboloidal

mirror. In the case of opaque materials, the directional emittance is derived from the measured value of hemispherical directional or directional hemispherical reflectance, using Eqns.2.23 and 2.24 respectively for the total and spectral quantities. This method, suitable for measuring either the spectral or the total directional emittance, has the advantage of using long established experimental techniques of spectrometry, together with a range of commercially available equipment. However the main disadvantage is that it is unsuitable for materials with low emittance values. The reason for this is that any small error in the reflectance measurement results is a large error in the derived emittance value, (e.g. with a sample of $\epsilon' = 0.1$, a 3% error in the reflectance causes a 30% error in the emittance value). It should also be noted that Eqns.2.23 and 2.24 (where the directional reflectance term represents either of the two reciprocally equivalent quantities) are only valid when the relevant restrictive conditions (Tables 2.2 and 2.3) are satisfied. It is often required that to be valid, the hemispherical illumination of the sample (or hemispherical detection of radiation from a sample) must be uniform in all directions. Difficulty in satisfying this requirement arises from the finite dimensions of the entrance/exit apertures of the enclosure and also from the non-isotropic emission of conventional radiation sources.

A radiometric transient method for measuring total normal emittance (called the 'sliding specimen technique') is

particularly suitable for use with metallic samples at high temperatures (1000 - 1500°C), and has been described by Bartsch et al (1970). In this method a radiometer 'sees' the front aperture of a long cylidrical blackbody cavity. The sample to be measured is mounted on a long push-rod which is then inserted into the blackbody cavity through the back aperture. The sample is allowed to heat up to the cavity temperature. After heating up, when the sample is still at the back of the cavity, the radiometer output is proportional to the total normal emissive power of the blackbody. This is because the radiometer receives only a negligible amount of flux from the sample. The sample is now rapidly moved forward up to the front aperture of the blackbody cavity and covers the field of view of the radiometer. It is held in this position for a few seconds during which the radiometer output drops due to sample cooling and then pulled back to the far end of the cavity. The rate of change of radiometer output when the sample is being brought up to the front aperture (due to increasingly seeing sample instead of blackbody) is much bigger than the rate of change due to cooling when the sample is at the front aperture. As the radiometer output is continuously monitored on a graph plotter, the point at which the rate of change of output suddenly changes is easily found. The ratio of the radiometer output at this point to that when the sample is at the back of the cavity yields the total normal emittance of the sample. The main advantage in using this method is that the sample temperature, although capable of being determined

accurately, is not directly involved in the calculation of emittance. However the drawback is that it cannot be used with samples having high emittance values.

The present directional emissometer is based on the direct radiometric method. In this, the flux emitted by the sample at a given temperature in a given direction is measured directly using a radiometer. This is then repeated, under identical conditions, with a reference sample of known directional emittance. From these two measurements and from the known value of the directional emittance of the reference sample, the directional emittance of the measured sample is derived (Section 3.3).

Fig.3.2 is a schematic diagram showing the main components of a direct radiometric emittance measurement apparatus. The design of the beam forming system usually varies between different designs and is totally absent in the much simpler portable instruments.

Most early designs of emissometers using the direct method have been restricted to measuring only the 'normal' emittance (Zerlaut, 1963, Snyder, 1955). The exception to this is the work of Schmidt (1935) whose apparatus enabled him to make directional emittance measurements at polar angles up to 85°. Measurements up to 88° on metallic ribbon samples have been reported by Rolling et al (1967) who studied the effect of surface roughness on the total directional emittance

distribution. Several of more recent emissometers (Huetz-Aubert, 1982, Hutchins, 1979), including the present design, have incorporated a beam chopper in modulating the measured flux. This technique has enormous advantages in discriminating against stray radiations (see Section 3.3) and also enables the use of a.c. signal detection and processing equipment (see Section 3.4.5). The type of radiation detector used in the present work, the Golay cell (Section 3.2.1.6), has a much higher detectivity and responsivity than ordinary thermopile detectors used in most 'non-chopped' systems (and in fact has the highest D^{**} (see section 3.4.5.1) among conventional thermal detectors - see Fig. 3.3). The main difficulty in using the direct radiometric method is in keeping the sample to be measured and the reference sample under identical conditions, most importantly the sample temperatures. This problem has been largely overcome by the measurement technique adopted in the present work, as described in sections 3.4.3 and 3.4.4. Sample and reference temperatures were the same and constant to within ± 0.2°C, and the actual temperature was 95°C ± 1.5°C.

3.2 Description of the Emittance Apparatus

The aim of this section is to give an overall view of the present system used for measuring total directional emittance, and in particular to give details of the emissometer construction. Many of the features described here will be referred to in later sections, in discussing

experimental details and the theory of measurement.

Fig. 3.4 shows schematically the layout of the experimental apparatus. It was necessary to base the overall design on equipment that was already available. This included a Golay cell, a beam chopper, a phase sensitive detector and reference unit, a stabilized d.c. power supply and a digital voltmeter. The basis of the present emissometer operation is that a regularly interrupted beam of flux from a heated sample is detected by the Golay cell and results in a modulated signal, the steady (r.m.s.) component of which is extracted by the processing electronics and displayed as a voltage. The sample chamber walls are cooled with liquid nitrogen in order to minimise their thermal emission, and the whole of the emissometer box is purged with dry nigrogen gas in order to prevent condensation of water vapour. The system external to the emissometer may be grouped into 3 parts,

a) sample heater power supply and temperature control section
b) nitrogen gas and liquid Nitrogen supplies
c) signal processing electronics

Brief descriptions of these three parts will follow in Section 3.4. the main discussion in this section is of the emissometer.

3.2.1 The Directional Emissometer

The emissometer forms the heart of the directional emittance measurement system and consists of the following main components.

1) Emissometer box
2) Sample Holder/Heater Assembly (SHHA)
3) Sample Chamber/LN_2 reservoir
4) Beam Chopper
5) 2nd Chamber
6) Golay cell

The arrangement of 2) - 6) within the emissometer box is shown in Fig.3.4. Details of these components will now be discussed.

3.2.1.1 Emissometer Box

This is a 60 cm x 29 cm x 30 cm fabricated aluminium box with a removable front cover (Fig.1.11). The latter has a 3mm dia. 'O-ring' fitted around the edge providing a gas tight seal, and also three inspection windows which are covered up when taking measurements. The top plate of the emissometer box has a 60 mm dia. circular opening fitted with a cylindrical section of the same diameter. This is the emissometer 'neck' where the O-rings on the SHHA form a 'dynamic seal' (Fig.3.8). Here, whenever the SHHA is not

used, a 'dummy plug' (a cylindrical block of black Nylon) of the same diameter and with two O-rings is used. The 'central rail' fitted to the base plate is a machined aluminium bar of 20mm square cross section, onto which the supports for the sample chamber, 2nd chamber and the Golay cell are mounted. This 'optical bench' like arrangements helps in the assembly of components in the emissometer and in maintaining alignment. All inside walls and most other surfaces within the emissometer box are coated with Nextel-Velvet.

3.2.1.2 Sample Holder/Heater Assembly (SHHA)

The main considerations in designing the SHHA were,

1) the ease of setting sample direction (i.e. the polar angle of emission)
2) the ease of removal and refitting into the emissometer box
3) the convenience in mounting the sample
4) to provide a heater/sample mount surface sufficiently isothermal over the area in contact with the part of the sample seen by the detector
5) to minimise conduction losses
6) to minimise misalignment of the sample due to thermal expansions or contractions.

Fig.3.5 is a cross-sectional drawing of the SHHA and a photograph of this is shown in Fig. 3.6. The SHHA consists of 4 inter-connected sections: the top section, middle

section, PTFE block and heater unit. The top section, with the graduated scale (marked at 1° intervals from 0° - 360°), sits within a recessed seating on the top plate of the emissometer box (Fig.3.7). The middle and the top sections are joined by a section of Brass tubing which forms a part of the 'axial cavity' running though the SHHA for carrying wires to and from the heater unit. Two 3mm dia. 'O-rings' fitted to the middle section (Fig.3.5) form a 'dynamic-seal' at the emissometer 'neck' (Fig. 3.8). This keeps the water vapour out during operation and yet allows easy removal and refitting of the whole assembly into the emissometer box. A smear of vacuum grease on the surface of the emissometer neck lubricates the dynamic seal and also helps in the smooth rotation of the SHHA in setting the sample direction.

The cylindrical (1 inch dia.) Polytetra-fluoro-ethylene (PTFE) block acts as the thermal insulator between the heater unit and the rest of the SHHA (the thermal conductivity of PTFE being 0.2 $Wm^{-1}K^{-1}$). This is screwed to the middle section and also glued using a low temperature adhesive obtained from Oxford Instruments.

The heater/sample mount is made of a copper block measuring 32 mm x 32 mm x 10 mm, drilled as shown in Fig.3.9. Six vitreous wirewound 1Ω resistors, placed within these holes and connected up in series forms the heating element. Good thermal contact between the resistor and the copper block is ensured by filling the cavity with a 'high thermal

conductivity compound' (RS Heat Sink Compound - thermal conductivity = 711.8 $Wm^{-1} K^{-1}$).

The sample to be measured and the reference sample are mounted on either side of the Cu block using four small PTFE pads and Nylon screws, as shown in Fig. 3.9. One of the pads on each side is fitted with a bead thermocouple for measuring the sample temperatures as shown in Fig. 3.10 (Section 3.4.3). The exposed surface on the sides of the Cu heater block are covered with RS Silicone Rubber Compound (working temperature range -50° to 250° degrees C) to reduce the heat loss. A Brass angled plate, fitted to the Cu block via thin brass strips (fig. 3.5), connects the heater to the PTFE block. Two slots cut in the angled plate (letting through the connecting screws) allows the heater unit to be moved in a direction normal to the sample surface and thus adjustment can be made to compensate for sample thickness (see section 3.4.5).

3.2.1.3 Sample Chamber/Liquid Nitrogen Reservoir

This unit (Fig.3.11) is made of two fibre-glass cylindrical sections (of outside diameter 130 and 50 mm, and 3 and 5 mm wall thickness) placed one inside the other and sealed at either end using disks of the same material. The space between the cylinders forms the liquid nitrogen reservoir while the space within the inner cylinder constitutes the sample chamber. The top disk has a central hole through

which the SHHA is let into the sample chamber. The detector views the sample through the exit port, formed by a section of tubing (20mm o/d) reaching the sample chamber through the outer reservoir. A cylindrical plug, with a 8 mm diameter central hole named 'APERTURE 1', determines the exit aperture. The sample chamber walls, the exit port and the plug are coated with highly absorbing NEXTEL 2010 - Velvet coating (see Fig. 3.35). Two short sections of 8mm dia. tubing fitting through the top disk into the liquid nitrogen reservoir serve as the inlet and the boil off tubes. These are connected to flexible tubing passing through the top plate of the emissometer box. A 'STYROFOAM' jacket covers the liquid nitrogen reservoir providing thermal insulation. The unit is supported from underneath on a movable platform (fig. 3.11) tracking the central rail (see section 3.2.1.6) thus allowing some X - Y movement in the horizontal plane during alignment.

3.2.1.4 2nd Chamber/Reservoir

This unit (Fig. 3.12) is made similar to the sample chamber/liquid nitrogen reservoir (using two fibre-glass cylindrical sections of outside diameters, 56 and 26 mm, and 3mm wall thickness), having an outer reservoir and an inner chamber. The latter however has clear access from both ends (Fig. 3.12). The 2nd chamber houses two aperture plugs, similar in construction to 'APERTURE 1 plug', at either end and a radiation baffle in between. The plug towards the

sample chamber has a 2mm dia. aperture, and is named 'APERTURE 2'. The plug towards the detector has an aperture of 3mm dia. and is named 'APERTURE 3'. The overall effect of these apertures is to limit the field of view of the Golay cell detector and thereby ensure that the radiation received, from the sample, is highly directional. The radiation baffle is made of seven circular (19mm dia.) Aluminium disks with a central 6mm dia. hole. These have been threaded on to two pieces of brass studding using spacers (Fig. 3.12). Both aperture plugs and the baffle have been thoroughly coated with NEXTEL paint.

3.2.1.5 Beam Chopper

A Brookdeal model 9479 fitted with a 3-slot blade and operating at a chopping frequency of 10 Hz (see Section 3.4.5.1) is used. The side of the chopper blade facing the detector is fully silvered. The unit is positioned such that when the sample beam is interrupted the detector only sees the Nextel coated side of the 2nd chamber/reservoir, reflected off the chopper blade, as shown in Fig.3.12.

3.2.1.6 Golay Cell

A 'Cathodeon IR-50' Golay cell fitted with a caesium iodide window is used as the radiation detector (Section 3.4.5.1). This is mounted on a movable platform tracking the rail as in the case with the sample chamber and is thus capable of

movement along the rail and normal to it during alignment. The distance from the cell window to the 'Aperture 3' plug is approx. 2 mm. In this position the 90° field of view of the detector is completely covered by the Aperture 3 plug coated with Nextel.

3.2.2 Sample Heater Supply and Temperature Control System

This is formed around a 'COMARK - 6400' Microprocessor Thermometer. This instrument has 10 thermocouple inputs and a separate control channel. The latter consists of a 'sensor' input (connected to the sample thermocouple measuring T_s) and a TTL compatible 'control' output (connected to the 'electronic switch' controlling the heater current - Fig.3.19). The control channel is capable of operating in several modes and the 'proportional control' mode is used for the present work (see Section 3.4.3). Temperatures of:

a) absorber sample surface - T_s;
b) reference sample surface -T_r;
c) outside wall of the 2nd chamber facing the chopper blade ('seen' by the detector reflected off the chopper blade see Fig.3.12) representing ambient temperature - T_0
d) inside wall of the sample chamber - T_w

are measured using type K twisted wire bead thermocouples.

3.2.3 Liquid Nitrogen and Nitrogen gas supplies

The (sample chamber) liquid nitrogen reservoir is filled through the funnel at the top of the inlet tube (Fig. 1.11). Both the inlet and the outlet tubes are lagged for insulation. The 2nd reservoir too may be filled with liquid nitrogen if necessary (Section 3.4.2) through its inlet tube. However in the present work it has been filled with water, (Section 3.4.3). N_2 gas is let into the emissometer box through a valve located near the sample chamber and the purging valve is at the other end of the emissometer box, fitted on to the front cover plate.

3.2.4 Signal Processing Electronics

The Golay cell output (modulated) is detected using a Brookdeal 9412A phase sensitive detector, 9422 reference unit and is displayed on a Keithly 169 Digital Voltmeter as shown in Fig. 3.4. This system is discussed in detail in Section 3.4.4.

3.3 Theory of Operation

The basis of the present method of determining emittance is a comparison of flux emitted by the absorber sample with that from a reference sample kept under near identical conditions. The three readings of emissometer output (i.e. the signal

displayed on the DVM) $V_S(\theta)$, V_R and V_W enable the total directional emittance of the sample to be calculated. (Eq.3.12).

$V_S(\theta)$ is the emissometer output when the absorber sample is oriented at a polar angle of θ (i.e. the angle between the 'radiometric axis' - section 3.4.5 - and the normal to sample surface). V_r represents the output with the reference sample, oriented at a polar angle of 15° (to minimise errors due to stray reflections - section 3.4.2), while V_W is the output with no sample at all i.e. with the SHHA removed from the emissometer box. In this case the detector sees the cold ($\simeq$ 77K) sample chamber wall, equivalent to seeing a 'NEXTEL' sample (the material with which the sample chamber walls are coated.)

The geometrical relationship between the sample and the detector, determined by the apertures, is shown (to scale) in Fig. 3.12. The detector is placed only 2-3 millimetres away from aperture 3 and therefore the latter is assumed to represent the detector active area in all following calculations. Aperture 1 is made sufficiently large (8 mm dia.) so as not to restrict the detected beam. Thus it is only the combination of apertures 2 and 3 that determines the extent of the detected beam. This in turn determines the size of the <u>effective sample area</u> shown in Appendix 3 to be approximately 8.7 mm^2 at an orientation of $\theta = 0°$.

At any given orientation θ, ($0° < \theta < 82°$) of sample the emissometer output can be written as,

$$V(\theta) = R \cdot \Delta E(\theta) \qquad (3.3)$$

Here R is the system responsivity (this is the overall responsivity of the Golay cell and the signal processing electronics) in $V\ W^{-1}$. $\Delta E(\theta)$ is the change in the incident flux at the detector when it alternately views the sample surface and the ambience (represented by the 2nd chamber wall), due to the rotation of the chopper blade. (The latter is silvered on the side facing the detector only.) This situation is shown in Fig. 3.12.

The flux incident on the detector when seeing a sample (i.e. either the absorber sample or the reference sample) consists mainly of 3 components E_1, E_2 and E_3 (see Fig.3.13). (There is a number of other radiation components, to be disucssed in Section 3.4.2. However these do not affect the discussion here.)

$$E_1(\theta) = L \cdot \epsilon_s'(\theta) \qquad (3.4)$$

$$E_2(\theta) = f\left[T_s, T_w, \epsilon_s'(\theta)\right] \qquad (3.5)$$

$$E_3 = f(T_0) \qquad (3.6)$$

where $\epsilon_s'(\theta)$ is really $\epsilon_s'(\theta,\Phi,T)$ with the assumption that there is negligible variation with Φ and where L is a function of the sample temperature and the 'geometrical

relationship' between sample and detector. Note that L contains no cosθ factor - the projected area of the sample (a_0) as seen by the detector is constant. E_1 is the flux emitted by the sample <u>effective area</u> (this is the area of the <u>sample surface</u> 'seen' by the detector) directly towards the detector while E_2 is the 'stray' component (section 3.4.2), originating within the sample chamber, that accompanies E_1. E_3 is the nearly constant background flux (described as component F in section 3.4.2), originating mostly within the 2nd chamber.

Radiation incident on APERTURE-2 other than within the 'cone of acceptance' (Fig.3.12) is strongly rejected by the baffles within the 2nd chamber. However any residual component 'creeping in' will be taken into account as the additional term e_4.

When the sample beam is interrupted by the chopper blade, the detector receives only 2 components of flux, E_3 and $E_4^{\dagger}$. The latter consists mostly of ambient flux arriving through APERTURE 2 reflected off the silvered side of the chopper blade, and also includes the slight emission from the blade itself (the blade emission, where $\epsilon'_{blade} = 1-\rho'_{blade}$, compensates for the flux lost in reflection, as the blade itself is at ambient temperature). A negligible component due to stray radiations of type A and D (Section 3.4.2) is also included.

Eq.3.3 may now be rewritten as,

$$V(\theta) = R\left[(E_1(\theta) + E_2(\theta) + E_3 + e_4) - (E_3 + E_4^+)\right]$$

However if we write, $E_4^+ - e_4 = E_4$

then, $$V(\theta) = R\left[(E_1(\theta) + E_2(\theta) - E_4\right]$$

Using this and Eq.3.4, the general equation for emissometer output now becomes,

$$V(\theta) = R\left[L\,\epsilon'(\theta) + E_2(\theta) - E_4\right] \qquad (3.7)$$

Using Eq.3.7, the three emissometer readings, V_S, V_R and V_W may be expressed as shown below.

$$V_S(\theta) = R\left[L_S\epsilon'_S(\theta) + E_{2S}(\theta) - E_4\right] \qquad (3.8)$$

$$V_R(15°) = R\left[L_R\epsilon'_R(15°) + E_{2R}(15°) - E_4\right] \qquad (3.9)$$

$$V_W = R\left[L_W\epsilon'_W(0°) - E_4\right] \qquad (3.10)$$

Here, $L_S = L_R$ (3.11)

provided that the absorber and the reference samples are at the same temperature when the measurements are taken. E_4 is practically constant as the ambient temperature changes very little (Fig.3.18) throughout a set of measurements (Section 3.4.7.3).

From Eqns. 3.8 - 3.11,

$$\frac{(V_S - V_W)}{(V_R - V_W)} = \frac{\epsilon'_S(\theta) + (E_{2S}/L_S - L_W\epsilon'_W/L_S)}{\epsilon'_R(15°) + (E_{2R}/L_S - L_W\epsilon'_W/L_S)}$$

therefore,

$$\epsilon'_s(\theta) = \left[\epsilon'_R(15°)\left[\frac{V_s - V_w}{V_R - V_w}\right]\right]\left[1 + \frac{E_{2R} - L_w\epsilon'_w}{L_s\epsilon'_R(15°)}\right] - \left[\frac{E_{2s} - L_w\epsilon'_w}{L_s}\right]$$

The first term on the right hand side represents the main contribution to $\epsilon'_s(\theta)$. The other two terms are only minor corrections as shown in Appendix 3. The multiplicative correction is seen to be close to unity. Thus the working equation of the emissometer is,

$$\epsilon'_s(\theta) = \left[\epsilon'_R(15°)\left[\frac{V_s - V_w}{V_R - V_w}\right]\right] - \left[\frac{E_{2s} - L_w\epsilon'_w}{L_s}\right] \qquad (3.12)$$

The additive term $\left[\frac{E_{2s} - L_w\epsilon'_w}{L_s}\right]$ varies from about -1% at low $\epsilon'_s(\theta)$ values to about +0.1% at high $\epsilon'_s(\theta)$ values. Table 3.2 gives the values of this term calculated for various $\epsilon'_s(\theta)$. Using Eq.3.12 the directional emittance profile of a given sample is obtained from a set of $V_s(\theta)$ measurements in the required directions and the two additional measurements V_r and V_w.

The reference sample used in the present work is NEXTEL-2010 black-Velvet on a highly polished Aluminium substrate (32 mm x 32 mm x 2 mm) spray coated 6 times. This was calibrated by the National Physical Laboratory, Teddington, Middlesex - NPL Reference No: 150583. They measured $\epsilon'_R\lambda(15°, 298K, \lambda)$, for $1\mu m \leq \lambda \leq 50\mu m$ (Figure 3.35). The total directional

emittance at a polar angle of 15°, $\epsilon'_R(15°\ 298K)$, was found to be 0.953 ± 0.005, and would not be significantly different at 358K. Measurements were made using the reference sample within 6 weeks of NPL calibration.

It is of interest to look again at the flux components E_1 and E_4 in detail, to see how these depend on the various parameters involved. Referring to Fig. 3.12, $E_1(\theta)$ may also be written as,

$$E_1(\theta) = \sigma T_s^4 \cdot a_0 \cdot \epsilon'_s(\theta) \cdot F_{a_0 \to d} \qquad (3.13)$$

where a_0 is the projected sample area and where $F_{a_0 \to d}$ is the geometrical configuration factor (GCF) between the projected sample area and the detector active area. (As the detector active area is only 2 mm away from Aperture 3 and also larger than Aperture 3, $F_{a_0 \to d}$ ≈ GCF between sample effective area and Aperture 3.)

E_4 can be approximated by the component of flux that will be received at Aperture 3 from a sample of NEXTEL (coating on the side of the 2nd chamber) of the same area as Aperture 2, placed at Aperture 2, (this assumes that NEXTEL coating is a Lambertian emitter). Thus, E_4 may be written as,

$$E_4 = \sigma T_0^4 \cdot A_2 \cdot \epsilon'_{NEXTEL} \cdot F_{2 \to 3} \qquad (3.14)$$

where A_2 is the area of APERTURE-2 and $F_{2 \to 3}$ the GCF between apertures 2 and 3. Now equations 3.13 and 3.14 may be written respectively as,

$$E_1(\theta) = k_1 \cdot \epsilon'_s(\theta) \cdot T_s^4 \tag{3.15}$$

and,

$$E_4 = k_2 \cdot T_0^4 \tag{3.16}$$

where,

$$\left.\begin{aligned} k_1 &= \sigma a_0 \, F_{a_0 \to d} \\ k_2 &= \sigma A_2 \, \epsilon'_{NEXTEL}(15°) \, F_{2 \to 3} \end{aligned}\right\} \tag{3.17}$$

using these new definitions of E_1 and E_4 (i.e. Eqns. 3.15 and 3.16) and neglecting the smaller term E_2, equations 3.8 - 3.10 may be approximated as,

$$V_s(\theta) \propto R \left[k_1 \, \epsilon'_s(\theta) \, T_s^4 - k_2 \, T_0^4\right] \tag{3.18}$$

$$V_R(15°) \propto R \left[k_1 \, \epsilon'_R(15°) T_R^4 - k_2 \, T_0^4\right] \tag{3.19}$$

$$V_W \propto R \left[k_1 \, \epsilon'_W(0°) \, T_W^4 - k_2 \, T_0^4\right] \tag{3.20}$$

the first term in brackets in Eq.3.20 is also negligible and therefore,

$$V_W \propto - R \, k_2 \cdot T_0^4 \tag{3.21}$$

Equations 3.18/19/21 are used in section 3.4.7 in estimating the effect on $\epsilon'_s(\theta)$, of small increments in T_s, T_0 and T_W.

3.4 Experimental Details

3.4.1 Emissometer Component Assembly and Alignment Check

In discussing the assembly of emissometer components and their alignment it is necessary to refer to an imaginary axis called the 'radiometric axis' (Fig.3.14). The latter is defined as the line running symmetrically above the 'central rail' (Section 3.2.1.6), parallel to it, at a height of 160 mm above the base plate of the emissometer. Correct alignment of the emissometer is said to be achieved when all the following conditions are satisfied at all orientations ($-80° \leq \theta \leq +80°$) of the sample.

1) The points A,B,C,D and E in Fig. 3.14, i.e. respectively the centres of the absorber sample (surface), apertures 1,2,3 and the detector window, are colinear and coincident with the 'radiometric axis'.

2) The SHHA axis L - L' (Fig.3.5) is normal to the base plate (and therefore to the top plate).

3) L - L' axis intersects the radiometric axis orthogonally.

4) L - L' axis passes along the front surface of the sample.

The first check was carried out before fitting any of the components into the emissometer, except the SHHA. A dummy sample (with dimensions the same as other absorber samples) with the surface marked as shown in Fig. 3.14 was carefully mounted symmetrically on the heater block, checking by eye that condition 4 was satisfied. The SHHA was then inserted into the emissometer box as usual, and the front cover of the box removed. A pre-levelled He-Ne laser, with the height of the beam adjusted to be equal to that of the radiometric axis, was shone on to the sample centre as shown in Fig. 3.15. (The laser, mounted on an adjustable stand, was levelled by shining at a target at the far end of the laboratory bench and comparing the height of the beam at either end). The SHHA was then rotated, both clockwise and anticlockwise, until the beam was at grazing incidence on the sample. In doing this, the illuminated area of the sample would show the following behaviour, if and only if conditions 2) and 4) were satisfied.

The illuminated patch on the sample <u>always</u>,
a) stayed centred on the horizontal D - D' line (Fig. 3.14).
b) covered the sample centre A.

This was observed, confirming that conditions 2) and 4) were satisfied at all orientations of the sample.

The SHHA was now removed from the emissometer box, and all the other components, except the Golay cell, were installed

using the supporting base blocks etc., The machined surfaces of the base blocks ensured that all components were approximately at the heights required, above the emissometer base plate. A machined (cylindrical) rod of ≃ 20 mm diameter was then used, pushed in through the 2nd chamber into the exist port of the sample chamber, to establish alignment. The SHHA fitted with the dummy sample was now inserted back into the emissometer to carry out the next check.

A plane mirror was carefully fitted on to the Golay cell base block such that when mounted in position on the central rail it deflected any radiation from the direction of the radiometric axis, in a direction normal to it, and parallel to the base plate, as shown in Fig. 3.16. A travelling microscope, levelled with the lab bench surface, and adjusted to be at the same height as the radiometric axis, was then positioned looking towards the mirror in a direction normal to the radiometric axis. The surface of the dummy sample was illuminated using a small electric bulb inside the sample chamber taking care not to obstruct the field of view. Now when the microscope was focussed on to either Aperture 2 or 3, a <u>circular</u> illuminated area was seen centred in the field of view. This indicated that the centres of Apertures 2 and 3 were colinear with the radiometric axis. When focussed on to the sample surface the line markings (Fig. 3.14) were seen coincident with the cross hairs. On rotating the SHHA, this stayed unchanged, until at approximately +83° - -83° the sample edges were just visible. At +90° and -90°, half of

the field of view was covered by the sample edge. These observations confirmed that the centre of the sample surface, point A in Fig. 3.14, was on the radiometric axis, and also that the SHHA axis L - L' is normal to the base plane of the emissometer at all orientations of sample.

An additional check on emissometer alignment was carried out with the He-Ne laser used earlier on. A small 10 mm diameter plane mirror sample was centrally mounted on the heater block, and the SHHA was oriented at $\theta = 0°$. The travelling microscope was then replaced by the laser, occupying the same position (Fig.3.16). A bright spot of (reflected) laser light was seen less than 2 mm away from the exit aperture of the laser. This reconfirmed the alignment and also verified the zero setting on the SHHA scale, to an accuracy of within $\pm$ 0.3° (0.3° is approximately half the angle subtended by Aperture 3 at the sample surface).

Finally, the Golay cell was mounted on the movable platform and positioned with the caesium iodide window approximately 2 mm way from Aperture 3. To enable lateral (i.e. normal to the radiometric axis) alignment of the detector a Nextel absorber sample was mounted on the SHHA and oriented at $\theta = 0°$. The sample temperature was then set to a convenient value to provide a reading on the digital volt meter (DVM). The Golay cell was now moved laterally until the reading was maximised and then locked in position. This process ensured that the detector was receiving maximum sample flux, which

occurs when the centre of the active area, the point E in Fig.3.14, is on the radiometric axis.

With the alignment of the emissometer completed, the front plate was carefully fitted by tightening the screw bolts sufficiently to provide an air-tight seal.

3.4.2 Minimizing Stray Radiation

In using the directional emissometer, the ideal situation regarding radiation received by the detector is as follows:

1) when 'seeing' the sample, the detector receives only the radiation emitted directly by the active area of sample. i.e. the E_1 component referred to in Section 3.3.

2) When the sample beam is interrupted, the detector receives only the radiation emitted by an isothermal blackbody ambience (i.e. the E_4 term in Section 3.3).

In practice however, 1) and 2) above can only be approximated and the detector receives various other 'stray' radiations as discussed below.

This stray radiation can initially be grouped into 2 categories.

a) a quasi-static background of near-blackbody emission

at approximately T_0 (ambient temperature inside emissometer box).

b) a superimposed modulation component whose intensity is highly dependent on direction and location within the emissometer box.

a) originates from the coating of NEXTEL-VELVET, covering most of the surfaces within the emissometer.

b) arises solely due to the rotating chopper blade. The latter, with one of its sides silvered, causes a changing pattern of reflected radiation during a chopping cycle. Further complications arise due to shadowing effects and other reflecting surfaces (any non-coated surfaces and also coated surfaces at large specular angles) causing multiple reflections. The result is a periodic but modulated stray component whose intensity and form of modulation is highly dependent on direction and the position within the emissometer box.

Fig. 3.17 shows a breakdown of the 'stray' radiation components reaching the detector. Each of these will be discussed, in order of increasing importance.

Referring to Fig. 3.17, let F and C represent radiations reaching the detector other than through Aperture 2. The component F is represented in Eq. 3.6 (Section 3.3) by the term

E_3. This component has negligible effect on the detector output as the latter responds only to changes in the incident flux, within a limited band of frequencies as shown in the detector response curve in Fig. 3.20. C on the other hand may have some effect depending on the intensity and the form of modulation. The intensity however is minimised by having the detector window positioned very close ($\simeq$ 2 mm) to Aperture 3. In this position the field of view of the detector (cone of half-angle 45°) falls well within the NEXTEL VELVET coated Aperture 3 plug. Due to the high absoptance and the highly diffuse reflectance of this coating, type C radiation reaching the detector is highly attenuated.

When the chopper blade interrupts the sample beam, the radiation emitted by the NEXTEL coating (within an area limited by the field of view of detector) on Aperture 2 plug is reflected off the silvered side of the blade, and reaches the detector. This radiation has near-blackbody characteristics (at a temperature T_0) and constitutes most part of the term E_4^+ in Section 3.3 page 54. Along with this radiation however there can be other weak components of stray radiation that would be reflected off Aperture 2 plug (from the area 'seen' by detector). Any quasi-static component of near-blackbody radiation at a temperature significantly different from T_0 is identified as of type D. Any modulated component (as described under category b) earlier) accompanying E_4^+ can be identified as of type A. Both A and D however are expected to be negligibly small, due to the high absorption

and diffusing properties of the NEXTEL VELVET coating, in comparison with E_4^+.

Stray components of types E and B are particularly likely to cause problems with samples of low thermal emittance (i.e. with high thermal reflectance). These are normally suppressed by surrounding the sample with a highly absorbing and cooled enclosure. Several emissometers have used water cooled enclosures or apertures (Zerlaut 1963, Van der Leij 1979). The present design however has a Nextel coated sample chamber whose walls are cooled by a surrounding Liquid N_2 reservoir. The value of E in this case is estimated in Appendix 1.

When a sample enclosure is used, B type stray radiation causes problems by increasing the magnitude of E_2 term in Eq. 3.5, only when the sample is oriented at or near 0° (polar angle). When in this situation, in the present apparatus, B consists mostly of radiation emitted by the Aperture 2 plug towards the sample, with a very small contribution from the emission of the detector itself. With the dimensions of the Apertures as used in the present work, B becomes significant only when the polar angle is within the range 6° to -6°. (For this reason, when taking the V_R reading (Section 3.4.6) the reference sample was always oriented at 15°). It is possible, if necessary, for this range to be brought down to well within +1° to -1°, by filling the 2nd (chamber) reservoir as well with LN_2. This will almost completely stop

the emission from Aperture 2 plug and B would then consist only of the very small component due to detector emission. When the emissometer is used in this latter mode the temperature at which the sample is measured could in principle be taken down to much below 273 K, limited only by the increasing value of the E_2 term in Eq.3.12. In practice however, this mode of operation allows samples to be measured conveniently down to about 273 K.

3.4.3 Temperature Measurements

In radiometric emittance measurements, apart from those where the sample is located within and radiatively heated by a blackbody-cavity, exact determination of sample temperature is complicated due to the following.

a) A temperature gradient is present within the sample in the direction of heat flow. In the case of samples heated from the back surface this occurs mainly in the direction normal to the surface (i.e. through the thickness of sample). Additional gradients along directions parallel to the sample surface will exist due to heat loss from sample edges.
b) The perturbation of the sample temperature distribution, by the measuring instrument itself (e.g. thermocouple) introduces an error.

Thermal radiation emitted from the surface of a heated solar absorber sample (or any other non-metal sample), consists of

components originating from various layers of the material at differing depths from the surface. If the sample is isothermal, contribution to the total emission from the various components, would decrease exponentially with depth of the originating layer, at a rate dependent on the extinction coefficient of the material. However, in the case of most solar absorber samples in emittance measurements, temperature gradients exist as described in a) above. The effect on sample emission of temperature increasing with depth is to increase with depth the intensity of emission from the various layers, in proportion to the fourth power of the absolute temperature. Hence, as the nett result, a more even contribution from the various layers involved is obtained. Nevertheless the determination of the appropriate sample temperature in a given situation is not at all straightforward. With this in mind, the present method was devised not to require the value of the absolute sample temperature, in order to derive it's emittance. Indeed it does not require the values of any of the temperatures measured, in order to calculate the sample emittance, as can be seen from Eq. 3.12. Temperature measurements are essential however, in monitoring the measurement conditions such that any drifts or sudden changes in ambient temperature etc. that will lead to errors can be detected (and also to establish <u>approximately</u> the sample temperature at which the measurements were made, as total emittance is a slowly varying function of temperature).

The temperature parameter having the most effect on the measurement, as shown in Section 3.4.7, is the difference between the temperatures of the absorber and the reference samples at the time of measurement. For small temperature differences, the percentage error in the directional emittance value is seen to be equal to the temperature difference in degrees Kelvin. To minimise this error it was necessary to have the absorber and the reference sample located in nearly identical environments at all times. This was achieved by mounting these on either side of the heater block (Section 3.2.1.1). Temperature measurement, on both samples, was carried out in identical fashion (see later) using matched thermocouples, one per sample.

The two other temperatures monitored were that of the sample chamber wall (T_w), and of the side of the 2nd chamber (T_0) representing the ambient temperature. Both of these were done using thermocouples attached to the surfaces with low temperature adhesive (Oxford Instruments). The T_w thermocouple is positioned approximately half way up the sample chamber wall, about 30mm above the top of the sample. Thus the falling of the liquid nitrogen level within the reservoir, indicated by a sudden rise in T_w is detected well before the immediate surroundings of the sample are affected. The drift in T_0 on the other hand is comparatively small and is caused mainly due to cooling by the liquid nitrogen reservoir. This has been significantly reduced to approx. 0.5 K per 15 minutes by having the 2nd reservoir filled with water (see Fig.3.18).

All four thermocouples used in the emissometer were of type K, constructed in the form of insulated wires twisted together at one end and the tip welded in a reducing Ar atmosphere. Type K is recommended for use within the temperature range -250 to 1260 degrees C (ASTM Manual 1981). These thermocouples were chosen to be closely matched in performance, in particular the sample and the reference thermocouples (Table 3.1). This was done using a water bath at approx. 100°C and an ice (slurry) bath at approx.0°C. All thermocouples tested were inserted together into a 25 cm long piece of glass tubing that had one of its ends sealed. This was then inserted into either bath thus providing nearly identical heat transfer conditions for all the thermocouples.

The mounting of thermocouples on to the absorber and the reference samples was done using small PTFE pads (5 mm x 5 mm x 5 mm). The ends of the thermocouples are permanently inserted into the pads as shown in Fig. 3.10. A small amount of Silicone grease is also applied onto the thermocouple beads. These pads are then screwed on to the heater block trapping the sample in between. This method was convenient to use and also ensured that the thermocouple bead was in good thermal contact with the sample surface. The PTFE pad covered only a minimal area of the sample and virtually eliminated the radiative losses and minimised the convective losses from the thermocouple bead. In order to

minimise the heat loss from the thermocouple wire, which is already in a varnish impregnated fibre-glass sleeving, it was lagged with PTFE tape and covered with plastic heat shrink sleeving. This meant that the main form of heat loss from the thermocouple bead was by conduction through the wires. Here the recommended procedure of carrying the wires along an isothermal region (the top part of sample surface) for at least 20 wire diameters, was followed thus transferring the point of perturbation away from the point at which temperature is measured.

3.4.4 Sample Temperature Control

The sample temperature control system consists of a 'Comark - 6400 Microprocessor Thermometer', a Farnell stabilized d.c. power supply, the 'electronic switch' and the sample and reference thermocouples, as shown in Fig.3.4. The heater element is made up of six 1Ω vitreous wirewound resistors connected in series (section 3.2.1.1) and receives its power from the d.c. supply via the electronic switch. The latter is a 3-stage Darlington amplifier with high power dissipation and high speed switching capability whose circuit diagram is shown in Fig.3.19. The signal input to this is provided by the TTL compatible output of the Comark unit control channel. Depending on the input signal, the 'electronic switch' switches the heater current on or off.

The control loop in this system is formed by the Comark unit,

the electronic switch and the feedback thermocouple which is the thermocople of the appropriate sample being measured. The intended sample temperature and other control information is initially entered into the Comark unit via the front keypad. The loop then operates as follows. The output of the thermcouple is automatically corrected for thermocouple type and then compared with the stored control information by the Comark unit. This then produces the input signal to the electronic switch which regulates the heater current.

The Comark unit is capable of operating in three different control modes. For the present purposes the 'proportional control' mode has been selected. This mode requires the intended sample temperature and another parameter called the 'activation band setting' to be entered into memory and the way it functions is best explained by considering the following example. Assume that the intended temperature setting was 95°C and the activation band setting 2°C. In this situation if the sample temperature fed back was less than 93°C, the control channel output would stay continuously on, switching power on to the heater element. As soon as 95°C is exceeded the control output would begin to switch between on and off, once every second. In doing this the length of the 'off' period would increase in proportion to the difference between the intended temperature (95°C) and that fed back. If and when the latter falls below the intended temperature, the length of the 'on' time increases in proportion to the temperature difference.

In all present work, the sample temperature and the activation band setting were respectively 95°C and ± 2°C the same as in the example above. The time taken for a sample to reach the set temperature was always less than 2 minutes. This temperature, once reached, was observed to be held to within ±0.2°C of the set value.

All absorber samples used in the present measurements (including metal and glass samples), and the reference sample, have equal surface areas of 32 mm x 32 mm, completely covering the front or the back surface of the heater block when mounted. However in a given measurement the absorber and the reference samples would normally have differing emittance characteristics. Therefore, even when placed in identical environments, and using identical measurement techniques, the temperatures of these samples would differ due to the unequal radiative losses. This difference was, as expected greater when measuring low emittance samples. Hence it was important to have the power to the heater block controlled such that each sample (i.e. either the absorber or the reference) was at the same set temperature when facing the detector. This was easily achieved by changing the input to the control channel (from the absorber sample thermocouple to the reference sample thermocouple and vice versa), as required, (see Section 3.4.6).

3.4.5 Radiation detection and Signal Processing

3.4.5.1 Radiation detection

As the present emissometer was designed to measure total directional emittance, a spectrally averaged quantity, it was essential to employ a radiation detector whose response does not depend on the wavelength of incident radiation. The CATHODEON IR-50 Golay cell has a flat response within 1-1000μ. This is a characteristic basic to most 'thermal detectors', as they work on the principle of raising the detection element temperature by the absorption of incident radiation. In the Golay cell detector a thin highly absorbing membrane is positioned immediately after the detector front window. A volume of Xenon gas is trapped between this membrane and another positioned further in. The outer surface of the second membrane is silvered and reflects a beam of light emitted by a photodiode towards a photodetector. Whenever radiation is incident on the detector, the black absorbing membrane is heated and this in turn heats up the trapped Xenon gas causing it to expand. This causes a deflection of the mirror membrane, resulting in a change of output from the photodetector. This is then amplified and produces the output signal of the Golay detector. A fine leak in the Xenon gas reserve which connects it to an outer ballast reservoir, ensures that the device is insensitive to slow ambient drifts.

The Cathodeon - IR50 Golay cell used in the directional emissometer is fitted with a caesium iodide window which limits its spectral response to between 0.5 and 50 μm as shown in Fig.3.20. At a typical sample temperature of 373 K, 98% of the blackbody emission lies within this range (see Fig.3.21). Therefore this wavelength range allows measurements to be made with good accuracy at sample temperatures 300 - 500K.

A useful figure of merit that describes the 'sensitivity' of a radiation detetor is its specific detectivity, D^*. With monochromatic incident radiation at a wavelength λ, the spectral D^*, symbolised by $D^*_\lambda(\lambda,f,1)$, is defined as the rms signal to noise (voltage or current) ratio in a 1 Hz (signal modulation bandwith centred around the frequency f, per unit rms incident power per square root of detector area (Kruse 1977). For background limited detection the detector field of view needs to be specified. However the quantity more relevant to the present work is blackbody D^*, symbolised by $D^*(T,F,1)$, defined the same as above except that the incident radiation is from a blackbody at a temperature T degrees Kelvin.

In the case of an ideal thermal detector $D^*(\lambda,f,1)$ would equal the value of $D^*(T,f,1)$ at all wavelengths and temperatures. In terms of other measurement parameters, D^*, whether spectral or blackbody (depending on the source), may be expressed as shown in Eq.3.22.

$$D^* = \frac{(A_d B)^{1/2}}{q_i} \left[\frac{v_S}{v_N}\right] \qquad (3.22)$$

where v_S and v_N are respectively the signal and noise voltages at the detector output, A_d the detector active area, B the signal modulation bandwidth and q_i the incident radiant power.

Jones (1960) has defined D^{**} ("dee-double-star") as shown in Eq.3.22.a removing the need to specify the field of view when listing D^*.

$$D^{**} = \frac{(A_d B\Omega)^{1/2}}{q_i} \left[\frac{v_S}{v_N}\right] \qquad (3.22.a)$$

where Ω is the field of view of the detector. The units of D^{**} are cm $Hz^{1/2}$ $ster^{1/2}/W$. Fig.3.3 compares the D^{**} of a Golay cell with other conventional thermal detectors. This parameter however is rarely quoted in manufacturers literature.

Responsivity on the other hand is a measure of the dependence of detector output on the input radiant power. The blackbody voltage responsivity, $R_v(T,f)$, is defined as the ratio of the signal output from the detector in volts to the radiant power input to the detector in Watts, the latter originating from a blackbody source at absolute temperature T and being modulated at a frequency f.

The detectivity and responsivity of the Cathodeon - IR50 are:

D^*(500 K, 11 Hz, 1 Hz) = 0.6×10^{10} cm $Hz^{1/2}W^{-1}$ (at a 45° (half angle) field of view).

R_V(500 K, 11 Hz) = 3.0×10^6 V W^{-1}.

The other most important parameter for a radiation detector is linearity which is quoted by the manufacturers of the IR50 to be better than 1%, up to the maximum allowed chopped (10 Hz) input power of 2.3 10^{-6}W.

The high performance of the Golay cell as a radiation detector is complemented in the present system by the use of the phase sensitive detection technique.

3.4.5.2 Phase Sensitive Detection

Most phase sensitive detectors (PSD's) are based on the principle of the synchronous switch (Fig.3.22). The signal voltage is periodically switched into the load resistor, the frequency and the phase of the switching operation being determined by the reference voltage. Therefore for signals having the same frequency and phase as the reference, the detected signal voltage is of the form shown in Fig.3.22. This is further improved by having a balanced system resulting in full wave rectification as shown in Fig.3.23. Thus if the reference voltage is taken as $V_R \sin \omega t$, where ω

is the angular frequency, and the signal voltage as $V_S \sin(\omega t + \alpha)$, where α is the phase angle, then the resulting d.c. output voltage is proportional to $V_S \cos \alpha$.

Mathematically the operation carried out by a PSD corresponds to multiplying any input signal $V_S f(t)$, by a squarewave $f_R(t)$ of the same frequency as the reference signal, where,

$$f_R(t) = \sin \omega t + \tfrac{1}{3}\sin 3\omega t + \ldots \qquad (3.23)$$

Therefore with a given output (filter) time constant Z, the PSD output V_{PSD} may be written as,

$$V_{PSD} = V_S \cdot \overline{f_S(t) \cdot f_R(t)} \qquad (3.24)$$

where the averaging time is Z. Thus a PSD essentially performs a Fourier Analysis of $f_S(t)$ and extracts the component corresponding to $\sin \omega t$ (and its odd harmonics).

The overall filter characteristic offered by the present PSD system is that of a second order band pass filter, centred on the reference frequency, whose noise equivalent bandwidth Δf_{out} equals 1/4Z (Brookdeal Manual). In the case of 'white' noise, the noise voltage generated is directly proprotional to the square root of the noise equivalent bandwidth. Hence from the value of Δf_{out} above and the value of the noise equivalent bandwidth at the signal input to the PSD, the improvement in voltage S/N ratio may be calculated as shown below.

$$\frac{\text{voltage S/N ratio at output}}{\text{voltage S/N ratio at input}} = \sqrt{\frac{\Delta f_{in}}{\Delta f_{out}}}$$

The present PSD has a noise equivalent input bandwidth of 3 MHz and the output filter used in all measurements has a time constant of 10 seconds. Hence

$$\text{the improvement in S/N for white noise} = \sqrt{\frac{3 \times 10^6}{1/4 \times 10}} \approx 60 \text{ dB}$$

3.4.6 Measurement Procedure

The procedure adopted in using the emittance measurement apparatus is given below as a sequence of operating instructions.

1) Fill the 2nd reservoir with water.
2) Insert dummy plus into emissometer.
3) Purge emissometer with dry nitrogen gas for approximately 15 minutes.
4) Switch on, in order, the Comark unit, d.c. power supply, all signal processing electronics, chopper unit and the Golay cell power supply.
5) Fill (sample chamber) liquid nitrogen reservoir. When this is done at the beginning of a measurement session, allow approximately 30 minutes for the system to stabilize before taking readings. Any

subsequent fillings only require about 10 minutes settling time.

6) (During the settling time in 5) - Mount sample on SHHA.

7) Check that reference sample thermocouple is plugged in at the Comark unit control input.

8) Enter required sample temperature, activation band, thermocouple type and, if necessary, high and/or low alarm temperatures, via keypad of the Comark unit.

9) Check 'zero level' on PSD unit: by disconnecting the signal input lead and also by phase shifting the reference signal by 90° observing that the DVM output falls to zero in each case. (see PSD manual). This procedure is essential only at the beginning of each measurement session. Adjust as necessary.

10) Take V_W, T_O, T_W readings.

11) Open purging valve (on emissometer front plate) and the outlet valve on N_2 cylinder in quick succession.

12) Remove dummy plug and insert SHHA into emissometer.

13) Close N_2 cylinder valve and the purge valve in quick succession.

14) Set the reference sample to face the detector at an orientation of $\theta = 15°$.

15) Take V_R, T_O, T_R, T_W readings.

16) Plug in absorber sample thermocouple into Comark unit control input.

17) Set absorber sample to face the detector at the required angle.

18) Take θ, V_S, T_S, T_O, T_W readings.

19) Repeat 17 and 18 the required number of times, changing θ each time.

20) Plug in reference sample thermocouple into Comark unit control input.

21) Repeat 14 and 15.

22) Repeat 11.

23) Remove SHHA and insert dummy plug.

24) Repeat 13.

25) Take (an additional set of) V_W, T_O, T_W readings.

26) Repeat steps 5 - 25 with any number of samples as required.

27) Switch off all equipment.

It must be mentioned that even with continuous purging (steps 10 - 12) inserting or removing the SHHA is carried out as quickly as possible. This minimises the chances for outside air to enter the emissometer, which must be kept purged of water vapour during use, to prevent any condensation.

The refilling of the sample chamber/reservoir may be done at any time, but is usually at the beginning of a set of measurements with a new sample. Except at the very first time (at the beginning of a session), each filling gives approximately 50 minutes working time before T_W begins to drop. Time taken for a set of measurements on a sample ($-80° \leq \theta \leq +80°$ at 10° intervals) is usually less than 10 minutes.

3.4.7 Experimental Accuracy

In all the following analyses, and in calculating the total error in the present emittance measurements, the additive correction term in Eq.3.12 is neglected as it never exceeds 2%. Any change in the errors with polar angle θ is accounted for in Appendix 1 and the resulting corrections have already been applied. Thus for the present purposes the directional dependence of ϵ is neglected and a simplified form of Eq.3.12, as shown by Eq.3.25, is assumed. Note that all directional and angular dependence notation i.e. the superscript ' and (θ) are dropped from the equations for convenience.

3.4.7.1 Sensitivity of the total error to errors in V_S, V_R, V_W measurements.

$$\epsilon_S = \epsilon_R\left[\frac{V_S - V_W}{V_R - V_W}\right] \tag{3.25}$$

A small increment in the sample emittance, ϵ_S, due to small increments in the values of V_S, V_R and V_W may be written as shown in Eq.3.26.

$$\Delta\epsilon_S = \frac{\partial\epsilon_S}{\partial V_S}\Delta V_S + \frac{\partial\epsilon_S}{\partial V_R}\Delta V_R + \frac{\partial\epsilon_S}{\partial V_W}\Delta V_W + \frac{\partial\epsilon_S}{\partial\epsilon_R}\Delta\epsilon_R \tag{3.26}$$

using Eqns.3.25 and 3.26 it can be shown that,

$$\Delta\epsilon_s = \frac{\epsilon_R}{(V_R - V_w)} \Delta V_s - \frac{\epsilon_s}{(V_R - V_w)} \Delta V_R + \frac{(\epsilon_s - \epsilon_R)}{(V_R - V_w)} \Delta V_w + \frac{\epsilon_s}{\epsilon_R} \Delta\epsilon_R$$

and then using the approximation, $\epsilon_R = 1$

$$\frac{\Delta\epsilon_s}{\epsilon_s} = \frac{1}{(V_s - V_w)} \left[\Delta V_s - \epsilon_s \Delta V_R + (\epsilon_s - 1) \Delta V_w\right] + \Delta\epsilon_R \qquad (3.27)$$

Eq.3.27 shows the sensitivity of $\Delta\epsilon_s$ to the terms ΔV_s, ΔV_R and ΔV_w. Each of the above terms are made up of both systematic and random errors of measurement. It can also be seen from Eq.3.27 that for high emittance samples the effect of ΔV_w is quite small.

3.4.7.2 Errors in Sample Temperature Measurement

Let ΔT_s and ΔT_R denote the absolute errors respectively in the measurement of T_s and T_R. If the resulting errors in V_s and V_R are respectively δV_s and δV_R, then, using Eqns. 3.18 and 3.19 (page 61).

$$\delta V_s = \frac{\partial V_s}{\partial T_s} \Delta T_s = 4R\, k_1\, \epsilon_s T_s^3 \cdot \Delta T_s \qquad (3.28)$$

$$\delta V_R = \frac{\partial V_R}{\partial T_R} \Delta T_R = 4R\, k_1\, \epsilon_R T_R^3 \cdot \Delta T_R \qquad (3.29)$$

The total effect of δV_s and δV_R on $\Delta\epsilon_s/\epsilon_s$, i.e. $\delta\epsilon_s/\epsilon_s$, may be derived using Eq.3.27.

$$\frac{\delta\epsilon_s}{\epsilon_s} = \frac{1}{V_s - V_w} \left[\delta V_s - \epsilon_s\, \delta V_R\right]$$

using Eqns. 3.18 , 3.21, 3.28 and 3.29 this becomes,

$$\frac{\delta\epsilon_s}{\epsilon_s} = \frac{4R\ k_1\ \epsilon_s}{R\ k_1\ \epsilon_s}\left[\frac{T_s^{\ 3}\Delta T_s - \epsilon_R T_R^{\ 3}\Delta T_R}{T_s^{\ 4}}\right] \qquad (3.30)$$

now $\epsilon_R \simeq 1$ and $T_s \simeq T_R$; therefore Eq.3.30 becomes,

$$\frac{\delta\epsilon_s}{\epsilon_s} = 4\,\frac{\Delta(T_s - T_R)}{T_s} \qquad (3.31)$$

It is thus only the difference between T_s and T_R that determines $\frac{\delta\epsilon_s}{\epsilon_s}$. The latter when taken as a percentage, is seen from Eq.3.31 to be approximately equal to the temperature difference $(T_s - T_R)$, for sample temperatures around 400 K.

3.4.7.3 Error due to Drift in Ambient Temperature

Consider $(T_0 + \Delta T_0)$ to be the ambient temperature when taking a given V_s reading and T_0 the temperature when taking the V_R and V_w readings. Then using Eqn. 3.18

$$V_s = R\left[k_1\epsilon_s T_s^{\ 4} - k_2(T_0 + \Delta T_0)^4\right]$$

As $T_R \simeq T_s$ and $\epsilon_R'(15°) \simeq 1.0$, Eq.3.19 gives,

$$V_R \simeq R\left[k_1\ T_s^{\ 4} - k_2 T_0^{\ 4}\right]$$

Eq.3.21 is reproduced below for convenience.

$$V_W \simeq -R\, k_2\, T_0^4$$

now, $(T_0 + \Delta T_0)^4 \simeq T_0^4 + 4\, T_0^3 \cdot \Delta T_0$

Thus using the expressions for V_S, V_R and V_W above, and taking $\epsilon_R \simeq 1$,

$$\epsilon_R \left[\frac{V_S - V_W}{V_R - V_W}\right] = \epsilon_S - \frac{4k_2 T_0^3}{k_1 T_S^4} \cdot \Delta T_0$$

Thus $\delta\epsilon_S$ (in neglecting the drift in T_0) $= \dfrac{4\, k_2 T_0^3}{k_1\, T_S^4} \cdot \Delta T_0$ (3.32)

For typical values of $T_0 = 293$ K and $T_S = 368$ K, using $\dfrac{k_2}{k_1} = 0.92$ (calculated using Eq.3.17);

$$\delta\epsilon_S \simeq 0.0051\ \Delta T_0 \qquad (3.33)$$

For a typical set of measurements on a sample, taking < 10 minutes, ΔT_0 is seen from Fig. 3.18 to be approximately 0.3 K. Consequently, $\delta\epsilon_S$ due to ambient temperature drift, is seen from Eq.3.33 to be 0.0015. V_R, V_W readings are taken immediately before and after a set of measurements on a sample and it is the average values that are used in calculating $\epsilon_S'(\theta)$. Therefore the effective drift in T_0 is only ± 0.15 (i.e. ± half of the full range considered above). Thus the resulting error $\delta\epsilon_S$ is only 0.0008 which amounts to 0.08% in the case of a sample with $\epsilon_S = 1.0$, or, ±0.8% in the case of a sample with $\epsilon_S = 0.1$.

Thus using Fig. 3.18 and Eq.3.32 it is possible to obtain corrections for the drift in T_0 for any given measurement of $\epsilon'_s(\theta)$. Such corrections were made, the remaining error being negligible compared to those discussed in the next section.

3.4.7.4 Estimation of total Error in the present Emittance Measurements

Main contributions to the total error are considered below.

1) The random error in the V_S,V_R,V_W readings due to the radiation detection and signal processing system, is estimated to be ± 0.5.

   The value of V_R is approximately +12V while that of V_W is approximately -7V. The value of V_S varies between +12V (high ϵ') and -5V (low ϵ'), depending on the sample being measured. The random errors in V_S,V_R and V_W are therefore estimated as: $\sigma(V_S)$ = ± 0.025V to ± 0.06V, $\sigma(V_R)$ = ± 0.06V, $\sigma(V_W)$ = ± 0.035V.

2) The difference in temperature (τ_S-τ_R) between the absorber and the reference sample surfaces, even when reading the same temperature on the 'Comark', is estimated to be less than 1.5°C. This is due to the difference in the responsivity of the thermocouples (<±0.3°C, see section 3.4.3) and other installation effects - other errors associated with the 'Comark',

e.g. zero error, cold junction compensation error etc., cancel out exactly, as the same measuring input is used for both measurements. The resulting error in ϵ'_s calculated using Eq.3.31 is = ± 1.63%.

The change in $(\tau_S - \tau_R)$ during a run was ≤ ± 0.2K and so the effect of non-zero $(\tau_S - \tau_R)$ can be treated as an uncorrected systematic error.

3) The values of τ_S and τ_R will in principle differ from the average temperatures of the emitting regions, $\bar{\tau}_S$ and $\bar{\tau}_R$. For the samples investigated here it has been estimated (B.W.Jones, private communication) that the worst case is for the glass sample for which, if $\tau_S = \tau_R$, $\bar{\tau}_S - \bar{\tau}_R \leq -1.2K$. No corrections (which would be ≤ 1%) have been made for this (uncertain) effect.

4) The calibrated emittance value of the reference sample is given by the National Physical Laboratory as 0.953 ± 0.005 (NPL Calibration certificate No.150583). This corresponds to a 0.52% systematic error.

These errors can now the combined in the manner shown by Eq.3.34, where F is a function of the independent variables (a,b,c...).

$$\sigma(F)^2 = \left[\frac{\partial F}{\partial a}\right]^2 \sigma(a)^2 + \left[\frac{\partial F}{\partial b}\right]^2 \sigma(b)^2 + \left[\frac{\partial F}{\partial c}\right]^2 \sigma(c)^2 + \ldots \qquad (3.34)$$

The total error (ramdom and systematic) in the present directional emittance measurements thus varies from $\simeq$ 0.002 at $\epsilon' \simeq 0.05$, rising to $\simeq \pm 0.02$ at $\epsilon' \simeq 1.0$ (the fractional error thus falling as ϵ' rises).

3.5 Discussion of Results

Several solar absorber and other materials have been investigated using the present directional emissometer. These are listed in Table 3.3.

The samples were received from the various manufacturers during September 1983. These were then cut to the size of 32 mm x 28 mm and stored in a relatively dust free environment and away from solvent and corrosive vapours. Subsequently the directional emittance measurements were carried out during October 1983.

The measured values of total directional emittance are given in Tables 3.4 to 3.6. This data is presented in the form of polar diagrams in Figs. 3.24 to 3.26. This form of presentation is adopted by most workers and therefore enables easy comparisons to be made. All graphs were plotted on a CALCOMP-81 flat bed digital plotter connected to the DEC-20 mainframe at the Open University. The Fortran programme 'POLAR' written by the author incorporating SIMPLEPLOT graphics routines (Bradford University Research Ltd) is listed in Appendix 4.

The total directional emittance $\epsilon'(\theta)$ was measured, on each sample, at polar angles of emission within -80° to +80°. However, as no significant difference was found between the $\epsilon'(+\theta)$ and $\epsilon'(-\theta)$ values (any small difference found was much less than the experimental error), only the data for the positive angles are presented. High repeatability of the measurements is indicated by the following values of $\epsilon'(60°)$ for Skysorb, obtained on five different days: 0.135, 0.137, 0.137, 0.137, 0.138.

All present directional emittance measurements were made at a sample temperature of 95 C°. The solid angle of the detected beam, in all the measurements, was 0.11 millisteradians, indicating high directional resolution.

The emittance data are also presented in the form of 'emissive powers' in Figs. 3.27 to 3.29. The total hemispherical emittance values calculated using Eq.2.3.c are compared with other published values in Table 3.7 and are seen to be in general agreement. This calculation was done by carrying out the following summation.

$$\sum_{\theta=0°}^{80} \frac{1}{2}[\epsilon'_s(\theta) + \epsilon'_s(\theta^*)] \cdot \sin(\theta + \theta^*) \cdot (\theta^* - \theta)$$

where θ^* represents the polar angle of the data-point immediately following θ. However the lack of measured data at $\theta = 0°$ and at $80° < \theta < 90°$ required the following

assumptions also to be made.

(i) in all samples $\epsilon_s'(0°) = \epsilon_s'(10°)$

(ii) in all metal samples and in Maxorb and Skysorb,

$$\epsilon_s'(90°) = \epsilon_s'(80°)$$

(iii) in all non-selective absorber/dielectric samples and in Solarcoat-100 and Cusorb,

$$\epsilon_s'(90°) = 0.0$$

Assumption (ii) compensates for the rise in $\epsilon_s'(\theta)$ beyond 80° and the rapid drop down to zero at $\theta = 90°$. (iii) above is not really an assumption as this condition is expected to be true for all materials. It must also be noted that the effect on the calculated ϵ value, of errors in $\epsilon_s'(\theta)$ at the extreme angles, is relatively small due to the weighting factor sin 2θ in Eq.2.3c.

The error in ϵ consists of the random and systematic errors in ϵ' and the errors associated with assumptions (ii) and (iii). For assumption (ii) the error is $< \pm 1\%$ in ϵ and for assumption (iii) $< \pm 2\%$. Thus the overall error in ϵ varies from $\simeq \pm 0.001$ at $\epsilon \simeq 0.02$ to $\simeq \pm 0.02$ at $\epsilon \simeq 0.9$.

The materials studied in the present work (Table 3.3) fall into 3 different categories.

a) metals

b) solar selective absorbers

c) dielectrics / non-selective absorbers.

The study of the directional emittance of metals was for two reasons. Firstly, almost all commercial solar selective absorbers consist of one or more relatively thin solar absorbing (i.e. dielectric) layers on a metal substrate. The latter causes the characteristic high thermal reflectance as well as providing good thermal contact with the heat exchange medium (e.g. air, water) when used in a collector. Secondly, theoretical models are available that describe the directional behaviour of $\epsilon'_\lambda(\theta)$ for metals. The latter, strictly applying in the case of perfectly smooth and uncontaminated surfaces, with optical constants invariant with wavelength over $\simeq$ 3 to $\simeq$ 50 μm (corresponding to most of black body radiation at 368K), would still allow comparisons to be made with the results of the present work.

There seems to be, however, some inconsistency in one of the theoretical models (Bennett and Bennett 1967) with the experimental data available for metals. Fig. 3.31 compares the $\epsilon'(\theta)$ behaviour versus θ for aluminium predicted by the Bennett and Bennett (1967) model, with the experimental data obtained in the present work and that obtained for $\epsilon'_\lambda(\theta)$ by Schmidt and Eckert (1935), and also with the $\epsilon'_\lambda(\theta)$ behaviour predicted for metals by the Eckert and Drake (1972) model and fitted to the value of $\epsilon'_\lambda 0°)$ of the present work. The

experimental curves, while similar to each other and to the Eckert and Drake curve, differ markedly from that predicted by Bennett and Bennett. Consequently, the approximate $\epsilon/\epsilon'(0°)$ ratio for Aluminium calculated from the Bennett and Bennett curve $\simeq$ 1.0, is significantly different from the experimental values provided by many workers (see Fig. 3.30) and from the theoretical values calculated by Jakob (1949) for smooth metals. Most of the experimental data on metals from the present work is seen to agree reasonably well with the directional behaviour predicted by the Eckert and Drake model and the $\epsilon/\epsilon'(0°)$ ratios calculated by Jakob.

Figure 3.25 presents the $\epsilon'(\theta)$ curves for the solar selective absorber materials studied in the present work. At relatively low angles ($0° < \theta < 50°$) all the solar selective materials show $\epsilon'(\theta)$ slightly increasing with θ. This is rather similar to the behaviour of metals at low angles. At larger angles however their $\epsilon'(\theta)$ versus θ behaviour is distinctly different. $\epsilon'(\theta)$ of Skysorb increases rapidly beyond $\simeq$ 50° clearly showing metallic behaviour. In the case of Maxorb the increase in $\epsilon'(\theta)$ with θ is much less rapid. Cusorb shows a slight decrease in $\epsilon'(\theta)$ beyond $\simeq$ 75° while with Solarcoat-100 $\epsilon'(\theta)$ decreases steadily beyond 65°C, as is the case with typical dielectric materials (Fig. 3.26).

The near normal emittance of Solarcoat-100 is seen from Fig. 3.25 to be approximately twice that of Cusorb. Both these materials have copper as the substrate metal. This suggests a

higher thickness x extinction coefficient product for the absorbing layer in Solarcoat-100, resulting in a bigger contribution of thermal emission from the absorbing layer. This suggestion also agrees with the observation that $\epsilon'(\theta)$ versus θ behaviour of Solarcoat-100 is more 'dielectric like' than that of Cusorb, as discussed below. In the case of Skysorb the value of the near normal emittance ($\epsilon'_{Skysorb}(10°)$ = 0.109, see Table 3.5) is very close to values published for the substrate metal. $\epsilon'(0°)$ of stainless steel 304 has been measured to be 0.111 at 362K by Lohrengel (1969) and to be 0.10 at 356K by van der Leij (1979). This indicates a relatively small thickness x extinction coefficient product for the absorbing layer in Skysorb, as is also suggested by the strongly metallic $\epsilon'(\theta)$ versus θ behaviour observed in Fig. 3.25.

A detailed analysis of the data in Fig.3.25 is beyond the scope of the present work and is anyhow difficult requiring a knowledge of many parameters like the effective complex indices of refraction of the absorbing layer and the substrate, thickness of the absorbing layer (Thakur and Raman 1983, Seredenko 1979) and the surface microstructure. However, the observed change in the behaviour of $\epsilon'(\theta)$ versus θ (from metallic at low θ to non-metallic at high θ) can be understood by simple considerations. Most solar selective surfaces consist of a thin dielectric solar absorbing layer on a metal substrate. In the direction of the surface normal and at relatively small polar angles away from it, thermal emission is essentially from the substrate only and this is

transmitted practially unattenuated through the solar absorbing layer. However, at larger angles, the path length through the absorbing layer increases and consequently also the contribution to the total sample emission. Additionally at larger angles, the emission from the substrate is further attenuated due to the increased path length through the absorbing layer. Thus, particularly in the case of selective surfaces using a relatively thick layer of absorbing material, dielectric-type behaviour (see Fig.3.26) is to be expected at larger angles away from the surface normal. A sharp decrease in the $\epsilon'(\theta)$ to zero is predicted for metals at a polar angle in the vicinity of $\theta = 90°$. However, the above discussed changes are expected to occur well before this). This effect is clearly demonstrated in the work of Papini and Papini (1982) who observed the change in the directional emittance characteristic of NiCu and NiP, respectively during electrolysis and chemical etching, while the surface layer of the sample changed from being a metal to a dielectric (see Fig. 3.32).

The measured directional emittance profiles of the non-selective solar absorber/dielectric materials are given in Fig. 3.26. In the case of the non-selective absorbers, at larger polar angles, $\epsilon'(\theta)$ is higher than that expected for a perfect dielectric material (Siegel and Howell 1981). This may possibly be due to some susbtrate emission, as a result of the much increased $\epsilon'(\theta)$ of metals at large angles, and/or a surface roughness effect of the dielectric surface.

Similar behaviour in the $\epsilon'(\theta)$ of a 100 μm thick PET (polyethylene terephthalate) film has been observed by Rubin (1982). With the glass sample however, the measured data are seen to agree well with the theoretical curve for a smooth ideal dielectric of refractive index $n \simeq 2.0$ (Siegel and Howell 1981). Note that the glass sample was optically thick with respect to radiation at 368K (Eckert and Drake (1972)), with an imaginary part of the refractive index $K \gg n$. Thus it can be considered to be an ideal dielectric, though note that the theory applies to a given n, whereas n is likely to vary somewhat over $\simeq 3$ to $\simeq 50$ μm though presumably some average n can be used. . However, in the case of highly absorbing and relatively smooth dielectric samples showing near ideal dielectric behaviour of $\epsilon'(\theta)$ versus θ, measurements of the spectral directional emittance can be a useful method of obtaining information on the real part of the complex index of refraction.

The near normal emittance of Nextel as measured in the present work was 0.975 ± 0.02. However the near normal emittance of the Nextel reference sample, as measured by the NPL, was 0.953 ± 0.005. Although these figures agree within experimental errors, any differences could be attributed to differences in the two separate Nextel preparations used and the differences in the methods of sample preparation. An aerosol can of Nextel spray was used on a polished aluminium substrate for preparing the reference sample. The other measured sample was dip-coated onto an unpolished aluminium

substrate.

The ratio $\epsilon/\epsilon'(0°)$ for a given solar absorber material is also of interest. The values for the materials studied in the present work are plotted as a function of $\epsilon'(0°)$ in Figure 3.30. Other published values and theoretical curves for smooth metal and dielectric samples (Jakob 1949) are also included in Fig. 3.30. It seems tha these theoretical curves apply to the total case (they certainly apply to the spectral case).

As might be expected Fig. 3.30 shows most of the metals and dielectrics to lie fairly close to the theoretical curves. The traditional use of this plot is in the estimation of ϵ from a known value of $\epsilon'(0°)$, as the latter tends to be the more readily available (Touloukian 1972). However, when the $\epsilon/\epsilon'(0°)$ ratios of solar selective absorber (SSA) materials are added to this plot, an interesting comparison (suggested by the author) can be made between a given SSA material and the metal used as the substrate. For the purpose of the following discussion a term 'ideal spectral selectivity' is defined as follows. A SSA material is said to be ideally spectrally selective if, <u>at the thermal wavelengths concerned</u>, the solar absorbing layer of the absorber is totally transparent. (We <u>do not</u> concern ourselves with the absorptivity of the material at solar wavelengths. Hence 'ideal spectral selectivity' should not be confused with 'ideal solar selectivity', which refers to a step function

like absorption characteristic with a cut off at about 2μ.)

Thus, when a given SSA material has 'ideal spectral selectivity', the two points in the $\epsilon/\epsilon'(0°)$ vs. $\epsilon'(0°)$ plot corresponding to the SSA material and the substrate metal would coincide. Unfortunately, the converse of this is <u>not necesarily</u> true. This is because it is not impossible for the $\epsilon'(\theta)$ characteristic of a SSA material to <u>differ</u> from that of the substrate metal yet keeping the ratio $\epsilon/\epsilon'(0°)$ unchanged. However this is exceptional (mostly to be expected with materials <u>highly</u> dependent on the surface roughness/wavefront discrimination technique) and with a majority of materials the 'relative displacement of the two points' is an indication of the 'spectral-selectivity' as explained below.

The solar absorbing layer of a SSA material, being a dielectric, adds to the emittance of the metallic substrate. This tends to increase the normal emittance and in the absence of other effects would cause the point for SSA material to be displaced along the increasing $\epsilon(0°)$ axis direction, away from that for the substrate metal. However, the entries for <u>Cusorb</u> and <u>Skysorb</u> in Figure 3.30 also show a downward displacement indicating a reduction in the value of $\epsilon/\epsilon'(0°)$. This is normally to be expected due to the following reasons. The $\epsilon/\epsilon'(0°)$ for a given material depends only on the <u>shape</u> of the directional emittance characteristic $\epsilon'(\theta)$ (assuming of course no dependence of ϵ' on Φ). Typical

$\epsilon'(\theta°)$ characteristics of metals have a large increase in $\epsilon'(\theta)$ at high θ before decreasing towards zero at grazing values of θ (see Fig. 3.24). This type of $\epsilon'(0)$ behaviour will always result in $\epsilon/\epsilon'(0°)$ values greater than unity as the range of angles at which $\epsilon'(\theta) < \epsilon'(0°)$ is quite small. For typical dielectric materials, on the other hand, $\epsilon'(\theta) < \epsilon'(0°)$ at all θ, resulting in values of $\epsilon/\epsilon'(0°)$ less than unity. Hence for SSA materials, the position on the $\epsilon/\epsilon'(0°)$ vs $\epsilon'(0°)$ diagram is expected to be lower than that for the substrate metal, due to the influence of the dielectric solar absorbing layer.

From the above considerations, one would expect that for SSA materials that show a highly metallic type $\epsilon'(\theta)$ behaviour, the 'relative displacement of the points' (i.e. the points for the SSA material and the substrate metal) in the $\epsilon/\epsilon'(\theta)$ vs. $\epsilon'(0°)$ plot would be small compared to the SSA materials that show a highly dielectric type behaviour. This is clearly seen by comparing Figs. 3.30 and 3.25. In the case of Skysorb the points are closest together (fig. 3.30) and in Fig. 3.25 a clearly metallic type $\epsilon'(\theta)$ behaviour is shown. For Cusorb and Solarcoat-100 the 'relative displacement of the points' are in agreement with the shape of their respective $\epsilon'(\theta)$ characteristics in Fig. 3.25.

This use of the $\epsilon'(\theta)$ vs. $\epsilon'(0°)$ plot becomes rather superfluous when $\epsilon'(\theta)$ data are available for a given sample. However when only ϵ and $\epsilon'(0°)$ values are known this analysis provides a useful indication of spectral selectivity.

Another important outcome of the present emittance work has been providing data contrasting with that of Hutchins (1979), one of the few other sources of experimental data on directional emittance of solar absorber materials. Hutchins' data at 310K for blue oxidized stainless steel is compared with that from the present work in Fig. 3.33. Total directional emittance curves obtained by the same author for other solar selective materials are shown in Fig. 3.34. The prominent peaking of $\epsilon'(\theta)$ seen in all of Hutchins' curves $0° < \theta < 30°$ (Fig.3.34) is not seen in any of the directional emittance curves obtained in the present work.

Hutchins (1979) believes that this unexpected peaking in $\epsilon'(\theta)$ is due to a surface roughness effect and refers to the work of Birkebak and Abdulkakir (1977). The latter propose a theoretical model for predicting the spectral directional emittance (ϵ'_λ) of roughened metal surfaces. This model assumes a random rough surface with a Gaussian distribution of heights and slopes (of the surface roughness elements), and also takes into account the random blockage of some elements by adjacent ones in the direction of observation. The general prediction is that ϵ'_λ of a rough metal surface increases with increasing surface roughness for angles up to about 60°. Beyond this, ϵ'_λ is smaller than that of the perfectly smooth surface (of the same material) and decreases with increasing roughness. This model does not predict the occurrence of a maximum in the directional distribution of

ϵ', nor a maximum in the directional distribution of ϵ'_λ, at approximately 25° away from the surface normal (nor indeed even at 60°) as quoted by Hutchins (1979). Maxima at approximately 25° are however seen in the plots of $\epsilon'_\lambda.\cos\theta$ versus θ, as presented by Birkebak and Abdulkadir (1977) (see Fig. 3.36).

The other drawback in Hutchins' (1979) explanation is that it implies nearly identical surface texture for all the samples he has studied (see Fig. 3.34), as the maxima in all the curves seem to occur at around 25°. This is rather unlikely as the various samples are on different substrate materials, and prepared using quite different techniques.

In Hutchins' (1979) directional emittance measurement apparatus, there was no sample enclosure (for example, like the cooled sample chamber used in the present work) other than a blackened cover over the whole of the apparatus. Thus a possible explanation for the observed peaks could be that they were caused by a stray component of radiation. If this is the case then this would highlight the importance of extreme care necessary in making directional emittance measurements, particularly in the suppression, or in accounting for, the various stray components that may also be highly directional and/or position dependent.

An earlier work reporting on the effect of surface roughness on the directional distribution of <u>total</u> emittance of metals

is that of Rolling et al (1967). They studied the effect of roughness on the ϵ' of Platinum at 865°K and some of their results are shown in Fig. 3.37. These data agree in general with the predictions of Birkebak and Abdulkadir (1977) except that the angle at which $\epsilon'(\theta)$ becomes smaller than that of the smooth material is approximately 75°, instead of 60° as predicted by the model.

The main conclusions arrived at in this section are summarized later in Section 5.3 along with some recommendations for future work. Comments on the overall performance of the directional emissometer and suggestions for improvement are given in Section 5.2.

CHAPTER 4 BIDIRECTIONAL REFLECTANCE (BDR) WORK

4.1 A brief survey on the applications of bidirectional reflectance measurements

The earliest known bidirectional reflectance (BDR) work is that by Bouguer (1760), in his attempts to verify Lambert's cosine law of diffuse reflection (Section 2.4). Since then similar investigations have been carried out by many workers using various forms of BDR apparatus (Wright 1900, Pokrowski 1924, Schulz 1925, Barkas 1939, Budde 1969, Hofert and Loof 1964, Look 1965). Apart from its recent application in characterising solar energy materials, measurement of BDR has been used in many other areas of work some of which are listed below.

1) Analysis and modelling of light baffles and the stray light rejection in Optical systems (Proceedings of SPIE vols. 257,362,384,511).
2) Measurement of reflectance properties of paints and colloids (Wyatt 1982)
3) Studies on reflectance properties of materials for space applications (Hubbs et al 1982)
4) Characterisation of radiometric reflectance standards (Stuhlinger et al 1981, Clarke et al 1977)
5) Radiation scattering studies of thin films and surfaces (Bosquet et al 1981)

6) Studies on the effect of surface roughness on reflectivity (Herold and Edwards 1966, Birkebak and Eckert 1965)

7) Radiation scattering studies of compact particulate media (Agnew et al 1953)

The first (known to the author) reference to bidirectional reflectance characteristics of solar energy materials was by Edwards and Catton (1966). They were investigating the spectral variation of directional emittance and bidirectional reflectance of various rough and oxidised metals over solar and thermal wavelengths. It was demonstrated that very slight changes in the surface texture of the samples led to large changes in the bidirectional reflectance distribution and also that sandblasting ordinary metals with very small particles (14 μm diameter) resulted in surfaces with significant solar spectral selectivity.

An illustrative example of the use of the BDR technique in studying the degradation of the radiative properties of solar absorbers is given by Egan and Hilgerman (1979). They made BDR measurements on several absorber samples before and after one year's exposure to solar radiation. Fig. 4.1 shows the results obtained for 'Alcoa Brown'. After exposure not only is there an increase in reflectance particularly at larger angles away from the incident direction but also a resulting shift in the specular peak. This is believed to be caused by a change in the surface microstructure due to heating of the

absorber to temperatures beyond the recommended range, under stagnation conditions.

The use of lasers as radiation sources for BDR measurements (as in the present work) has been reported by several groups (Stuhlinger et al 1981, Bousquet et al 1981, Hsia and Richmond 1976, Choudhury and Sehgal 1982 and Nepogodin et al 1984). Stuhlinger et al (1981) worked at 0.633, 3.39 and 10.6 μm wavelengths using a focussed input beam forming a 10 mm diameter illuminated area on the sample (see Section 4.3 on methods of illuminating sample). The work of Bousquet et al (1981) also involved a focussed input beam at 0.633 μm. Hsia and Richmond (1976) investigated the bidirectional reflectance of black optical coatings, using equipment similar to that described above, at 0.633, 1.15 and 3.39 μm. The BDR measuring apparatus used by the last three groups mentioned above have used a 'double detector' system as has been done independently in the present work (Section 4.3.3).

Although the BDR technique has been used by several groups in characterising mirror materials (e.g. Petit 1977), the only other measurements reported (apart from the present work) on the bidirectional reflectance of solar absorber materials are by Choudhury and Sehgal (1982), Egan and Hilgerman (1979) and Van Heeraveld et al (1984). The first group made measurements around the specular direction for several incident angles on 'black Cobalt', at 0.633 μm. The third group have reported BDR measurements in the plane of

incidence at θ_i = 20° for rough copper samples at several wavelengths between 0.6 and 1.0 μm.

The BDR work reported in this work is on six different solar absorber materials. Measurements have been made on each sample using near collimated beams from two laser sources (0.633, 1.15 μm), at two angles of incidence, 0 and 40 degrees, and over a wide range of reflectance angles in and around the plane of incidence (Section 4.7.1). These two incident angles were chosen for the following reasons. θ_i = 0° is unique and is an important direction in the radiometric characterization of a surface and in radiation exchange calculations. θ_i = 40° provides a direction sufficiently away from the surface normal, yet at which the area of the illuminated patch on the sample is only slightly bigger.

4.2 Description of the present BDR apparatus

The present BDR apparatus is of the type where the sample is oriented with respect to a fixed incident beam, and the direction of the detected beam is then set as required. The design of this instrument is based on a unique device, called the 'Sample and Detector Assembly' (SDA). The latter is used for mounting, positioning and orienting both the sample and the detector (see Fig. 4.2). The polar and azimuthal angles of the detected beam can be set totally independently of θ_i, the polar angle of incidence. A change in the φ_i setting, $\Delta\varphi_i$ say, affects all φ_r readings by adding only a

constant offset of the same magnitude and polarity ($\Delta\varphi_i$). (All measurements in this thesis however have been carried out at a constant φ_i setting for any given sample.) All angles are read directly off the calibrated scales of the SDA, eliminating the need to use complicated trigonometric transformations. The other main feature of the SDA is its compact size, enabling it to be housed within a light-tight enclosure (called the BDR box) measuring only 395 mm x 335 mm x 275 mm. The relatively small dimensions of the SDA were possible because the samples for which this device has been mainly designed for, i.e. solar absorber materials, by requirement have low reflectance values. Hence multiple reflections between the detector and sample are negligibly small for most measurement geometries. Particular care however needs to be taken in choosing the solid angle of detection and the incident beam width if measurements are to be made very close to the incident direction at normal (or near normal) incidence. Details of the SDA are discussed in Section 4.4.1.

Figure 4.3 is a schematic diagram of the complete experimental apparatus. It is seen that two radiation detectors (both RS large area - 100 mm^2 - photodiodes) are used within the BDR box. The first detector, mounted on the SDA, measures flux reflected off the sample. The second detector receives a component of flux reflected off the beam splitter. The ratio of the power in this component to that in the incident beam remains a constant. Hence the output of

the second detector is directly proportional to the intensity of the incident laser beam. By taking the ratio of the outputs from detectors 1 and 2 (at the ratiometer), the value of the relectance measured is made highly insensitive to any changes in the incident intensity, particularly due to thermal drift in the laser output. This is further discussed in Section 4.4.2.

The two lasers used are a Melles Griot (LHR321) 633 nm unpolarized 3mW He-Ne laser and an Aerotech (1S5R) 1152nm unpolarised 1mW He-Ne laser. The latter has the laser tube and the power supply within the same housing while in the former the cylindrical laser tube and the power supply come as two separate units. The 633nm laser tube was therefore mounted on top of the infrared laser housing using two 'V-blocks' as shown in Fig. 4.4. The infrared laser itself is mounted on an adjustable platform above the base plate, as shown in the photograph. The 1/2" thick steel base plate, on which all components are mounted (excepting signal processing electronics), provided a useful datum during the assembly of components external to the BDR box.

The required laser beam (i.e. the red or the infrared) is obtained by first opening the beam output shutter on the laser head and then by having the rotatable mirror M2 (Fig.4.3) in the appropriate position. In one position M2 deflects the red beam into the BDR box while in the other it allows the infrared beam through. The other mirror in the

beam steering pair for the red beam, M1, is kept fixed after initial setting up and alignment.

The selected beam then passes through a beam chopper (Ortec Brookdeal 9479) placed immediately after the mirror assembly and enters the BDR box through the filters and the baffle tube. Inside the BDR box, a X10 beam expander (ORIEL- 1560 series Galilean Telescope design and without spatial filtering) and an adjustable mirror (M3) are mounted on an optical bench as shown in Figure 4.5. The expanded beam is then deflected towards the sample by the mirror M3 and passes through a variable aperture. This allows the diameter of the beam incident on the sample to be varied. In the present work two separate beam diameters have been used, a) approximately 1.5 mm diameter, called the NARROW BEAM, b) approximately 5.0 mm diameter, called the WIDE BEAM. Mirror M3, the beam expander the variable aperture and the second detector are all enclosed within a light baffle made of matt black paper. This has a 10 mm square exit aperture which stops much of the scattered light and lets through only the direct beam exiting from the beam splitter towards the sample. The second detector is separately shielded from scattered light and only receives the beam reflected off the beam splitter. The overall level of scattered light within the BDR box is highly reduced by having all the inside walls and most surfaces coated with highly absorbing Nextel Velvet.

The total number of optical components employed within the BDR box has been kept to a minimum. No collimating optics were necessary due to the use of a highly collimated laser beam (to better than 0.5 m radians - see Instruction Manuals) as the radiation source and also no collection optics were necessary due to the choice of the large area photodiode as the detector (see also Section 4.4.2). Fewer optical components meant that scattered light was reduced and that the opportunities for optical misalignment were less.

Incorporating the beam chopper and the phase sensitive detection system offers the same high level of performance as discussed earlier in Section 3.4.2.

The method of operation is as follows. First the sample is mounted on the SDA and the required directions of the incident and the detected beams are set. The BDR box cover is then replaced and the reflectometer output signal is processed by the 'electronics' and read off the digital voltmeter. Details of the measurement procedure are given in Section 4.4.4.

4.3 Methods of Illumination and Detection and Definition of Sample Area.

In Section 2.2.2 a definition for spectral bidirectional reflectance has been given involving quantities of infinitesimal extent in,

a) solid angle of incidence and exitance ($d\omega_i$, $d\omega_r$)

b) sample surface area (dA)

c) wavelength ($d\lambda$)

In practice however, what is measured is a quantity involving averages over finite intervals of $\Delta\omega_i$, $\Delta\omega_r$, ΔA and $\Delta\lambda$. These must be made 'sufficiently small' for the measured quantity to be a good approximation to the derivative. The 'sufficiently small' condition has been defined by McNicholas (1928) as "... that a further decrease will not alter measurably either the angular distribution of the reflected flux or its ratio to the incident flux".

$\Delta\omega_i$ and $\Delta\omega_r$ in a given measurement depend respectively on the source and collection optics used. The incident beam may either be focussed onto the sample or left as a collimated beam, while the detected beam may or may not be focussed on to the detector active area. A focussed incident beam in general involves a smaller sample area and consequently results in a higher incident intensity. Also, measurements can be made at more extreme angles, before the illuminated area begins to spill over the sample edges. A collimated incident beam, on the other hand, does not restrict angular resolution as it effectively means a solid angle of zero for the incident beam (Mille and Vun Kannon, 1967).

The use of a laser as a source however combines the above advantages (obtained when using either focussed or collimated illumination from conventional sources) as a highly collimated yet a small diameter beam is obtained from most common lasers. (The present 633 nm beam has a divergence of approximately 1 mrad. and a beam diameter of approximately 0.8 mm at the $1/e2$ limit of the Gaussian power distribution.) A beam expander may be used if desired. In the present BDR apparatus however the beam expander/limiting aperture combination offers the advantage of much more uniform intensity across the beam width than the 'Gaussian-form' obtained with only the direct beam. The high intensity of a laser source is particularly useful when measuring a strongly absorbing sample with a highly diffuse reflectance (see Section 4.4.2) as in the case with most non-selective solar absorber coatings. A possible disadvantage however in using laser sources is the restricted range of wavelengths available.

The interval ΔA (in the definition of BDR) depends on the adopted definition of 'sample area'. The latter may be defined in 3 ways as shown in Figure 4.6 (Nicodemus, 1977).

a) as the illuminated area on sample
2) as the area of sample surface 'seen' by the detector
3) as the exposed area of sample, limited for example by a mask placed on top or, by the sample edges.

Any of the above methods may be used with any combination of focussed or collimated illumination and detection. Method 3 however involves over-illumination and over-detection and therefore extreme care is needed in avoiding stray reflections from the edges of sample or from the mask, sample mount etc. Method 1 is used in the present work and the illuminated area of sample at normal incidence is approxmately 1.5 mm diameter with the narrow beam and approximately 5 mm diameter with the wide beam.

4.4 Experimental Details

4.4.1 Sample and Detector Assembly (SDA)

Figure 4.2 shows a sketch of the SDA. The main components of the assembly, listed below have been machined out of 'Duralumin'.

1) base plate
2) support block
3) quadrant plate
4) detector tracking arm
5) detector carriage

The function of the SDA is to accommodate the sample and the detector and to allow the directions of the incident and the detected beams to be set to the required polar and azimuthal angles. This is easily done by orientating the sample in two

ways and by moving the detector relative to the sample in two ways. All these adjustments are carried out with reference to a unique point on the SDA, called the 'centre of rotations'- C - (see Fig. 4.2)about which all rotations of the SDA occur. This point can be defined using an imaginary line normal to the quadrant plate and passing through the centre of the sample holder recess. The plane of the quadrant plate surface facing the tracking arm, is then intersected by the imaginary line at the 'centre of rotations'.

Mounting the sample

The sample holder diameter is 30 mm (see Fig. 4.2). Therefore a sample of a suitable size, typically 15-20 mm square, is lightly glued onto the sample holder and partially inserted into the recess on the quadrant plate. Two polished metal slabs (approx. 50 mm long) are then placed across the sample holder, catching the sample at only near the edges. The sample holder is then pushed home by pressing on to the metal slabs until they touch the surface of the quadrant plate and the slabs are then removed. This method ensures that the surface of the sample is flush with the quadrant plate surface, containing the 'centre of rotations'. The hole at the centre of the recess is lined with a Nylon bush providing smooth movement of the sample holder stem through it.

Orientating the sample

The quadrant plate (now containing the sample) can be rotated around a horizontal axis, M-M', parallel to the edge of the quadrant plate and passing through 'C', as shown in Fig. 4.2. This allows the polar angle of incidence to be continuously varied from 0° to near 90°. This setting is done by loosening a locking screw on the far face of the support block, which also contains a graduated scale for reading the angle.

The azimuthal angle of incidence is set by turning the sample holder around its own axis. The latter is in a direction normal to the sample surface and passing through 'C'.

Mounting and orientating the detector

The 1" diameter disc shaped photodiode casing is glued at the back, centrally onto a 10 mm dia. support rod as shown in Fig.4.2. The photodiode - support rod combination is held by the detector carriage and can be moved towards or away from the sample, changing the solid angular extent of the detected beam. The latter is thus continuously variable within the range 0.1 - 0.02 steradians (or less if a smaller area detector is used).

The detector carriage can slide along the calibrated tracking arm, continuously changing the polar angle of detection

within the range 0° - 80°, and is locked in position using the knurled knob.

The tracking arm is fitted into an accurately machined slot on the quadrant plant, and locked in position using a 'winged screw'. Ten identical slots have been machined regularly along the edge of the quadrant plate as shown in Figure 4.2. Therefore when changing the azimuthal angle of detection the tracking arm is simply unscrewed and fitted into the required slot. This procedure allows accurate positioning and re-positioning of the tracking arm with the azimuthal angle of detection set at any one of the 10 angular positions, 180°-270° (at 10° intervals) relative to the plane of incidence.

4.4.2 Radiation Detection and Signal Processing

The two radiation detectors used in the present BDR apparatus are both infrared enhanced Silicon photodiodes. The first detector, i.e. the one measuring flux reflected off the sample, also has a diffuser plate mounted in front of it. The purpose of this is to compensate for any polarization dependance in the photodiode response and it also helps to overcome any point to point variations in the sensitivity of the photodiode. This is necessary because although the radiation incident on the sample is unpolarized, (see appendix 2), the beam that is reflected towards the detector is in general slightly polarised. The diffuser plate

therefore performs the function of a depolariser. In the case of the second detector this is not required, as the geometry of measurement remains unchanged.

The spectral responsivity of the photodiode is shown in Fig. 4.7. The responsivity at 1150 nm, although aproximately a factor of ten down from that at 633 nm, is still adequate for the present work as will now be shown. Consider the following situation. The sample to be measured is highly absorbing and has only a 3% spectral directional-hemispherical reflectance at 1150 nm. (typical of many high α solar absorber materials). If the sample is also assumed to be perfectly diffuse, then the power incident on the photodiode active area (100 mm^2) positioned 70 mm away from the sample surface, when using the 1150 nm/1 mW laser, is of the order of 2.0×10^{-8}W. If however the sample is assumed to be non-uniformly diffuse, then there could conceivably be a further reduction of a factor of ten in the reflectance in certain directions, bringing the power incident on the photodiode down to $\simeq 2.0 \times 10^{-9}$W. The noise equivalent power of the photodiode at 1150 nm being 20 pW (measured at 10 V bias, 1 kHz chopping frequency and 1 Hz electrical bandwidth) would still result in a signal to noise ratio of apporoximately 40 dB. This detector therefore has the attractions of extended spectral response, low noise equivalent power, large active area and ruggedness in use.

It was necessary however to incorporate a dual channel preamplifier within the BDR box as the current responsivity of the photodiode at 1150 nm is only 30 nA/μW. This was designed (see Figure 4.8 for circuit diagram) around the CA3130 op amp integrated circuit. The latter device has a MOSFET input stage and hence an input impedence of $\simeq 1.5 \times 10^{-12}\Omega$ and an input bias current of only 5 pA. Even if the photodiode was operating with the incident power level at only 3 nW, the input signal current to the op amp would still be 90 pA. This is sufficiently above the input bias curent of the op amp and therefore results in negligibile non-linearity at the output.

The first and the second detector outputs from the preamplifier are fed into two separate phase sensitive detectors (PSD'S) - Ortec Brookdeal 9421A - as shown in Fig. 4.3. Inputs to the two reference units (Ortec-Brookdeal 9422) are provide by the beam chopper unit (Ortec-Brookdeal 9479). The ratio of the phase sensitively detected signals in channels 1 and 2 is obtained using a ratiometer (Ortec-Brookdeal 9547) and is displayed on a digital multimeter (Keithly 169). This signal is shown in Section 4.5.2.1. to be directly proportional to the spectral bidirectional reflectance (ρ_λ'') of the sample under the given geometrical configuration of measurement.

4.4.3 Optical Alignment

The source unit, consisting of the two lasers mounted one on top of the other, is initially aligned before being fitted on to the BDR apparatus. The two beams are made to be parallel to one another and also to be in the same vertical plane when fitted in position. The alignment is carried out by placing the source unit on the laboratory bench and shining both beams on to a target at the far end of the room. The infrared beam is located using an infrared beam probe (OPTICAL ENGINEERING surface 3). Any adjustments to the red beam direction is done by placing thin metal shims on the V-block supporting the laser tube.

Next the beam steering mirror assembly is fitted on to the source unit and the mirrors are adjusted until both beams (selected by rotating mirror M2 in Fig.4.3) illuminate the same spot on the target.

The source unit is now fitted onto the BDR apparatus and mirror M2 is set to the position to let the red beam through. The beam expander is removed from the BDR box and both lasers are switched on. Then using a white card, the beam position is checked to be roughly at the centre of the 3mm aperture (on the front face of the filter holder - Figure 4.3) and going through the variable aperture, with the latter set to approximately 1.5mm diameter. The source unit positioning is adjusted until the above condition is achieved, and at the

same time, the laser beam is incident approximately at the centre of rotations, C.

Now, selecting the infrared beam and using the IR probe, the above checks are repeated.

SDA/incident beam alignment

This is carried out using a special test sample, with the SDA set to a zero polar angle of incidence. The criterion here is that the laser beam should be incident normal to the sample surface and centred on C, the centre of rotations.

The test sample is made using a 10 mm diameter, front silvered mirror mounted on a sample holder identical to that used for mounting absorber samples. A thin black opaque disk of the same diameter as the sample holder, with a 1 mm diameter hole drilled accurately at the centre, is carefully glued onto the silvered face of the mirror.

The test sample is now mounted as usual on the SDA and the scale on the support block (reading the polar angle of incidence) is set to read zero. Additionally, a 1 mm diameter pinhole is mounted between mirror M3 and the position usually occupied by the beam expander. This is adjusted until the laser beam is seen to pass through it symmetrically.

Now, two observations are necessary to satisfy the alignment criterion.

A) The incident beam illuminates symmetrically, the hole at the centre of the test sample.

B) the reflected beam from the test sample follows back on its original path and illuminates the pinhole circumference symmetrically.

Any small adjustments are carried out by tilting mirror M3 and/or moving it along the optical bench. The whole of the SDA is also rotable around an axis through 'C' perpendicular to the base plate.

When A) and B) above are seen to be satisfied with the red beam, the infrared beam is selected. Using the IR probe the beam is checked to be passing though the pinhole and the variable aperture. In order to repeat the checks A) and B) above however, use is made of the low intensity visible component of the infrared laser output. This is available when the GaAs filter at the front of the laser head is removed. Once A) and B) are satisfied with the infrared laser, the red beam is selected again.

Now the beam expander is put back in position and adjusted until the expanded beam illuminates the back face of the pinhole symmetrically, still satisfying conditions A) and B).

This alignment procedure ensures that the near-axial rays of the expanded beam (and therefore the whole of the collimated output of the beam expander) are incident normally on the test sample, centred on 'C'

The pinhole is removed from the BDR box when alignment is completed.

It is shown in Fig. 4.10 that for a given 1 mm, say, displacement of the reflected beam from the pinhole centre, the corresponding misalignment in θ is only $\simeq 0.2°$. In carrying out the check B) above, alignnment to within 0.5 mm (from the centre of pinhole) is easily obtainable, resulting in a maximum misalignment in θ of only 0.1°.

4.4.4 Measurement Procedure

The following is the measurement procedure initially adopted. Section 4.4.5 describes a revised procedure subsequently used.

1) Both lasers are switched on and left for approximately an hour for outputs to stabilize.
2) SDA/incident beam alignment is done using the test sample as described in section 4.4.3 (source alignment too may be carried out however this is only necessary after long periods of non-use).

3) Radiation detectors and the signal processing electronics are switched on.

4) Sample to be measured is lightly glued to a sample holder and this is then carefully mounted on the SDA as described in section 4.4.1.

5) The angles of incidence and detection are now set to the required values and the BDR box cover is replaced.

6) The DVM reading (V_S) and the corresponding angular data are recorded.

7) Steps 5-6 are repeated with a given sample covering the required range of incidence and/or detection angles.

8) Steps 4 - 7 are repeated for each new sample.

9) Determination of V_R in Eq.4.8 (Section 4.5): A calibrated attenuating filter (of optical density = 3.02 at 633 nm, 2.80 at 1150 nm) is first inserted into a holder placed immediately after the beam splitter. The sample holder is now demounted from the SDA. The tracking arm is then fitted to the θ_r = 180° slot on the quadrant plate (i.e. the one in the plane of incidence) and the detector set to θ_r = 0°. The SDA is now rotated by 180° around a vertical axis through the centre of rotations C. In this configuration the laser beam passes through C and is normally incident on the centre of the detector active area. The BDR box cover is now replaced and the DVM reading (V_R) is recorded. (ρ''_λ corresponding

to each V_S reading may now be calculated using Eq.4.8.)

10) All equipment is switched off.

4.4.5 Revised Measurement Procedure

This procedure was adopted following the occurrence of an occasional differential between the two detectors for some unknown reason. Here only the first detector is used and the laser required for the measurement is separately mounted onto an adjustable platform. This method also requires the laser to be left switched on for a much longer period, to allow the outputs to become highly stable, before any measurements can be taken. Thus the measurement sequence is as follows.

1) Both lasers are switched on and left for at least 4 hours.
2) Same as in Section 4.4.4.
3) " "
4) " "
5) Incident direction is set on the SDA.
6) A 'reference' θ_r angle is arbitrarily chosen for the set of measurements in the given azimuthal plane (i.e. at constant φ_r).
7) θ_r (reference) is set on the SDA and the BDR box cover is replaced. DVM reading is recorded.
8) θ_r is now set to the required direction and BDR

box cover replaced.

9) DVM reading and the angular data are recorded.

10) Repeat steps 8-9 as required with sufficient 'reference checks' (i.e. step 7) to ensure constant incident intensity.

11) Change φ_r to the required setting and repeat steps 6-10.

12) Change θ_i to the required setting and repeat steps 5-10.

13) Determination of V_{R1} in Eq.4.8a - the sample is taken out and a small calibrated mirror (fitted onto a separate sample holder) is mounted on the SDA. A calibrated attenuating filter is now put into the filter holder. SDA is set for $\theta_i = 40°$, $\varphi_r = 80°$, $\theta_r = 40°$. In this configuration the attenuated beam is reflected directly onto the detector by the calibrated mirror. The DVM output is now recorded.

14) Steps 4-13 are repeated with all other samples to be measured.

15) All equipment is switched off.

4.5 Derivation of the Working Equation

First consider the method of using two detectors. Assume that the radiant powers incident on the sample and the second detector, <u>as fractions</u> of the total radiant power output q_I of the laser source, are respectively h_1 and h_2 see Fig.

4.9). Also assume that the effective voltage responsivities of the corresponding 'detector : pre-amp : PSD' combinations are respectively R_1 and R_2 and that the effective voltage gain of the ratiometer is G. Using the definition of ρ''_λ as in Eq.4.1 (see also Section 2.2.2), the radiant power (reflected off the sample) incident on the first detector (q_{d1}) may be written as shown in Eq.4.2.

$$\rho''_\lambda = \frac{I_r''(\lambda,\theta_i,\varphi_i\theta_r,\varphi_r,T)}{I'_i(\lambda,\theta_i,\varphi_i,T)\cos\theta_i d\omega_i} \tag{4.1}$$

Here I'_i is the directional incident intensity and I''_r is the bidirectional reflected intensity. The latter is defined as the reflected intensity in the (θ_r,φ_r) direction due to the incident flux of intensity I'_i. $d\omega_i$ is the solid angular extent (in steradians) of the narrow incident beam.

$$q_{d1} = \rho''_\lambda \cdot \frac{h_1 q_I}{A_S} \cdot \Delta\omega_r \cdot A_r \tag{4.2}$$

Here A_r is the projected area of illuminated sample surface A_s in the direction (θ_r,φ_r).

$$q_{d1} = \rho''_\lambda\, h_1 q_I \Delta\omega_r \cos\theta_r \tag{4.2a}$$

The radiant power incident on the second detector (q_{d2}) may be written as,

$$q_{d2} = h_2 q_I \tag{4.3}$$

The corresponding signal outputs of the PSD units are therefore,

$$V_1 = R_1 \rho''_\lambda\, h_1 q_1\, \Delta\omega_r \cos\theta_r \tag{4.4}$$

$$V_2 = R_2 h_2 q_I \tag{4.5}$$

The signal voltage displayed on the DVM, V_s (in volts), can now be given as in Eq.4.6.

$$V_s = G \cdot \frac{V_1}{V_2} = C \cdot \rho''_\lambda \, \Delta\omega_r \cos\theta_r \tag{4.6}$$

where G is the voltage gain of the ratiometer, and

where $C = G \cdot \frac{R_1 h_1}{R_2 h_2}$

Equation 4.6 shows that V_s is independent of q_I and is therefore not affected by drifts in the radiant power output of the laser source. The constant C is determined by having the laser beam incident directly on the first detector , as described in section 4.4.4. In this situation the signal displayed on the DVM, V_R, is given by Eq.4.7.

$$V_R = C \times 10^{-d} \tag{4.7}$$

where d is the total optical density of any additional filters used. Using equations 4.6 and 4.7, the expression for ρ''_λ is as given in Eq. 4.8.

$$\rho''_\lambda = \frac{V_s 10^{-d}}{V_R \Delta\omega_r \cos\theta_r} \tag{4.8}$$

This is the working equation of the present bidirectional reflectance apparatus when used in the two detector mode.

When only the first detector is used and with a calibrated mirror to obtain V_R then it is readily shown that, in place of Eq.4.8, with V_{R1} in place of V_R,

$$\rho''_\lambda = \left[\frac{V_s}{V_{R1}}\right] \frac{\rho'_{\lambda,m}\ (10^{-d})}{\cos\ \theta_r\ \Delta\omega_r} \qquad (4.8a)$$

where $\rho'_{\lambda,m}$ is the directional hemispherical reflectance of the calibrated mirror at the angle at which it is used to obtain V_{R1}.

In all the BDR results presented in this thesis the one detector method was used. (This was because of the occasional differential drift between the two detectors, referred to in Section 4.4.5.)

4.6 Experimental Accuracy

When making any BDR measurement, the uncertainty of measurement is usually due to the following.

1) uncertainty in the properties of the incident beam of radiation. e.g. power, wavelength purity, polarization, beam dimensions.
2) errors in the radiation detection and signal processing system due to non-linearities, thermal noise, 1/f noise, stray pick-up.
3) uncertainty in determining the directions and the extents of the incident and the detected beams.

In the present BDR apparatus, when using the two detector method, measurement errors due to drifts in the power output of the radiation source were almost totally eliminated as described earlier in sections 4.4.2. The spectral purity of the laser beam (Table 4.1) is seen to be very high. An angular drift of < 0.03 milliradians in the incident beam, as specified, corresponds only to a < 0.03 mm shift in the beam spot position, at a distance of 1 m away from the output aperture of the laser. The uncertainty in the direction of the detected beam thus caused is < 0.025° (and a much less figure in the case of the uncertainty in the incident direction) and has therefore been neglected.

Also when using the two detector system, most systematic errors in radiation detection and signal processing are eliminated by taking the ratio of the detector outputs as indicated by Eq.4.6. The use of 'phase sensitive detection' with a long time constant (10 sec.) and the use of a high chopping frequency (300 Hz) has resulted in considerable suppression of noise and pick-up referred to earlier. For example, the improvement in S/N ratio (in the case of white noise) by the above use of phase sensitive detection (PSD) may be calculated using Eq.4.9 and is seen to be approximately 70 dB.

$$\text{improvement in S/N ratio} = \frac{\Delta f_{in}}{\Delta f_{out}} = \frac{\Delta f_{in}}{1/4z} \qquad (4.9)$$

(Δf_{in} = PSD input bandwidth = 3 MHz; z = PSD output time constant, Brookdeal Manual 1974).

Uncertainty in the directions of the incident and the detected beams is mainly due to the error in reading the scales on the SDA and the tolerances specified in the machining of its components (better than 0.1 mm on all linear dimensions and better than 0.1° on all angular dimensions). Any effect on the incident direction due to slight misalignment between the incident beam and the SDA was shown in section 4.4.3 to be less then 0.1°. Using this information the uncertainties in the angles of incidence and detection have been estimated as given below.

the error in the θ_i, φ_i readings = ± 0.75°

the error in the θ_r, φ_r readings = ± 0.25°

The solid angular extent of the beam incident on the sample is essentially zero because of the near collimated output of the laser source - see section 4.3. The value of this parameter however does not influence the present ρ''_λ measurement, as is seen from Eq.4.8a, because the McNicholas criterion (section 4.3) with respect to ω_i is easily satisfied. The solid angular extent $\Delta\omega_r$ of the detected beam is the solid angle subtended by the effective area of the detector (93.2 mm²) at the centre of rotations C. Any uncertainty in this arises from the errors in determining the effective area, (a), and the distance between the latter and C, (ℓ).

a_d was measured using a 'Magiscan 2A' Image Analyser (JOYCE-LOEBL) as 93.2 ± 0.5 mm².

ℓ was measured as 68.0 ± 0.5 mm.

Now, $$\omega = \frac{a_d}{\ell^2}$$

therefore

$$\left[\frac{\sigma(\omega_r)}{\omega_r}\right]^2 = \left[\frac{\sigma(a_d)}{a_d}\right]^2 + \left[\frac{2\sigma(\ell)}{\ell}\right]^2 \qquad (4.10)$$

substituting the values of $a_d, \sigma(a_d), \ell, \sigma(\ell)$ given above in Eq.4.10,

$$\frac{\sigma(\omega_r)}{\omega_r} = 1.1\%$$

Using Eqns.3.34 and 4.8, it is readily shown that,

$$\left[\frac{\sigma[\rho''_\lambda]}{\rho''_\lambda}\right]^2 = \left[\frac{\sigma[V_s]}{V_s}\right]^2 + \left[\frac{\sigma[V_R]}{V_R}\right]^2 + \left[\tan\theta_r\ \sigma(\theta_r)\right]^2$$

$$+ \left[\log_e 10\ \sigma(d)\right]^2 + \left[\frac{\sigma(\omega_r)}{\omega_r}\right]^2 \qquad (4.11)$$

Each of the first two terms on the R.H.S. is due to the overall measurement error of the radiation detection and signal processing system estimated to be better than ± 1.5% within the full working ranges of the input and the output. This takes into account the non-linearity of the system, other systematic errors in the instruments and the overall random error indicated by the jitter on the DVM readings. The filter calibration error is quoted by the National

Physical Laboratory as ± 0.8% in 10^d at 633 nm, and ± 5% at 1152 nm. Using this information and the values of $\sigma(\theta_r)$ and $\sigma(\omega_r)/\omega_r$ estimated earlier in Eq.4.11, an expression for the percentage error in the present bidirectional reflectance measurements is derived below.

$$\left[\frac{\sigma[\rho''_\lambda]}{\rho''_\lambda}\right]^2 = \left[9.10 + \left[0.25\ \frac{\tan\theta_r}{\theta_r}\right]^2\right]$$

This amounts to an approximately 3% error for $0° \leq \theta_r \leq 80°$.

The values of $\frac{\sigma[\rho''_\lambda]}{\rho''_\lambda}$ calculated for various θ_r at 633 nm are given in Table 4.1. At 1152 nm the error is about double.

4.7 Discussion of Results.

4.7.1 Summary of measurements made

4.7.1.1 BDR measurements

Bi-directional reflectance measurements were made on the same samples of solar absorber materials whose directional emittance had been measured earlier. These are Nextel and Solarcoat-50 which are non-selective absorbers and Skysorb, Maxorb, Cusorb and Solarcoat-100 which are solar selective

absorber materials. Each sample was cut to the size of 19 mm x 19 mm to be accommodated into the BDR apparatus. Some initial BDR measurements were carried out on these samples during April - June '84. Subsequently imrovements to the BDR apparatus were carried out, particularly in providing additional baffling. BDR data presented in this thesis were all obtained during the period October '85 to March '86. During the time when no measurements were made the samples were kept in a relatively dust free environment.

With each sample, BDR measurements were made at two wavelengths, 633 mm and 1152 nm, and at the shorter wavelength using two different sizes of the incident beam ($\simeq$ 1.5 mm diameter and $\simeq$ 5.0 mm diameter). With the 'NARROW' beam, at 633 nm, measurements were made on three different locations ('spots') on the sample surface, in order to study any local variation in the BDR characteristic. One location was at approximately the centre of the sample surface (named the 'CENTRE position') and the other two approximately 2 mm either side of this (named the 'R.H.S. position' and 'L.H.S. position').

At each location ρ''_λ with λ = 633 nm, Φ_i = 0° (i.e. parallel to a selected sample edge) and 79° $\geq \theta_r \geq$ 0° was measured for the following geometries for all the samples.

1) $\theta_i = 0°$ and $\Phi_r = 180°$

2) $\theta_i = 0°$ " $\Phi_r = 270°$

3) $\theta_i = 40°$ " $\Phi_r = 180°$

4) $\theta_i = 40°$ and $\Phi_r = 270°$

(In the case of Solarcoat-100 data for a few additional geometries are also presented).

Following the narrow beam work, the above ρ''_λ measurements with the geometries 1) - 4) were repeated using the 'WIDE beam' at both 633 and 1152 nm wavelengths.

Thus with each sample 5 sets of measurements were obtained as shown below.

1) 633 nm ; NARROW beam ; CENTRE position

2) " ; " ; L.H.S. position

3) " ; " ; R.H.S. position

4) 633 nm ; WIDE beam ; CENTRE position

5) 1152 nm ; " ; CENTRE position

All narrow beam work in this thesis was carried out during September 1985. Only relative reflectance measurements were made (i.e. excluding step 13 in the measurement procedure - Section 4.4.5) as the initial purpose was only to investigate any local variations in the BDR characteristics. However in January 1986 additional calibration measurements were made on the same samples, with the narrow beam incident on the same

positions. These measurements allowed the earlier (September '85) results to be converted to absolute reflectance values. However, the latter are slightly 'less absolute' due to the time lag between the two sets of measurements.

All BDR data presented in the wide beam curves were obtained during October 1985, by making absolute reflectance measurements (i.e. including step 13 in section 4.4.5). Hence these data are 'more absolute' than the narrow beam data.

All BDR graphs were plotted on a CALCOMP-81 flat bed digital plotter driven by the mainframe DEC 20 at the Open University. The computer programs 'PLOTBD' and 'EGRAPH', written by the author incorporating SIMPLEPLOT graphic routines (Bradford University Research Ltd.), are given in Appendix 4.

4.7.1.2 Other measurements/characterisations

1) The spectral directional hemispherical reflectances of the samples were measured, by the National Physical Laboratory, using a Varian - 2300 spectrophotometer with an integrating sphere attachment. 19 readings were taken at every 100 nm intervals between 400 nm and 2000 nm including readings at the 633 nm and 1152 nm wavelengths (see Figs. 4.43 to 4.48). The beam was incident on the sample at a polar angle (θ_i) of 3.3 degrees with a maximum half angle of cone of 2 degrees.

2) Photographs were taken of the sample surface using a PHILIPS 5010 scanning Electron Microscope at the Open University SEM Suite at Milton Keynes. Samples were viewed at many angles of incidence and magnifications and some of the photographs taken are shown in the odd numbered figures between 4.49 and 4.59.

3) Surface roughness of the samples was measured on a FORM-TALYSURF machine at Rank Taylor Hobson Ltd., Leicester. This data is shown in the even numbered figures between 4.50 and 4.60. The stylus force on the samples was between 0.7 and 1.0 mN and the resolution of the instrument is quoted as being to the nearest 10 nm. After the measurements were made a magnified view of the sample surface failed to show any markings left as a result of contact with the stylus tip.

4.7.2 Discussion of Results

One of the main purposes of the present BDR work has been to make extended BDR measurements on commercial solar absorber materials, thus obtaining data hitherto unavailable. These data would be of use to, among others, workers involved in detailed modelling and analysis of solar collectors as described earlier in Section 1.4 Any detailed quantitative analysis of these data is thus left to the intended user. As far as the author is aware there is no other source of detailed BDR measurements on commercial solar absorber

materials and in any case this is the first time that any BDR measurements on solar absorber materials have been reported in directions other than in the plane of incidence.

4.7.2.1 Summary of BDR Figures

Figures 4.11 - 4.40 show the complete set of BDR data obtained in the present work, sample by sample. Corresponding to each sample there are 5 Figures (with consecutive Figure numbering), each presenting data in the format described in section 4.7.1.1. The only exception to this format is with the narrow-beam Figures for Solarcoat-100, where measurements at some additional geometries are also included.

It must be noted, that with each sample, the reference direction for measuring the azimuthal angles (φ_i, φ_r) was chosen as being parallel to a given sample edge. The choice of this edge has little effect when the sample surface shows no markings or striations in a preferred direction, as is the case with Nextel, Solarcoat-50 and Solarcoat-100. However, with Skysorb, Maxorb and Cusorb, the SEM photographs show striations, roughly parallel to a sample edge. With Maxorb and Cusorb the reference φ direction was chosen to be along this sample edge, while with Skysorb the sample edge normal to the striations provided the reference direction for measuring φ. Thus in the former case the sample striations

were roughly parallel to the plane of incidence while in the latter they were roughly normal to the plane of incidence (φ_i = 0° in all BDR measurements).

Figure 4.41 facilitates the comparison of wide-beam 'specular' reflectances at 633 nm. Specular reflectance here refers to the bidirectional reflectance of a sample in the specular direction (i.e. $\theta_r = \theta_i$, $\varphi_r = \varphi_i + 180°$). Thus only the wide-beam $\rho''_{\lambda=633\ nm}(\theta_i = 40°, \varphi_r = 180°)$ curves for each sample appear in this Figure. Fig.4.42 compares the wide-beam specular reflectances at 1152 nm.

The spectral directional hemispherical reflectance data measured by the National Physical Laboratory (NPL) are presented in Figs. 4.43 - 4.48. Wide-beam reflectance data at normal incidence in the 'plane of incidence' (i.e. θ_i = 0° φ_r = 180°) are also included in each Figure.

The reader is reminded that the error in all ρ''_λ measurements is approximately ± 3% and the error in the θ_r measurement is ± 0.5°. The error quoted by the NPL for their measurements is approximately ± 0.5%.

The results will now be discussed, sample by sample.

4.7.2.2 NEXTEL (Figs.4.11 - 4.15)

By comparing Figs.4.11 to 4.13, the point to point variations in the measured $\rho''_{\lambda=633\ nm}$ characteristics over a distance of a few millimetres, are seen to be minimal. Therefore, as expected, the $\rho''_{\lambda=633\ nm}$ curves obtained using the 'wide beam' (Fig.4.14) are seen to be quite similar in shape to the 'narrow beam' curves. However an overall increase in the absolute reflectance is seen in the wide beam curves, compared to the corresponding narrow beam curves (i.e. an upward shift of all curves in Fig. 4.14). The main reason for this is presumably that the absolute reflectance measurements for the narrow beam data were done at a much later time (several months after the rest of the measurements (see Section 4.7.1.1). The absolute reflectance of Nextel has been observed by us to vary significantly with time. $\rho''_{\lambda=633\ nm}(\theta_i = 40°, \varphi_r = 180°, \theta_r = 40°)$ of the same Nextel sample measured during the six months following the data of October 1985 in Figure 4.14 showed differences of up to 20%. This is suspected as being due to the condition of the sample surface varying with ambient temperature and humidity and calls for further investigation.

Excepting $\rho''_{\lambda=633\ nm}(\theta_i = 40°, \varphi_r = 180°)$ all other $\rho''_{\lambda=633\ nm}$ curves for Nextel are seen to lie quite close together and fairly parallel to the θ_r axis. This indicates good diffuse reflectance behaviour except near the plane of incidence. It is therefore reasonable to apply the perfect

diffuser approximation to Nextel and thereby calculate the spectral directional hemispherical reflectance, using Eq.2.4. The values thus calculated are compared in Table 4.2 with the values experimentally determined by the National Physical Laboratory (Fig.4.43). There is good agreement between the two sets of figures, bearing in mind that both the ρ_λ^* measurements and the NPL measurements were carried out fairly close together in time.

The sharp rise in the $\rho^*_{\lambda=633\ nm}(\theta_i = 40°, \varphi_r = 180°)$ characteristic towards larger θ_r angles is thought to be related to the 'off specular peak' phenomenon first reported by Torrance and Sparrow (1965). They attribute this increase in reflectance at angles away from the specular direction to the particulate nature of the surface involved. Such a surface is indeed observed in the SEM photographs of Nextel (Fig. 4.49).

Only a small difference is seen between the wide beam - red and wide beam - infrared curves (Figs. 4.14, 4.15) with $\theta_i = 0°$. The spectral directional ($\theta_i \simeq 3°$) hemispherical values measured by the NPL also show no difference at these wavelengths. The infrared curves with $\theta_i = 40°$ however show an overall lower reflectance than the corresponding red curves.

A feature that is observed in all the figures from 4.11 to 4.40 is that the intersection of the two $\theta_i = 40°$ curves

always occurs at $\theta_r = 0°$. This must be expected, because with a constant θ_i value, $\theta_r = 0°$ refers to the same measurement geometry for bidirectional reflectance, for all φ_r.

4.7.2.3 SOLARCOAT-50 (Figs.4.16 - 4.20)

Comparing Figs 4.16 - 4.18 there is very little point variation of ρ''_λ characteristics, as was the case with Nextel. Thus the 633 nm wide beam curves are very similar to the narrow beam curves, both in shape and magnitude. The absence of any significant shift along the BDR axis between the two sets of curves suggests that, unlike Nextel, the absolute reflectance of Solarcoat-50 does not vary much with time (see Section 4.7.1.1).

When comparing the spectral bidirectional reflectance properties of Solarcoat-50 with those of nextel, all ρ''_λ curves for Solarcoat-50 show a lower reflectance than the corresponding curves for Nextel. This supports the claim by the manufacturers of a higher α_{solar} for Solarcoat-50 than for Nextel. (Manufacturer's data: α_{solar}(NEXTEL) = 0.95, α_{solar}(SOLARCOAT-50) = 0.98)

At either wavelength, 'the off specular peak' effect is barely seen in Solarcoat-50. The SEM photographs of Solarcoat-50 (Fig.4.51) show a surface structure quite different to that of Nextel.

Thus compared with Nextel, Solarcoat-50 is even a better diffusely reflecting material (i.e. all ρ''_λ curves are approximately coincident and parallel to the θ_r axis), a property useful in solar collector design and also highly desirable in other fields of applications such as optical baffling.

4.7.2.4 Skysorb (Figs.4.21 - 4.25)

The bidirectional reflectance characteristics of Skysorb are in complete contrast with those of Nextel and Solarcoat-50 (note the change of scale on the BDR axis to logarithmic). This is not surprising as Skysorb is one of the visually most specular of the samples. From the information in Figs. 4.21 - 4.25, $\rho''_{\lambda=633\ nm}(\theta_i = 40°, \varphi_r = 180°, \theta_r = 40°)$ of Skysorb (with the sample surface striations roughly normal to the plane of incidence) is approximately 600 times larger than $\rho''_{\lambda=633\ nm}(\theta_i = 40°, \varphi_r = 180°, \theta_r = 0°)$ and at the 1152 nm wavelength this factor is about 1000 (see also Table 4.3). These figures however are dependent upon the solid angle of detection (ω_r) which in the present case is about 0.02 steradians, corresponding to a θ_r resolution of about 9°. Hence for more accurate figures ω_r should be reduced, for example by using a smaller area detector.

as before with the other samples, the point to point variations in the $\rho''_{\lambda=633\ nm}$ characteristics are seen to be small. The differences observed in the $\rho''_{\lambda=633\ nm}(\theta_i = 40°, \varphi_r = 180°)$ curves in Figs. 4.21 - 4.23 within the range $30° < \theta_r < 50°$ are merely due to additional data points (the computer draws straight lines between adjacent data points) and do not represent any real variation in the ρ''_λ characteristic.

Figs. 4.21 - 4.24 show that in the $\rho''_{\lambda=633\ nm}(\theta_i = 40°, \varphi_r = 180°)$ curves, the ρ''_λ values at $\theta_r = \theta_i \pm 40°$ (i.e. at 0° and 80°, being 40° either side of the specular direction) are unequal. The approximately five fold increase in the ρ''_λ at $\approx 80°$ (relative to the ρ''_λ at $\theta_r = 0°$) is reminiscent of the off specular peak effect as was seen with Nextel and Solarcoat-50. However, unlike with either of these samples, the increase in Skysorb of the ρ''_λ at $\theta_r \approx 80°$ is very much less at 1152 nm (Fig.4.25) when compared to the increase at 633 nm. This suggests a wavelength dependent effect, possibly due to a residual particulate nature of the surface, that diminishes with increasing wavelength and should be further investigated.

The other prominent feature in all of the Skysorb ρ''_λ curves is the higher values of $\rho''_\lambda(\theta_i = 0°, \varphi_r = 180°)$ over the corresponding values of $\rho''_\lambda(\theta_i = 0°, \varphi_r = 270°)$, at both wavelengths. This clearly indicates surface anisotropy, confirmed by the striations shown in the x2500 magnification

SEM photograph in Fig. 4.53. Bearing in mind that it is only in Skysorb that the striations were at right angles to the plane of incidence (Section 4.7.2.1), one would expect the $\rho''_{\lambda}(\theta_i = 0°, \varphi_r = 180°)$ and $\rho''_{\lambda}(\theta_i = 0°, \varphi_r = 270°)$ characteristics to be significantly different from that of either Maxorb or Cusorb. This is indeed seen to be the case in that only in Skysorb is the $\rho''_{\lambda=633\ nm}(\theta_i = 0°, \varphi_r = 180°)$ curve positioned above the $\rho''_{\lambda=633\ nm}(\theta_i = 0°, \varphi_r = 270°)$ curve, whereas both in Maxorb and Cusorb the reverse is true.

It is also seen from Figs. 4.24 and 4.25, that while there is only a small difference between the $\rho''_{\lambda}(\theta_i = 0°, \varphi_r = 270°)$ curves at the two wavelengths, the $\rho''_{\lambda=1152\ nm}(\theta_i = 0°, \varphi_r = 180°)$ curve is roughly an order of magnitude larger than the $\rho''_{\lambda=633\ nm}(\theta_i = 0°, \varphi_r = 180°)$ curve. In other words the differences between the two $\rho''_{\lambda}(\theta_i = 0°)$ curves at 1152 nm is much larger than at 633 nm. Such behaviour is to be expected if the dominant surface roughness parameter is either slightly larger than or comparable with 1152 nm (when it is larger than both the wavelengths, the radiation at the longer wavelength is likely to be affected more by the effects of surface anisotropy than the radiation at the shorter wavelength). This view is supported by the SEM photographs in Fig. 4.53 where the typical separation between the ridges on the sample surface is shown to be a few microns.

4.7.2.5 Maxorb (Figs.4.26 - 4.30)

Maxorb is also a highly specularly reflecting material but has a smaller peak at 633 nm (i.e. in the $\rho''_{\lambda=633\ nm}(\theta_i = 40°, \varphi_r = 180°)$ curve) when compared with Skysorb (see Figs. 4.26 - 4.29).

The differences between the $\rho''_{\lambda=633\ nm}(\theta_i = 0°, \varphi_r = 180°)$ and $\rho''_{\lambda=633\ nm}(\theta_i = 0°, \varphi_r = 270°)$ curves are larger than in the case of Skysorb. However, unlike in Skysorb, these differences are seen to decrease when going over to the longer wavelength (1152 nm - see Fig. 4.30). This suggests a surface roughness effect where the dominant roughness parameter is smaller than either of the wavelengths considered. In such a case any surface anisotropy is expected to be 'felt' more by the radiation of the shorter wavelength. The SEM photographs of Maxorb reveal a surface structure of a typical roughness less than 0.5μ (Fig. 4.55, 10,000 magnification). It is felt that, for both Maxorb and Skysorb, further BDR, measurements particularly varying φ_i with respect to the striations on the sample surface, together with more extensive roughness measurements would yield useful information on the dependence of ρ''_λ on surface structure.

Another difference between the ρ''_λ characteristics of the two samples is the following. With Skysorb, when going from 633 nm to 1152 nm, there is an approximately 4 times increase in $\rho''_\lambda(\theta_i = 40°, \varphi_r = 180°, \theta_r = 0°)$ or equivalently in

$\rho''_\lambda(\theta_i = 40°, \varphi_r = 270°, \theta_r = 0°)$. In the case of Maxorb this value actually decreases by half at 1152 nm but with an accompanying sharp rise in the 'peakiness' of the $\rho''_{\lambda=633\ nm}(\theta_i = 40°, \varphi_r = 180°)$ curve. This difference indicates that there is increased 'specularity' (i.e. reflected flux being more concentrated in and around the specular direction with less scattered flux in other directions) at 1152 nm in Maxorb (typical surface roughness $< 0.5\mu$ - Fig. 4.55), whilst in Skysorb there is not so much increased specularity but a general increase in reflectance (see the spectral directional hemispherical reflectance curve in Fig. 4.45).

An 'off specular peak' type increase in $\rho''_{\lambda=633\ nm}(\theta_i = 40°, \varphi_r = 180°, \theta_r = 80°)$ over $\rho''_{\lambda=633\ nm}(\theta_i = 40°, \varphi_r = 180°, \theta_r = 0°)$, as was seen in Skysorb, is also seen in the 633 nm ρ''_λ curves of Maxorb, admittedly to a much lesser extent. Again, similar to Maxorb, this increase is barely seen at 1152 nm.

The narrow-beam ρ''_λ characteristics at the LHS and RHS positions are virtually identical (Figs. 4.27 and 4.28). The narrow-beam characteristics at the CENTRE position (Fig. 4.26) shows an overall lower reflectance by a factor of approximately 0.5. However, the 633 nm wide-beam characteristics are quite close to the narrow-beam RHS/LHS curves. This therefore suggests a relatively isolated lower absolute reflectance area at the CENTRE position.

4.7.2.6 Cusorb (Figs 4.31 - 4.35)

The ρ''_λ characteristics of Cusorb seem to have the combined features of specular and diffuse surfaces studied earlier. Figs. 4.31 - 4.34 show strong resemblances to the ρ''_λ characteristics of both Nextel and Solarcoat-50, excepting the specular peak seen in the Cusorb ($\theta_i = 40°$, $\varphi_r = 180°$) curve. Another small difference between Cusorb and the other diffusely reflecting/non-selective absorber materials (i.e. Nextel and Solarcoat-50) is that in these materials most of the ρ''_λ curves curl upwards at the larger θ_r angles. In Cusorb the curling is very slightly downwards.

The features identified with the specularly reflecting solar selective absorber materials are clearly seen in Cusorb. The first is that in going over to 1152 nm (Fig. 4.35) the specular peak in the ρ''_λ ($\theta_i = 40°$, $\varphi_r = 180°$) curve becomes larger and more symmetrical around the specular direction. However, unlike with Skysorb or Maxorb a superimposed increase in ρ''_λ is still retained at 1152 nm.

The second feature concerns the difference between the $\rho''_\lambda(\theta_i = 0°, \varphi_r = 180°)$ and $\rho''_\lambda(\theta_i = 0°, \varphi_r = 270°)$ curves, believed to be related to the anisotrophy of the sample surface structure (Fig. 4.57). In going from the shorter to the longer wavelength, this difference is seen to increase, as was the case with Skysorb. From Fig. 4.34 the ratio

$$\frac{\rho''_\lambda(\theta_i = 0°,\ \varphi_r = 270°,\ \theta_r = 15°)}{\rho''_\lambda(\theta_i = 0°,\ \varphi_r = 180°,\ \theta_r = 15°)}$$ is seen to be

approximately 1.3 at 633 nm. In Fig. 4.35, at 1152 nm, this value is over 2.0. This behaviour is similar to that observed with Skysorb, believed to be due to surface roughness of dimensions larger than 1152 nm. Such a roughness is seen in the SEM photographs in Fig. 4.57.

Another feature observed is that similar to the case with Maxorb, the values of $\rho''_\lambda(\theta_i = 40°,\ \varphi_r = 180°,\ \theta_r = 0°)$ and $\rho''_\lambda(\theta_i = 40°,\ \varphi_r = 270°,\ \theta_r = 0°)$ are practically unchanged in going over to the longer wavelength.

As with most other samples there is very little point to point variations in the $\rho''_{\lambda=633\ nm}$ characteristics.

4.7.2.7 Solarcoat-100 (Figs.4.36 - 4.40)

The narrow-beam data for Solarcoat-100 (Figs 4.36 - 4.38) show additional ρ''_λ curves (i.e. for additional measurement geometries) than for the rest of the samples studied in the present BDR work. This is simply because Solarcoat-100 was the initial sample to be studied, after which the regular set of 4 curves (per each position on sample) were decided upon. These additional curves in Solarcoat-100 show that useful information on the extent of the reflection peak can be

obtained by measurements in other azimuthal planes (i.e.270° < φ_r < 90°) near to the plane of incidence. Figs.4.36 - 4.38 also show that in the case of Solarcoat-100 the effect of the specular reflection extends very little beyond φ_r = 210°.

The specular reflection peak of Solarcoat-100 (with θ_i = 40°) is lower than that of either Skysorb or Maxorb, but is much broader. (In fact Solarcoat-100 has the highest spectral directional hemispherical reflectance value amongst the samples at both wavelengths). This suggests a more 'diffusing' surface. The SEM photographs (Fig. 4.59) and the roughness measurement (Fig. 4.60) show a surface where the typical roughness parameter is greater than either with Skysorb or Maxorb, but comparable with that of Cusorb. Solarcoat-100 also shows a significant increase in the $\rho''_{\lambda=633\ nm}(\theta_i = 40°, \varphi_r = 180°, \theta_r = 80°)$ over $\rho''_{\lambda=633\ nm}$ $(\theta_i = 40°, \varphi_r = 180°, \theta_r = 0°)$ similar to the case with Cusorb. The $\rho''_{\lambda=633\ nm}(\theta_i = 40°, \varphi_r = 180°)$ curves of the latter two samples are also seen to be somewhat similar in shape (Fig. 4.41). The other similarity with Cusorb is the increased difference between $\rho''_{\lambda}(\theta_i = 0°, \varphi_r = 180°)$ and $\rho''_{\lambda}(\theta_i = 0°, \varphi_r = 270°)$ curves at 1152 nm. These observations are also supported by the similarity in the surface structure of the two samples, as can be seen by comparing the two higher magnification SEM photographs in Figures 4.57 and 4.59. (Note the difference in magnification).

Point to point variations in Solarcoat-100 are observed to be minimal.

The main conclusions in the discussion of BDR results and suggestions for future work are given in Section 5.5. Overall evaluation of the performance of BDR apparatus and some suggestions for improvement are given in Section 5.4.

CHAPTER 5 CONCLUSIONS AND RECOMMENDATIONS

5.1 Summary

The two sets of apparatus, namely the directional emissometer and the bidirectional reflectance apparatus, have performed satisfactorily to yield useful information on the directional behaviour of the radiative properties measured. The results of these measurements have been discussed in detail at the end of the respective chapters. The main conclusions of these discussions are summarized here in sections 5.3 and 5.5. Discussions on the performance of each measurement apparatus is given in Sections 5.2 and 5.4, together with suggestions for improvement.

5.2 Directional Emissometer

This instrument was found to be easy to use and enabled total directional emittance measurements to be made with an accuracy of ± 0.002 at $\epsilon' \simeq 0.05$, rising to $\simeq \pm 0.02$ at $\epsilon' \simeq 1.0$ (the fractional error thus falling). This accuracy compares very favourably with that obtained by other workers. The liquid nitrogen cooled sample chamber and extensive baffling were particularly important in mimimising measurement error. Convenience in use was mainly due to,

1) The design of the Sample Holder Heater Assembly (SHHA) and the 'dynamic seal' arrangement for incorporating the SHHA into the emissometer box.
2) Microprocessor control of the sample temperature.

Changing the polar angle of measurement (θ), and also taking a reading with the reference sample, was carried out simply by rotating the top section of the SHHA. The resulting output signal was immediately displayed on the digital voltmeter. In this manner it took less than 10 minutes to acquire 20 data points per given sample. The advantage of having the sample temperature under microrocessor control (COMARK CONTROLLER UNIT) was that, after the initial entering of sample temperature and other data into the controller unit memory, the only other instance that required attention was when changing the input to the control channel (i.e. from the absorber sample thermocouple when taking V_S readings and from the reference sample thermocouple when taking the V_R reading). This was easily carried out by interchanging the thermocouple plugs at the control channel socket on the COMARK CONTROLLER unit.

An improvement that is readily carried out on the emissometer is to provide better insulation around the sample chamber/reservoir. This would reduce the rate of decrease of the ambient temperature elsewhere in the emissometer box, and reduce the error in $\epsilon'(\theta)$ thus caused. In addition, this will also allow a longer period of operation with each filling of the liquid Nitrogen reservoir.

The following suggestions require either substantial modification to the existing emissometer, or, complete

rebuilding of the instrument (as a Mark II version).

1) increasing the sample chamber volume

2) measurements to be made in vacuo.

The reason for wanting a bigger sample chamber is that this would reduce the thermal gradients across the sample and would therefore provide a more isothermal sample surface, and would also make the measured sample temperature more representative of the average temperature of the emitting region. Increased surface area of the sample chamber would however require a larger volume of liquid nitrogen if the time of operation with each filling is to remain the same. This would of course tend to increase the rate of cooling within the emissometer unless insulation around the reservoir is further improved.

Working in vacuo would reduce thermal gradients into the sample, and would thus also make the measured temperature more representative of that of the emitting region. It can be achieved in one of the following ways.

a) using a vacuum-tight emissometer box.

b) having an evacuated compartment within the emissometer box.

c) using an evacuated sample chamber.

In all three cases above, the rotation of the sample holder

will need to be carried out by an electric motor positioned within the evacuated system, controlled externally. a) will require the use of a Golay cell especially designed for vacuum use while in b) the present Golay cell can be used when kept external to the evacuated compartment. The attraction in deciding upon a new evacuated sample chamber (option c) however is that this can be designed to be sufficiently large and also to enable total hemispherical emittance measurements to be made. The main considerations in designing a total hemispherical emissometer are, the minimizing of conduction losses and ensuring that the sample mostly 'sees' a cooled and highly absorbing chamber wall, as discussed earlier in Section 3.1. However care will need to be taken in measuring solar absorber materials in a vacuum, for example with possible outgassing from the coatings.

5.3 Total Directional Emittance of solar absorber and other samples measured.

Three categories of samples were investigated. These were,

a) metals
b) solar selective absorbers
c) non-selective absorbers/dielectrics

All the samples of type a) and c) were found to have directional emittance characteristics that generally agreed

with the predictions of electromagnetic theory (Jakob, 1949, Siegel & Howell 1981), insofar as these theories, which assume given values of the optical constants can be applied to total emittances.

In the case of metals, the shape of the characteristics (Fig.3.24) followed the form predicted by theory reasonably well (Fig.3.31), and agreed well with the results obtained by other workers (Schmidt, 1935). All the metal samples were polished and hence probably approached ideal surface conditions, particularly with regard to surface roughness. The effect of any residual surface roughness would anyway be 'felt' to a lesser degree at the thermal wavelengths (sample temperature = 95°C), when compared with the much shorter optical wavelengths. A possible area of future work however, is the study of the behaviour of the $\epsilon'(\theta)$ characteristic of metals with increasing thickness of oxide layer.

In the case of type c) materials, the directional emittance curve for glass (Fig.3.26) is seen to be quite close to that predicted by theory with the same caveat as on the preceding page (Siegel & Howell, 1981). Similar arguments concerning surface roughness, as in the case of metals, apply here as well. The two other materials of type c, Nextel and Solarcoat-50, however show slightly increased $\epsilon'(\theta)$ at larger values of θ than predicted by electromagnetic theory. Though this may possibly be explained as a metal substrate 'see-through' effect (as $\epsilon'(\theta)$ increases rapidly at large θ for

metals), it is unlikely because at $\theta < 80°$ this would still require $\epsilon'_{metal}(\theta)$ to increase approximately 6-8 times before equalling the $\epsilon'(\theta)$ of a dielectric material. A more likely explanation is that this is a surface roughness effect, and needs to be further investigated.

With the type b) materials (i.e. solar selective absorbers) there are no theoretical curves available for comparison and other experimental data is available only in the case of Skysorb. Interestingly however, the data from this source (Hutchins 1979) disagrees with that obtained in the present work. A peak in the distribution of $\epsilon'(\theta)$ of Skysorb occurring at θ approximately 20° - 30° shown in Hutchins' work (1979) is not observed in the present work. It is argued (Section 3.5) that Hutchins' (1979) peak was a pseudo effect, quite likely to have been caused by a 'stray' component of thermal radiation.

A general observation about the $\epsilon'(\theta)$ characteristics of the solar selective absorber materials is that they show somewhat 'metallic' behaviour up to about $\theta = 60°$, and beyond that a more 'dielectric type' behaviour. The exception to this is Skysorb where the $\epsilon'(\theta)$ characteristic is distinctly metallic at all θ angles. The increase in $\epsilon'(\theta)$ at the larger angles can be explained by considering the contribution to $\epsilon'(\theta)$ from the relatively thin solar radiation absorbing layer on the metal substrate. As θ increases, the path length through the absorbing layer traversed by the substrate emission,

increases. The substrate emission is thus attenuated more, but the contribution from the absorbing layer increases. In the case of Skysorb however the absorbing layer is much less optically thick than with the other samples and therefore has little effect on $\epsilon'(\theta)$ even at the larger θ angles. For solar selective absorber materials in general, the influence of the solar absorbing layer on the $\epsilon'(\theta)$ distribution is thus important at the larger θ angles. Therefore the effects of changes in the solar absorbing layer, such as due to high stagnation temperatures, humidity, and dust accumulation, on the $\epsilon'(\theta)$ characteristic needs to be investigated.

The author has also suggested a novel use of the $\epsilon/\epsilon'(0°)$ versus $\epsilon'(0°)$ plot, for solar selective absorber materials. This is the comparison between the point in this plot that relates to the solar selective absorber material and the point relating to the metal substrate. If the solar absorbing layer is completely transparent to the thermal wavelengths considered, these points would coincide. Thus the separation between these points indicates the extent to which the absorbing layer is transparent at the thermal radiation. This is a useful indicator of spectral selectivity when no spectral data are available.

In view of the present directional emittance work, a recommendation to the solar absorber manufacturing industry is that measurements of the total directional emittance (say at every 10° of polar angle, at one or two representative

sample temperatures) of most commercial solar absorber materials should be made in order to provide the users with a better description of their emittance behaviour. Such data, in addition to specifying the emittance behaviour, also provides an indication of the spectral selectivity of the material, as seen in the results of the present work.

Finally, the present total directional emittance measurement technique would also be extremely useful in providing a detailed description of the $\epsilon'(\theta)$ of any sample to be used as a working standard in making emittance measurement. Thus, this technique will also allow its emittance characteristics to be monitored over periods of time.

5.4 Bidirectional Reflectance Apparatus

The overall simplicity in the design of the bidirectional reflectance apparatus has resulted in the ease of use of the instrument and the accuracy of the measurements obtained. The major features of the instrument are the novel design of the Sample and Detector Assembly (SDA) and the use of lasers as radiation sources. Thus a high intensity, highly directional beam was incident on the sample using only a relatively small number of optical components. The relatively small dimensions of the SDA allowed it to be easily housed within a light tight enclosure (BDR box) minimising problems with stray light. In addition the incident laser beam was mechanically chopped, further

discriminating against stray light and also enabling the detector output signal to be processed using phase sensitive detection techniques. Extensive baffling was used within the BDR box, isolating the SDA from the main sources of scattered light (i.e. lenses, mirrors, apertures). Setting of the angles of incidence and detection was carried out directly with relative ease, without the need for angle conversions using trigonometric transformations, due to the novel design of the SDA.

However a problem encountered with the BDR apparatus was an intermittent drift in the output signal of the 2nd detector (i.e. a differential drift between the firt and the second detectors even when both were simply monitoring the input beam). The cause of this effect, although believed to be due to slow creeping of a metal component, was not positively identified. Although the single detector method later developed, allowed BDR measurements to be made with good accuracy (± 3% at 633 nm, ± 6% at 1152 nm), the double detector method has the obvious advantage of making the measurement procedure highly independent of source fluctuations. Therefore a recommendation (currently being carried out) for a Mark II version is to mount all components on a heavy gauge optical table. The increase in the overall size of the apparatus is compensated for by the better stability provided and in requiring fewer optical components (i.e. mirror M3 not required). Co-linear mounting of optical components would further simplify the alignment procedure and

also eliminate any reflection induced polarization.

The other major recommendation for improving the SDA is the adding of an extension to the quadrant plate, or, the use of a new semicircular plate. Such a modification would allow φ_r to be varied between 180° and 360° (instead of the present range of 180° - 270°) and would therefore allow <u>every</u> combination of $\theta_i, \theta_r, \varphi_i, \varphi_r$. (An extension to the quadrant plate is currently being built.)

It is also felt that a more powerful infrared laser would improve the performance of the BDR apparatus at the infrared wavelength. (Since the completion of the present work such a laser has been purchased.) A similar effect may be achieved by using a different radiation detector of higher sensitivity at the infrared wavelength. However the former method, where the same detector is used at both wavelengths is preferable.

Using the above recommended linear optical configuration, it would be a relatively easy task to add polarizing optics, in order to study the variation of ρ''_λ with polarization of the incident beam. The need for such polarization data arises when the radiation incident on an absorber is significantly polarized. Such a situation occurs, in practice, when plane mirrors are used (at large incident angles) to supplement the flux incident on a flat plate collector.

Much more extensive elaborations of the BDR apparatus would be the automation of the setting of incidence and reflection angles, and the automation of the collection and analysis of ρ''_λ data, using a dedicated microcomputer. Such a system would not only mean easier use and hence the ability to collect more data, but would also allow the possibility of "intelligent" gathering of data. This refers to programming the computer to carry out tasks such as identification of a particular feature (e.g. a peak in the distribution of ρ''_λ) and storing information only relevant to this feature, or, adjusting the frequency of taking measurements to match the variations in the ρ''_λ characteristic (e.g. only a few readings to represent a relatively flat part of a curve). The latter mode of data collection is particularly attractive if large amounts of data pertaining to a given sample are to be gathered.

5.5 Spectral Bidirectional Reflectance of Solar absorber materials

In all of the six samples studied, the point to point variation in the measured ρ''_λ characterstics over a distance of a few millimetres was found to be quite small, indicating homogeneity of the surface properties that relate to reflection, over this range. This suggests that an incident beam of 1-2 mm diameter may be used, without too much concern for exact repositioning on the sample in any future work, where repeated measurements on a sample need to be made for

instance, in the study of the effects of heat cycling or weathering on the ρ''_λ characteristics of a solar absorber material.

The present ρ''_λ measurements on Nextel have shown this material to be a good absorber at solar wavelengths and a good diffuse reflector except in the plane of incidence. Figs. 4.11 - 4.15 show the increase in ρ''_λ with θ_r in the plane of incidence (i.e. $\varphi_r = 180°$). This effect is believed to be related to the 'off specular peak phenomenon' (Torrance and Sparrow, 1965) which occurs with surfaces of a particulate nature. Such a surface is indeed revealed in the SEM photographs in Fig. 4.49. Another important observation on Nextel has been the variability in the absolute reflectance of the ρ''_λ curves obtained over a period of time (i.e. very little change in the shape of the ρ''_λ curve but a significant change in the absolute values of ρ''_λ). Variations of up to 20% have been recorded over a period of about 6 months. Further work is recommended for this matter to be pursued.

Using the perfect diffuser approximation a spectral directional hemispherical reflectance ρ'_λ value has been calculated (Eq.2.4) for Nextel. This compares well with the value measured by the NPL (see Table 4.2) bearing in mind that these measurements were carried out relatively close together in time. The differences between $\rho''_{\lambda = 633\ nm}$ wide beam and $\rho''_{\lambda = 1152\ nm}$ wide beam characteristics are

relatively small. This is in agreement with the NPL measured spectral directional hemispherical reflectance characteristic showing a constant value of ρ'_λ at the two laser wavelengths.

As far as radiative properties are concerned, Solarcoat-50 seems to be a better solar absorber material than Nextel. Not only is the ρ''_λ slightly lower than in Nextel at most measurement geometries, also the rise in ρ''_λ at larger θ_r in the plane of incidence is much less. Thus Solarcoat-50 would also be highly desirable as an optical baffle material.

Compared to the non-selective absorber materials (i.e. Nextel and Solarcoat-50) Skysorb has been shown to be a highly specular material, as was also suggested by its visual appearance. The ratio

$$\frac{\rho''_\lambda\ (\theta_i = 40°,\ \varphi_r = 180°,\ \theta_r = 40°)}{\rho''_\lambda\ (\theta_i = 40°,\ \varphi_r = 180°,\ \theta_r = 0°)}$$

(being subject to the averaging effect due to the 0.02 steradian solid angle of detection) is seen to be (Fig. 4.24, 4.25) approximately 600 at 633 nm and approximately 1000 at 1152 nm. Several other interesting features (described below) have also been identified and these call for further investigations to be undertaken.

The first feature concerns the symmetry of the specular peak in the ρ''_λ ($\theta_i = 40°$, $\varphi_r = 180°$) distribution, around the direction $\theta_r = 40°$. At 633 nm, the ρ''_λ values at $\theta_r > 40°$ are seen to be much larger than the ρ''_λ at corresponding values of $\theta_r < 40°$. For example $\rho''_{\lambda=633\ nm}(\theta_i = 40°, \varphi_r = 130°, \theta_r = 80°) > \rho''_{\lambda=633\ nm}(\theta_i = 40°, \varphi_r = 180°, \theta_r = 0°)$. However at 1152 nm these differences are much less. This suggests an 'off-specular peak' type effect that is wavelength dependent.

The second feature identified is the anisotropy of the surface with respect to reflection characteristics. At both wavelengths, the $\rho''_\lambda(\theta_i = 0°, \varphi_r = 180°)$ curve shows higher ρ''_λ values when compared with the $\rho''_\lambda(\theta_i = 0°, \varphi_r = 270°)$ curve. Anisotropy in the surface morphology is also indicated in the SEM photograph (see Fig. 4.35 magnification 2500).

The third feature is that the differences between the two $\rho''_\lambda(\theta_i = 0°)$ curves at 1152 nm is larger than the differences at 633 nm. This suggests a dominant surface roughness parameter of a dimension larger than 1152 nm.

Maxorb is also seen to be a highly specular material. However the asymmetry of the specular peak in the $\rho''_{\lambda=633\ nm}(\theta_i = 40°, \varphi_r = 180°)$ curve is seen (Fig. 4.29) to be much less than with Skysorb. The differences between the $\rho''_{\lambda=633\ nm}(\theta_i = 0°, \varphi_r = 180°)$ and $\rho''_{\lambda=633\ nm}(\theta_i = 0°,$

$\varphi_r = 270°$) curves are bigger than was the case with Skysorb. However, unlike in Skysorb, these differences are seen to decrease when going over to the 1152 nm wavelength (Fig. 4.30). This suggests a surface roughness effect where the dominant surface roughness parameter is smaller than 633 nm. Such a roughness is seen in the SEM photograph in Fig. 4.55 (magnification of 10,000).

It is felt that for both Maxorb and Skysorb further BDR measurements, particularly varying φ_i with respect to the striations on the sample surface, and additional roughness measurements would shed more light on these features and provide better understanding of the dependence of ρ''_λ on surface roughness.

A general recommendation to manufacturers of highly specular solar selective absorbers such as Skysorb and Maxorb is the following. In view of the present ρ''_λ measurements it is clear that a significant improvement in solar absorptance (several percent) could be achieved if these strong specular peaks were to be suppressed, without raising the level of the diffuse reflection component. The method by which this can be achieved however needs to be carefully considered.

The other difference observed between the ρ''_λ characteristics of Maxorb and Skysorb is the following. In going over to the longer wavelength the 'peakiness' of the specular reflection in the $\rho''_\lambda(\theta_i = 40°, \varphi_r = 180°)$ curve increases considerably

in Maxorb, whilst in Skysorb the 'peakiness' is much the same but there is an accompanying general increase in ρ''_λ at all θ_r angles.

The ρ''_λ characteristics of Cusorb seem to combine the features of the highly 'diffuse' samples with those of the highly specular samples. Figs. 4.31 - 4.34 show strong resemblances to the ρ''_λ characteristics of Nextel and Solarcoat-50, yet a specular peak is seen in the $\rho''_\lambda(\theta_i = 40°, \varphi_r = 180°)$ curves. Another feature in common with the other specular samples is the increase in symmetry, around the specular direction of the $\rho''_\lambda(\theta_i = 40°, \varphi_r = 180°)$ curve, when going over to the longer (1152 nm) wavelength. Also in Cusorb the differences between the $\rho''_\lambda(\theta_i = 40°, \varphi_r = 180°)$ and the $\rho''_\lambda(\theta_i = 40°, \varphi_r = 270°)$ curves increase when going over to the longer wavelength. This indicates a dominant surface roughness parameter of a dimension greater than 1152 nm, as was the case with Skysorb. This view is supported by the information in the SEM photograph of Fig.4.57.

The specular reflection peak of Solarcoat-100 (in the $\rho''_\lambda(\theta_i = 40°, \varphi_r = 180°)$ curve is broader than that of either Skysorb or Maxorb (Figs. 4.41, 4.42), at both wavelengths. This suggests a more diffusely reflecting surface. Both the SEM photographs (Fig. 4.59) and the stylus measurements (Fig. 4.60) show a typical surface roughness greater than that of either Skysorb or Maxorb, but also show a roughness of a much

smaller and larger dimension. The roughness seen is in fact comparable with that of the Cusorb sample (Figs. 4.57, 4.58). Therefore, as expected, the ρ''_λ characteristics of Solarcoat-100 show a resemblance to the ρ''_λ charateristics of Cusorb.

APPENDIX 1

ESTIMATION OF E_2.

E_2 is the stray component of thermal flux originating within the sample chamber, as referred to in Section 3.2.2. In this appendix E_2 will be estimated for two types of ideal sample

(a) specular in reflection

(b) diffuse in reflection.

In both cases the sample is diffuse in emission, the chamber walls are diffuse in reflection and in emission, and the sample and chamber walls are "grey".

Most polished metals behave approximately like specular reflectors, and so type (a) behaviour at thermal wavelengths can be associated with solar selective absorbers. Type (b) behaviour at thermal wavelengths can be associated with non-selective absorbers.

E_2 consists of two components q_w and q_s. The component q_w is the emission from the sample chamber wall that is reflected towards the detector by the sample. The component q_s is the flux emitted by the sample that is reflected back towards it by the chamber wall such that the sample then reflects it towards the detector.

In all cases considered it is the ratio E_2/E_1 that is important, where E_1 is the main flux component (Section

3.2.2) and consists of the direct emission from the sample. We can write

$$E_1 = \left[\epsilon_s'(\theta)\frac{\sigma}{\pi} T_s^4\right](a_0\overline{\Delta\omega_s}) \qquad (A1.1)$$

where (Figure A1.1) a_0 is the projected area (independent of θ) of the sample surface as seen from the detector, and $\overline{\Delta\omega_s}$ is the solid angle subtended by the detector aperture at the centre of the sample. Note that for a diffuse emitter $\epsilon_s'(\theta)$ is independent of θ and so E_1, on this assumption, is also independent of θ.

In calculating E_2 the following additional assumptions have been made, and the following values of various quantities have been adopted.

(i) The sample chamber is treated as a sphere of radius 22mm.

(ii) When allowance is made for vignetting (see Appendix 3) then $a_0 = 8.7$ mm^2.

(iii) For the chamber walls $\epsilon_w' = 0.953$, $\rho_w' = 0.047$.

Estimation of q_w - sample specular in reflection

The sample acts like a mirror, and so the detector "sees" an area a_w of sample chamber wall that is greater than a_0 because of the increased distance (by 22 mm) - see Figure A1.2.

$$q_w = \left[\epsilon_w'(0)\frac{\sigma T_w^4}{\pi}\right](a_w\overline{\Delta\omega_w})\rho_s'(\theta) \qquad (A1.2)$$

where $\rho'_s(\theta)$ is the hemispherical-directional total reflectivity of the sample. From the geometrical considerations $a_w\overline{\Delta\omega_w} = a_0\ \overline{\Delta\omega_s}$.

and furthermore

$$\rho'_s(\theta) = 1 - \epsilon'_s(\theta)$$

Thus, from equations (A1.1) and A1.2)

$$\frac{q_w}{E_1} = \epsilon'_w(0)\left[\frac{T_w}{T_s}\right]^4 \frac{(1 - \epsilon'_s(\theta))}{\epsilon'_s(\theta)} \qquad \text{(A1.2a)}$$

If $T_w = 77K$, $T_s = 368K$, and $\epsilon'_w(\theta) = 0.953$, then

$$\frac{q_w}{E_1} = 0.0018\ \frac{(1 - \epsilon'_s(\theta))}{\epsilon'_s(\theta)} \qquad \text{(A1.3)}$$

Estimation of q_s - sample specular in reflection

Each point on the sample contributes to q_s. Consider an arbitrary point P, as in Figure A1.3, making a typical contribution Δq_s to q_s.

$$\Delta q_s = I_w\ a_w\ \overline{\Delta\omega_w}\ (1 - \epsilon'_s(\theta)) \qquad \text{(A1.4)}$$

where I_w, for diffuse reflection, is independent of α_r, though $\alpha_r = 0$ because of the specular reflection at the sample (Figure A1.3). It is shown in the next subsection that

$$I_w = \frac{\rho'_w(\alpha_i)\ \Delta q_i}{\pi a_w}$$

Thus, from equation (A1.4),

$$\Delta q_s = \rho'_w(\alpha_i)\left[\frac{\overline{\Delta q_w}}{\pi}\right](1 - \epsilon'_s(\Theta))\ \Delta q_i \qquad \text{(A1.5)}$$

It remains to sum over all points on the sample making the simplifying assumption that $\rho'_w(\alpha_i)$ is independent of α_i. We can write (Figure A1.4)

$$\Delta q_i = \left[\epsilon'_s \frac{\sigma T_s^4}{\pi}\right]\ (\Delta A \cos\beta\ \Delta\omega(\beta))$$

where ϵ'_s is independent of β, because the sample is diffuse in emission. This equation can be re-written as

$$\Delta q_i = (\epsilon'_s \sigma T_s^4)\ \Delta A\ \Delta F_{\Delta A \to a_w} \qquad \text{(A1.6)}$$

where

$$\Delta F_{\Delta A \to a_w} = \frac{\cos\beta\ \Delta\omega(\beta)}{\pi}$$

is the configuration factor from ΔA to a_w. From Siegel and Howell (1981), page 178, we have a reciprocity relation such that

$$\Delta A \Delta F_{\Delta A \to a_w} = a_w\ \Delta F_{a_w \to \Delta A}$$

Thus, from equation (A1.6)

$$\Delta q_i = (\epsilon'_s\ \sigma T_s^4) a_w\ \Delta F_{a_w \to \Delta A}$$

and so

$$\int \Delta q_i = (\epsilon'_s\ \sigma T_s^4) a_w \int_A \Delta F_{a_w \to \Delta A}$$

$$= (\epsilon'_s \sigma T_s^4) a_w\ F_{a_w \to A} \qquad \text{(A1.7)}$$

Siegel and Howell (1981), pages 825/6, list configuration factors that we can use to estimate $F_{a_w \to A}$, treating a_w as a small area. Thus, at $\theta = 0$,

$$F_{a_w \to A} \simeq \frac{\ell^2}{\ell^2 + r^2}$$

where r = 22mm and ℓ = 18mm.

Thus,

$$F_{a_w \to A} \simeq 0.40 \qquad (\theta = 0) \tag{A1.8}$$

At $\theta = 90°$,

$$F_{a_w \to A} \simeq \frac{H}{2}\left[\frac{Z}{\sqrt{(Z^2 - 4R^2)}} - 1\right]$$

where $H = (\sqrt{a_w/\pi})/r$, $R = \ell/r$, $Z = 1 + H^2 + R^2$. Thus, with $a_w \simeq 9mm^2$

$$F_{a_w \to A} \simeq 0.14 \qquad (\theta = 90°) \tag{A1.9}$$

Clearly the worst case is at $\theta = 0°$, and this is the case we shall use. Thus, from equations (A1.7) and (A1.8),

$$\int \Delta q_i = (\epsilon'_s \sigma T_s^4)\, a_w \,(0.40)$$

Thus, from equation (A1.5)

$$q_s = \rho'_w \left[\frac{\overline{\Delta_{\omega_w}}}{\pi}\right] (1 - \epsilon'_s(\theta))\, \epsilon'_s(\theta) \sigma T_s^4 a_w \,(0.40)$$

and therefore, using equation (A1.1), and the relation

$$a_w \overline{\Delta\omega_w} = a_0 \overline{\Delta\omega_s}$$

$$\frac{q_s}{E_1} = 0.40\ \rho'_w\ (1 - \epsilon'_s) \qquad (\theta = 0) \qquad \text{(A1.10)}$$

$$= 0.14\ \rho'_w\ (1 - \epsilon'_s) \qquad (\theta = 90°) \qquad \text{(A1.10a)}$$

If $\rho'_w = 0.047$ then

$$\frac{q_s}{E_1} = 0.019\ (1 - \epsilon'_s) \qquad (\theta = 0) \qquad \text{(A1.11)}$$

$$= 0.007\ (1 - \epsilon'_s) \qquad (\theta = 90°) \qquad \text{(A1.11a)}$$

Estimation of q_w - sample diffuse in reflection

Each part of the sample chamber wall "seen" by the sample contributes to q_w. Figure A1.5 illustrates the contribution Δq_w made by a typical part of this wall.

$$\Delta q_w = I\ \overline{\Delta\omega_s}\ (\Delta A \cos\theta) \qquad \text{(A1.12)}$$

where I is independent of θ (wall diffuse in emission, sample diffuse in reflection), and where $\Delta A \cos\theta = a_0$. We obtain I as follows (Figure A1.5).

$$dq = I d\omega\ (\Delta A \cos\theta') \qquad \text{(A1.13)}$$

where

$$\int_H dq = \rho'_s(\alpha)\ \Delta q_i \qquad \text{(A1.14)}$$

where $\rho_s'(\alpha)$ is the directional-hemispherical total reflectance of the sample. Thus, from equations (A1.13) and (A1.14)

$$I = \frac{\rho_s'(\alpha)\ \Delta q_i}{\pi\ \Delta A} \tag{A1.15}$$

where we have used $\int_H \cos\theta'\ d\omega = \pi$

Thus, from equations (A1.12) and (A1.15)

$$\Delta q_w = \left[\frac{\overline{\Delta\omega_s}}{\pi}\right] \cos\theta\ \rho_s'(\alpha)\ \Delta q_i \tag{A1.16}$$

Furthermore (Figure A1.5)

$$\Delta q_i = \epsilon_w(0)\left[\frac{\sigma T_w^4}{\pi}\right]\ \Delta\omega\ \Delta A_w \tag{A1.17}$$

Thus, from equations (A1.16) and (A1.17)

$$\Delta q_w = \left[\frac{\overline{\Delta\omega_s}}{\pi}\right] \cos\theta\ \rho_s'(\alpha)\ \epsilon_w(0)\left[\frac{\sigma T_w^4}{\pi}\right]\Delta\omega\ \Delta A_w \tag{A1.18}$$

Now (Figure A1.5 and A1.6)

$$\Delta\omega\ \Delta A_w = \Delta\omega'\ \Delta A \cos\alpha \tag{A1.19}$$

Thus, assuming that $\rho_s'(\alpha)$ is independent of α, and replacing ΔA by $a_0/\cos\theta$ and $\int_H \cos\alpha\ \Delta\omega'$ by π, equations (A1.18) and (A1.19) yield

$$q_w = \left[\frac{\overline{\Delta\omega_s}}{\pi}\right] \rho_s'\ \epsilon_w(0)\sigma\ T_w^4\ a_0 \tag{A1.20}$$

From equations (A1.1) and (A1.2)), and using $\rho'_s = (1 - \epsilon'_s)$,

$$\frac{q_w}{E_1} = \epsilon'_w(0) \left[\frac{T_w}{T_s}\right]^4 \frac{(1 - \epsilon'_s)}{\epsilon'_s} \qquad \text{(A1.21)}$$

This is the same as equation (A1.3) except that in equation (A1.21) ϵ'_s is independent of angle.

Putting in the same values as before,

$$\frac{q_w}{E_1} = 0.0018 \frac{(1 - \epsilon'_s)}{\epsilon'_s} \qquad \text{(A1.22)}$$

Estimation of q_s - sample diffuse in reflection

Here we have to combine elements of the case of q_s for a sample diffuse in emission and specular in reflection, with elements of the case of q_w for a sample diffuse in reflection.

We start with equation (A1.18), replacing $\epsilon_w(\sigma T_w^4/\pi)$ with $\rho'_w(\alpha_i)\Delta q_i/(\pi \Delta A_w)$ (see Figure A1.7).

$$\text{Thus } \Delta(\Delta q_s) = \left[\frac{\overline{\Delta\omega_s}}{\pi}\right] \cos\theta\, \rho'_\sigma(\alpha) \left[\frac{\rho'_w(\alpha_i)\ \Delta q_i}{\pi\ \Delta A_w}\right] \Delta\omega\ \Delta A_w \qquad \text{(A1.23)}$$

To obtain Δq_s we must include all Δq_i, and then to obtain q_s we must include all ΔA_w.

To include all Δq_i note from equation (A1.7) that

$$\int \Delta q_i = \epsilon_s' \sigma T_s^4 \Delta A_w \, F_{\Delta A_w \to A} \tag{A1.24}$$

where ϵ_s' has been assumed to be independent of angle.

Thus, from equations (A1.23) and (A1.24)

$$\Delta q_s = \left[\frac{\overline{\Delta\omega_s}}{\pi}\right] \cos\theta \; \rho_s'(\alpha) \left[\frac{\rho_w'}{\pi \, \Delta A_w}\right] (\epsilon_s' \sigma T_s^4 \, \Delta A_w \, F_{\Delta A_w \to A}) \Delta\omega \Delta A_w \tag{A1.25}$$

where we have assumed that ρ_w is independent of α_i.

To include all ΔA_w the treatment parallels that in obtaining equation (A1.20). Thus,

$$q_s \simeq 0.3 \left[\frac{\overline{\Delta\omega_s}}{\pi}\right] \rho_s' \, \rho_w' \, \epsilon_s' \sigma \, T_s^4 \, a_0 \tag{A1.26}$$

where ρ_s' has been assumed to be indpendent of α, and where the factor 0.3 is our estimate of $F_{\Delta A_w \to A}$: this is a rough average of 0.40 at $\theta = 0$ and 0.14 at $\theta = 90°$ (see equations (A1.8) and (A1.9)).

Thus from equations (A1.1) and (A1.26), and using $\rho_s' = (1 - \epsilon_s')$,

$$\frac{q_s}{E_1} \simeq 0.3 \rho_w' \, (1 - \epsilon_s') \tag{A1.27}$$

This is the same form as equations (A1.10) and (A1.10a), the average configuration factor substituting for the values at $\theta = 0$ and $\theta = 90°$ in those earlier equations.

If $\rho'_w = 0.047$ then

$$\frac{q_s}{E_1} \simeq 0.014\ (1 - \epsilon'_s) \qquad \text{(A1.28)}$$

Summary

The algebraic expressions for q_w and q_s are collected below, and are enumerated with $T_w = 77K$, $T_s = 368K$, $\epsilon'_w = 0.953$, $\rho'_w = 0.047$.

	q_w/E_1		q_s/E_1
sample <u>specular</u> in reflection	$\epsilon'_w(0)$	$\left[\frac{T_w}{T_s}\right]^4 \frac{(1 - \epsilon'_s(\theta))}{\epsilon'_s(\theta)}$	$0.40\ \rho'_w(1-\epsilon'_s)$ at $\theta=0$ $0.14\ \rho'_w(1-\epsilon'_s)$ at $\theta=90°$
	0.0018	$\frac{(1-\epsilon'_s(\theta))}{\epsilon'_s(\theta)}$	$0.019\ (1-\epsilon'_s)$ at $\theta=0$ $0.007\ (1-\epsilon'_s)$ at $\theta=90°$
sample <u>diffuse</u> in reflection	$\epsilon'_w(0)$	$\left[\frac{T_w}{T_s}\right]^4 \frac{(1 - \epsilon'_s)}{\epsilon'_s}$	$0.3\ \rho'_w\ (1-\epsilon'_s)$
	0.0018	$\frac{(1 - \epsilon'_s)}{\epsilon'_s}$	$0.014\ (1-\epsilon'_s)$

Now $E_2 = (q_w + q_s)$. Thus, we get the final result

$$\frac{E_2}{E_1} \simeq 0.0018\ \frac{(1 - \epsilon'_s)}{\epsilon'_s} + 0.014\ (1 - \epsilon'_s) \qquad \text{(A1.29)}$$

which is good enough for all cases, Appendix 3 showing that the correction terms associated with E_2/E_1 are small.

APPENDIX 2

The effect on input beam polarisation in using front silvered mirrors in the BDR apparatus

Three high quality front silvered mirrors are used in the BDR apparatus, for steering the red laser beam on to the sample, as shown in Fig.4.3. Using the approximation $n^2 + k^2 \gg 1$ (n,k are the real and imaginary parts of the complex index of refraction), applicable to metals in the visible and the near infrared regions (Heavens 1965), the reflection coefficients for the normal (ρ_n') and the parallel (ρ_p') polarization components of the beam can be written as shown in Eqns.A2.1 and A2.2.

$$\rho_n' = \frac{(n^2+k^2)\cos^2\beta - 2n\cos\beta + 1}{(n^2+k^2)\cos^2\beta + 2n\cos\beta + 1} \qquad \text{(A2.1)}$$

$$\rho_p' = \frac{(n^2+k^2) - 2n\cos\beta + \cos^2\beta}{(n^2+k^2) + 2n\cos\beta + \cos^2\beta} \qquad \text{(A2.2)}$$

where β is the angle of incidence and reflection ($\beta = 45°$ at all 3 reflections in the BDR apparatus).

Assuming a totally unpolarized beam output from the laser (as specified by the manufacturer, and as we have confirmed by measurement), and carefully noting that the 'n' and the 'p' components interchange in the reflection at mirror M3, the resultant reflection coefficients (of all 3 reflections) for the n and

the p components are respectively $(\rho'_n)^2\rho'_p$ and $(\rho'_p)^2\rho'_n$. Hence the fraction of polarized radiation in the beam, after all the reflections at mirrors M1, M2 and M3, is given by Eq.A2.3.

$$\text{polarized fraction} = \frac{(\rho'_p)^2\rho'_n - (\rho'_n)^2\rho'_p}{(\rho'_p)^2\rho'_n + (\rho'_n)^2\rho'_p} \qquad \text{(A2.3)}$$

In the case when only mirror M3 is used, there is only one reflection and therefore,

$$\text{polarized fraction} = \frac{\rho'_p - \rho'_n}{\rho'_p + \rho'_n} \qquad \text{(A2.4)}$$

Using published data for n and k in Eqns. A2.1 and A2.2, (American Institute of Physics Handbook, 1972) the polarized fractions have been calculated and given in Table 4.4.

APPENDIX 3

CALCULATION OF THE MULTIPLICATIVE AND ADDITIVE CORRECTION TERMS IN EQUATION 3.12.

First we calculate the terms L_S and L_W that first appear in equations (3.8) - (3.10), and that consequently appear in the correction terms in equation (3.12). Equations (3.8) - (3.10) can be written as

$$V_S(\theta) = R(E_{1S}(\theta) + E_{2S}(\theta) - E_4) \qquad (A3.1)$$

$$V_R(15°) = R(E_{1R}(15°) + E_{2R}(\theta) - E_4) \qquad (A3.2)$$

$$V_W = R(E_{1W}(0) - E_4) \qquad (A3.3)$$

where

$$E_{1S} = L_S\ \epsilon'_S(\theta) \qquad (A3.4)$$

$$E_{1R} = L_S\ \epsilon'_R(15°) \qquad (A3.5)$$

$$E_{1W} = L_W\ \epsilon'_W(0) \qquad (A3.6)$$

Clearly

$$E_{1S} = \epsilon'_S\left[\frac{\sigma T_S^4}{\pi}\ a_0\ \overline{\Delta\omega_S}\ \right]$$

therefore

$$L_S = \frac{\sigma T_S^4}{\pi}\ a_0\ \overline{\Delta\omega_S} \qquad (A3.7)$$

where $\overline{\Delta\omega_s}$ is the solid angle subtended by aperture 3 at the centre of the sample (Figure A3.1) and where a_0 is such that

$$a_0 \overline{\Delta\ \omega}_s = \int \Delta\omega_s(y)\ 2\pi y\ dy$$

(also see Figure A3.1). It is readily established that

$$\overline{\Delta\omega_s} = 1.13 \times 10^{-4}\ \text{sr}$$

$$a_0 = 8.7 \times 10^{-6}\ \text{m}^2$$

$$a_0 \overline{\Delta\omega_s} = 9.8 \times 10^{-10}\ \text{m}^2\text{sr}$$

The same expression for L_s can be used in E_R, because

$$a_{0R}\ \overline{\Delta\omega_R} = a_0\ \overline{\Delta\omega_s}.$$

Similarly

$$L_w = \frac{\sigma T_w^4}{\pi}\ a_w\ \overline{\Delta\ \omega}_w$$

$$= \frac{\sigma T_w^4}{\pi}\ a_0\ \overline{\Delta\ \omega}_w \qquad \text{(A3.8)}$$

Thus, if $T_s = 368\text{K}$ then

$$L_s = 3.24 \times 10^{-7}\ \text{W} \qquad \text{(A3.9)}$$

and if $T_w = 77\text{K}$ then

$$L_w = 6.22 \times 10^{-10}\ \text{W}. \qquad \text{(A3.10)}$$

The multiplicative term M in equation (3.12) can be written as

$$M = \left[1 + \frac{E_{2R}}{E_{1R}} - \frac{L_w\ \epsilon'_w}{L_s\ \epsilon'_R(15°)}\right]$$

and, to a sufficient degree of approximation, this is

$$M \simeq \left[1 + \frac{E_{2R}}{E_{1R}} - \frac{L_w}{L_s}\right]$$

Now, from equation (A1.29),

$$\frac{E_{2R}}{E_{1R}} \simeq 0.0018 \frac{(1 - \epsilon'_R(15°))}{\epsilon'_R(15°)} + 0.014\ (1 - \epsilon'_R(15°))$$

and thus, with the values of L_s and L_w in equations (A3.9) and (A3.10), and with $\epsilon'_R(15°) \simeq \epsilon'_w \simeq 0.953$,

$$M \simeq (1 + 7.47 \times 10^{-4} - 1.92 \times 10^{-3})$$
$$\simeq 0.9988 \qquad \text{(A3.11)}$$

The additive term A in equation (3.12) can be written as

$$A \simeq -\left[\frac{E_{2s}}{L_s} - \frac{L_w\ \epsilon'_w}{L_s}\right]$$

Now

$$\frac{E_{2s}}{L_s} = \frac{E_{2s}}{E_{1s}} \cdot \epsilon'_s(\theta) = 0.0018\ (1-\epsilon'_s(\theta)) + 0.014\ \epsilon'_s(\theta)(1-\epsilon'_s(\theta))$$

Thus, with the above values of L_w, L_s and ϵ'_w

$$A = 0.00183 - 0.0018(1-\epsilon'_s(\theta)) - 0.014\ \epsilon'_s(\theta)(1-\epsilon'_s(\theta)) \qquad \text{(A3.12)}$$

Clearly the multiplicative term M (Equation (A3.11) is close to unity, and the additive term A depends on $\epsilon'_s(\theta)$. Figure A3.2 shows the values of A and $A/\epsilon'_s(\theta)$ as a function of $\epsilon'_s(\theta)$. These are also listed in Table 3.2.

APPENDIX 4

COMPUTER PROGRAMS

1) PLOTBD

This is the fortran program used for plotting Figures 4.11 to 4.40

2) EGRAPH

This is the fortran program used for plotting Figures 4.41 to 4.48

3) POLAR

This fortran program was used for plotting all the directional emittance curves.

```
C       program PLOTBD used for plotting bidirectional reflectance graphs.
c       This program will accomodate upto 10 different curves,each of a
C       maximum of 20 data-points.
C
        PROGRAM PLOTBD
        CHARACTER *3,THETA,PHI
        CHARACTER *6,WVLEN,SPOT
        CHARACTER *6,BEAM
        CHARACTER *55,TITEL1
        CHARACTER *9,TITEL3
        CHARACTER *40,TITEL4,FIGURE
        CHARACTER *50,BDRCAP
        CHARACTER *8,BDUNIT
        CHARACTER *35,TLINE
        CHARACTER *10,SAMPLE
        CHARACTER *4,NUMBER
        CHARACTER *80, TITEL
        CHARACTER *1, REPLY,REPLY1,REPLY2,REPLY3,REPLY4

        DIMENSION  X(10,20) , Y(10,20)
        DIMENSION ITHETA(10),IPHI(10)

        common/jbou/ioulin,oueps
        oueps=0.0
        ioulin=3

        TYPE*,'is the  BDR axis  LOGARITHMIC ?  (Y or N) '
        ACCEPT 1000, REPLY1
        TYPE*,'OK... your reply is ',REPLY1


10      TYPE *,'NO: OF CURVES IN THIS FIGURE ?'
        ACCEPT *,ICOUNT
        DO 200  I=1,ICOUNT
        TYPE*,'give THETA-i value followed by  PHI-r  value in CURVE',I
        ACCEPT*,ITHETA(I),IPHI(I)
        TYPE *,'NO: DATA-POINTS IN CURVE ',I,'?'
        ACCEPT *,JCOUNT
        X(I,0)=JCOUNT
        TYPE*,'BDR MULTIPLIER ?'
        ACCEPT*,BMULT
50      TYPE *,'GIVE ANGLE FOLLOWED BY BDR-VALUE'
        DO 100 J=1,JCOUNT
        ACCEPT *, X(I,J), Y(I,J)
        Y(I,J)=Y(I,J)*BMULT
        IF (REPLY1.EQ.'Y'.OR.REPLY1.EQ.'y') THEN
        Y(I,J)=Y(I,J)*0.001
        END IF
100     CONTINUE
```

```
200     CONTINUE
        IF(REPLY1.EQ.'Y'.OR.REPLY1.EQ.'y') THEN
        GOTO 230
        END IF

        TYPE*,'GIVE BDR AXIS UNIT (e.g. 3.456E-3 )'
        ACCEPT 1003,BDUNIT
230     TYPE*,'GIVE MAXIMUM VALUE FOR BDR AXIS'
        ACCEPT*,BDMAX
        BDRCAP='BDR     ( '//BDUNIT//' per steradian )'
        IF (REPLY1.EQ.'Y'.OR.REPLY1.EQ.'y') THEN
        BDRCAP='BDR     ( per steradians )'
        END IF

        CALL PAGE(21.0,29.7)
        CALL SETPNS(1,2,3,4)
        CALL PEN(1)
        CALL SCALES(0.0,80.0,1,0.0,BDMAX,1)
        IF (REPLY1.EQ.'Y'.OR.REPLY1.EQ.'y') THEN
        CALL YSCALE(0.0001,BDMAX,2)
        END IF
        CALL AXES('THETA - r  (degrees)',20,BDRCAP,LEN(BDRCAP))
        DO 400 I=1,ICOUNT
        KCOUNT = I
        CALL PEN(KCOUNT)
        DO 300 J=1,X(I,0)
        CALL JOIN PT(X(I,J),Y(I,J))
        CALL MARK PT(X(I,J),Y(I,J),KCOUNT)
300     CONTINUE
        CALL BREAK
400     CONTINUE

        CALL PEN(1)
        TYPE *,'give FIGURE NO: '
        ACCEPT 1005,NUMBER
        FIGURE='figure  '//NUMBER
        DO 420,M=1,3
420     CALL TITLE('H','L','   ',3)
        CALL TEXTMG(1.4)
        FIGURE='                                '//FIGURE
        CALL TITLE('H','L',FIGURE,LEN(FIGURE))
        CALL TEXTMG(1.0)
        CALL TITLE('H','L','
     1                                          ----------------',60)
        CALL TITLE('H','L','   ',3)
```

```
      TYPE*,'NORMAL TITLES ? (Y or N)'
      ACCEPT 1000,REPLY1
      IF (REPLY1.EQ.'N'.OR.REPLY1.EQ.'n') THEN
      GOTO 470
      END IF
      TYPE *,'SAMPLE NAME ?'
      ACCEPT 1004,SAMPLE
430   TYPE*,'RED or INFRARED measurements (type R or I)'
      accept 1000,REPLY2
440   TYPE *,'WIDE or NARROW beam ? (type W or N )'
      ACCEPT 1000,REPLY3
450   TYPE *,'LHS ,CENTRE ,or RHS  spot ? (type L ,C or R)'
      ACCEPT 1000,REPLY4


      IF (REPLY2.EQ.'R'.OR.REPLY2.EQ.'r') THEN
      WVLEN='632.8'
      ELSE IF (REPLY2.EQ.'I'.OR.REPLY2.EQ.'i') THEN
      WVLEN='1152.3'
      ELSE
      GOTO 430
      END IF

      IF (REPLY3.EQ.'W'.OR.REPLY3.EQ.'w') THEN
      BEAM='WIDE'
      ELSE IF (REPLY3.EQ.'N'.OR.REPLY3.EQ.'n') THEN
      BEAM='NARROW'
      ELSE
      GOTO 440
      END IF

      IF (REPLY4.EQ.'L'.OR.REPLY4.EQ.'l') THEN
      SPOT='L.H.S.'
      ELSE IF (REPLY4.EQ.'C'.OR.REPLY4.EQ.'c') THEN
      SPOT='CENTRE'
      ELSE IF (REPLY4.EQ.'R'.OR.REPLY4.EQ.'r') THEN
      SPOT='R.H.S.'
      ELSE
      GOTO 450
      END IF

      TITEL1='spectral BDR of '//SAMPLE//' sample'
      TITEL3=WVLEN//' nm'
      TITEL4=BEAM//' beam incident on '//SPOT//' position'
      CALL TITLE('H','L',TITEL1,LEN(TITEL1))
      CALL TITLE('H','L',TITEL3,LEN(TITEL3))
      CALL TITLE('H','L',TITEL4,LEN(TITEL4))
```

```
470     TYPE *,'ANOTHER LINE OF TITLE ?'
        ACCEPT 1000,REPLY
        IF (REPLY.EQ.'N'.OR.REPLY.EQ.'n') THEN
        GOTO 480
        ELSE IF (REPLY.EQ.'Y'.OR.REPLY.EQ.'y') THEN
        TYPE *,'GIVE TITLE (max 80 chars)'
        ACCEPT 1001,TITEL
        CALL TITLE('H','L',TITEL,80)
        GOTO 470
480     END IF

        CALL SET KY('L','C',(3*ICOUNT),37)
        DO 500 I=1,ICOUNT
        LCOUNT=I
        CALL BLNK KY
        CALL PEN(LCOUNT)
        WRITE(THETA,1010) ITHETA(LCOUNT)
        WRITE(PHI,  1010) IPHI(LCOUNT)
        TLINE=' THETA-i = '//THETA//'   ;   PHI-r = '//PHI
        CALL BOTH KY(0,LCOUNT,TLINE,LEN(TLINE))
        CALL BLNK KY
500     CONTINUE
        CALL END PLT

1000    FORMAT(A1)
1001    FORMAT(A80)
1002    FORMAT(A2)
1003    FORMAT(A8)
1004    FORMAT(A10)
1005    FORMAT(A4)
1006    FORMAT(A6)
1010    FORMAT(I3)
        STOP
        END
```

```
C       program EGRAPH used for plotting the graphs with bidirectional
C       reflectances in the specular direction and the spectral-hemispherical
C       reflectance.
C
        PROGRAM EGRAPH

        CHARACTER *45,BDRCAP

        DIMENSION X(4,20),Y(4,20)
        DIMENSION  X1(30),Y1(30)

        TYPE*,'ARE THE BDR CURVES LOGARITHMIC ? (Y OR N)'
        ACCEPT 5000,REPLY1


        DO 500 N=1,4
        TYPE*,'NO: OF POINTS IN CURVE',N,'?'
        ACCEPT*,X(N,0)
        TYPE*,'BDR MULTIPLIER FOR CURVE','N','?'
        ACCEPT*,BMULT
        TYPE *,'TYPE  ANGLE FOLLOWED BY BDR VALUE FOR CURVE',N
        DO 300 M=1,X(N,0)
        ACCEPT*,X(N,M),Y(N,M)
        Y(N,M)=Y(N,M)*BMULT
        IF (REPLY1.EQ.'Y'.OR.REPLY1.EQ.'y') THEN
        Y(N,M)=Y(N,M)*0.001
        END IF
300     CONTINUE
500     CONTINUE


        TYPE*,'NO OF DATA-POINTS IN SPECTRAL CURVE ?'
        ACCEPT*,IPOINT
        TYPE*,'GIVE WAVELENGTH FOLLOWED BY REFLECTANCE'
        DO 1000 J1=1 ,IPOINT
        ACCEPT*,X1(J1),Y1(J1)
1000    CONTINUE


        TYPE*,'BDR AXIS..MAX VALUE ?'
        ACCEPT*,BDMAX
        BDRCAP='BDR   (1.000E-3 per steradian)'
        IF (REPLY1.EQ.'Y'.OR.REPLY1.EQ.'y') THEN
        BDRCAP='BDR   (per steradian)'
        END IF
```

```
      CALL GROUP(1,2)
      CALL SCALES(0.0,80.0,1,0.0,BDMAX,1)
      IF (REPLY1.EQ.'Y'.OR.REPLY1.EQ.'y') THEN
      CALL SCALES(0.0,80.0,1,0.0001,BDMAX,2)
      END IF

      CALL AXES('THETA - r  (degrees)',20,BDRCAP,LEN(BDRCAP))
      CALL PEN(1)
      DO 2000 J4=1,4
      J2=J4
      IF (J2.GT.2) THEN
      CALL PEN(2)
      END IF
      DO 1500 J3=1, X(J2,0)
      CALL JOIN PT(X(J2,J3),Y(J2,J3))
      CALL MARK PT(X(J2,J3),Y(J2,J3),J2)
1500  CONTINUE
      CALL BREAK
2000  CONTINUE
      CALL PEN(1)
      CALL SET KY('T','L',3,6)
      CALL PEN(2)
      CALL LINE KY(0,' 633nm',6)
      CALL BLNK KY
      CALL PEN(1)
      CALL LINE KY(0,' 1152nm',7)


      CALL SCALES(0.4,2.0,1,0.0,60.0,1)
      CALL PEN(1)
      CALL AXES('WAVELENGTH  (micrometers)'
     1 ,25, 'hemispherical REFLECTANCE   (%)',33)
      CALL PEN(2)
      CALL DRAW LN(0.633,60.0)
      CALL PEN(1)
      CALL DRAW LN(1.152,60.0)
      CALL BREAK

      DO 3000 I=1,IPOINT
      CALL JOIN PT(X1(I),Y1(I))
      CALL MARK PT(X1(I),Y1(I),4)
3000  CONTINUE
      CALL BREAK
      CALL END PLT
5000  FORMAT(A1)
      STOP
      END
```

```
C       program POLAR used for plotting the directional emittance graphs.
C       This will accomodate upto 10 curves,each of a maximum of 20
C       data-points.
C
        PROGRAM POLAR
        CHARACTER *80,TITEL,TITEL1
        CHARACTER*25,DESCRI

        DIMENSION TH(10,20),R(10,20)
        DIMENSION NPOINT(10)
        DIMENSION R1(20),TH1(20)

        common/jbou/ioulin,oueps
        oueps=0.0
        ioulin=3



        CALL PAGE(21.0,29.7)
        CALL NEWPIC
        TYPE*,'GIVE MAX VALUE ON EMITTANCE AXIS'
        ACCEPT*,EMAX
        CALL SCALES(0.0,EMAX,1,0.0,EMAX,1)
        CALL DEGS
        CALL GRIDS(2)
        CALL XAXIS(0.0,5.0,0.0,'directional EMITTANCE',21)
        CALL THAXIS(5.0)

        TYPE*,'NO: OF CURVES IN THIS GRAPH ?'
        ACCEPT *,NCURVS
        DO 500 J=1,NCURVS
        TYPE *,'NO: OF POINTS IN CURVE ',J
        ACCEPT*,NPOINT(J)
        TYPE*,'GIVE ANGLE FOLLOWED BY VALUE IN CURVE ',J
        DO 300 K=1,NPOINT(J)
        ACCEPT*,TH(J,K),R(J,K)
        TH(J,K)=(90 - TH(J,K))
300     CONTINUE
500     CONTINUE

        CALL CV TYPE(2)

        DO 650 J=1,NCURVS
        J1=J
        CALL PEN(J1)
        DO 600 K1=1,NPOINT(J1)
        R1(K1)=R(J1,K1)
        TH1(K1)=TH(J1,K1)
600     CONTINUE
```

```
      CALL DRAW CV(R1,TH1,NPOINT(J1))
      DO 630 K=1,NPOINT(J1)
      K2=K
      CALL MARK PT(R1(K2),TH1(K2),J1)
630   CONTINUE


650   CONTINUE

      CALL PEN(1)
      CALL SET KY('H','R',3*NCURVS,25)
      DO 700 J=1,NCURVS
      J1=J
      CALL PEN(J1)
      CALL BLNK KY
      TYPE*,'GIVE DESCRIPTION OF CURVE',J1
      ACCEPT 1001,DESCRI
      CALL BOTH KY(0,J1,DESCRI,LEN(DESCRI))
      CALL BLNK KY

700   CONTINUE

      CALL PEN(1)
      TYPE*,'GIVE TITLE OF GRAPH'
      ACCEPT 1002,TITEL
      TITEL='          '//TITEL
      CALL TEXTMG(1.15)
      CALL TITLE('L','L',TITEL,LEN(TITEL))


      CALL END PLT
      STOP
1000  FORMAT(A1)
1001  FORMAT(A25)
1002  FORMAT(A80)
      END
```

LIST OF REFERENCES

Agnew J.T. and Mcquistan R.B. 1953
J.Opt.Soc.Am. 43, 999

Agnihotri and Gupta 1981, Solar Selective Surfaces
(John Wiley & Sons)

American Institute of Physics Handbook 1972, McGraw-Hill

ASTM Manual on the Use of Thermocuples in Temperature
Measurement (ASTM STP 470B) 1981.

Barkas W.W. 1939, Proc. Phys. Soc.London 51 274

Bartsch K.O. et al 1970, AIAA 8th Aerospace sciences
meeting, New York (AIAA paper No. 70-68).

Bennett H.E. and Bennett J.M. 1967, Physics of Thin Films
(ed. by G.Hass and R.E. Thun) 4, 1

Birkebak R.C. and Eckert E.R.G. 1965, J.Heat Transfer
(February issue) 87, 85.

Bouguer P. 1760, Optical treatise on the gradation of light,
translated by W.E.Knowles Middleton, 1961
(Univ. Toronto Press)

Bousquet P. et al 1981, J.Opt.Soc.Am 71, 1115

Brookdeal Instruction Manual for 9421A Phase sensitive detector 1974

Budde W. 1960, J.Opt.Soc.Am. 50, 217

Butler C.P. and Inn C.Y. 1959, First symposium on Surface Effects on Spacecraft Materials, Calif. U.S.A. (ed by F.J.Clauss) 195

Call P.J. 1978, National Plan for Absorber Surfaces R & D SERI Rep., SERI/TR-31-103

Instruction Manual for model IR50 Golay Detector, Cathodeon Ltd., Cambridge

Choudhury C. and Sehgal H.K. 1982, Solar Energy 28, 25

Clarke F.J.J. 1973, Proc. Colour 73-Int. Colour Assoc.Congress

Duffie J.A. and Beckman W.A. 1980, Solar Engineering of Thermal Rousses (Wiley and Sons)

Eckert E.R.G. and Drake R.M. 1972, Analysis of Heat and Mass Transfer (McGraw Hill)

Edwards D.K. and Catton I. 1965, Advances in Thermophysical Properties at Extreme Temperatures and Pressures (ASME New York) 189

Egan W.G. and Hilgeman T.W. 1979, Optical Properties of Inhomogeneous Materials (Academic Press)

Gray W.A. and Muller 1974, Engineering Calculations in Radiative Heat Transfer (Pergamon Press)

Green A.A. 1983, University College, Cardiff - internal report No.1058

Harrison W.J. 1963, Measurement of Thermal Radiation Properties of Solids - NASA SP31 - (ed by J.C.Richmond)

Heavens O.S. 1965, Optical Properties of Thin Solid Films (Dover Publications)

Helmholtz 1909, Physiological optics 3rd ed. Vol.1 page 231 (translated by J.P.C.Southall) Optical Society of America, 1924.

Herold L.M.and Edwards D.K. 1966, AIAA Jornal 4 10,1802.

Hofert H.J. and Loof H. 1964, Die Farbe 13, 53

Hottel H.C. and Serafim A.F. 1967, Radiative Transfer (McGraw-Hill)

Hsia J.J. Richmond J.C. 1976, Jnl. of Research NBS part A, 80A, 189

Hubbs J.E. et al 1982, Applied Optics 21, 18

Huetz-Aubert M. and Sacadura J.F. 1982 Revue.phys. Appl. 17,251

Hunter W.R. and Tousey 1964, J.Phys.(Paris) 25, 148

Hutchins M.G. 1979, Proc. IEE conference on 'Future Energy Concepts', London, 249

Jakob M. 1949, heat Transfer Vol.2 (John Wiley & Sons)

Jones B.W. and Oreszczyn 1981, Energy Research Group, The Open University, Milton Keynes, U.K.

Jones B.W. and Oreszczyn T. 1986, Applied Energy 22, 107.

Koltun M.M. 1981, Selective Optical Surfaces for Solar Energy Converters - translated by S.Chomet and ed. by D.P. Siddons (Allerton Press, New York)

Kruse P.W. 1977, in Optical and Infrared Detectors - ed. by R.J.Keys - Springer Verlag) 44

Lambert J.H. 1760, Photometria Augsburg (German edition by Anding Leipzig 1892)

Lohrengel J. 1969, Doctoral Thesis, Technische Hochschule Aachen, West-Germany

Look D.C.Jnr. 1965, J.Opt.Soc.Am. 55,12,1628

MacFadyen K.A. 1963, A Physics Laboratory Handbook for Students (University of London Press)

McNicholas H.J. 1929, Jnl.of Research (Bureau of Standards) 29

Meinel A.B. and Meinel M.P. 1976, Applied Solar Energy (Addison-Wesley Publishing)

Miller E.R. and Vun Kannon R.S. 1967, Thermophysics of Spacecraft and Planetary Bodies (AIAA Thermophysics Specialist Conference, 1967) ed. by G.B.Heller (Academic Press) 219

Musa A.H. 1980, Ph.D Thesis, University of Aston, Birmingham

Nepogodin I.A. et al. 1984, Sov.J.Opt.Technol. 51,3,144

Nicodemus F.E. et al 1977, Geometrical Considerations and Nomenclature for Reflectance (National Bureau of Standards USA)

Papini M. and Papini F. 1982, Optical Coatings for Energy Efficiency and Solar Applications SPIE, Vol.324, 163

Pettit R.B. 1977, Solar Energy 19, 733

Planck M. 1901, Ann. Phys. 4, 3, 553

Pokrowski G.I. 1924, Z.Physik. 30, 66

Robinson N. (ed) 1966, Solar Radiation (Elsevier, Amsterdam)

Rolling R.E. 1976, Thermophysics of Spacecraft and Planetary Bodies, ed by G.B.Heller (Academic Press) 91

Rubin M. 1982, Solar Energy Materials 6,375

Schmidt E. and Eckert E. 1935, Forsch. Gebiete Ingenieurw. 6, 175

Schrieder Y.A. (ed) 1964, Method of Statistical Testing - Monte Carlo Method (American Elsevier Publishing Company Inc. NY)

Schultz H. 1925, Z.Physik 31, 496

Seredenko M.M. 1979, Soviet J.Opt.Technol 46, 5

Siegel R. and Howell J.R. 1981, Thermal Radiation Heat Transfer (McGraw Hill)

Seraphin B.O. (ed.) 1976, Optical Properties of Solids - New Developments (American Elsevier)

Snyder N.W. et al 1955, Trans ASME 77, 1011

Stuhlinger T.W. et al 1981, Applied Optics 20, 15, 2648

Tabor H. 1955, Bull.Res.Council, Israel 5A, 119

Touloukian Y.S. et al 1972, Thermophysical Properties of Matter, Vol.9 (IFI/Plenum, New York - Washington)

Thakur A and Raman R, 1983, Applied Energy 15 (1983)

Torrance K.E. and Sparrow E.M. 1965, J. Opt. Soc. Am. 57, 1105

van der Leij M. 1979, PhD Thesis Delft University, The Netherlands

van Heereveld A.A.M.T. et al 1984, SPIE 505 Advances in Optical Materials, 244

Willrath H, 1979, Ph.D Thesis NSWIT, Sydney, Australia

Wright H. 1900, Ann.Physik 1, 17

Wyatt P.J. 1982, Applied Optics 21, 14

Yoshida S. 1978, Applied Optics 17, 145

Zerlaut G.A. 1963, Measurement of Thermal Radiation
Properties of Solids - NASA SP31 -
(ed by J.C.Richmond) 275

LIST OF FIGURES

LIST OF TABLES

FIGURES

SOLAR RADIATION

FIGURE 1.1

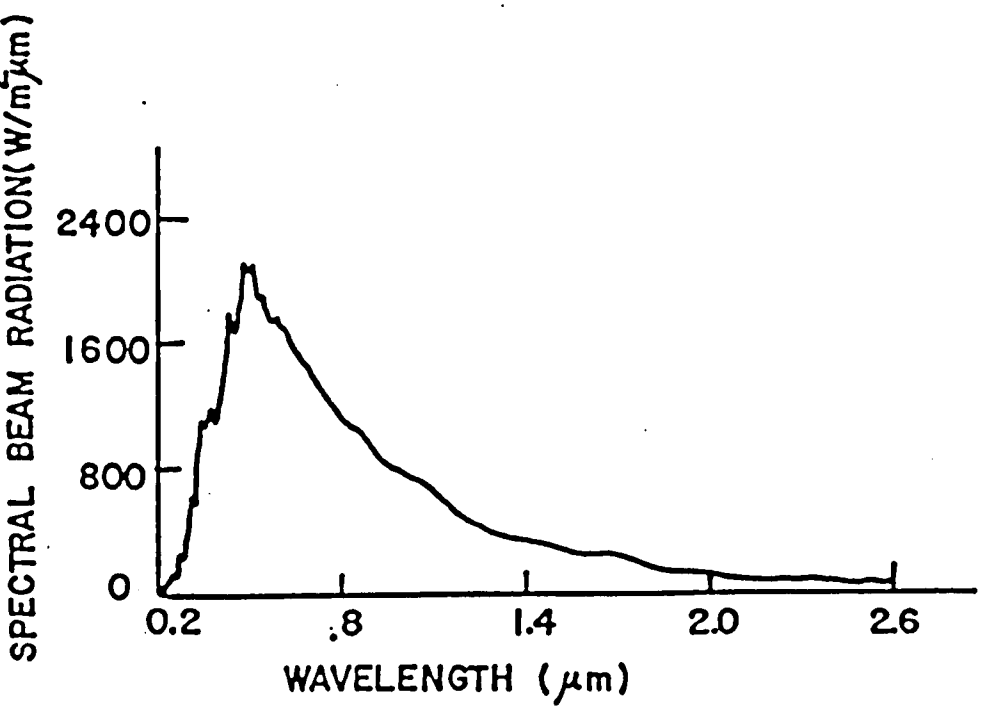

The NASA (1971) standard spectral irradiance at the mean sun-earth distance and a solar constant of 1353 W/m^2 (429.2 $Btu/ft^2/hr$). The peaked region of the curve represents the majority of sunlight's energy. The distribution shown here is further exaggerated after passing through the earth's atmosphere.

SOLAR COLLECTOR CONFIGURATIONS FIGURE 1.2

flat plate collector

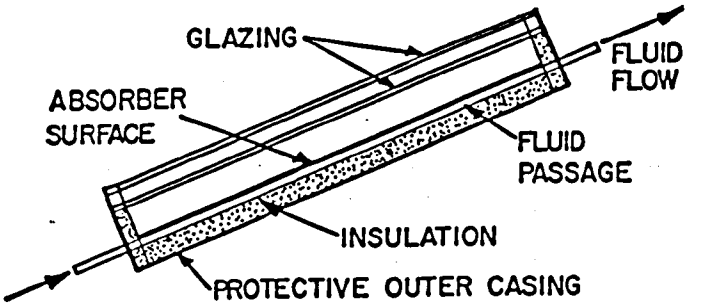

spiral collector

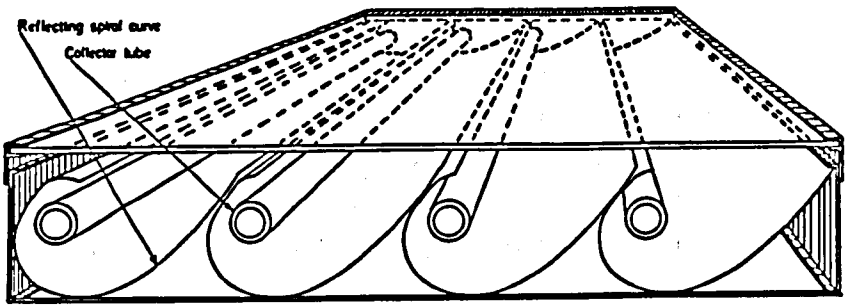

compound parabolic concentrators

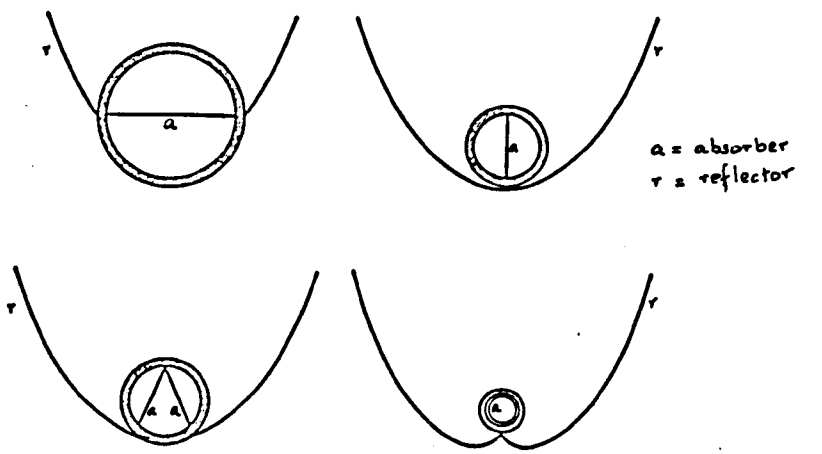

FIGURE 1.3

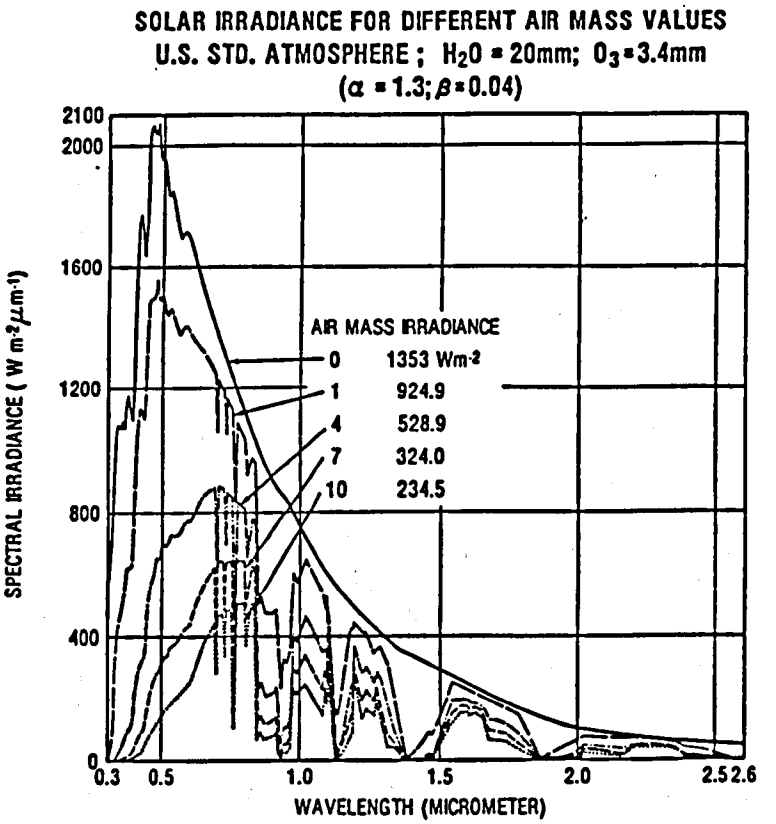
SOLAR IRRADIANCE FOR DIFFERENT AIR MASS VALUES
U.S. STD. ATMOSPHERE ; H_2O = 20mm; O_3 = 3.4mm
(α = 1.3; β = 0.04)
SPECTRAL IRRADIANCE (W m^{-2} μm^{-1})
2100
2000
1600
1200
800
400
0
AIR MASS IRRADIANCE
0 1353 Wm^{-2}
1 924.9
4 528.9
7 324.0
10 234.5
0.3
0.5
1.0
1.5
2.0
2.5
2.6
WAVELENGTH (MICROMETER)

COMPARISON OF SOLAR AND THERMAL SPECTRA FIGURE 1.4

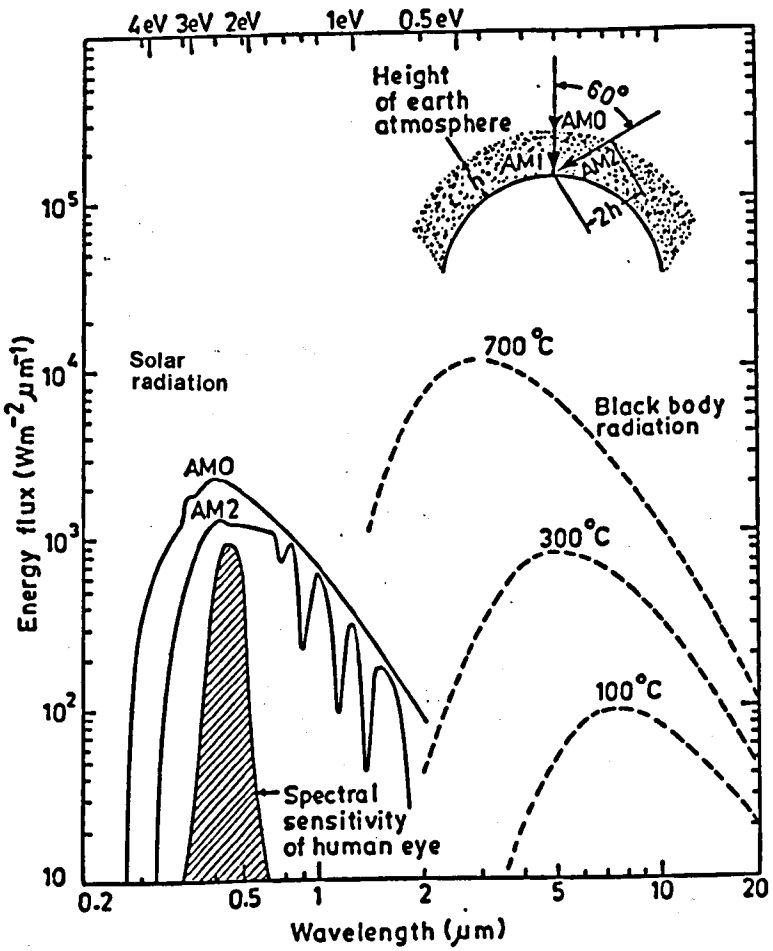

(Energy flux is measured per unit area facing the source)

'POLAR' AND 'AZIMUTHAL' ANGLES FIGURE 1.5

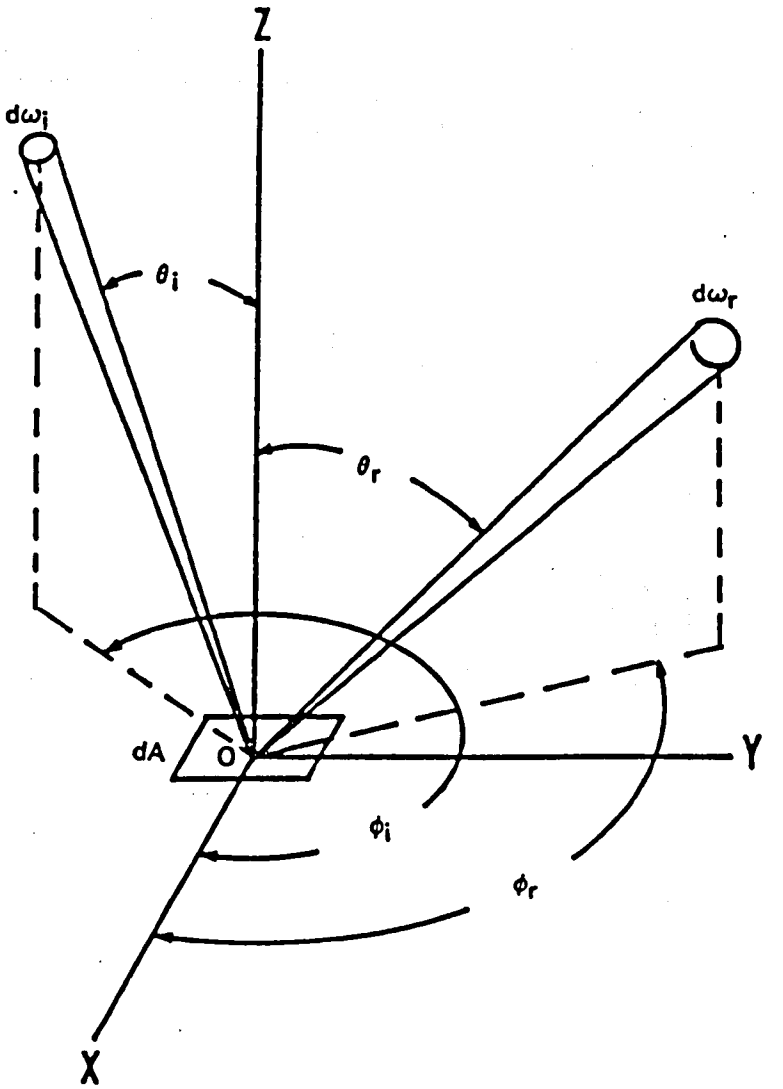

FIGURE 1.6

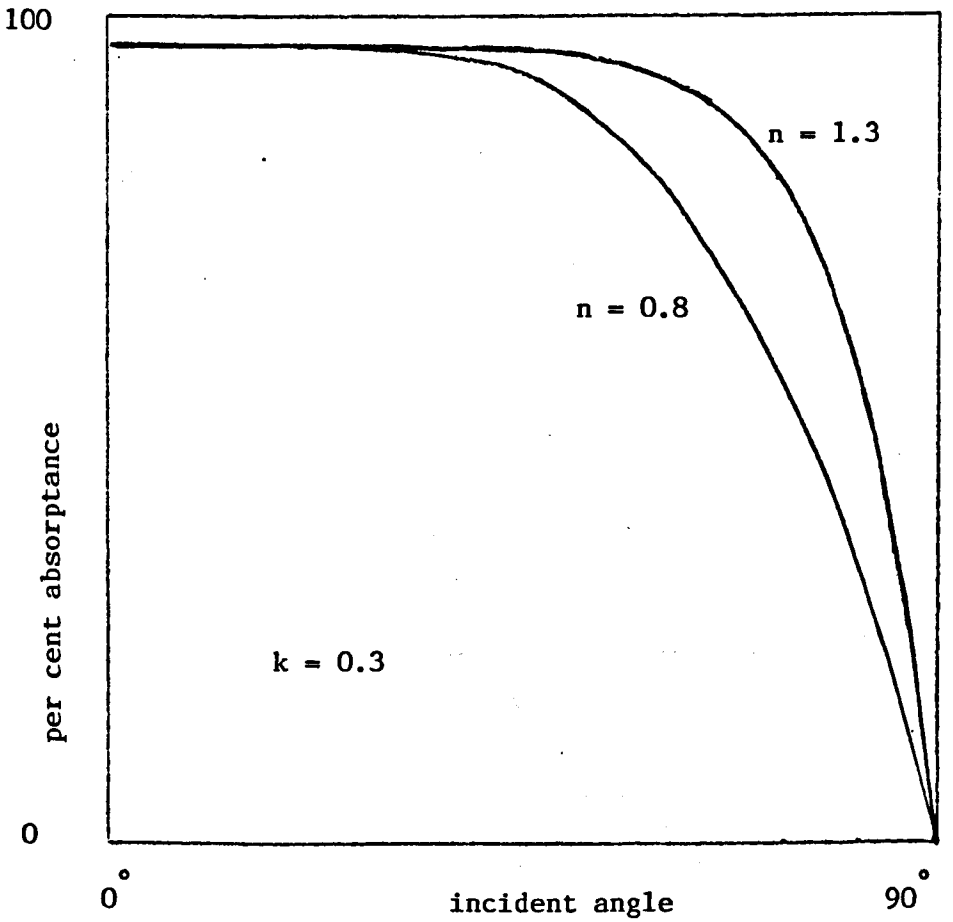

VARIATION OF ABSORPTANCE WITH INCIDENT POLAR ANGLE FOR IDEAL DIELECTRIC MATERIAL

FPC'S WITH 'SPECULAR' AND 'DIFFUSE' ABSORBERS

FIGURE 1.7

collector A

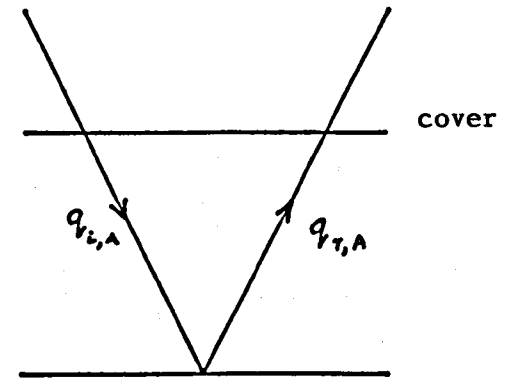

specularly reflecting absorber

collector B

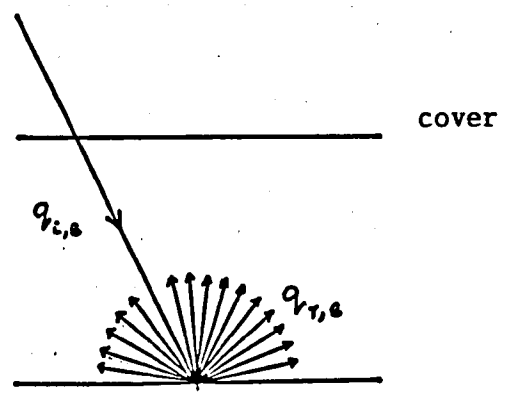

diffusely reflecting absorber

FIGURE 1.8

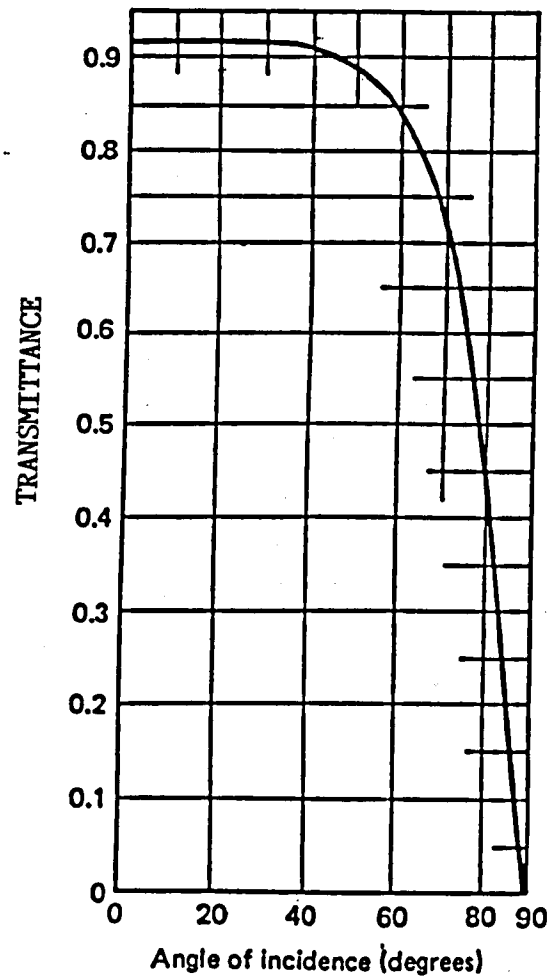

TYPICAL VARIATION OF TRANSMITTANCE WITH INCIDENT ANGLE FOR COMMON COVER MATERIALS

COLLECTOR IN YOSHIDA'S ANALYSIS

FIGURE 1.9

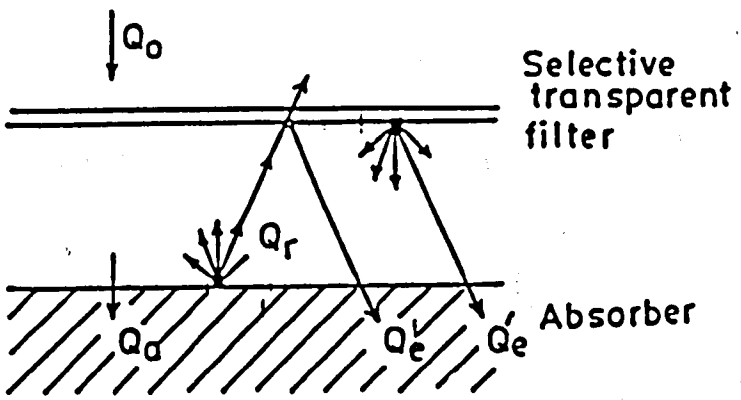

FIGURE 1.10

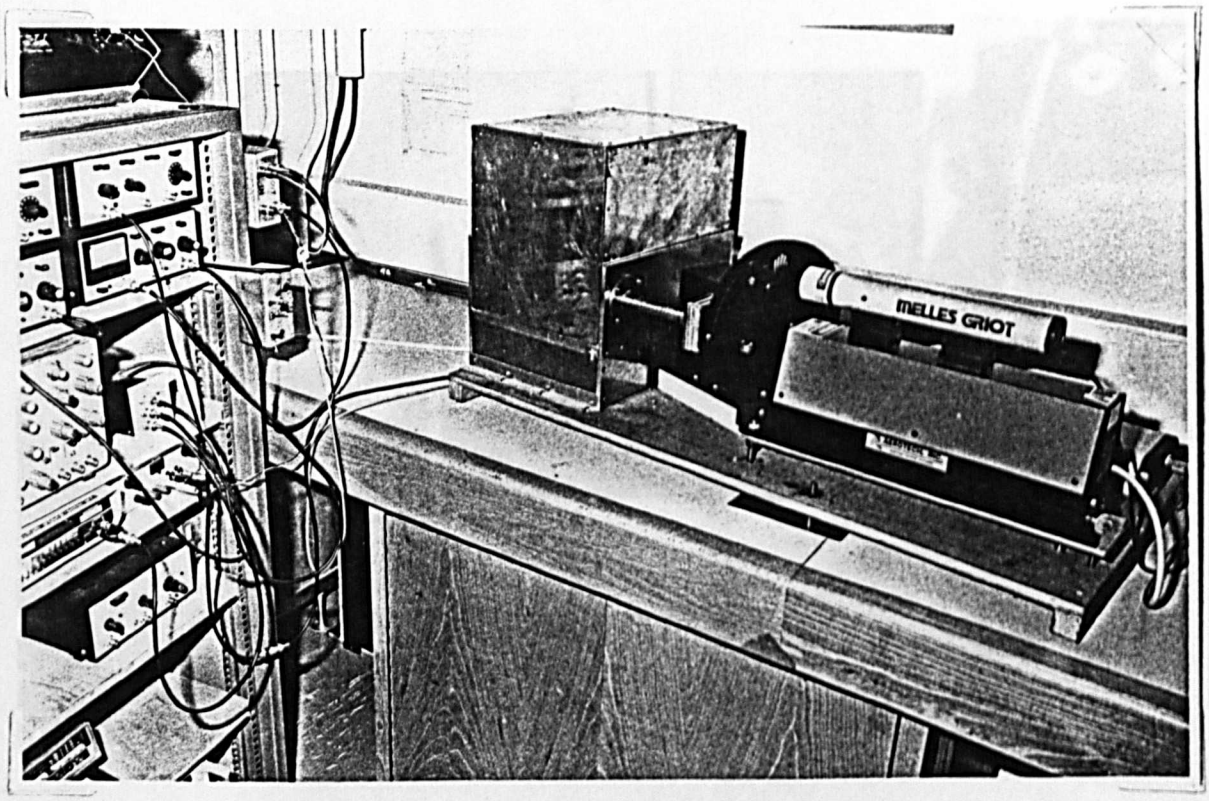

BIDIRECTIONAL REFLECTANCE APPARATUS

FIGURE 1.11

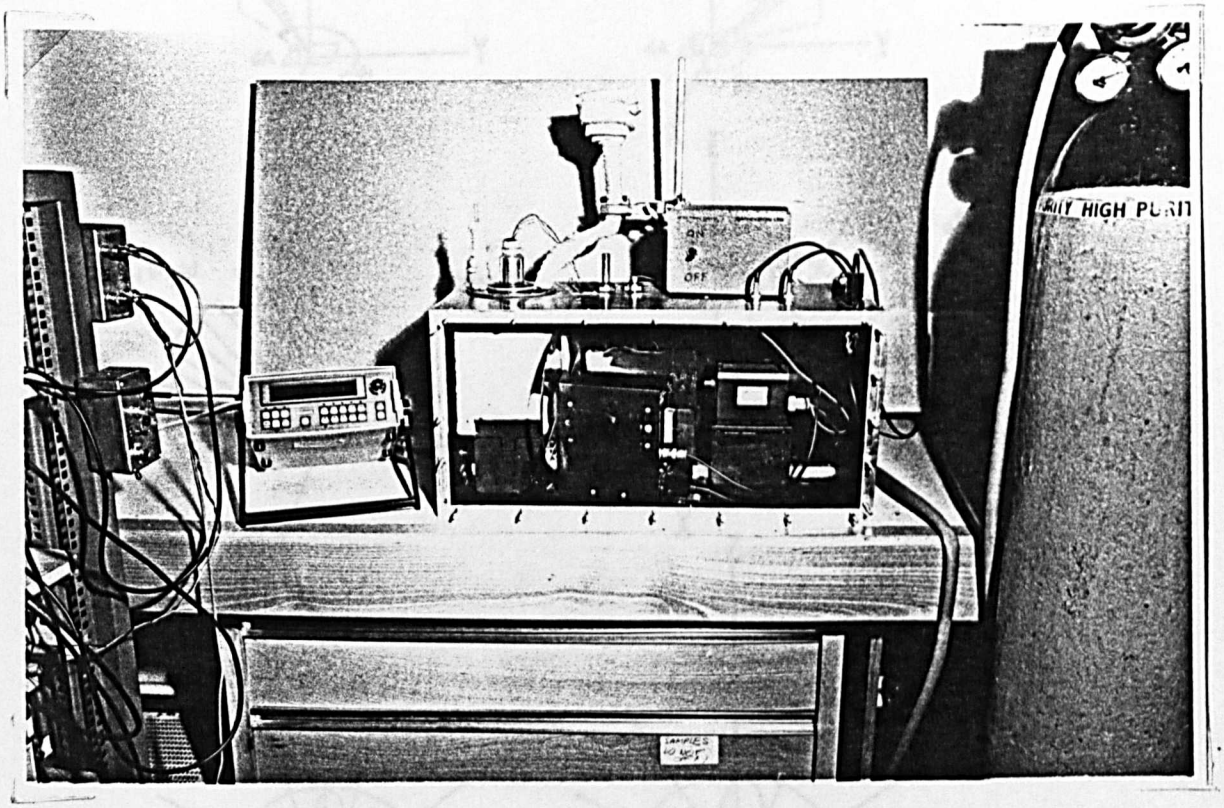

DIRECTIONAL EMITTANCE APPARATUS

FIGURE 2.1

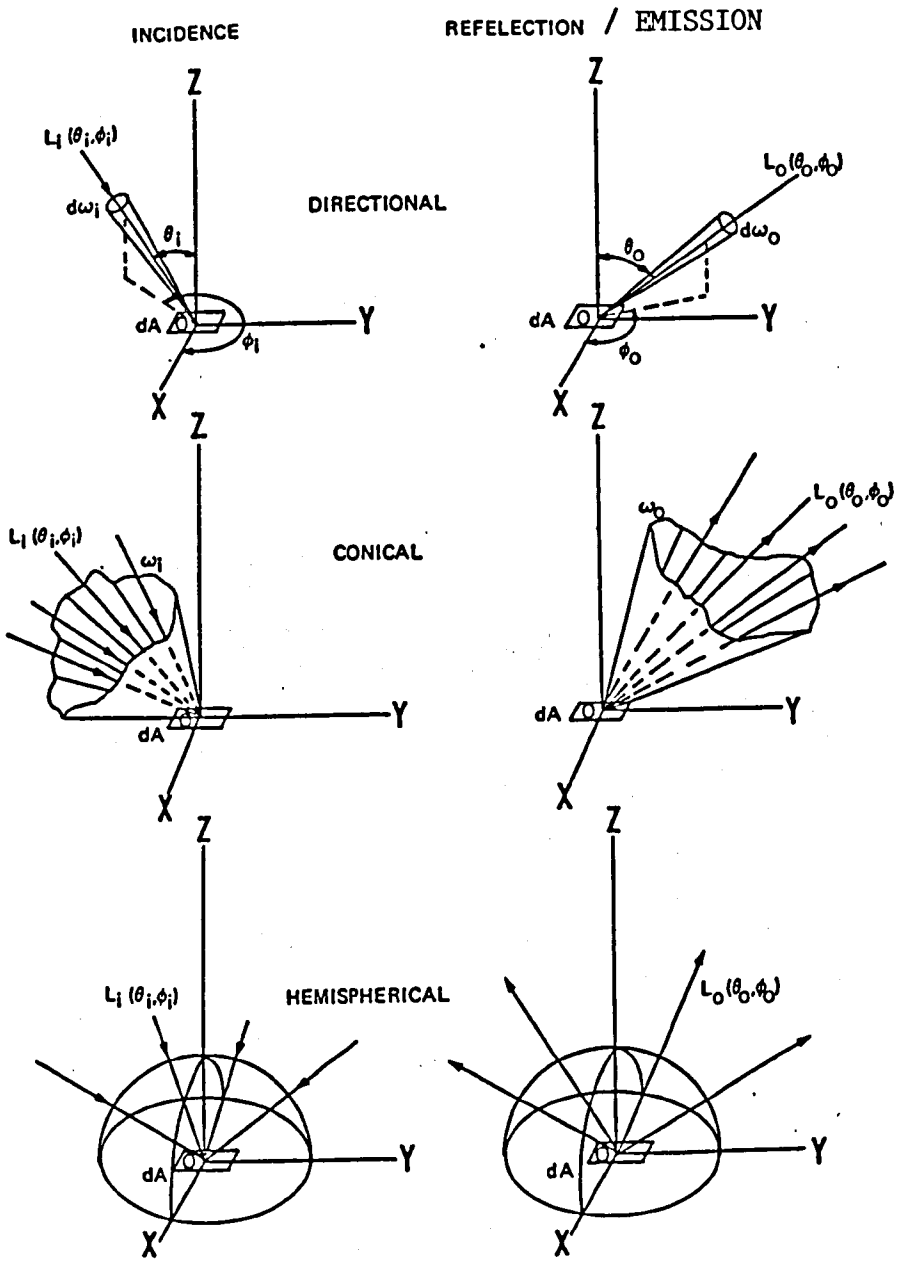

SOME 'DESCRIPTORS' FOR GEOMETRICAL CONFIGURATION OF MEASUREMENT

L_i is the incident flux and L_o is the outgoing(i.e. either emitted or reflected) flux.

BIDIRECTIONAL REFLECTANCE

FIGURE 2.2

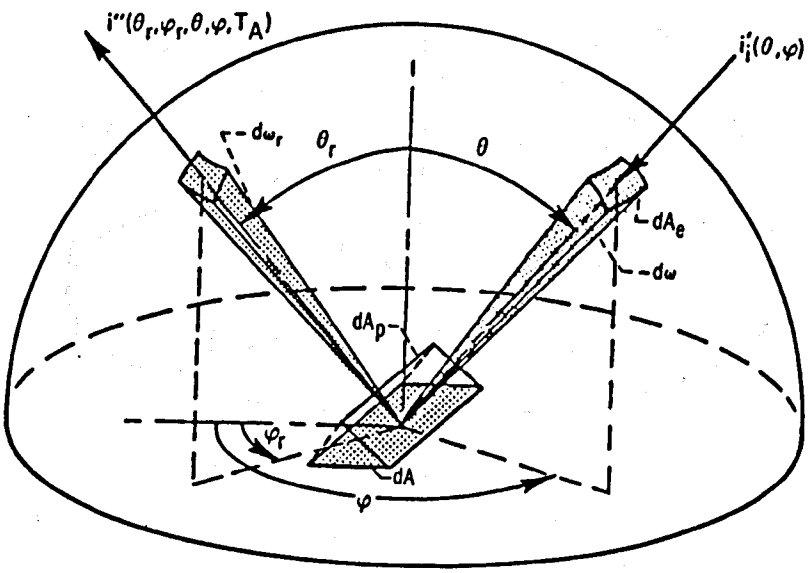

FIGURE 2.3

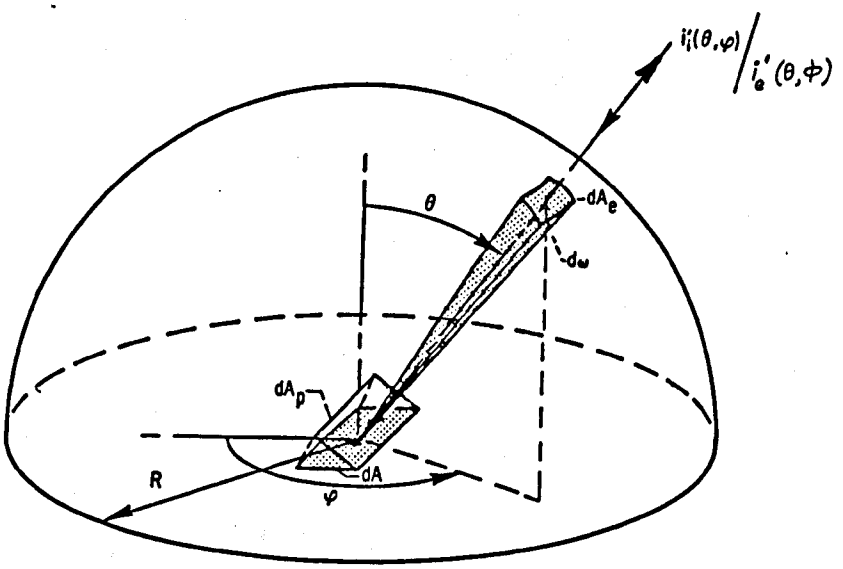

INCIDENT / EXITENT INTENSITY

FIGURE 2.4

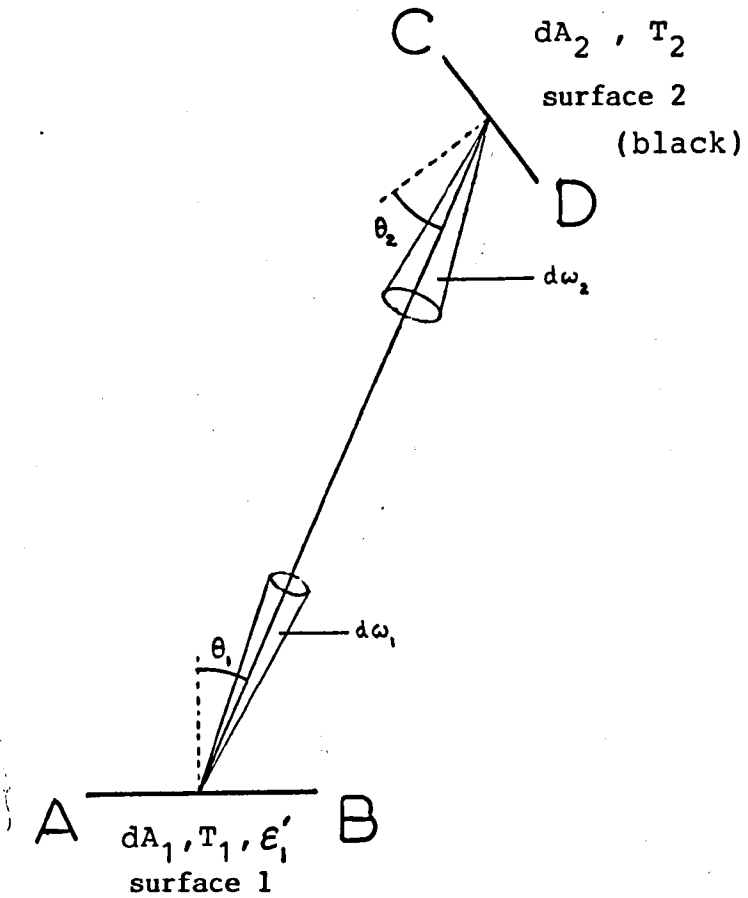

RADIATION EXCHANGE BETWEEN A BLACK AND A SEMIDIFFUSE-GRAY SURFACE

FIG. 3.1 EMITTANCE MEASUREMENT TECHNIQUES

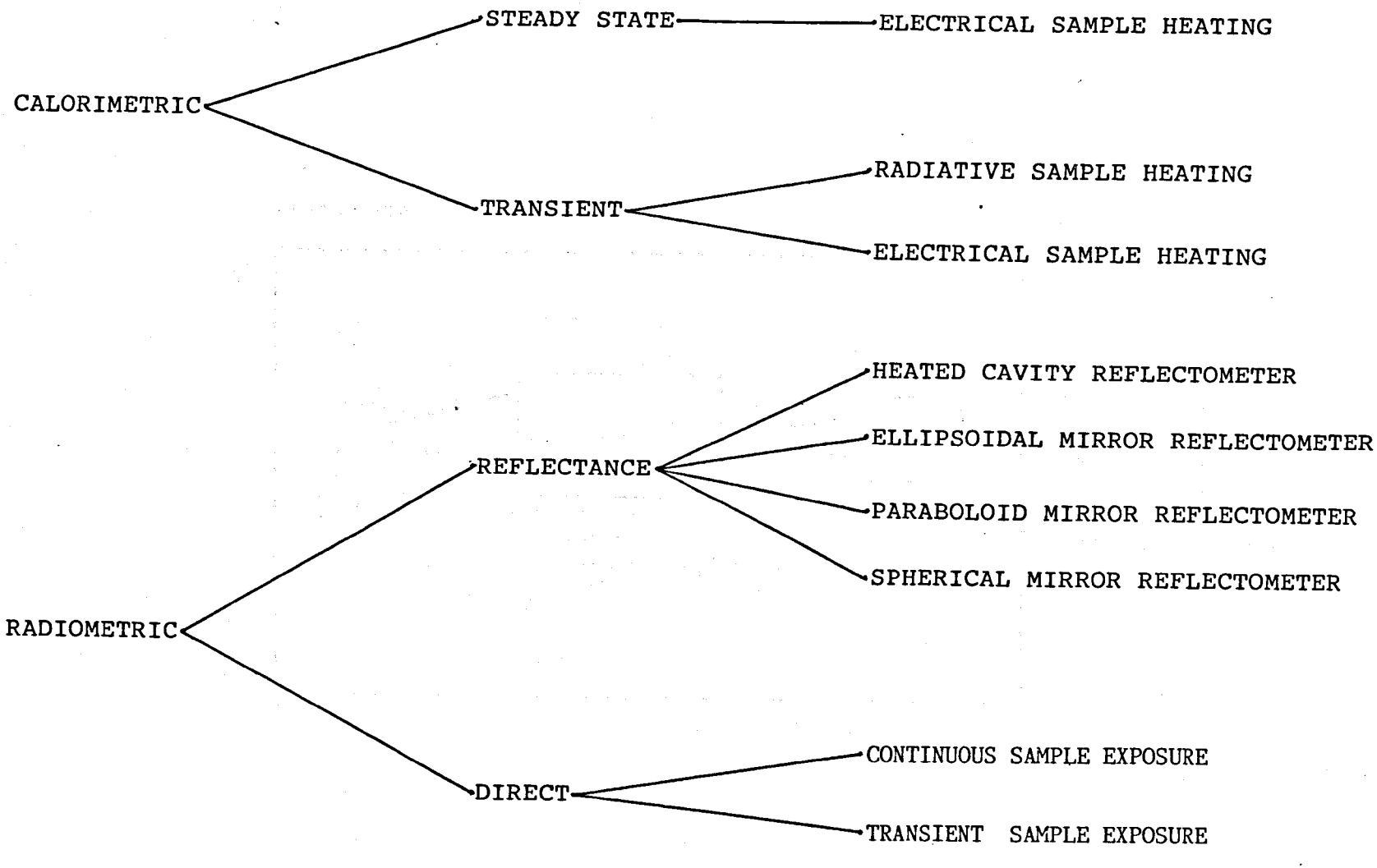

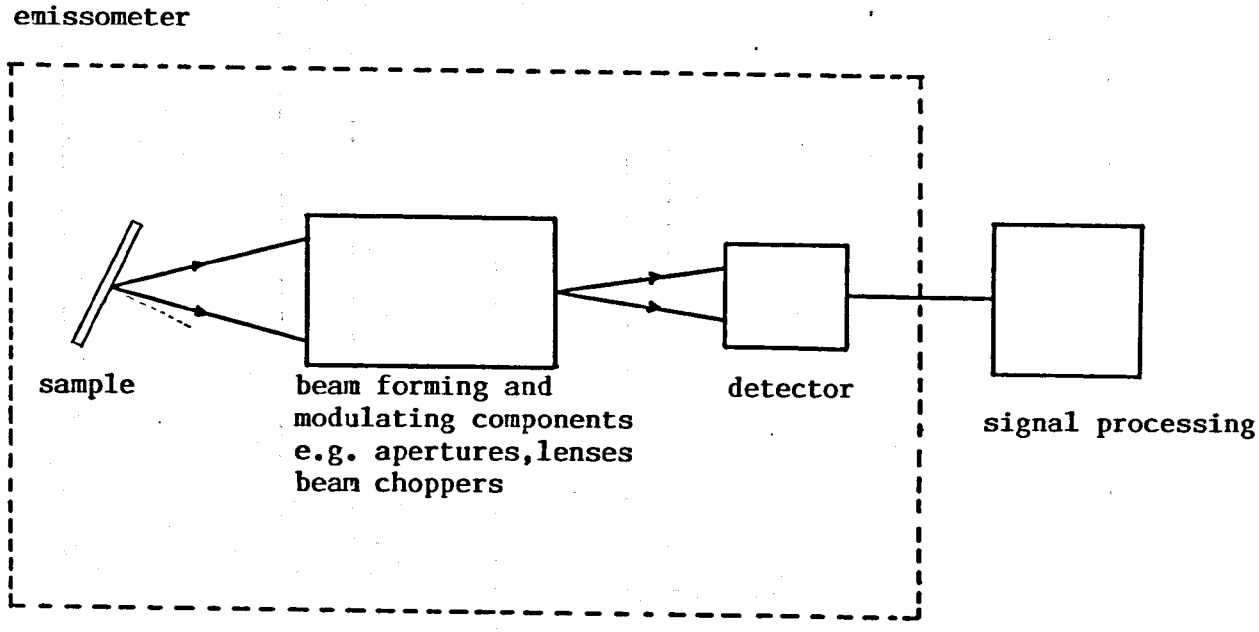

FIGURE 3.2

THE DIRECT RADIOMETRIC METHOD

FIGURE 3.3

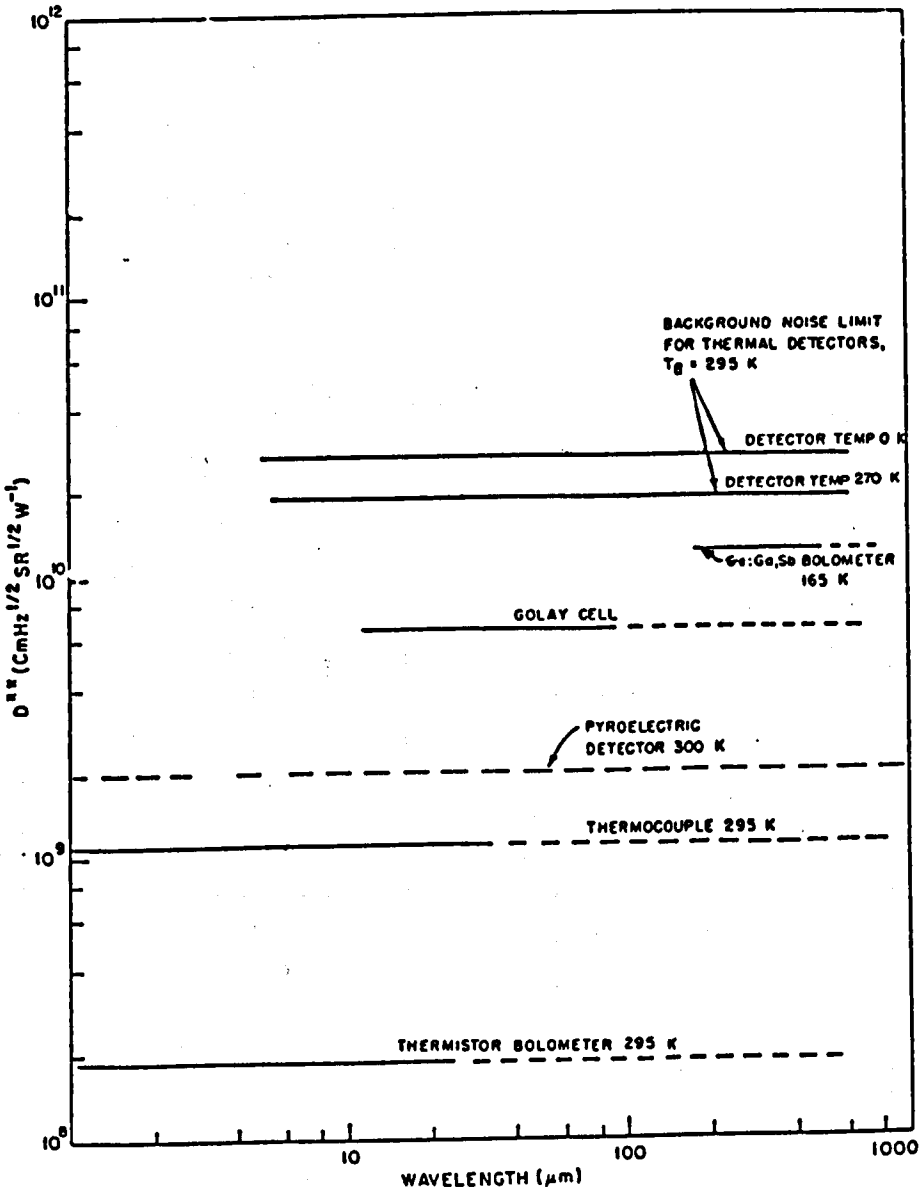

DETECTIVITIES OF THERMAL RADIATION DETECTORS

FIGURE 3.4

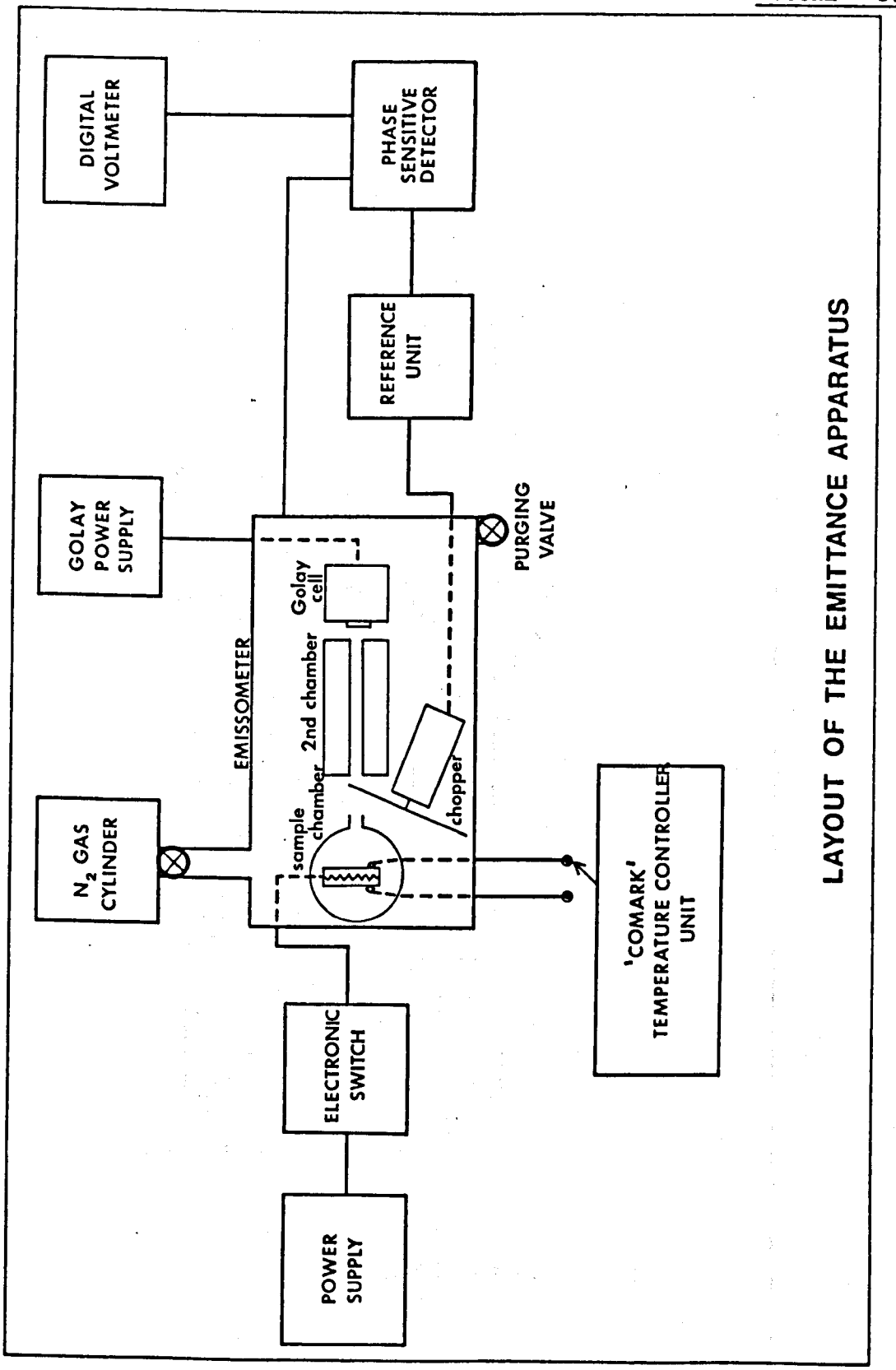
DIGITAL VOLTMETER
PHASE SENSITIVE DETECTOR
REFERENCE UNIT
GOLAY POWER SUPPLY
PURGING VALVE
Golay cell
2nd chamber
EMISSOMETER
chopper
sample chamber
N_2 GAS CYLINDER
'COMARK' TEMPERATURE CONTROLLER UNIT
ELECTRONIC SWITCH
POWER SUPPLY
LAYOUT OF THE EMITTANCE APPARATUS

FIGURE 3.5

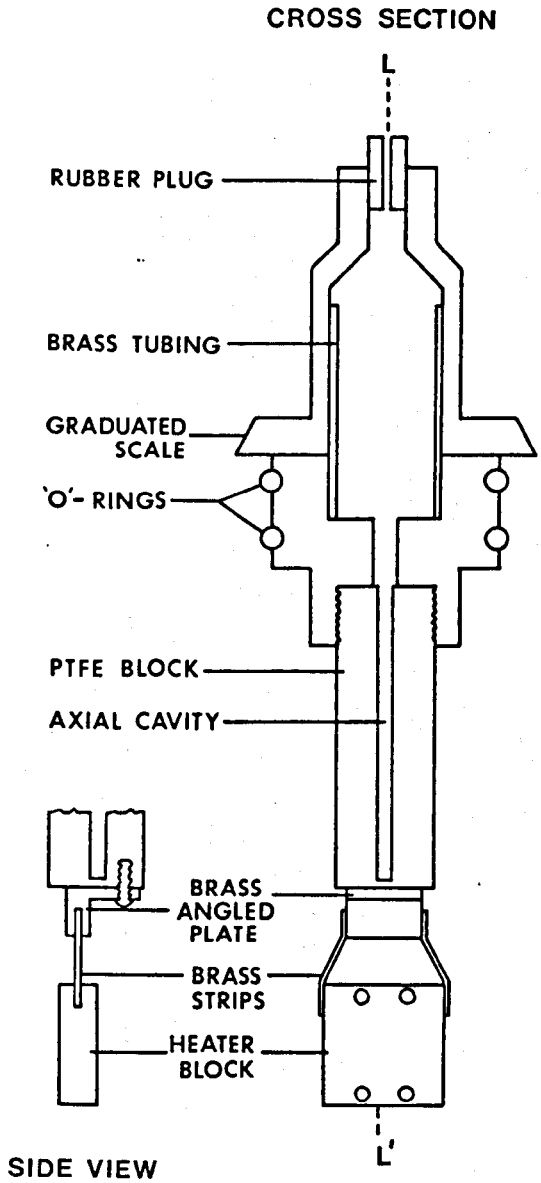

DRAWING OF SHHA

FIGURE 3.6

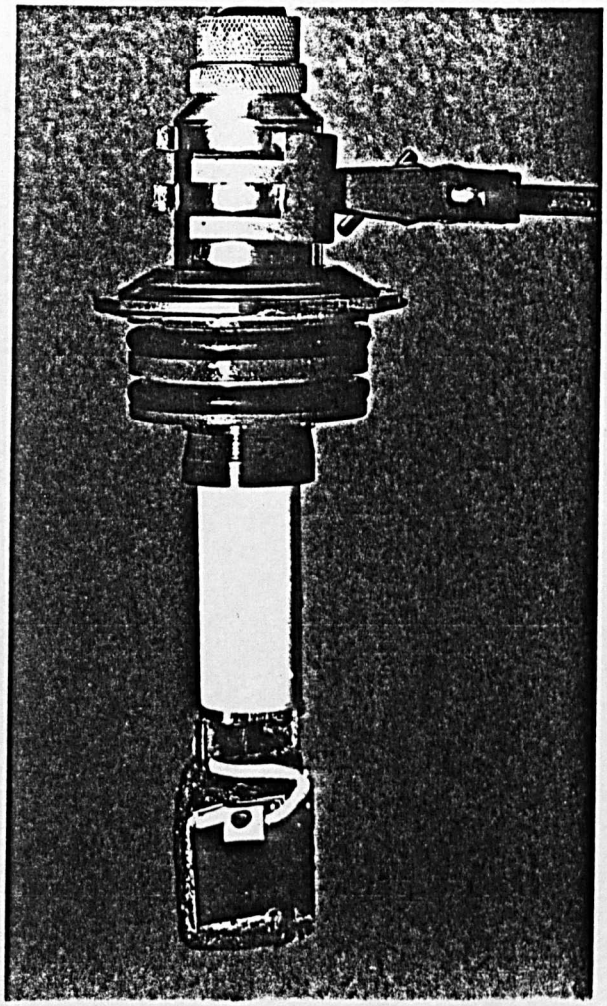

SAMPLE HOLDER HEATER ASSEMBLY

FIGURE 3.7

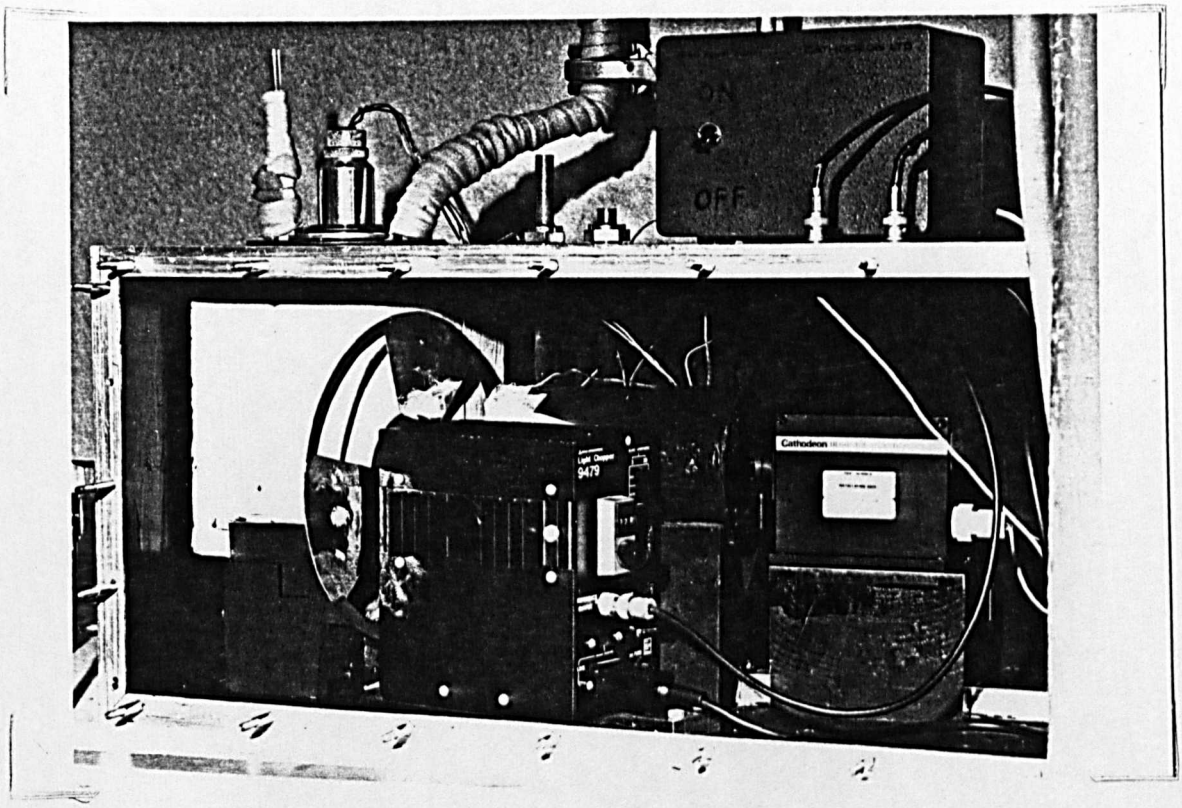

DIRECTIONAL EMISSOMETER

THE 'DYNAMIC SEAL'

FIGURE 3.8

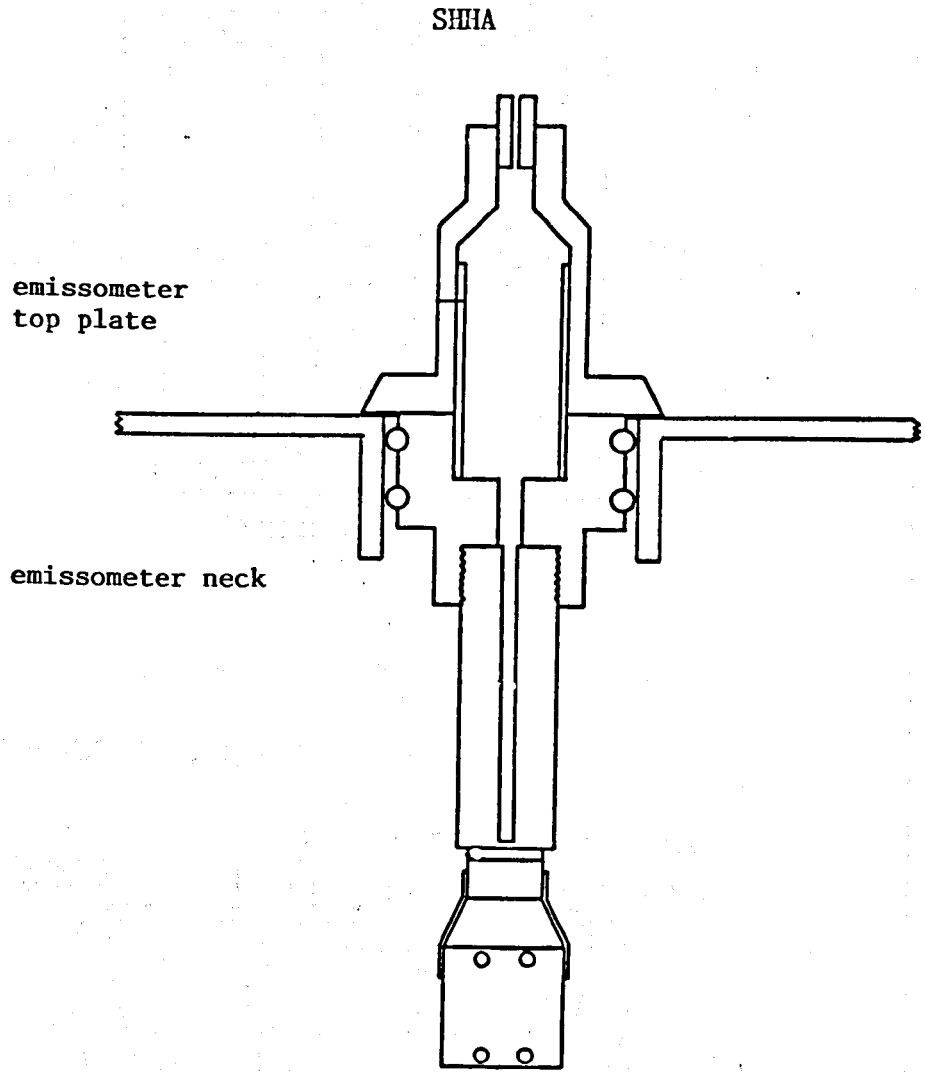

FIGURE 3.9

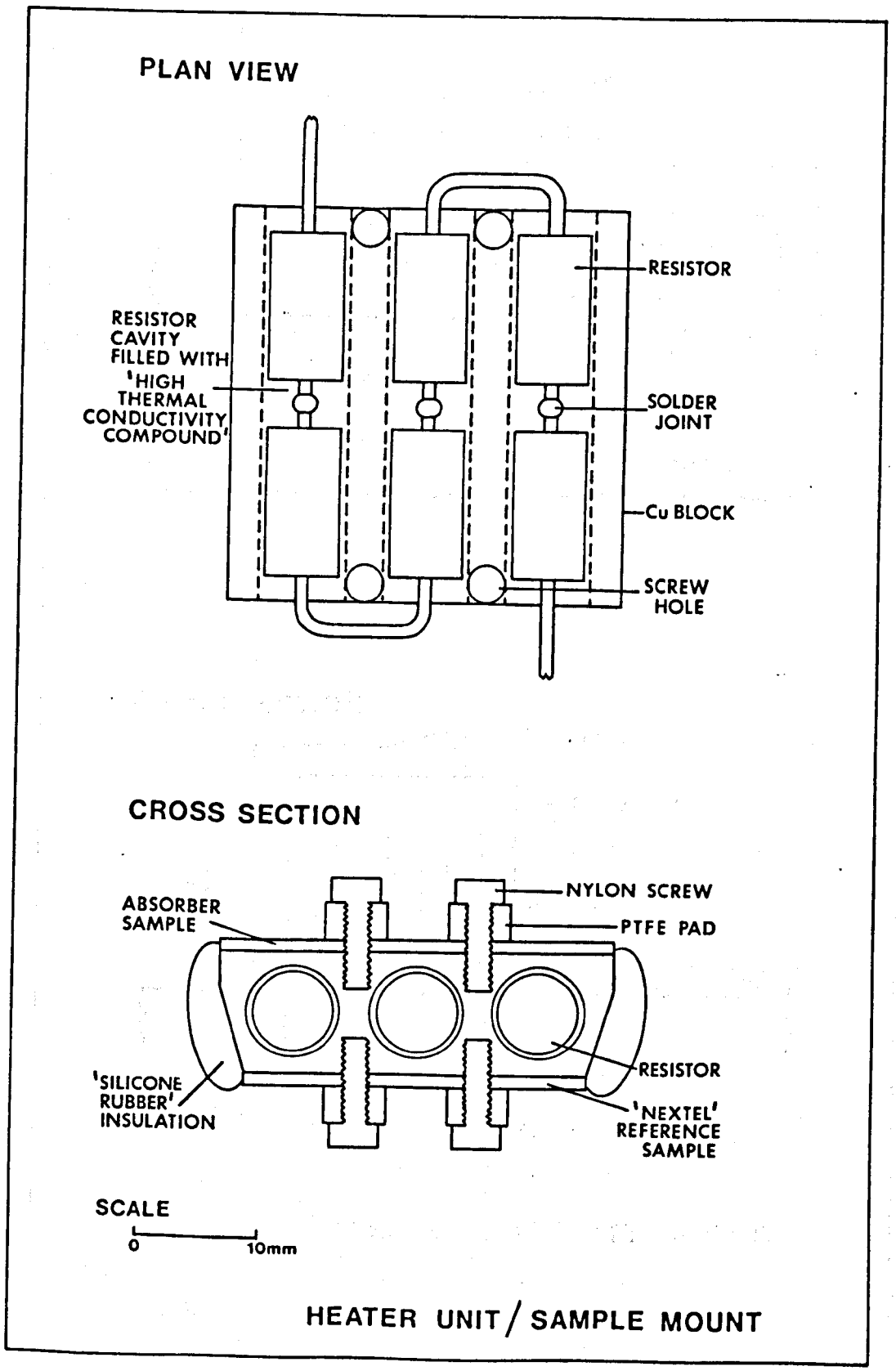
PLAN VIEW
RESISTOR
RESISTOR CAVITY FILLED WITH 'HIGH THERMAL CONDUCTIVITY COMPOUND'
SOLDER JOINT
Cu BLOCK
SCREW HOLE
CROSS SECTION
NYLON SCREW
ABSORBER SAMPLE
PTFE PAD
RESISTOR
'SILICONE RUBBER' INSULATION
'NEXTEL' REFERENCE SAMPLE
SCALE
0
10mm
HEATER UNIT / SAMPLE MOUNT

FIGURE 3.10

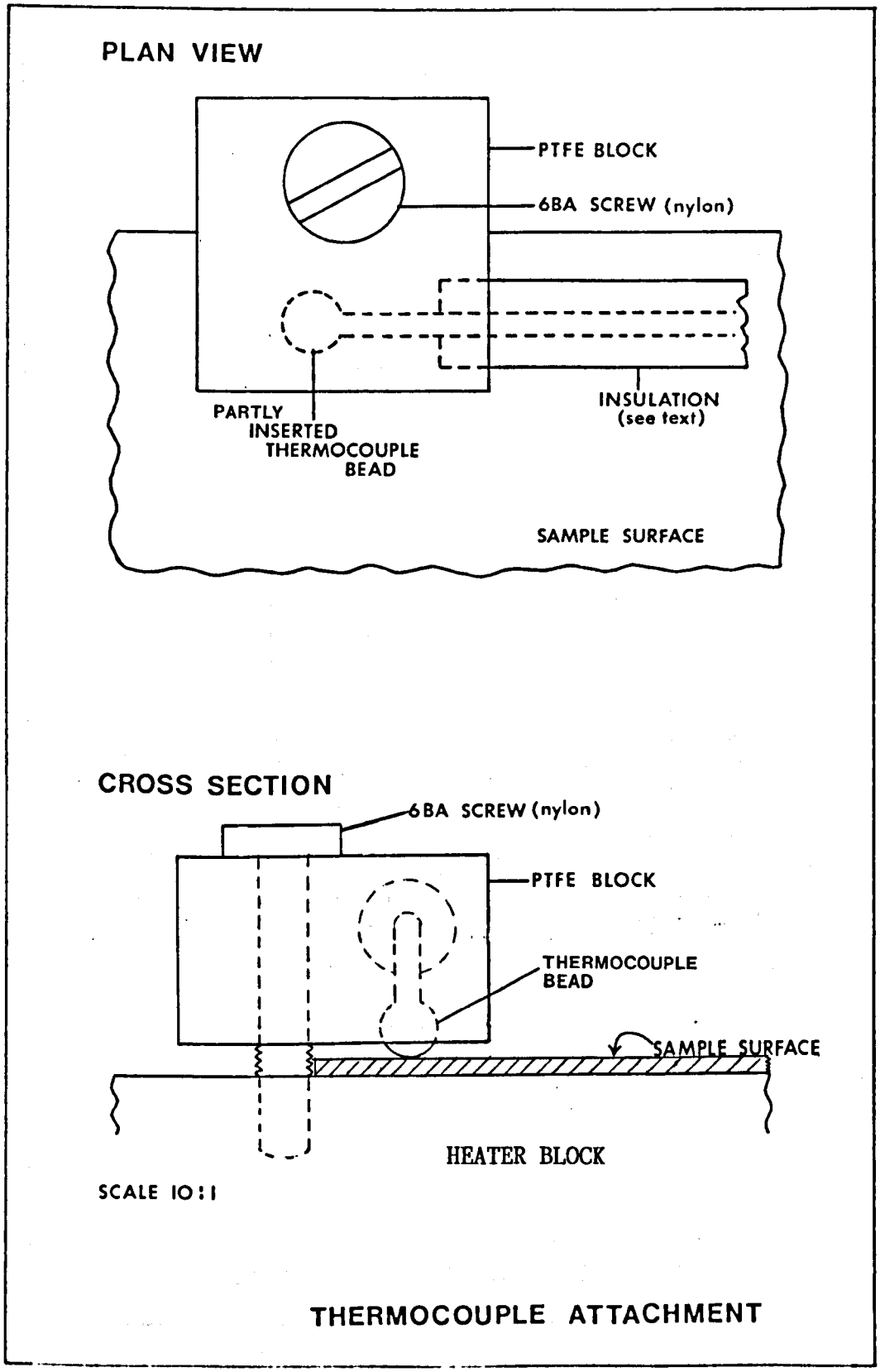

THERMOCOUPLE ATTACHMENT

FIGURE 3.11

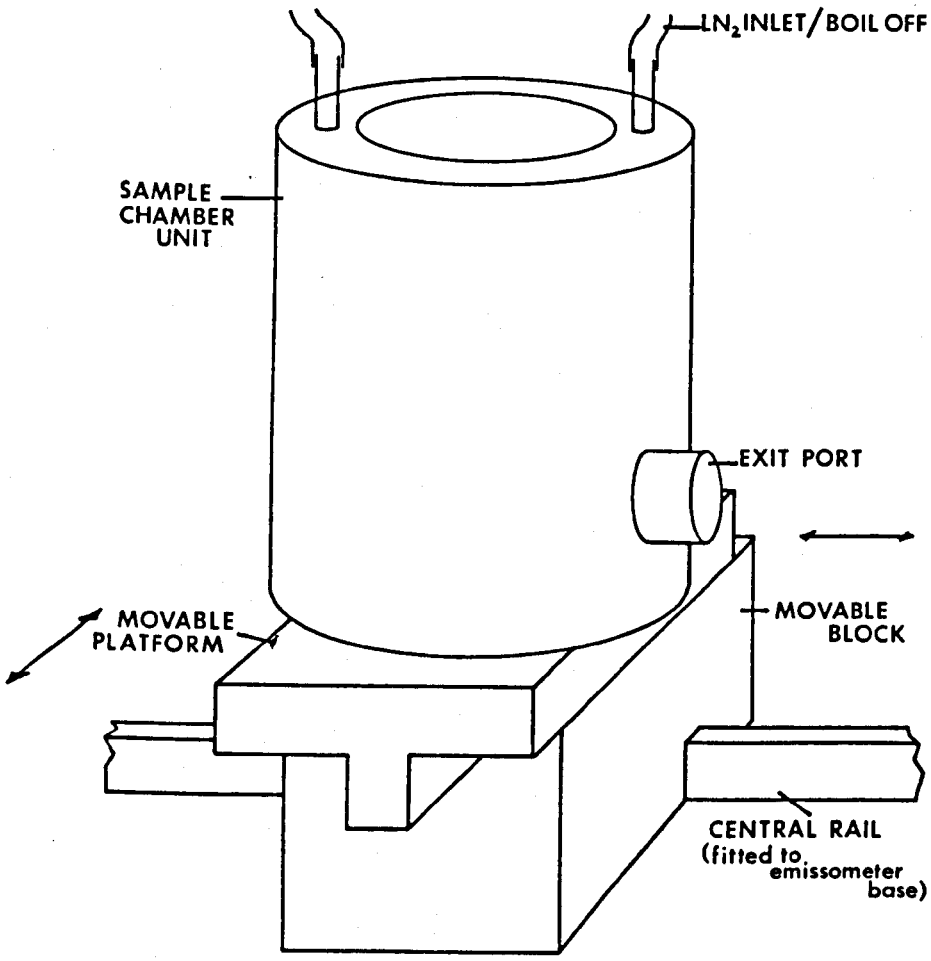

ARRANGEMENT FOR
POSITIONING SAMPLE CHAMBER

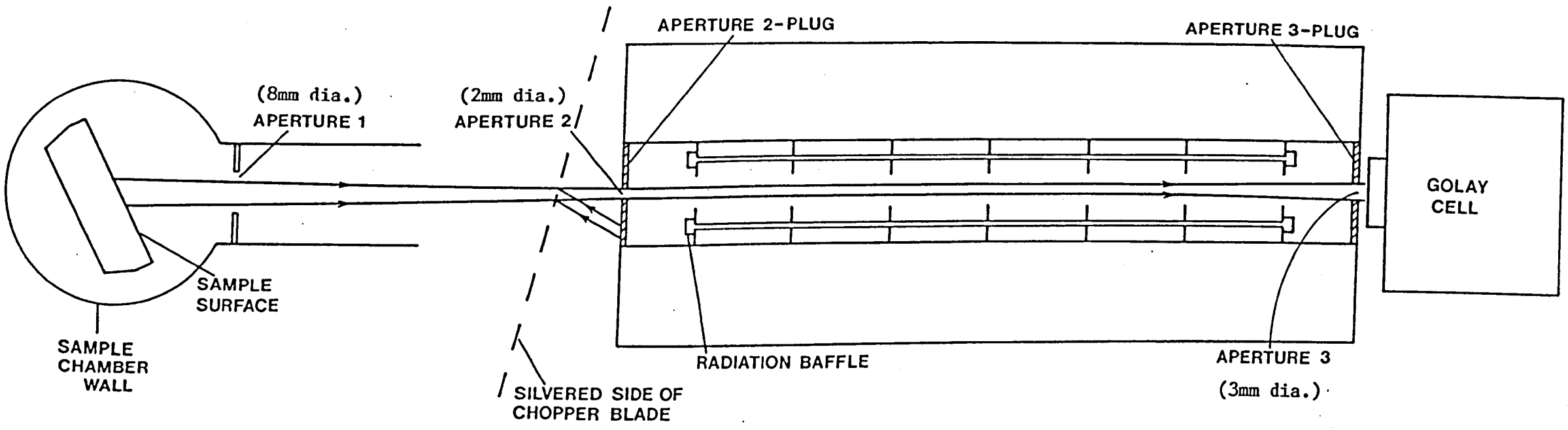

SCALE 1:1

(EXCEPT GOLAY CELL)

FIG. 3.12 SCALE DRAWING OF EMISSOMETER SHOWING ALTERNATE RADIATION BEAMS

FIGURE 3.13

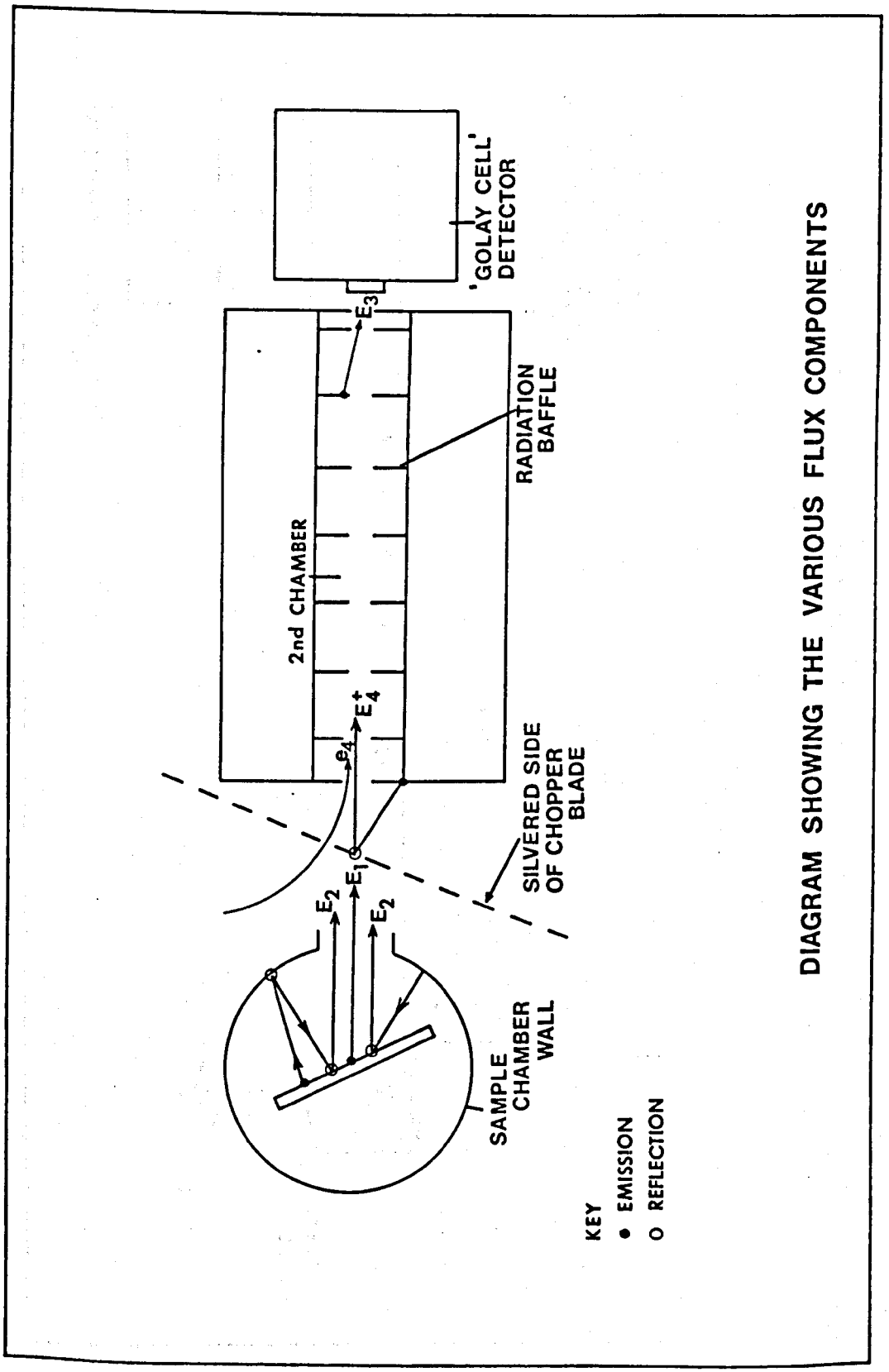
DIAGRAM SHOWING THE VARIOUS FLUX COMPONENTS
'GOLAY CELL' DETECTOR
E_3
RADIATION BAFFLE
2nd CHAMBER
E_4^+
e_4
SILVERED SIDE OF CHOPPER BLADE
E_1
E_2
E_2
SAMPLE CHAMBER WALL
KEY
• EMISSION
O REFLECTION

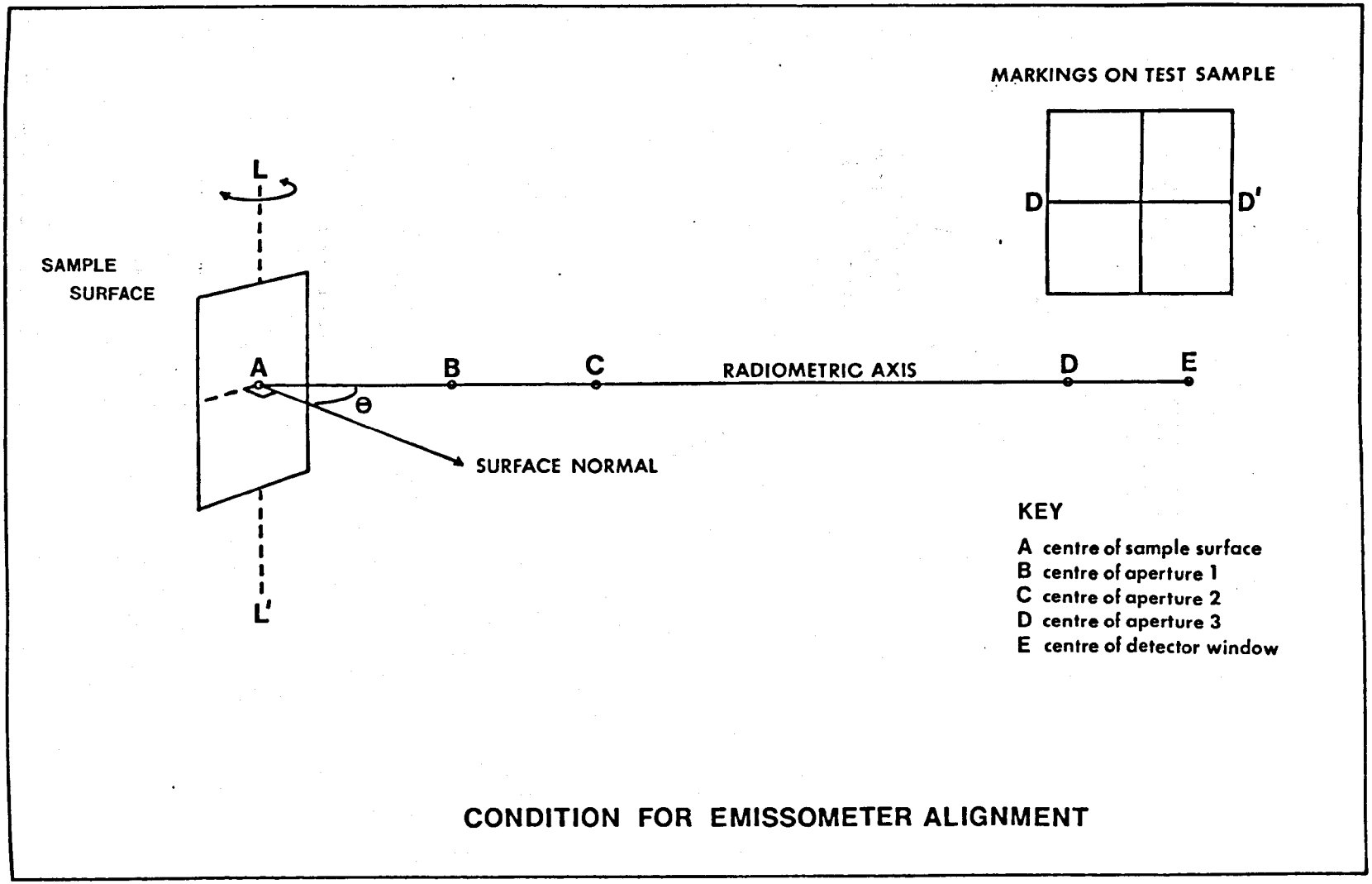

CONDITION FOR EMISSOMETER ALIGNMENT

FIGURE 3.14

FIGURE 3.15

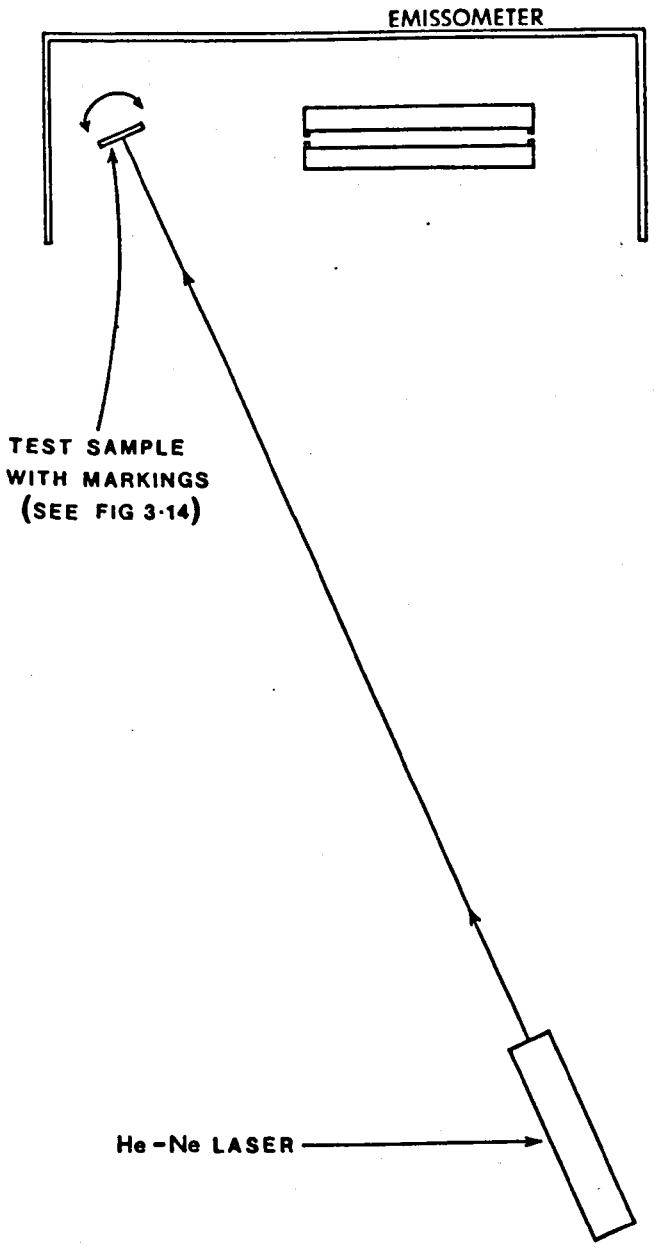

ALIGNMENT USING TEST SAMPLE
(WITH MARKINGS)

FIGURE 3.16

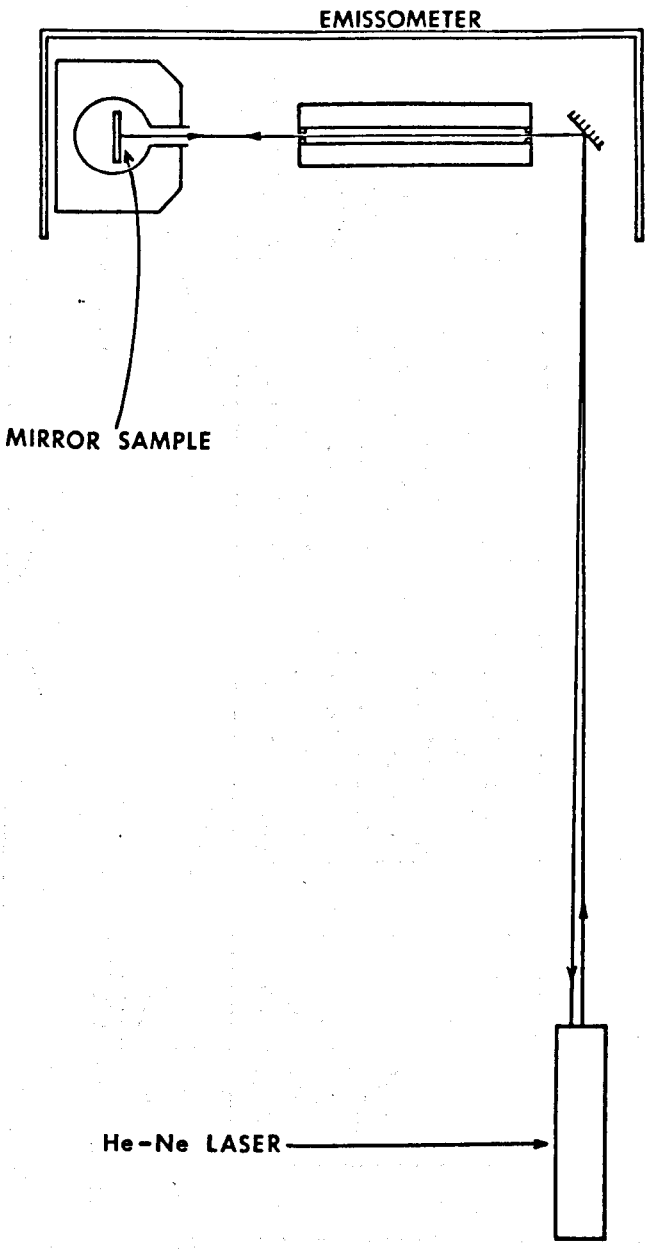

ALIGNMENT USING MIRROR SAMPLE

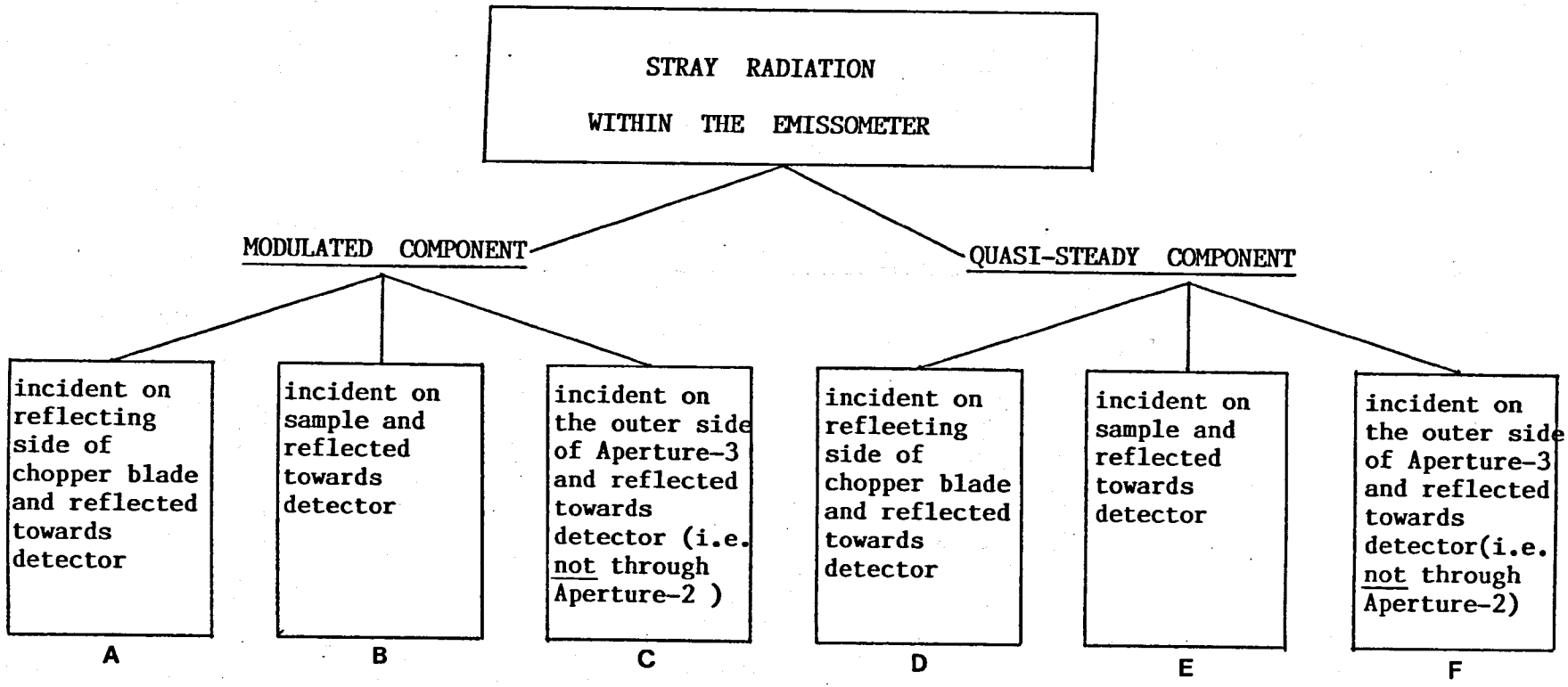

DIAGRAM SHOWING STRAY RADIATION COMPONENTS REACHING THE DETECTOR

FIGURE 3.17

Figure 3.18

COOLING CURVES for 2nd CHAMBER

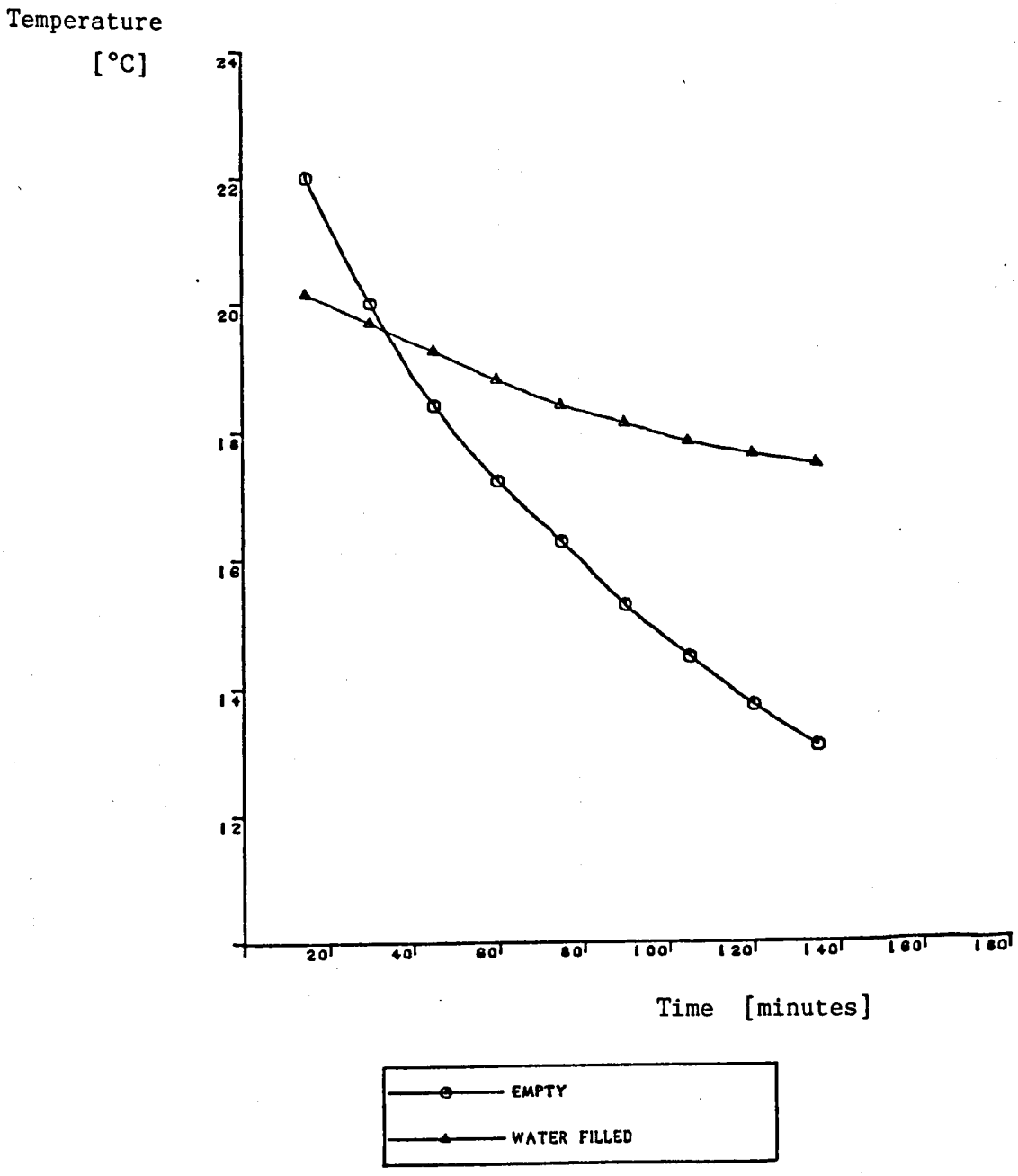

FIGURE 3.19

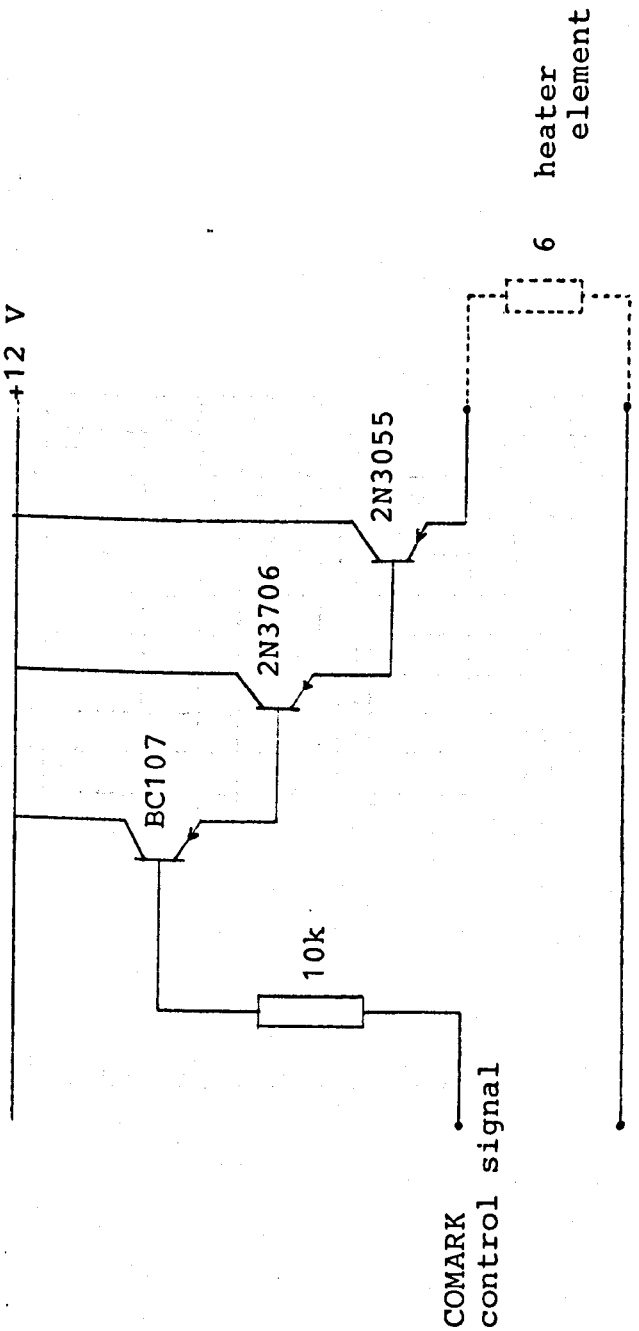

CIRCUIT DIAGRAM OF ELECTRONIC SWITCH

FIGURE 3.20

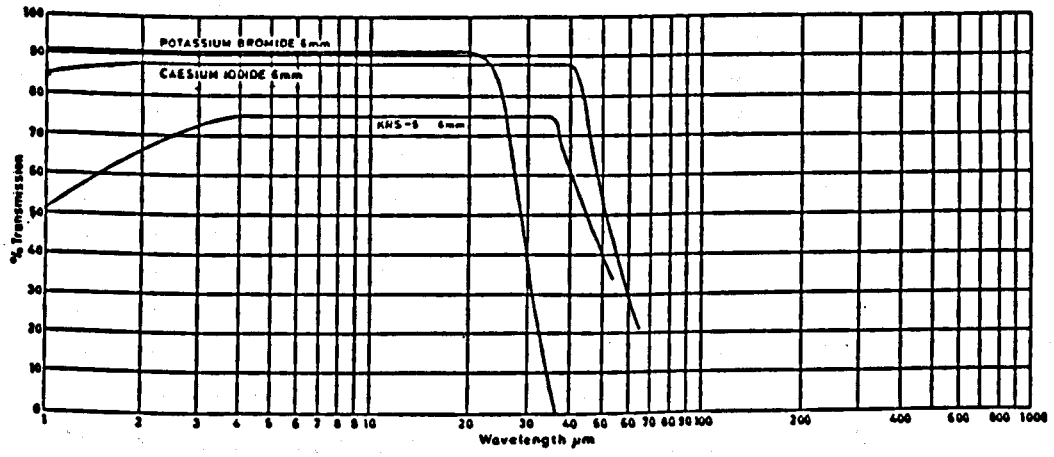

SPECTRAL CHARACTERISTICS OF SOME I-R WINDOW MATERIALS

FIGURE 3.21

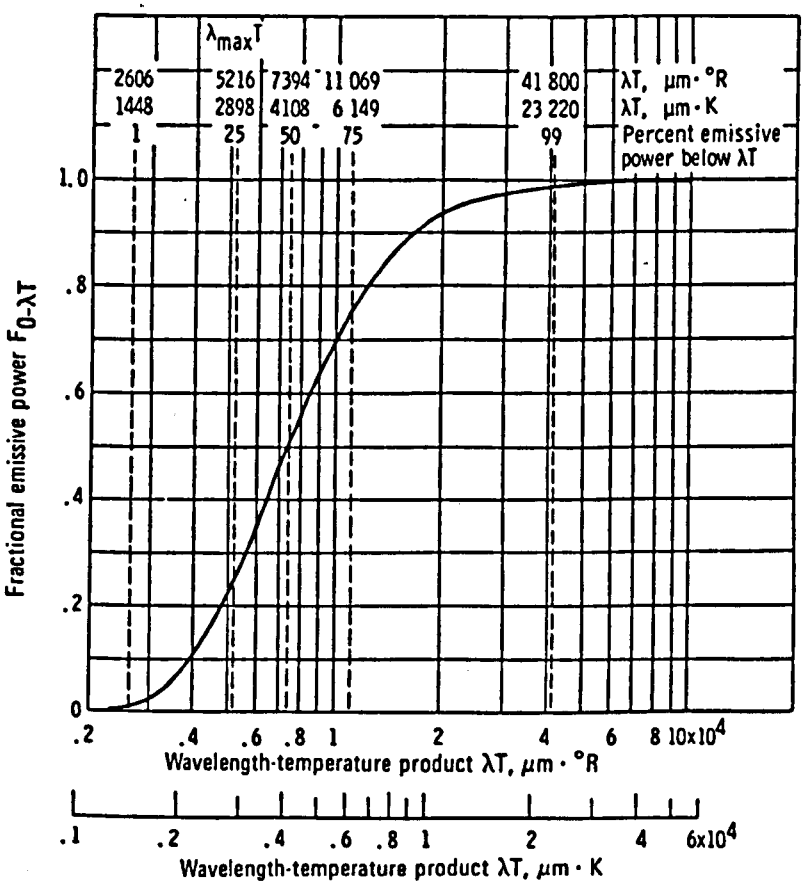

FRACTIONAL BLACKBODY EMISSIVE POWER IN RANGE 0 to λT

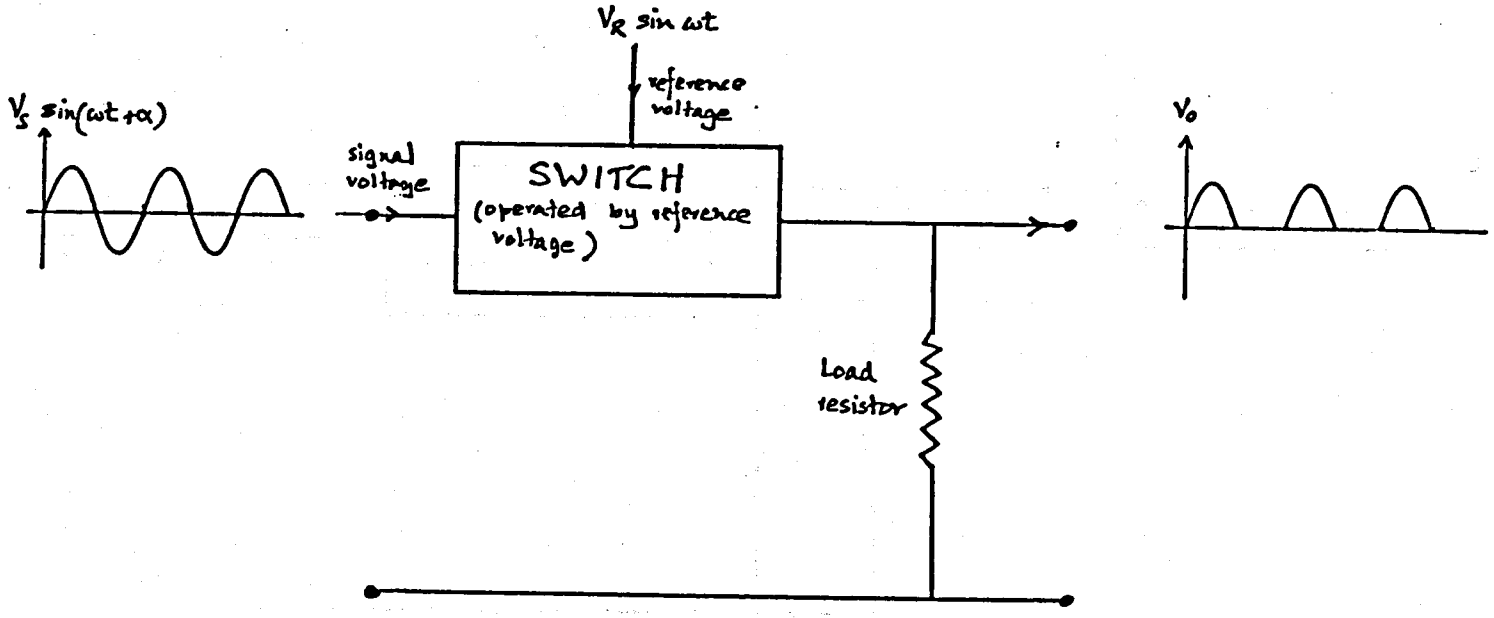

PHASE SENSITIVE DETECTION - HALF WAVE

FIGURE 3.22

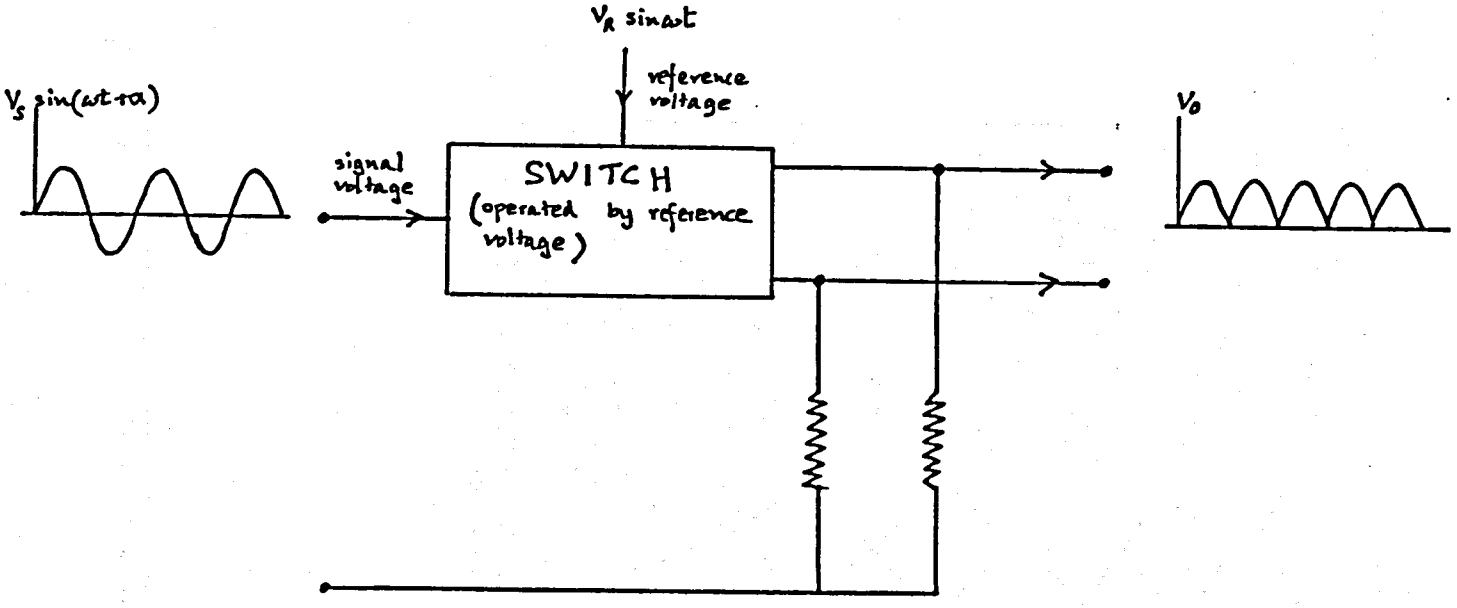

PHASE SENSITIVE DETECTION – FULL WAVE

FIGURE 3.23

FIGURE 3.24

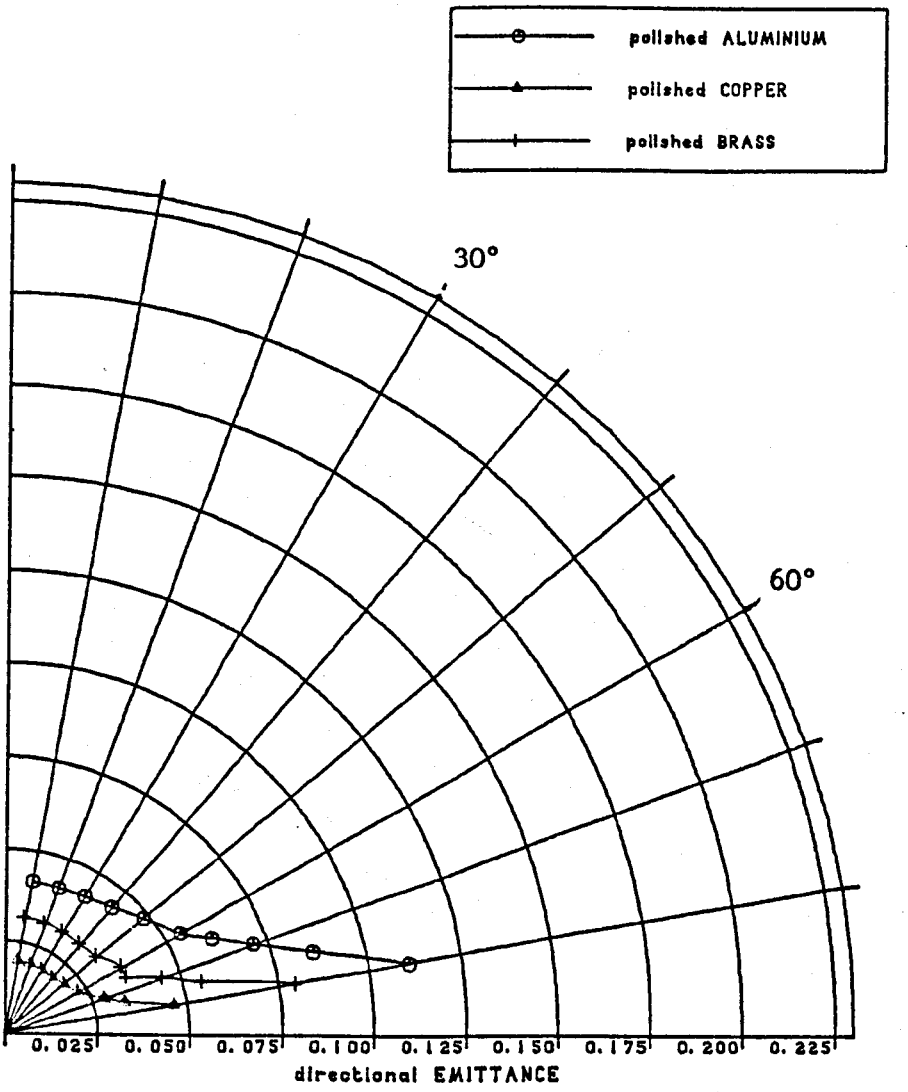

TOTAL DIRECTIONAL EMITTANCE OF METAL SAMPLES

FIGURE 3.25

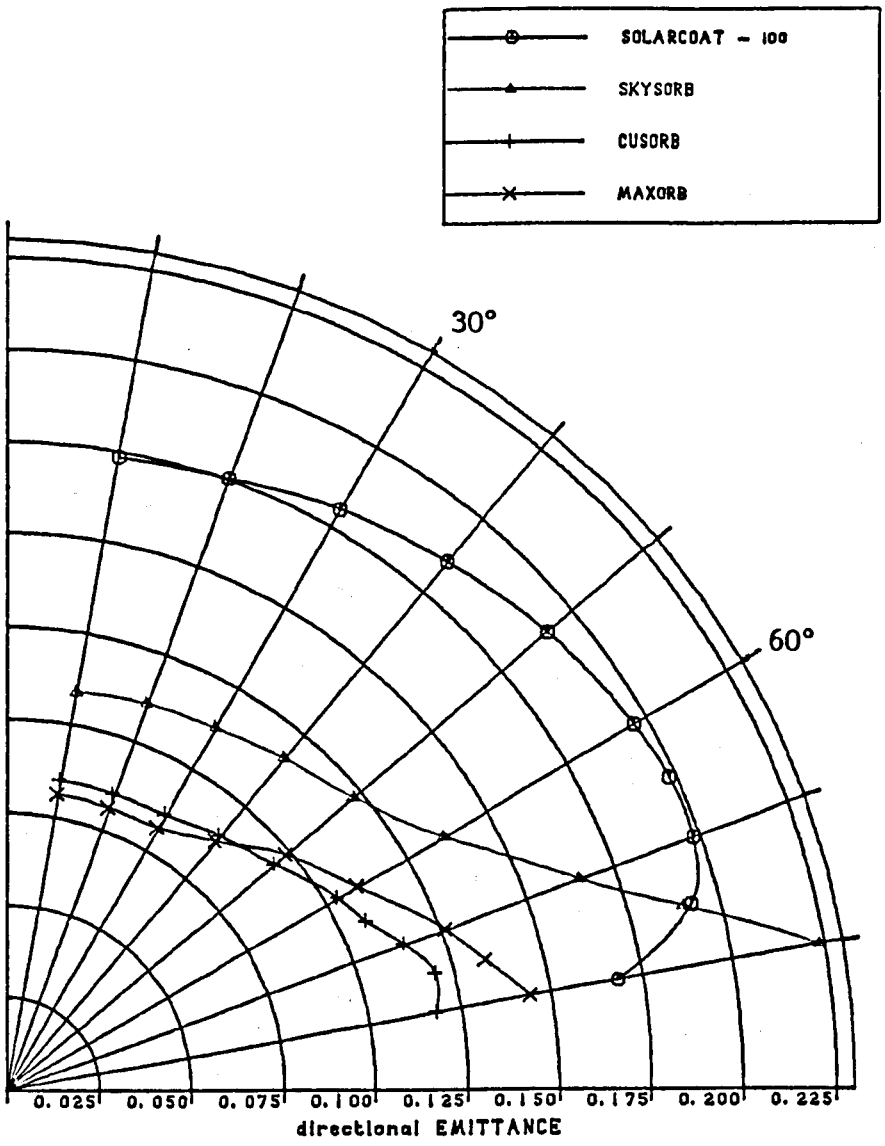

TOTAL DIRECTIONAL EMITTANCE OF SOLAR SELECTIVE ABSORBER SAMPLES

FIGURE 3.26

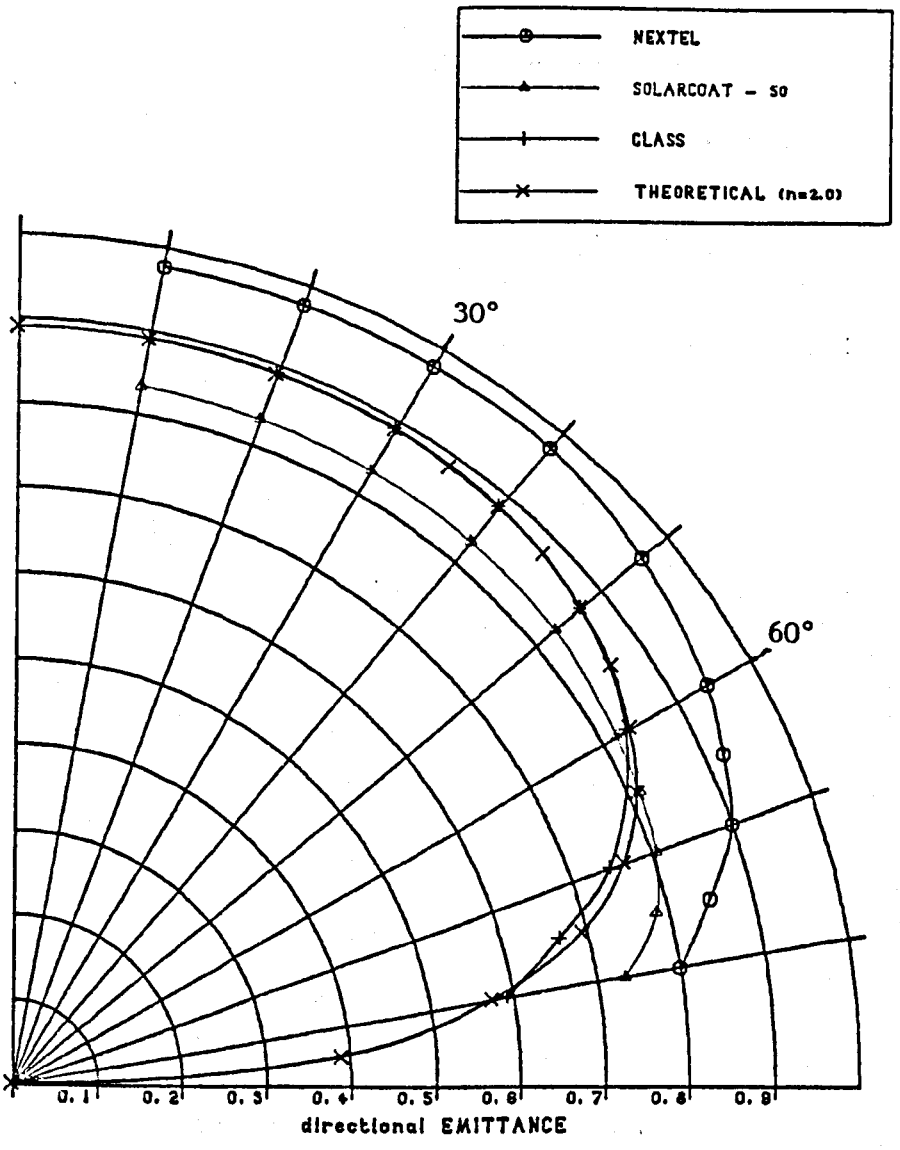

TOTAL DIRECTIONAL EMITTANCE OF NON - SELECTIVE ABSORBER

SAMPLES

FIGURE 3.27

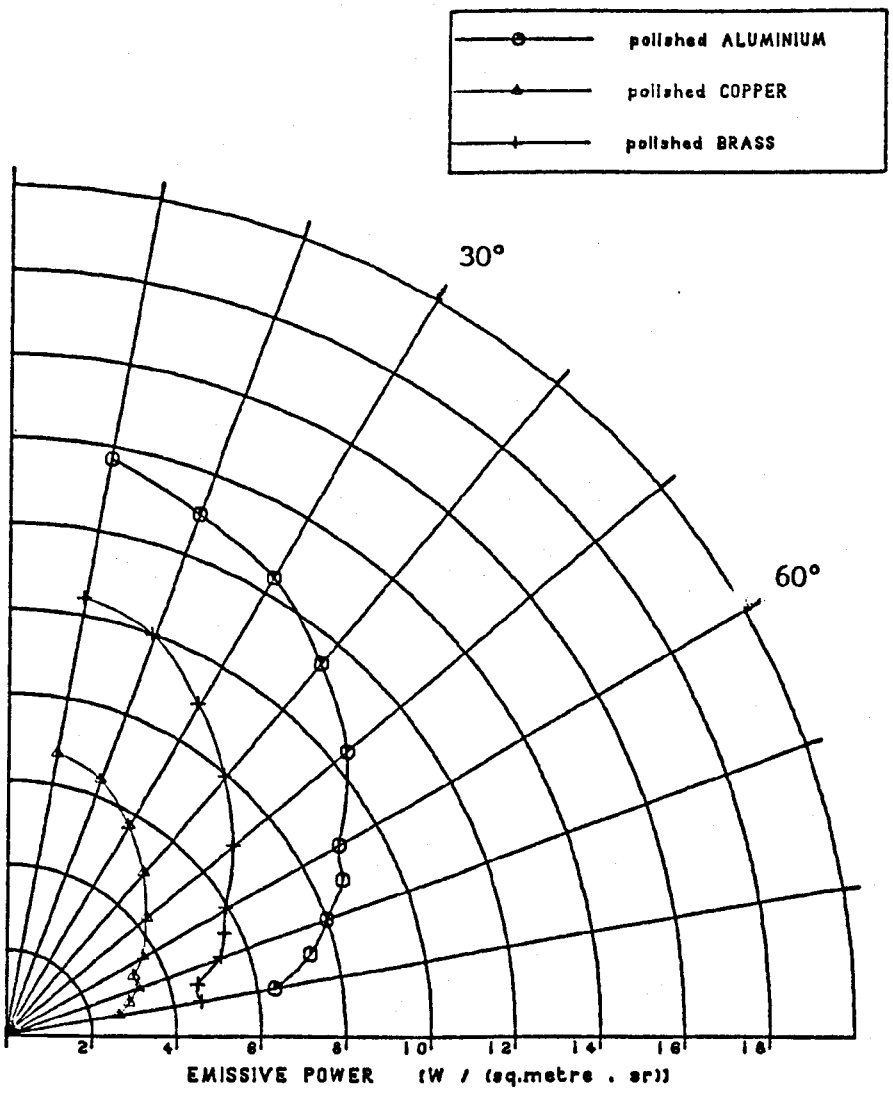

TOTAL DIRECTIONAL EMISSIVE POWER OF METAL SAMPLES

FIGURE 3.28

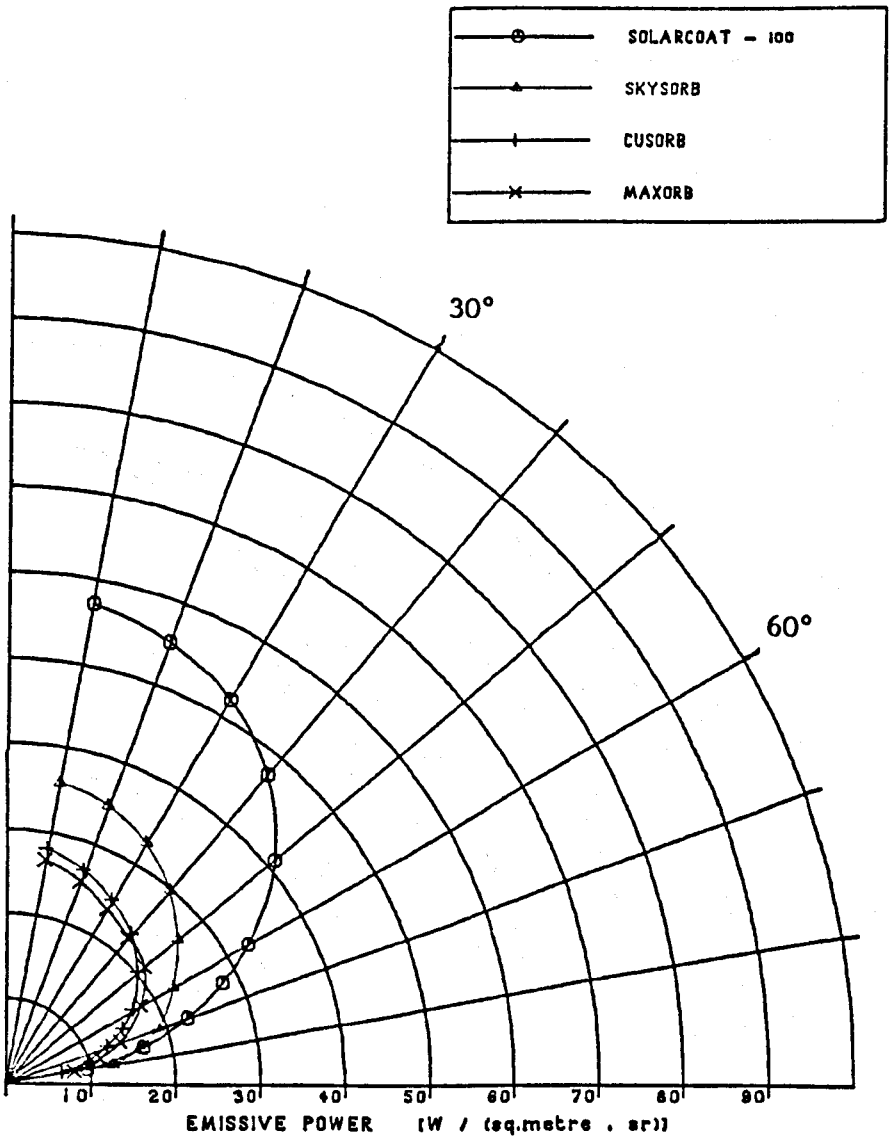

TOTAL DIRECTIONAL EMISSIVE POWER OF SOLAR SELECTIVE ABSORBER SAMPLES

FIGURE 3.29

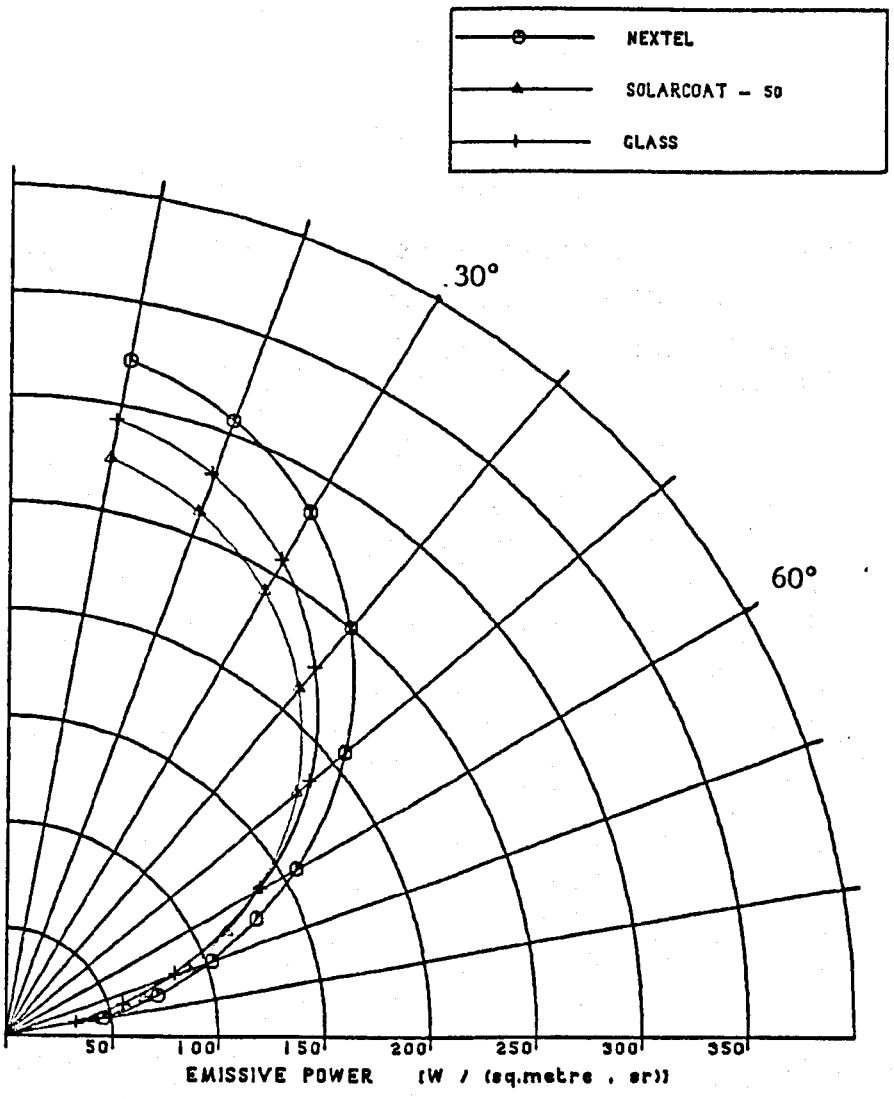

TOTAL DIRECTIONAL EMISSIVE POWER OF NON - SELECTIVE

ABSORBER SAMPLES

FIGURE 3.30

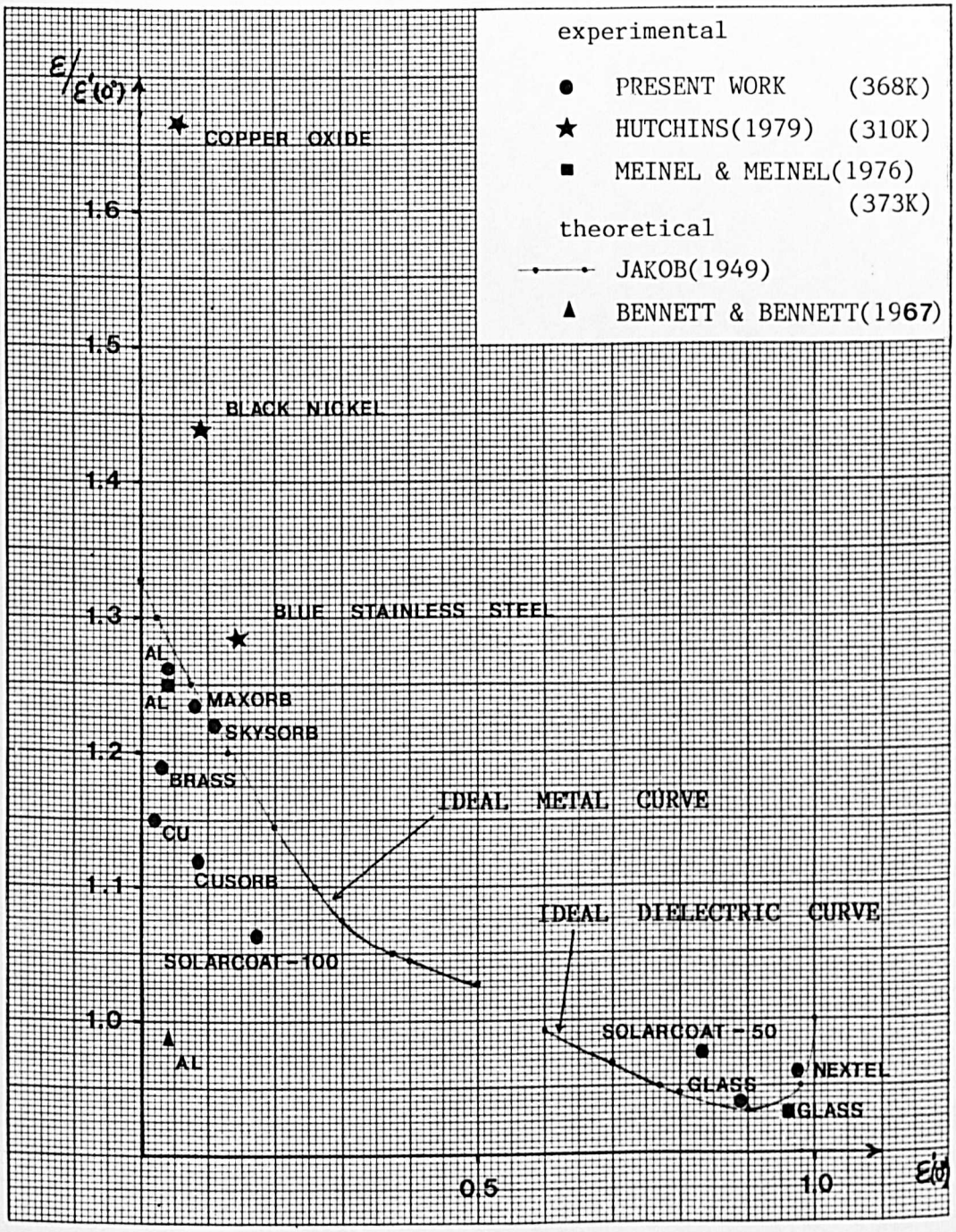

GRAPH OF $\varepsilon/\varepsilon'(0°)$ VS $\varepsilon'(0°)$

FIGURE 3.31

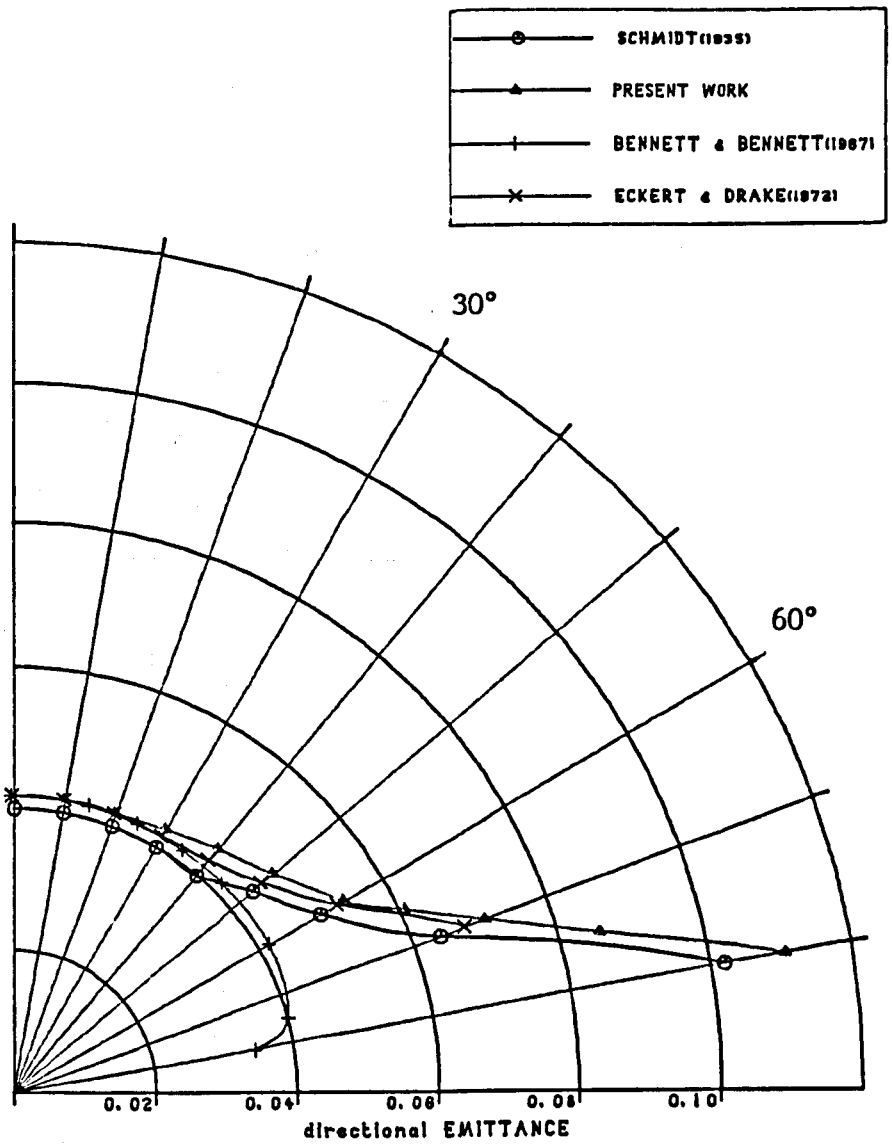

TOTAL DIRECTIONAL EMITTANCE OF ALUMINIUM

COMPARISON OF PRESENT WORK WITH PUBLISHED DATA

FIGURE 3.32

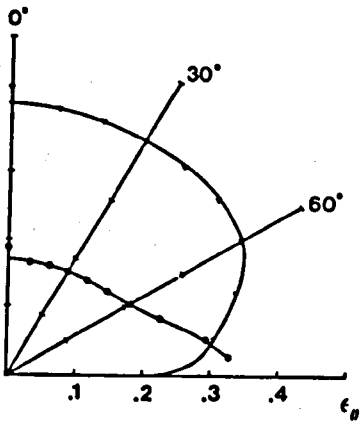

Nickel-copper compound ; solution b1. Total directional emissivity ϵ_θ, versus emission angle θ ; T = 100°C.
- ● t = 1.5 minute
- ◂ t = 5 minutes

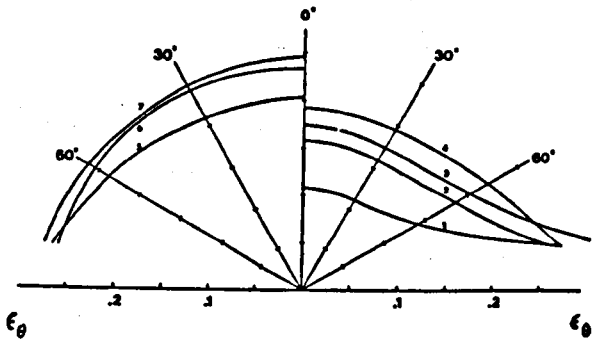

Nickel-phosphorus compound. Total directional emissivity ϵ_θ, versus emission angle θ (T = 120°C).
- 1 t = 0 second (non etched sample)
- 2 t = 5 seconds
- 3 t = 10 seconds
- 4 t = 15 seconds
- 5 t = 20 seconds
- 6 t = 35 seconds
- 7 t = 35 seconds (after ageing)

WORK OF PAPINI & PAPINI (1982)

FIGURE 3.33

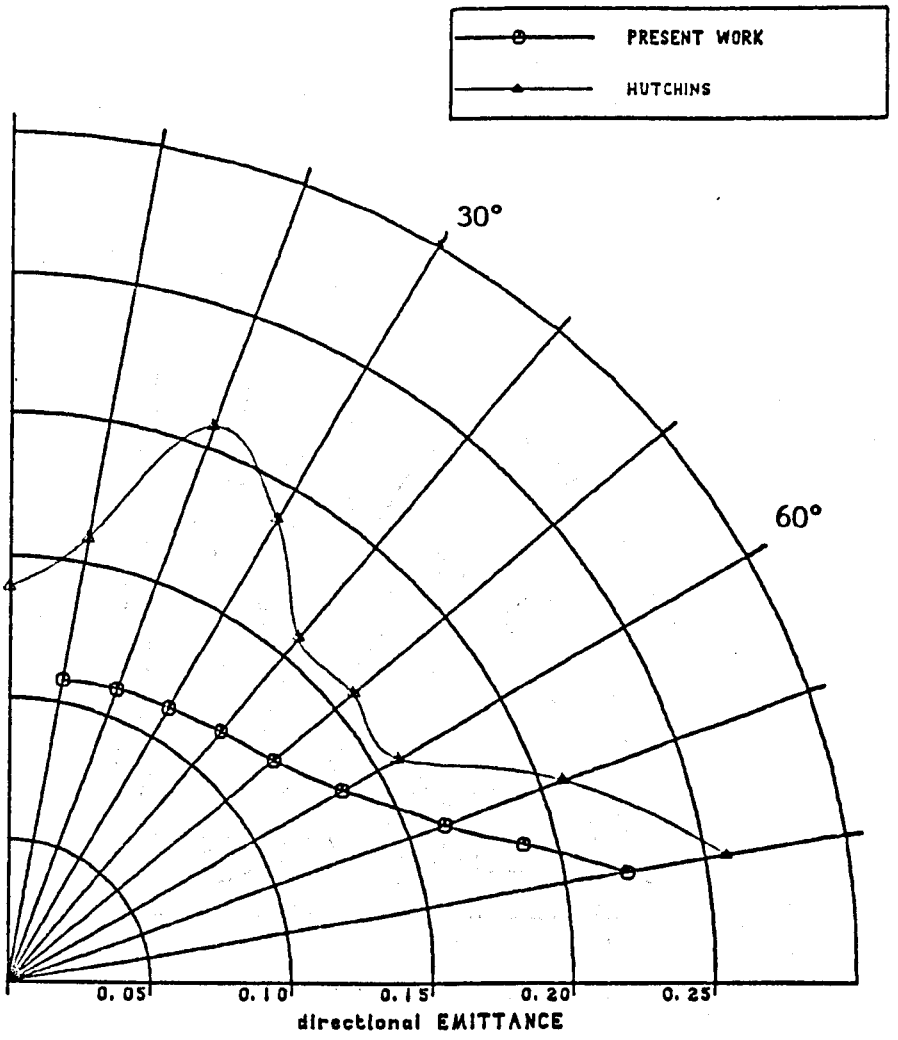

TOTAL DIRECTIONAL EMITTANCE OF BLUE STAINLESS STEEL

COMPARISON OF PRESENT WORK WITH HUTCHINS'(1979) DATA

WORK OF HUTCHINS(1979)

FIGURE 3.34

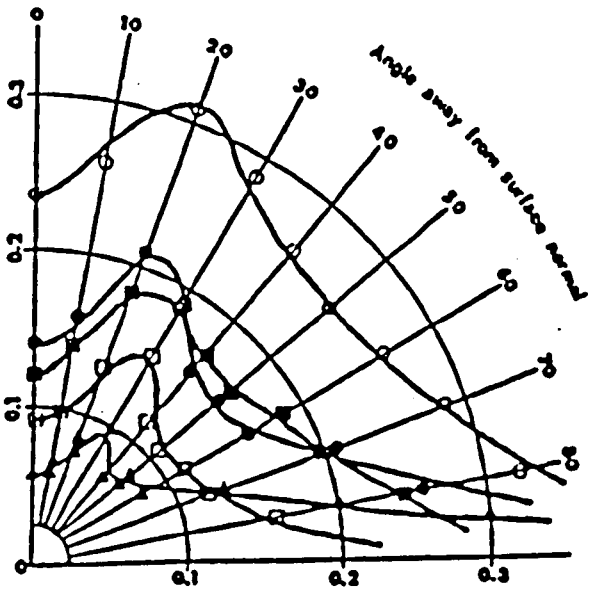

Total Directional Emittance of
▲copper oxide, □ black nickel, ■ black chrome
●blue stainless steel, and O chromated zinc.

FIGURE 3.35

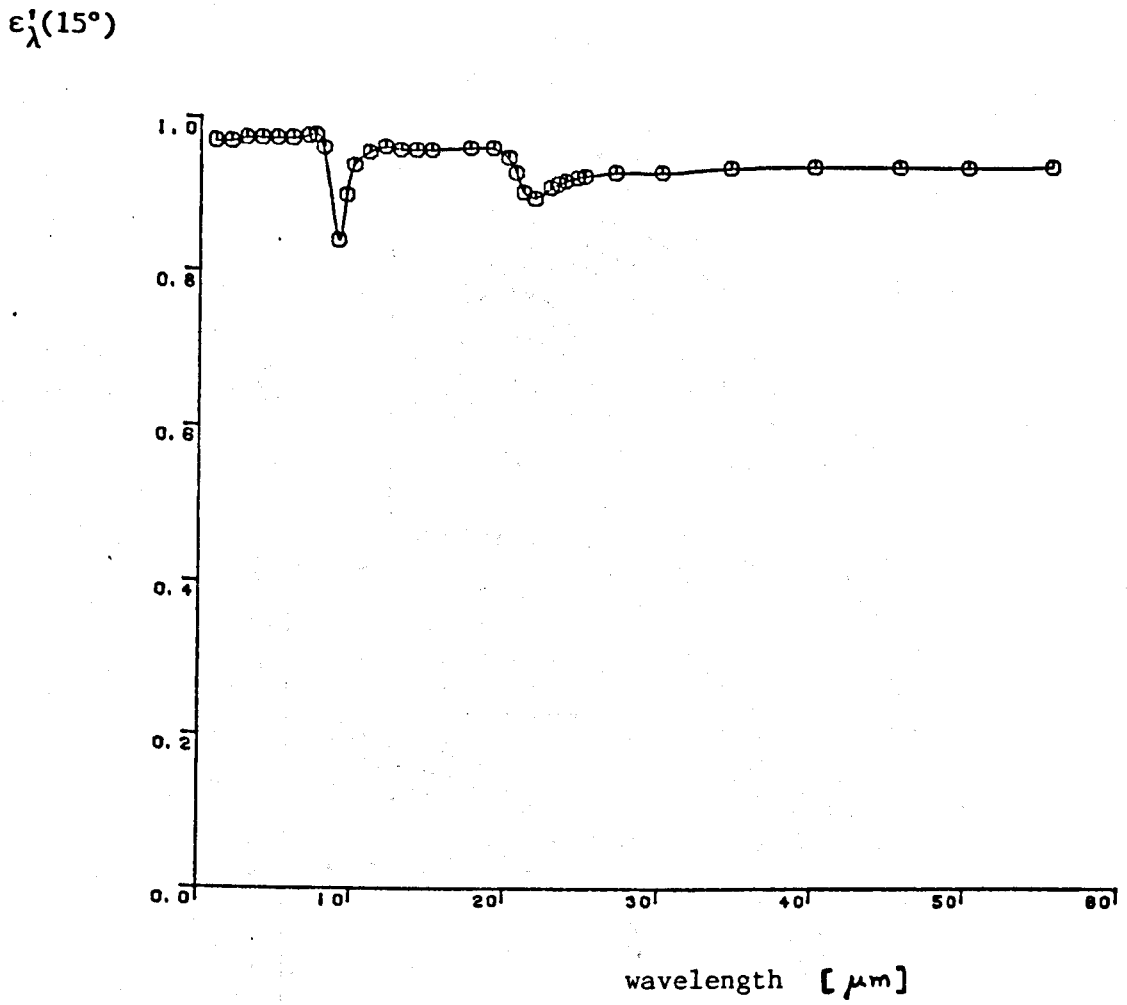

SPECTRAL DIRECTIONAL(15°) HEMISPHERICAL REFLECTANCE OF NEXTEL (NPL calibration)

FIGURE 3.36

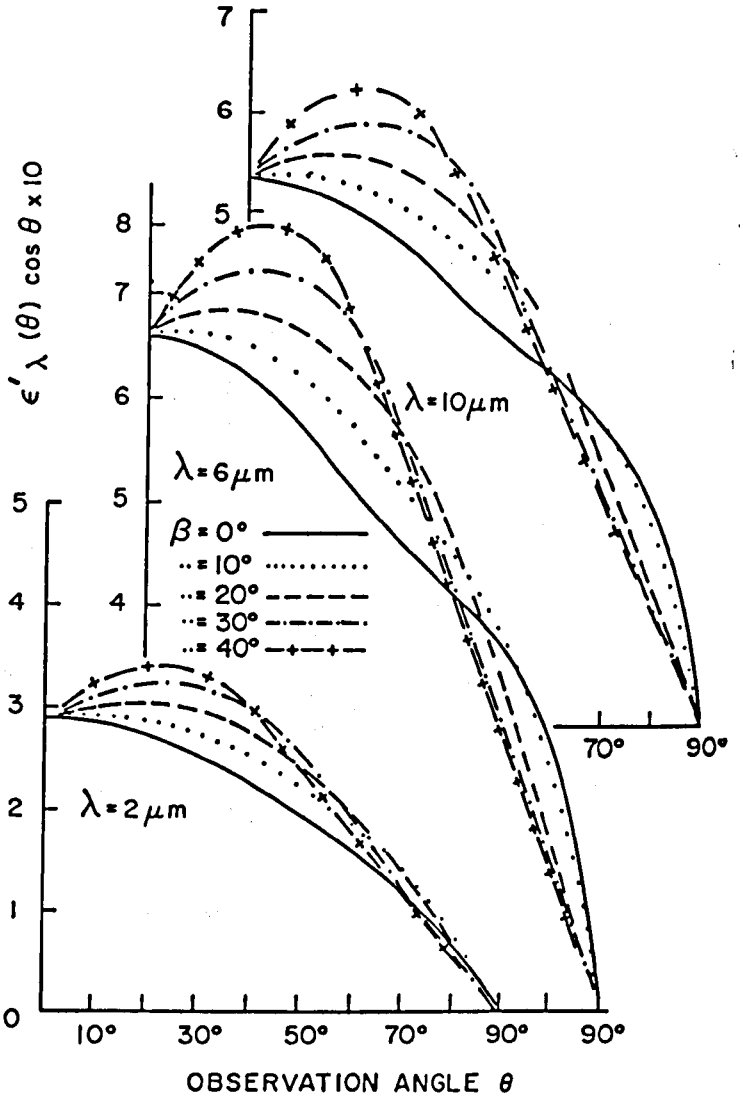

$\varepsilon'_\lambda \cos\theta$ vs. θ , of a randomly rough Gold surface

β = standard deviation of the sloping angle distribution

WORK OF BIRKEBAK & ABDULKADIR(1977)

FIGURE 3.37

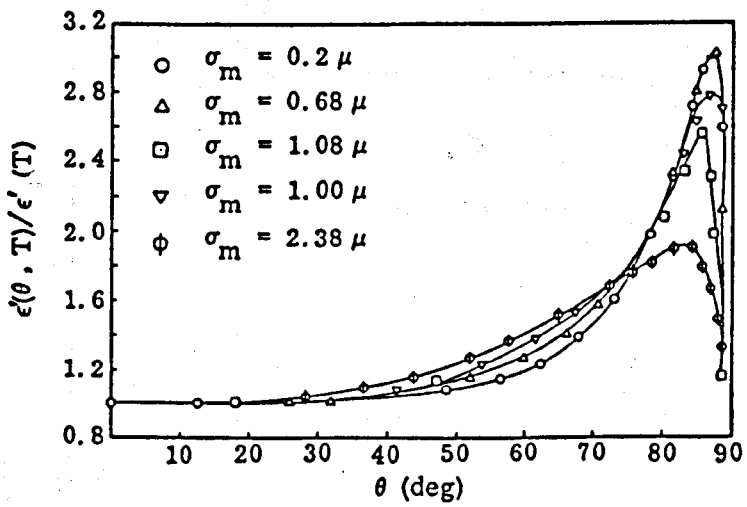

Effect of roughness on total directional emittance of platinum at 865°K.

σ_m = rms value of overall surface roughness

WORK OF ROLLING ET AL (1967)

FIGURE 4.1

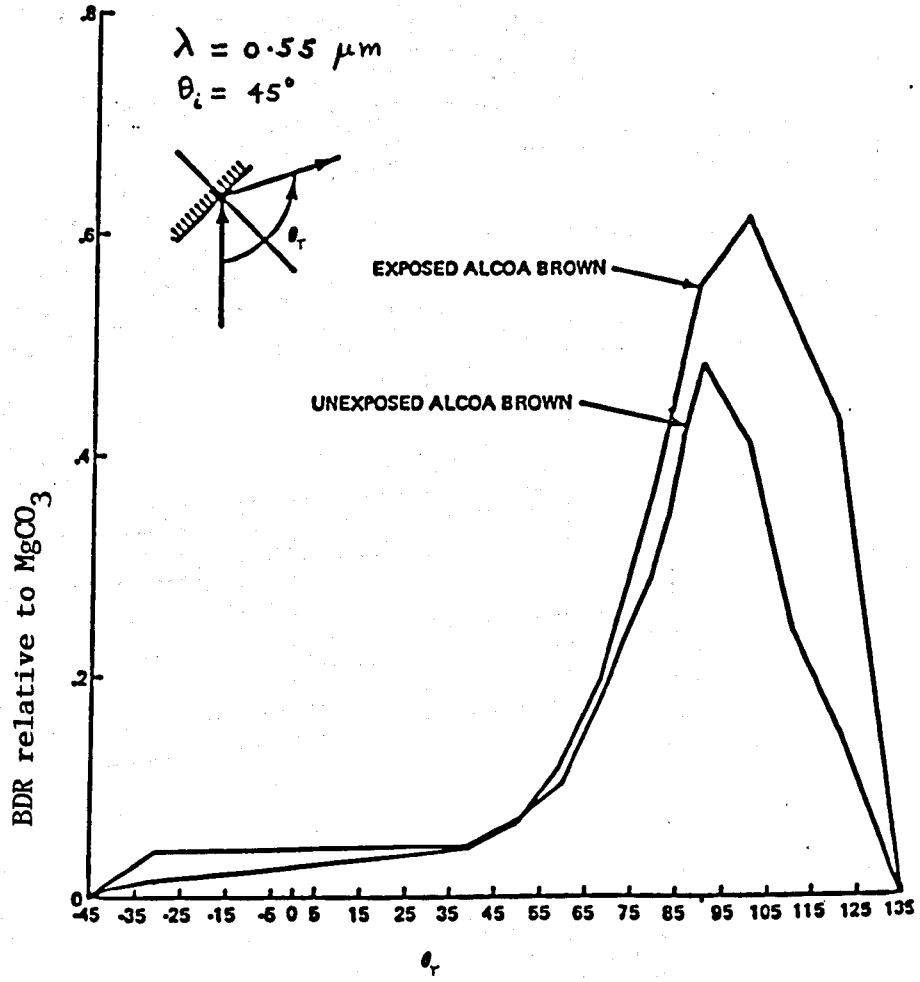

BDR MEASUREMENTS ON 'ALCOA-BROWN'(EGAN & HILGEMAN 1979)

FIGURE 4.2

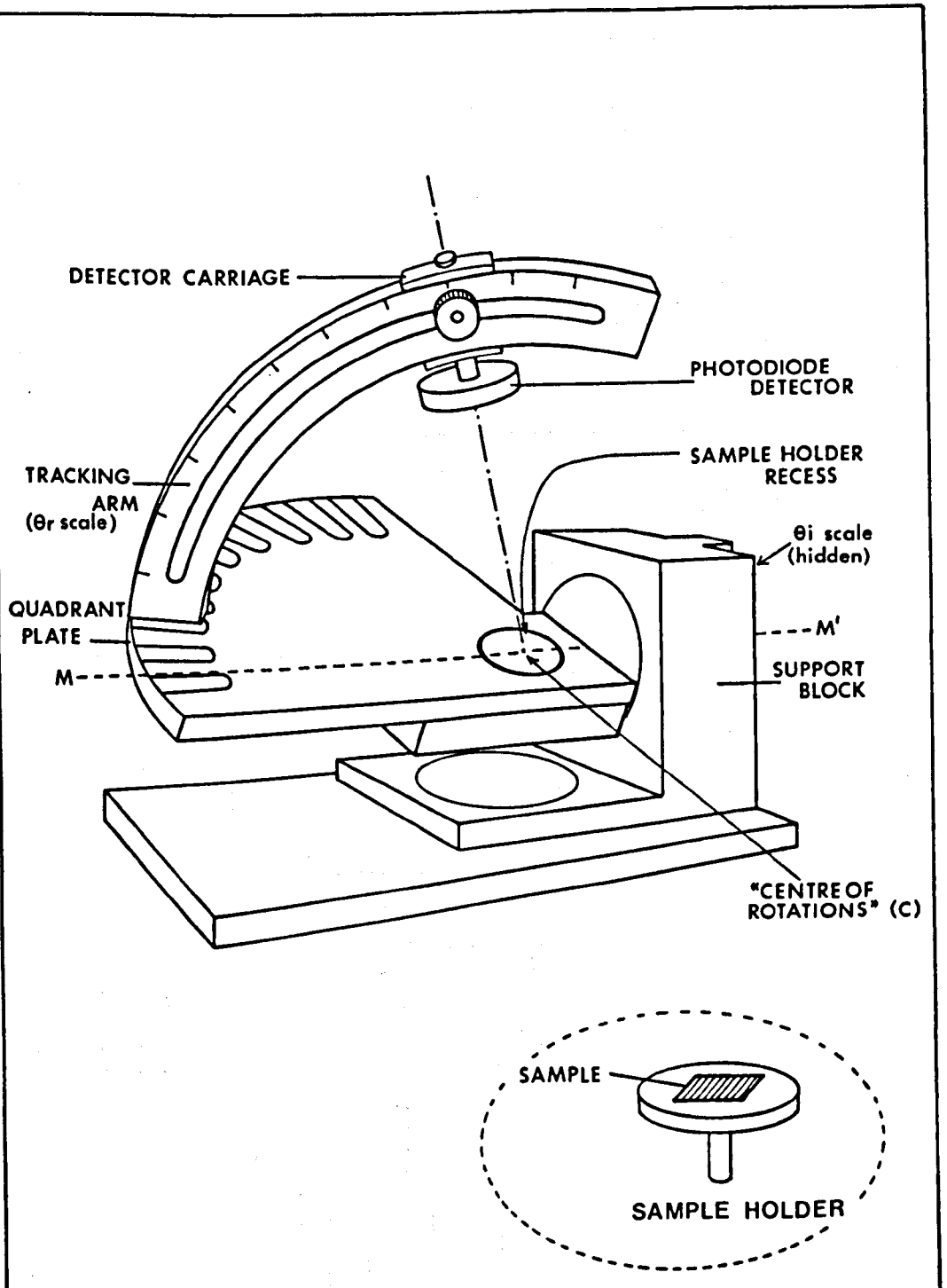

SAMPLE AND DETECTOR ASSEMBLY (SDA)

FIGURE 4.3

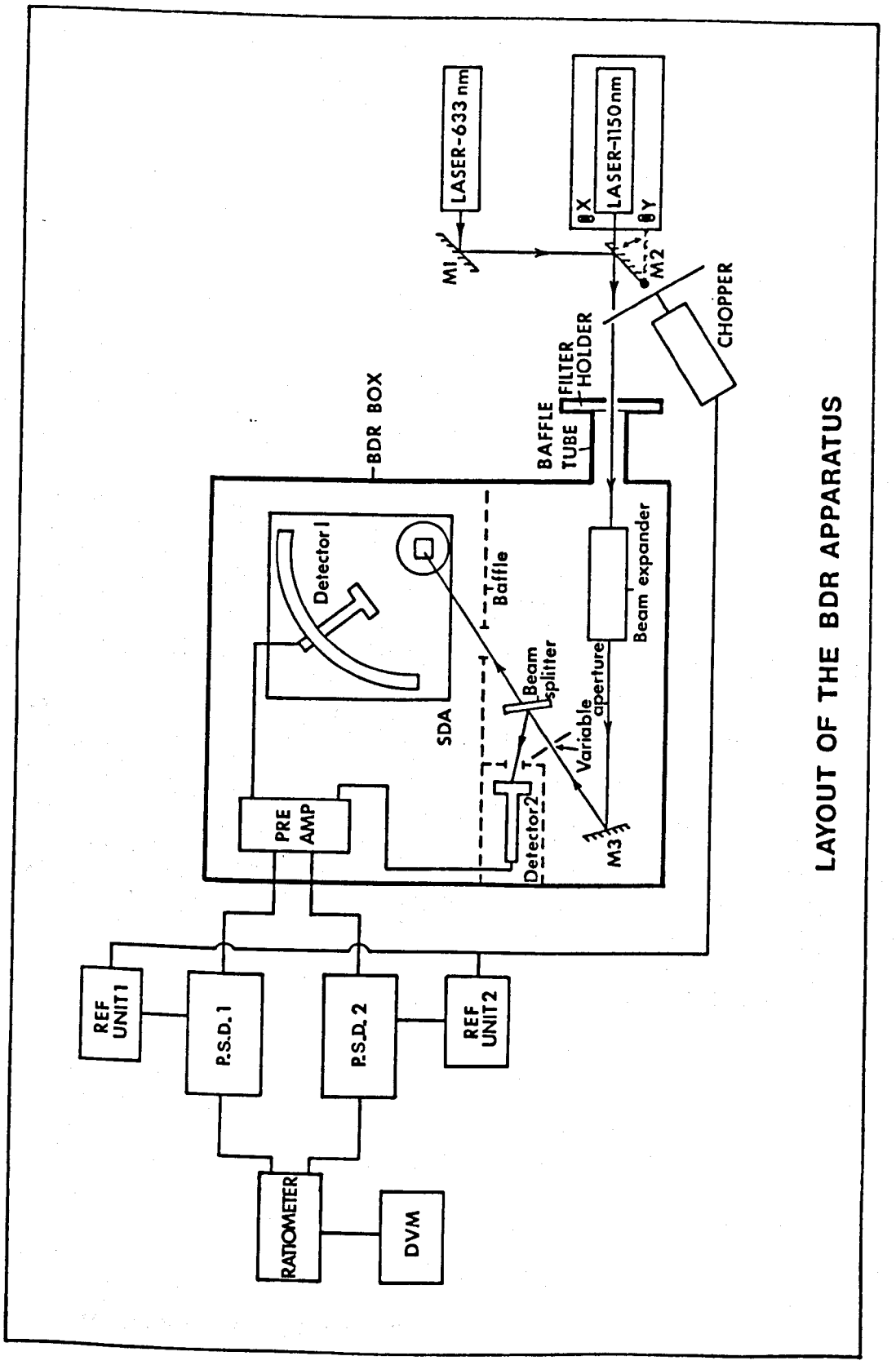
LASER-633 nm
LASER-1150nm
X
Y
M1
M2
M3
CHOPPER
FILTER HOLDER
BAFFLE TUBE
BDR BOX
Detector 1
Baffle
Beam splitter
Beam expander
Variable aperture
SDA
Detector 2
PRE AMP
REF UNIT 1
P.S.D. 1
P.S.D. 2
REF UNIT 2
RATIOMETER
DVM
LAYOUT OF THE BDR APPARATUS

FIGURE 4.4

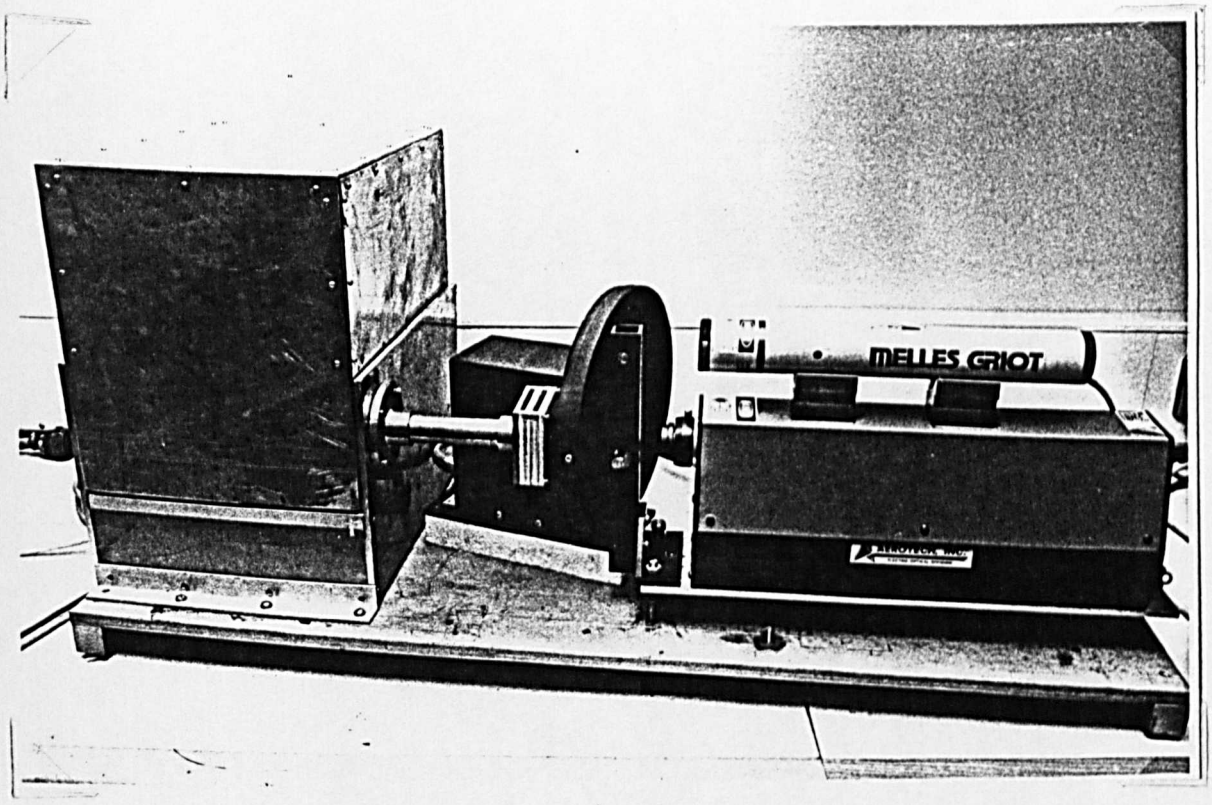

BIDIRECTIONAL REFLECTOMETER

FIGURE 4.5

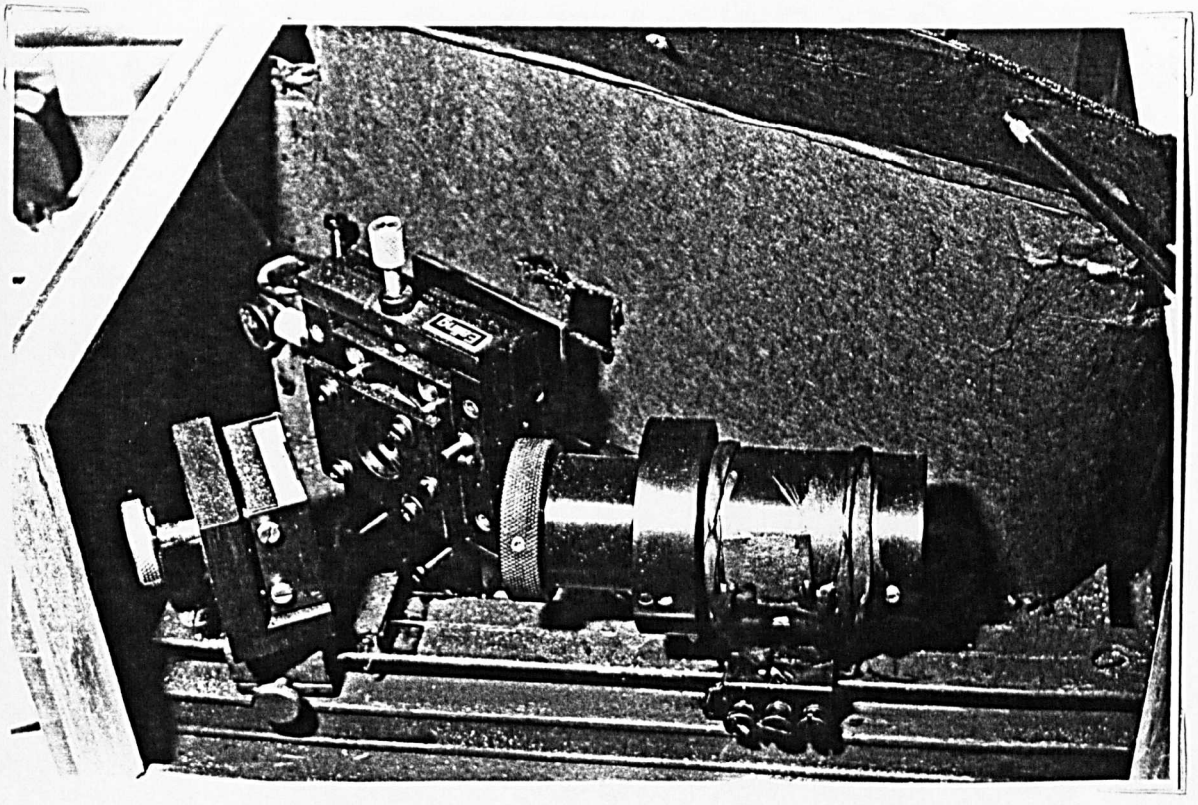

BDR BOX - BEAM FORMING OPTICS

THREE CONFIGURATIONS FOR PHYSICALLY DEFINING SAMPLE AREA

FIGURE 4.6

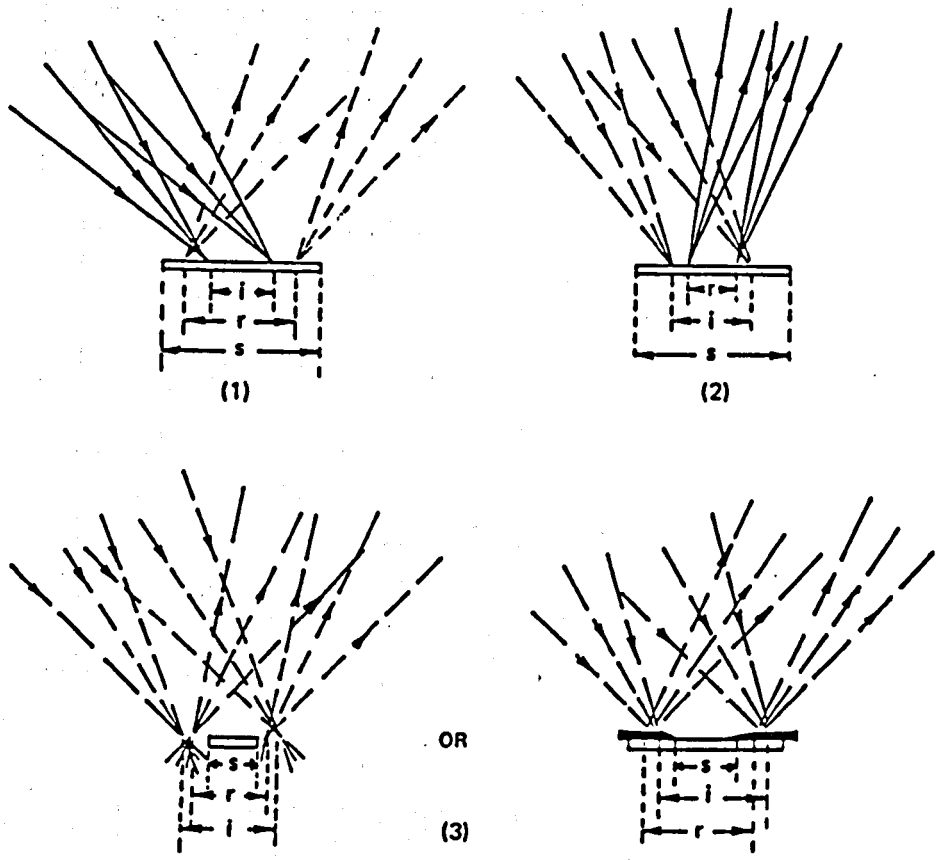

i – WIDTH OF INCIDENT BEAM [DEFINES REFLECTING AREA IN (1)].
r – WIDTH OF REFLECTED BEAM (THAT CAN BE ACCEPTED AND MEASURED) [DEFINES AREA IN (2)]
s – WIDTH OF EXPOSED SAMPLE SURFACE [DEFINES REFLECTING AREA IN (3)].

ONLY THE EXTREME RAYS OF EACH BEAM ARE SHOWN.
SOLID RAYS MUST BE SHARPLY FOCUSED TO DEFINE THE REFLECTING AREA.
DASHED RAYS NEED NOT BE SO SHARPLY FOCUSED.
IN CONFIGURATION (3) IT IS IMMATERIAL WHETHER $i > r$ OR $i < r$ OR $i \approx r$.

NICODEMUS et al, 1977

FIGURE 4.7

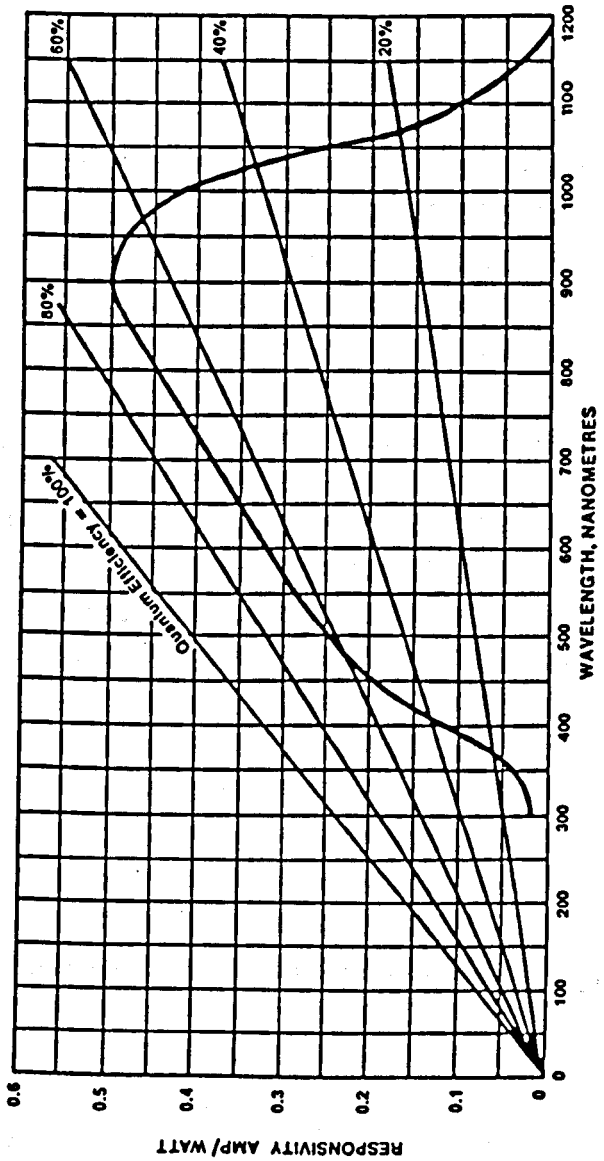

CURRENT RESPONSIVITY OF PHOTODIODE

FIGURE 4.8

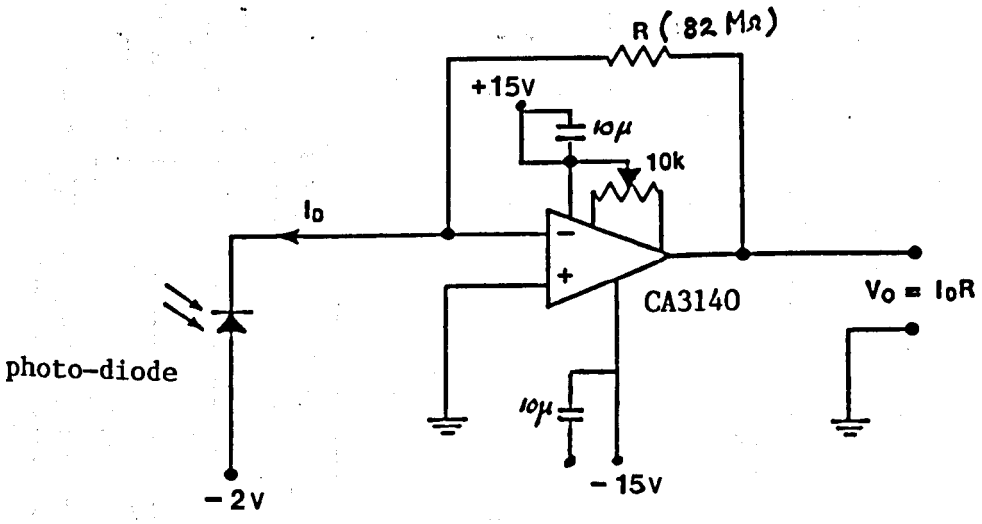

CIRCUIT DIAGRAM OF (a single channel of) PREAMPLIFIER

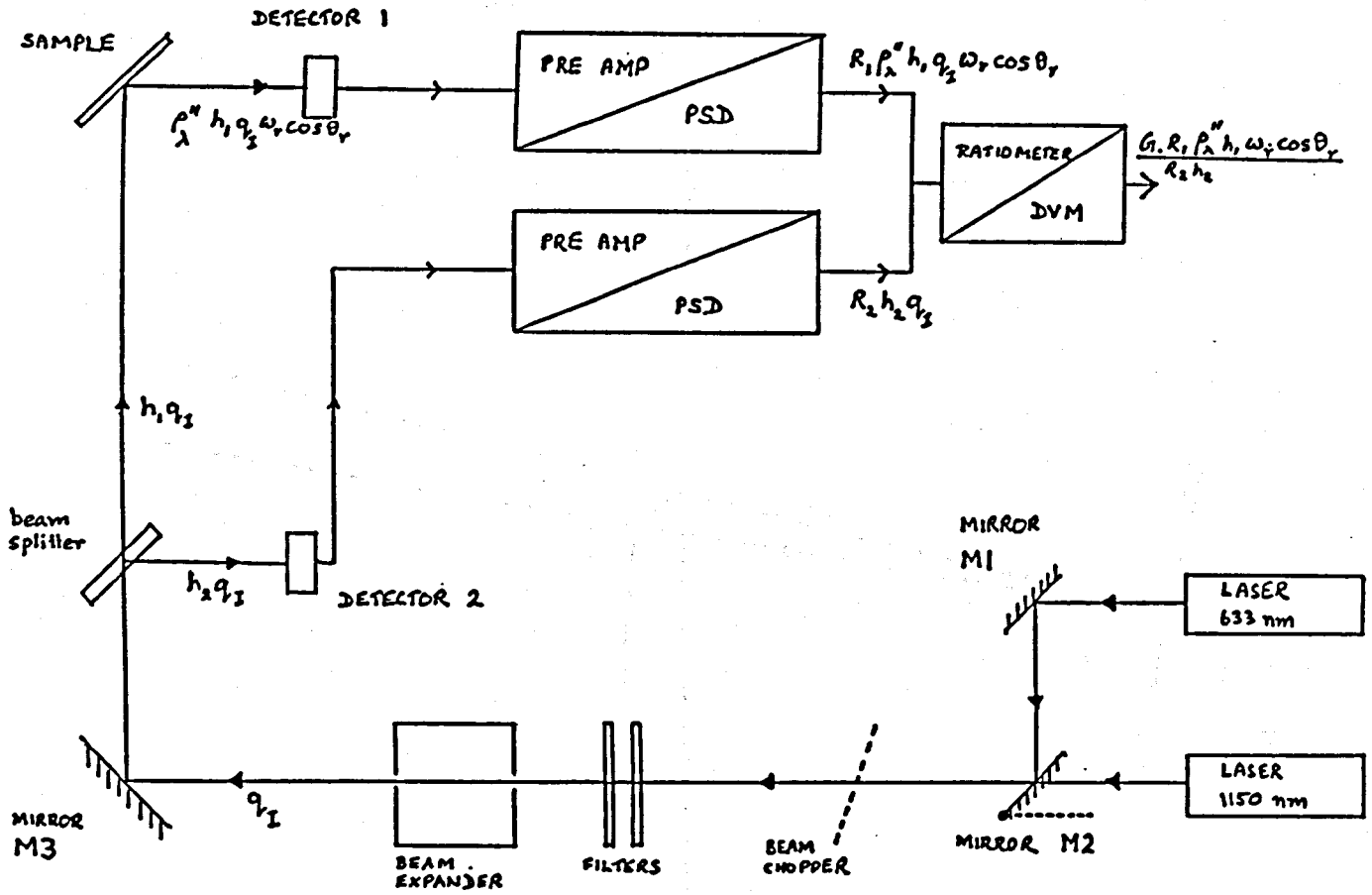

SCHEMATIC REPRESENTATION OF BDR MEASUREMENT

FIGURE 4.9

INCIDENT BEAM ALIGNMENT – SDA

FIGURE 4.10

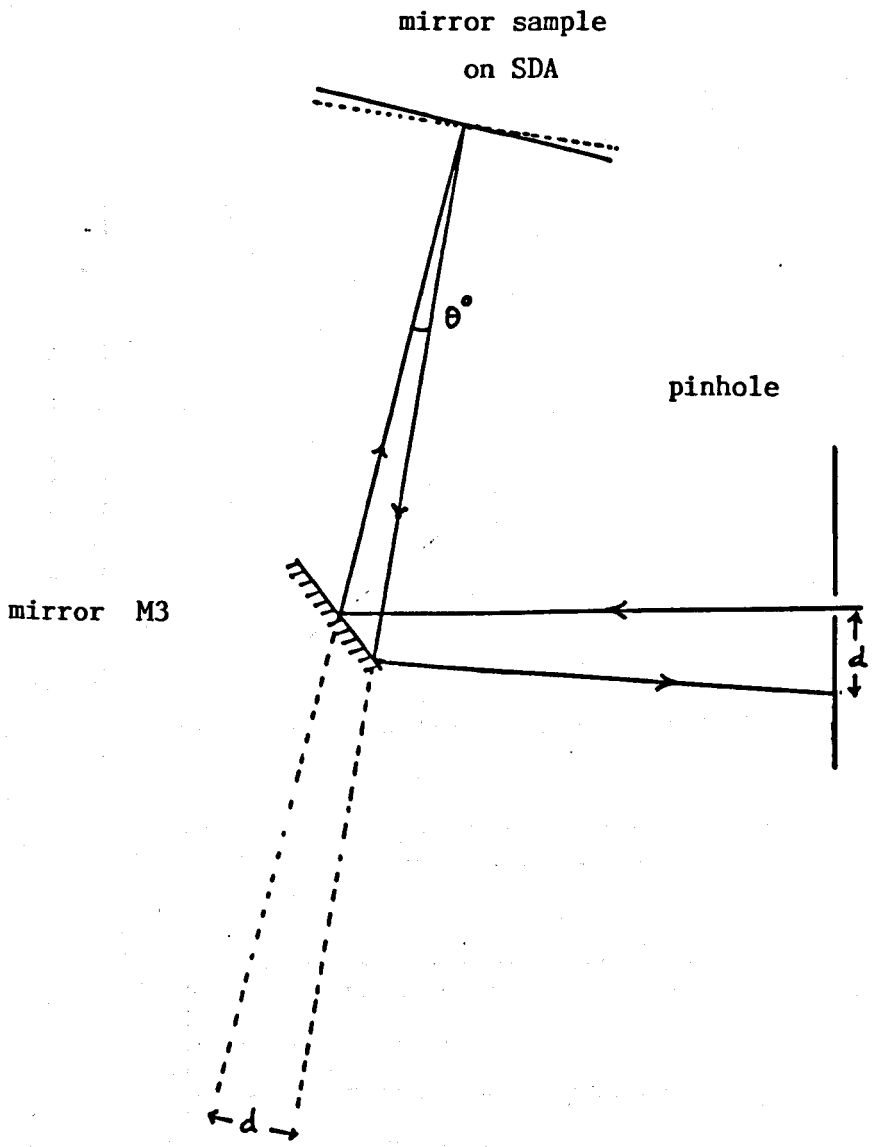

$$\theta = \frac{d}{SM + MP} \simeq \frac{d\ (mm)}{250} \quad \text{radians}$$

Figure 4.11

spectral BDR of NEXTEL sample
632.8 nm
NARROW beam incident on CENTRE position

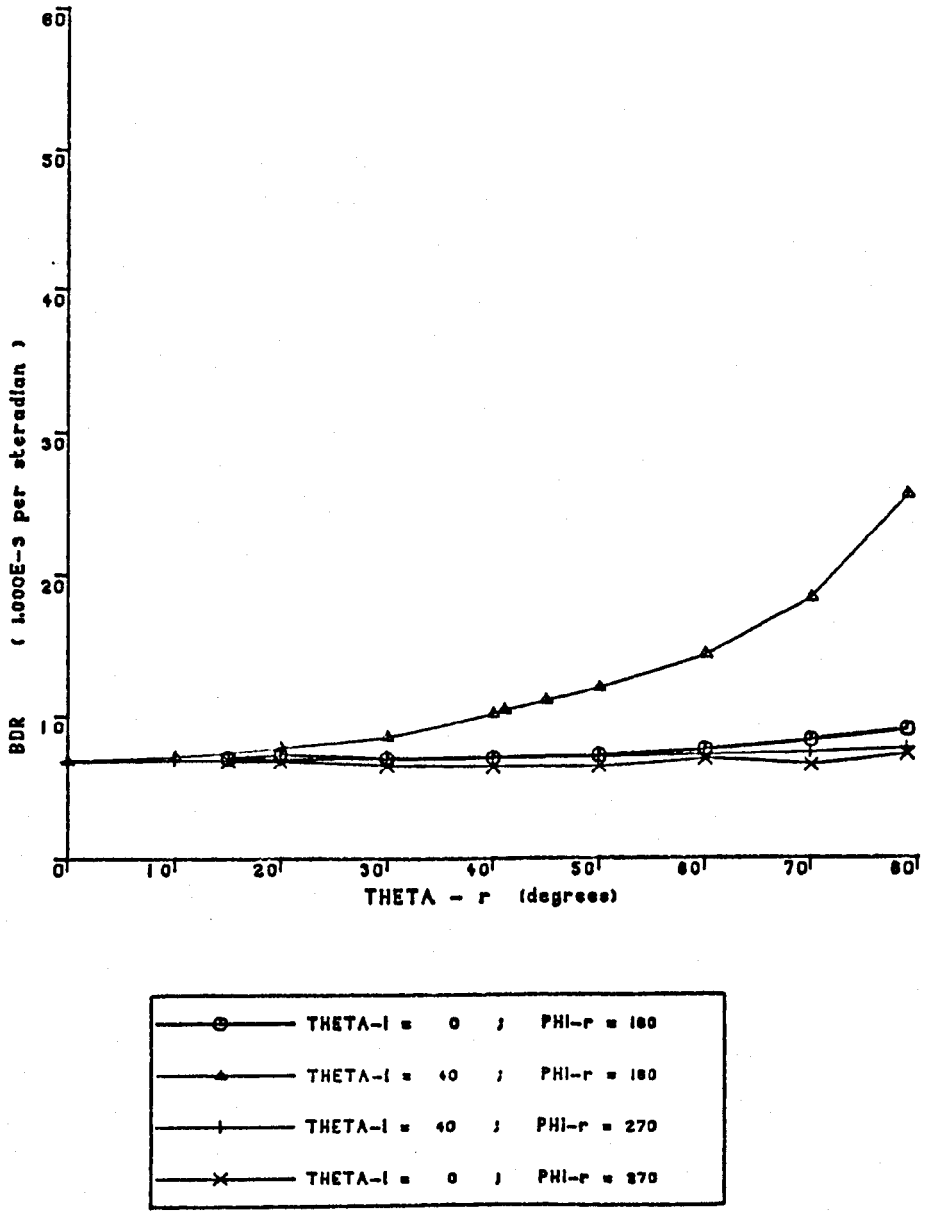

Figure 4.12

spectral BDR of NEXTEL sample
632.8 nm
NARROW beam incident on L.H.S. position

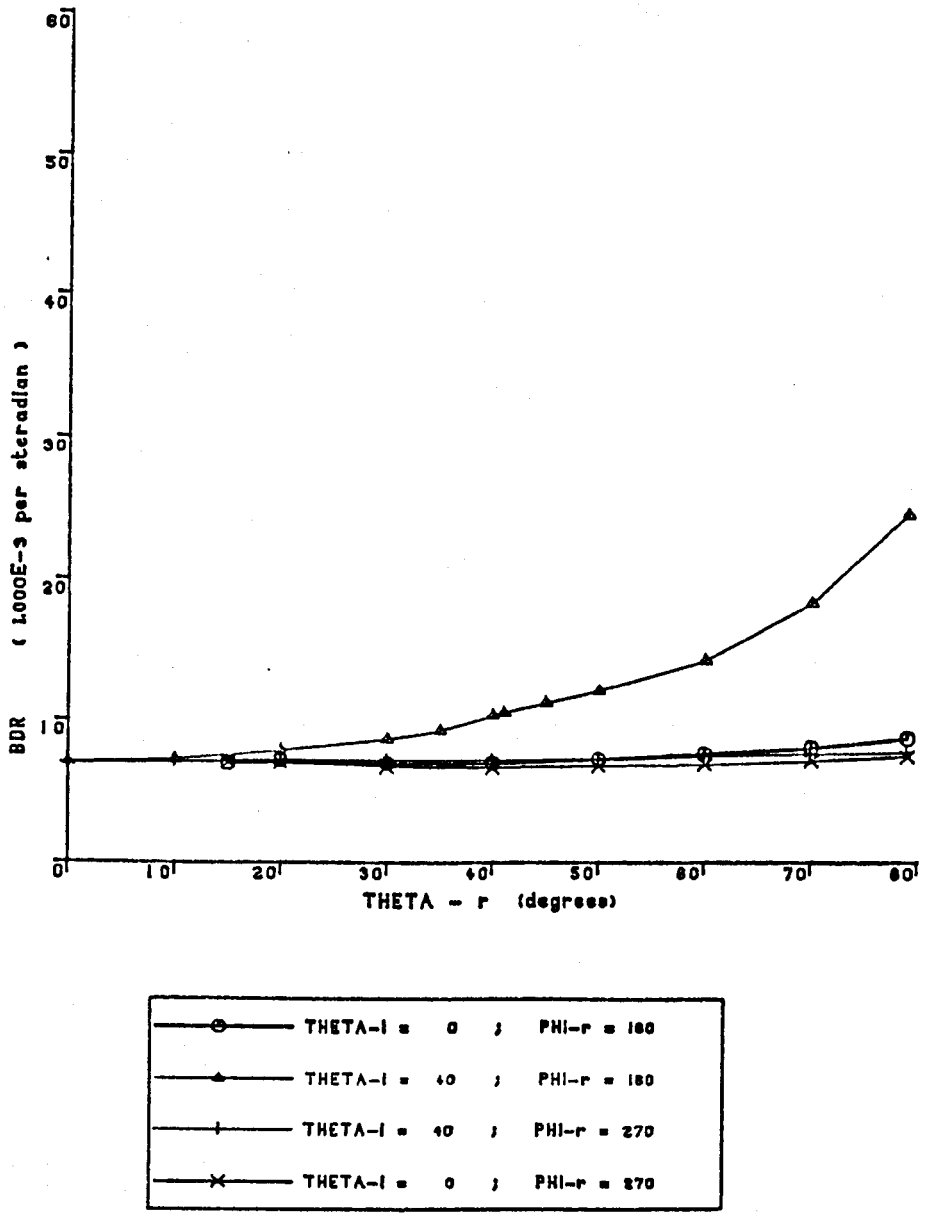

Figure 4.13

spectral BDR of NEXTEL sample
632.8 nm
NARROW beam incident on R.H.S. position

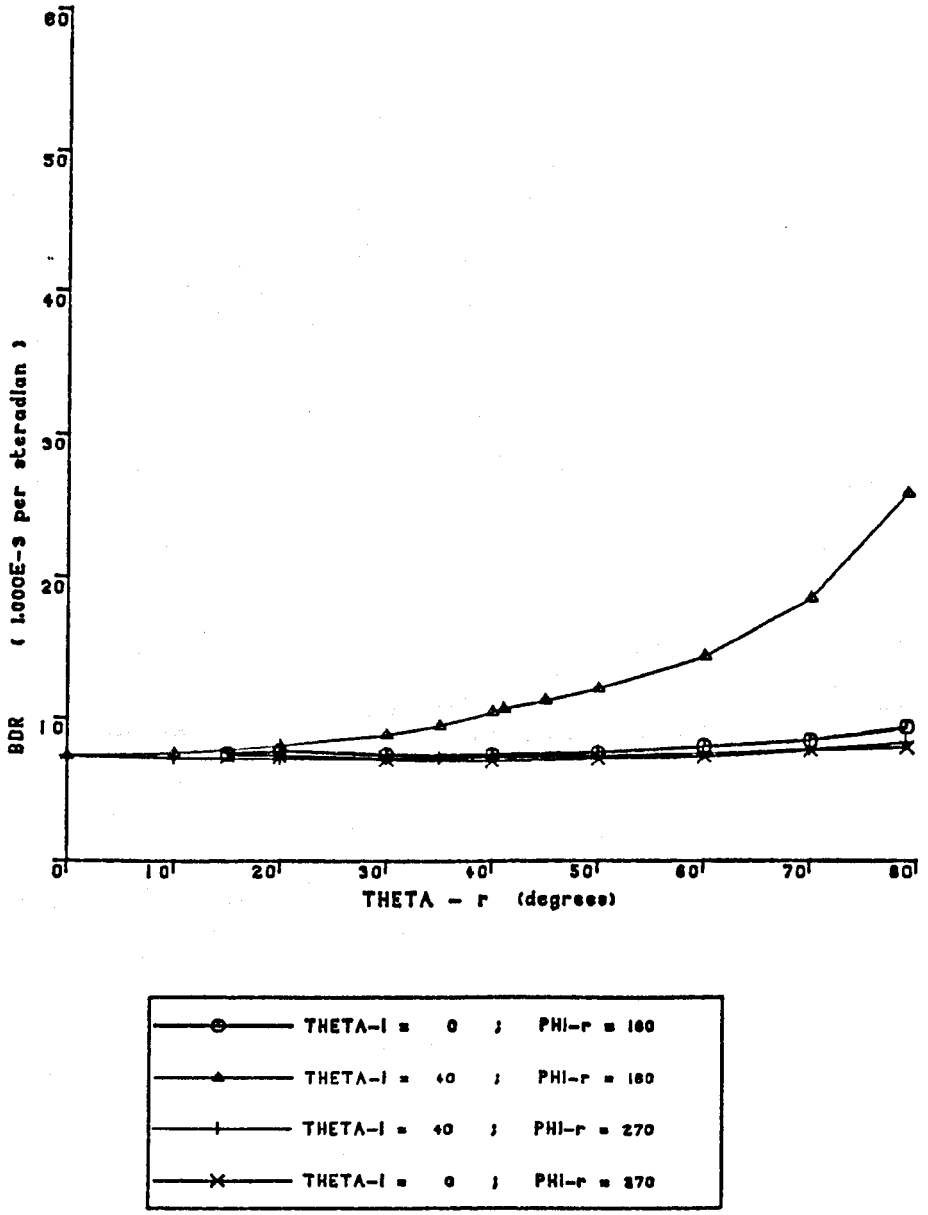

Figure 4.14

spectral BDR of NEXTEL sample
632.8 nm
WIDE beam incident on CENTRE position

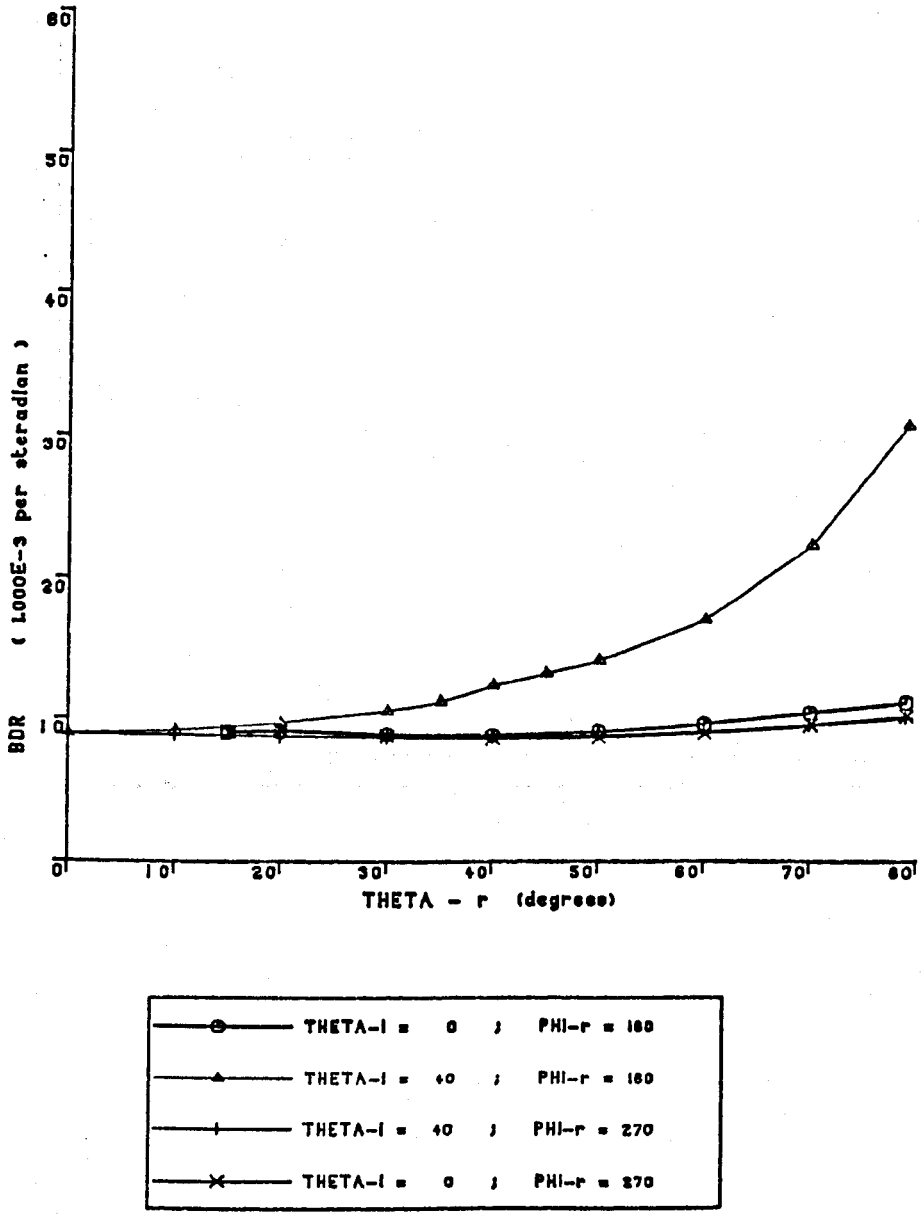

Figure 4.15

spectral BDR of NEXTEL sample
1152.3 nm
WIDE beam incident on CENTRE position

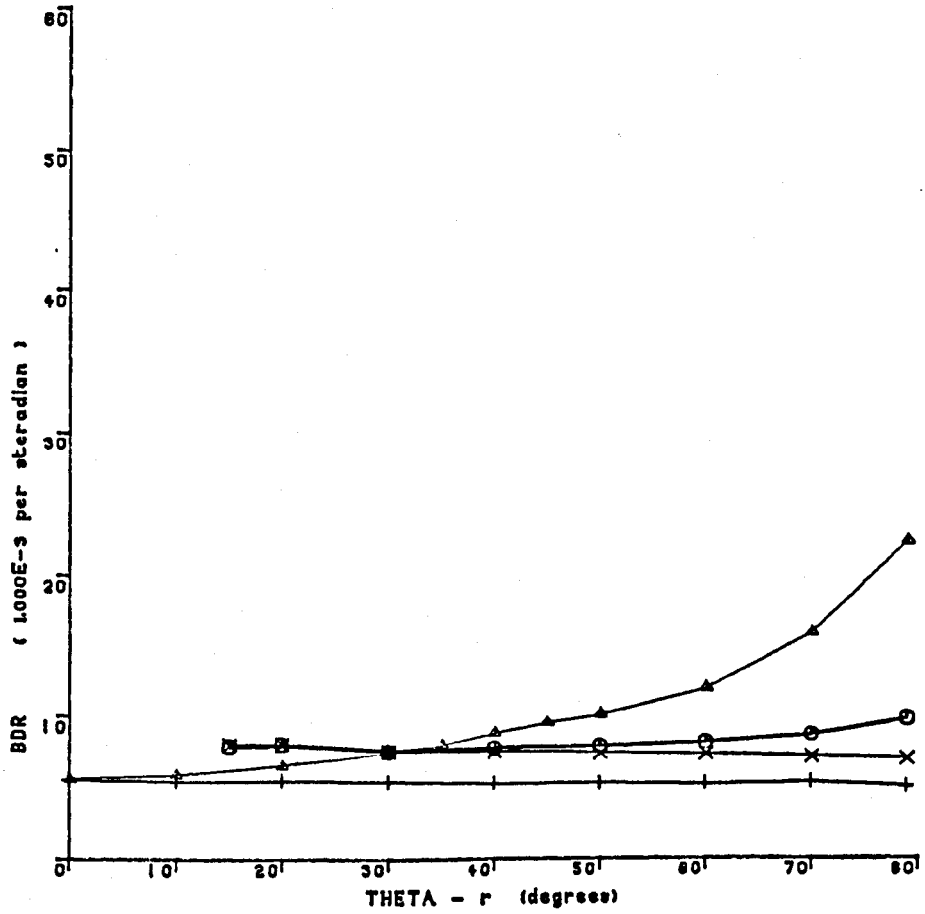

Figure 4.16

spectral BDR of S'COAT -50 sample
632.8 nm
NARROW beam incident on CENTRE position

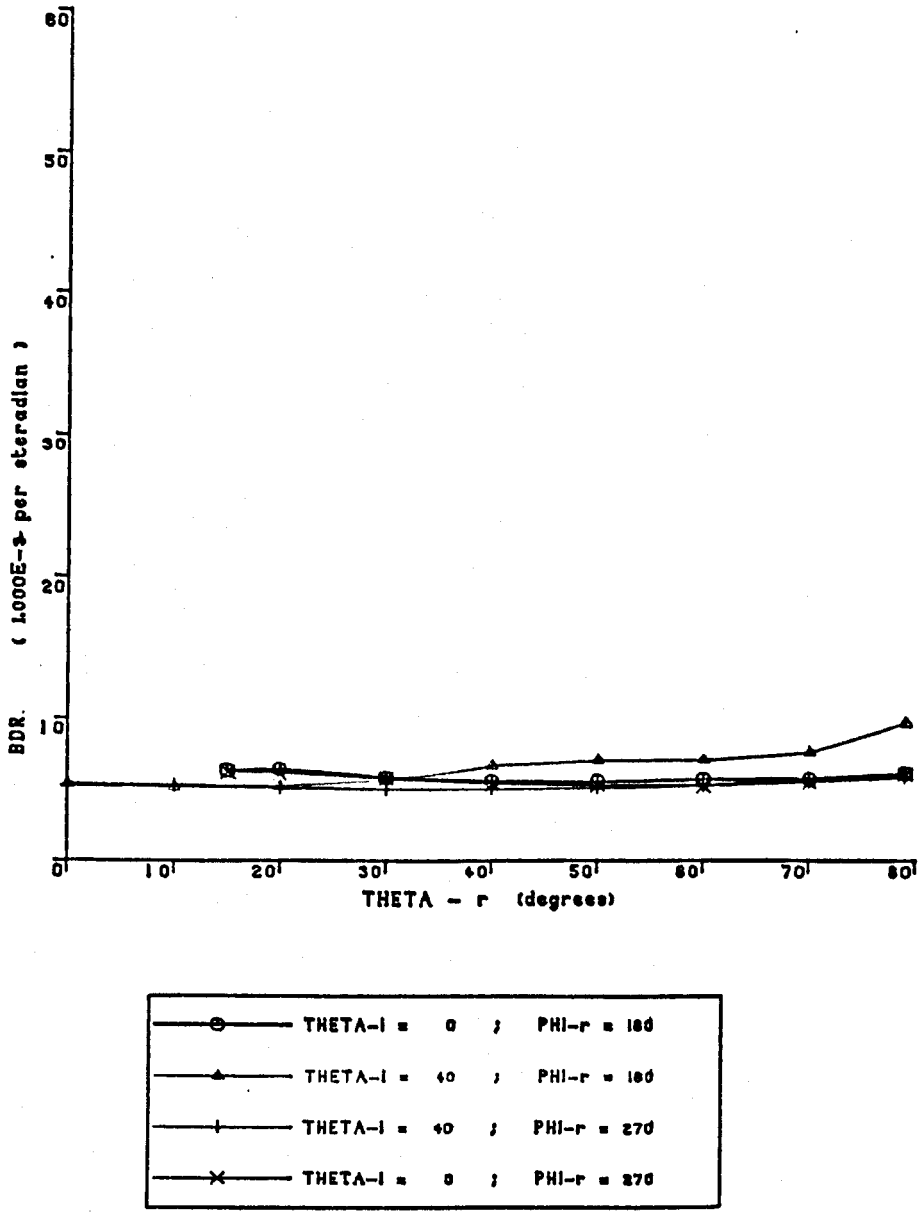

Figure 4.17

spectral BDR of S'COAT -50 sample
632.8 nm
NARROW beam incident on L.H.S. position

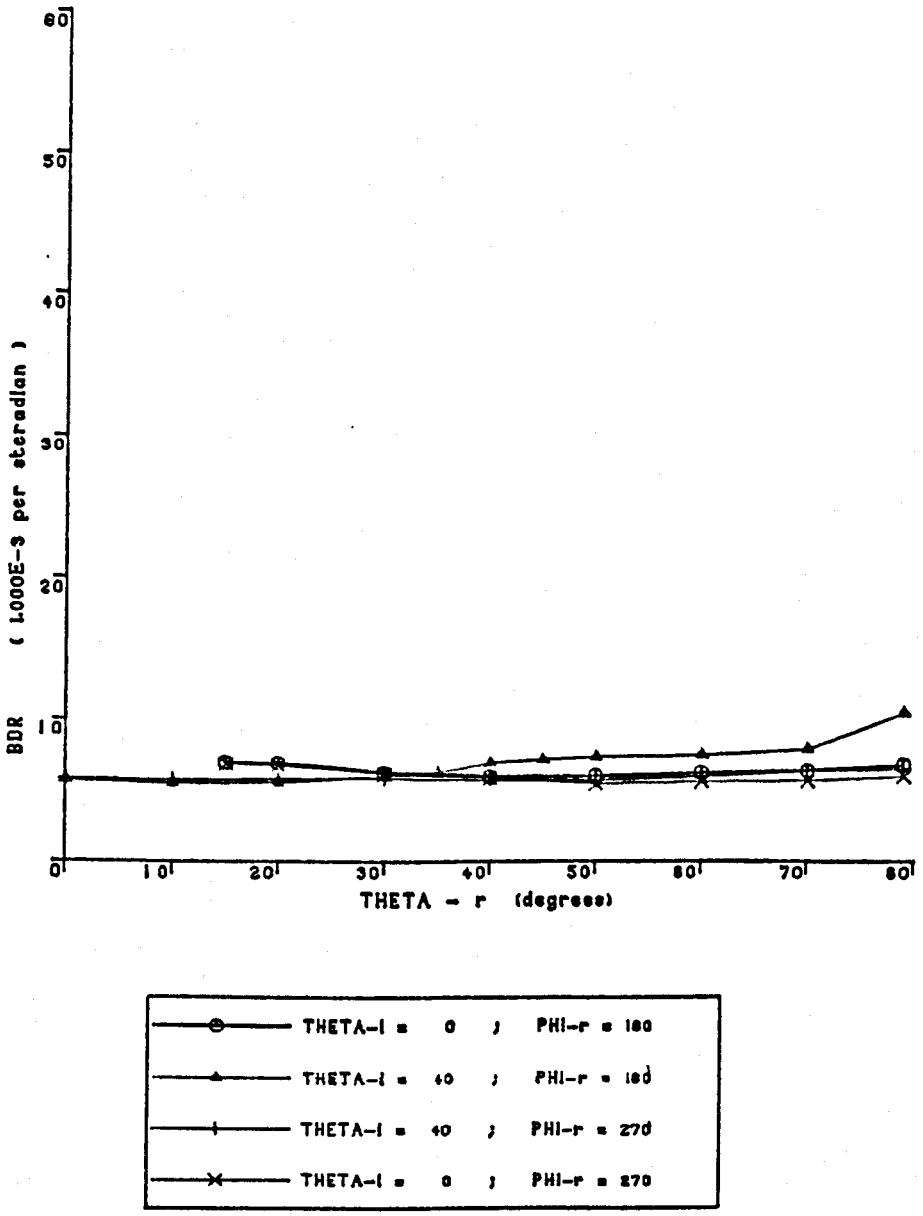

Figure 4.18

spectral BDR of S'COAT -50 sample
632.8 nm
NARROW beam incident on R.H.S. position

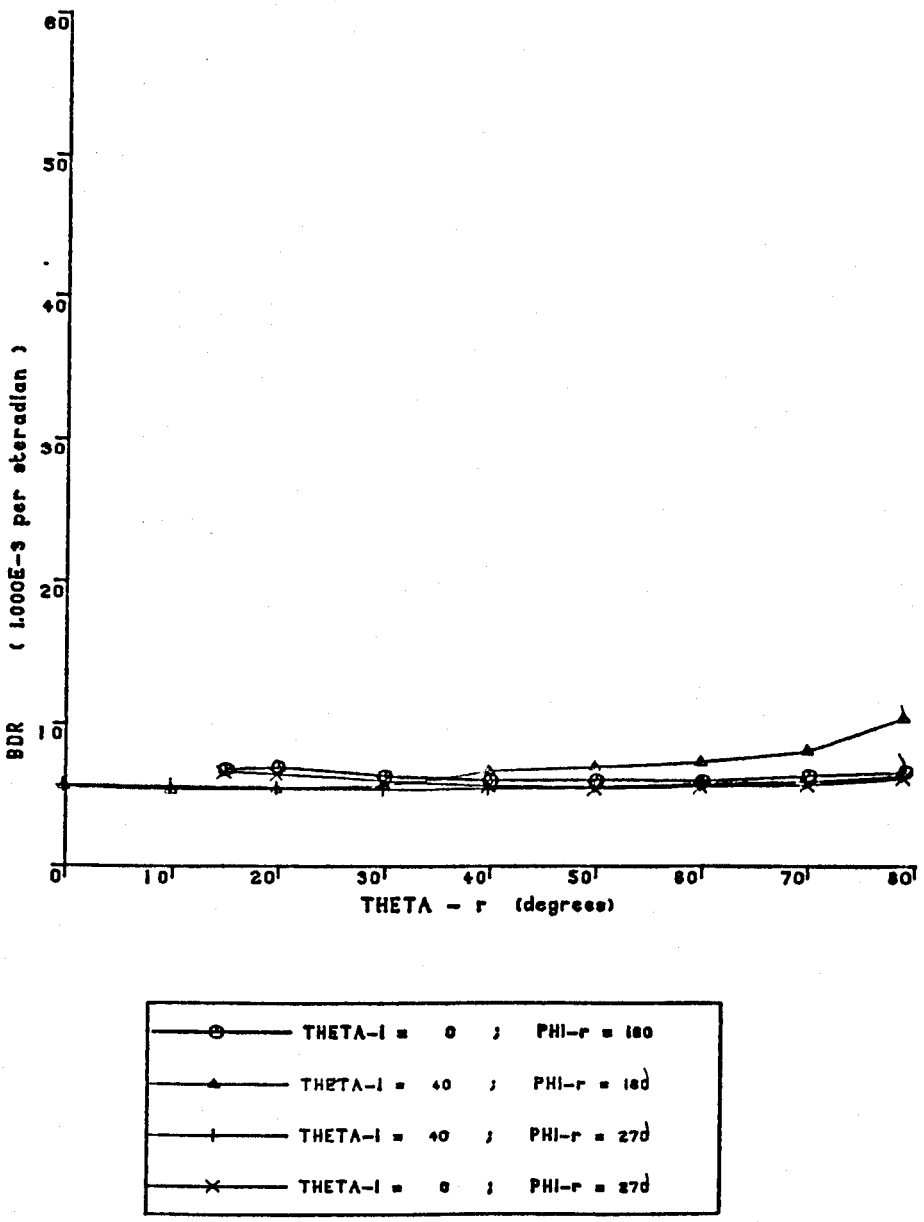

Figure 4.19

spectral BDR of S'COAT -50 sample
632.8 nm
WIDE beam incident on CENTRE position

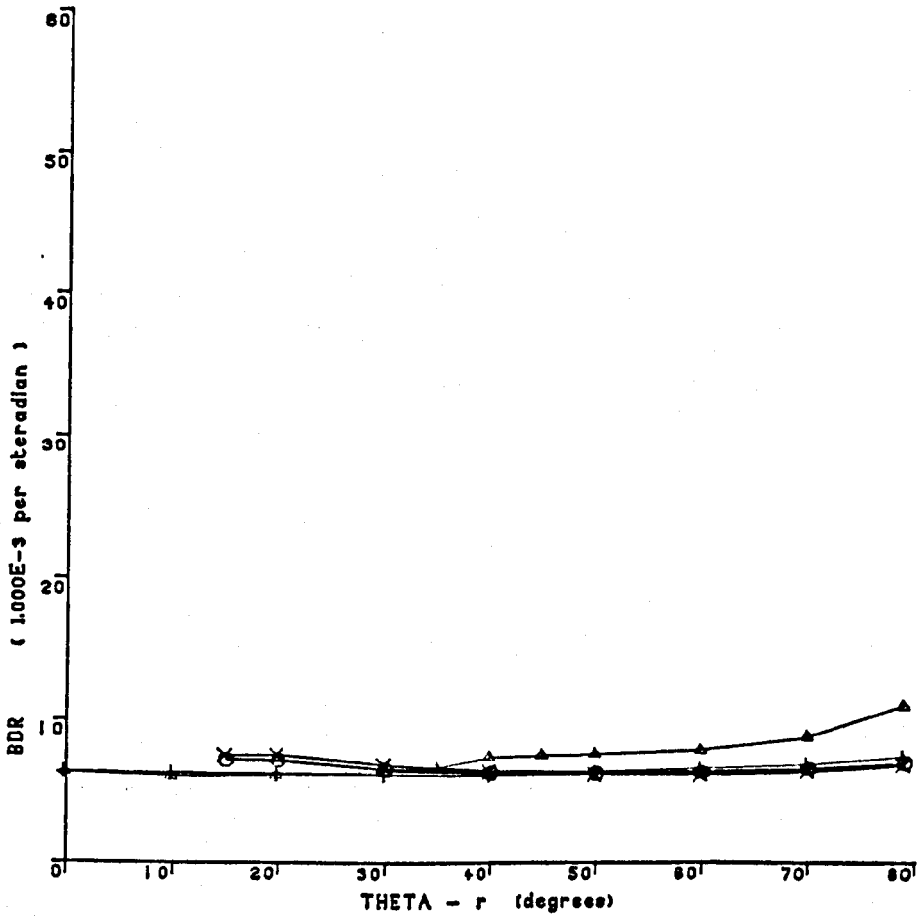

Figure 4.20

spectral BDR of S'COAT -50 sample
1152.3 nm
WIDE beam incident on CENTRE position

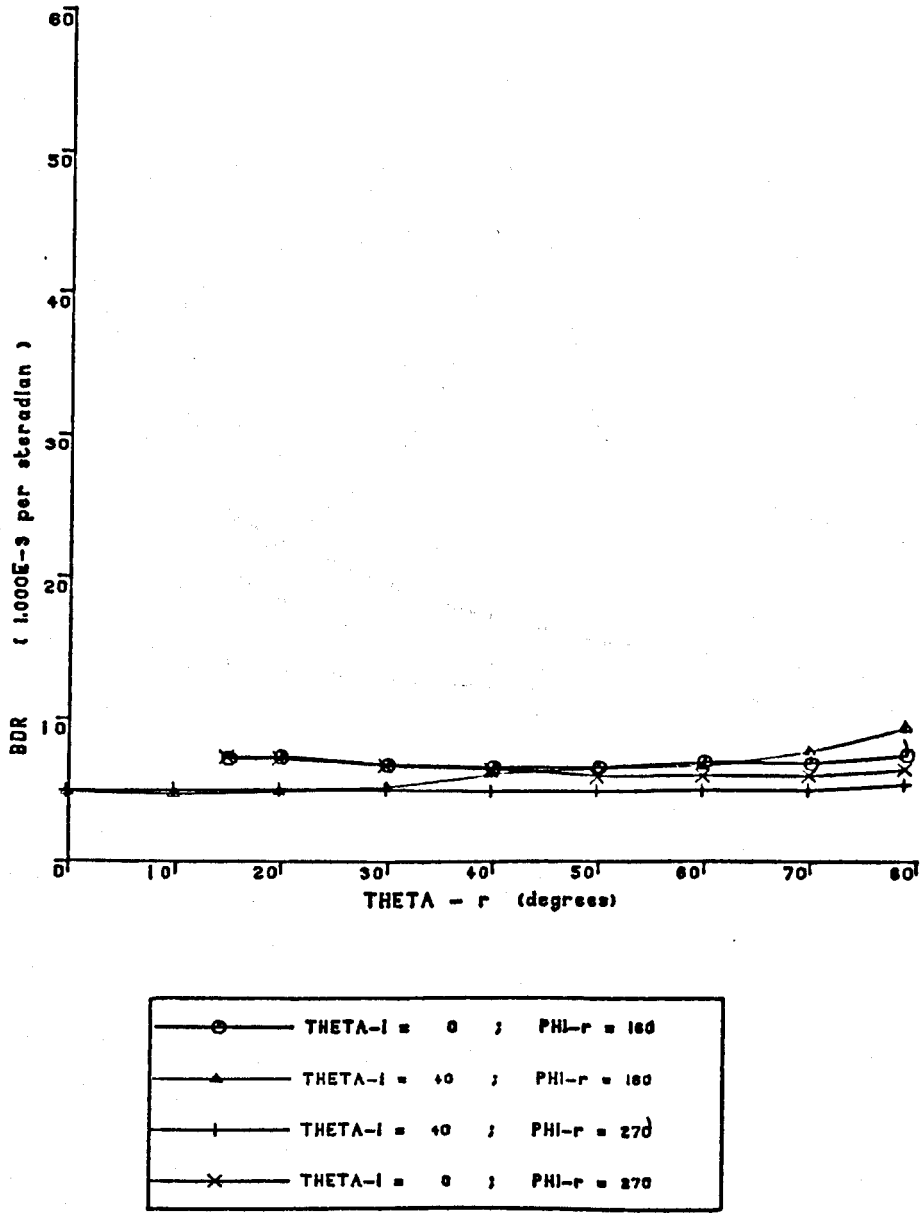

Figure 4.21

spectral BDR of SKYSORB sample
632.8 nm
NARROW beam incident on CENTRE position

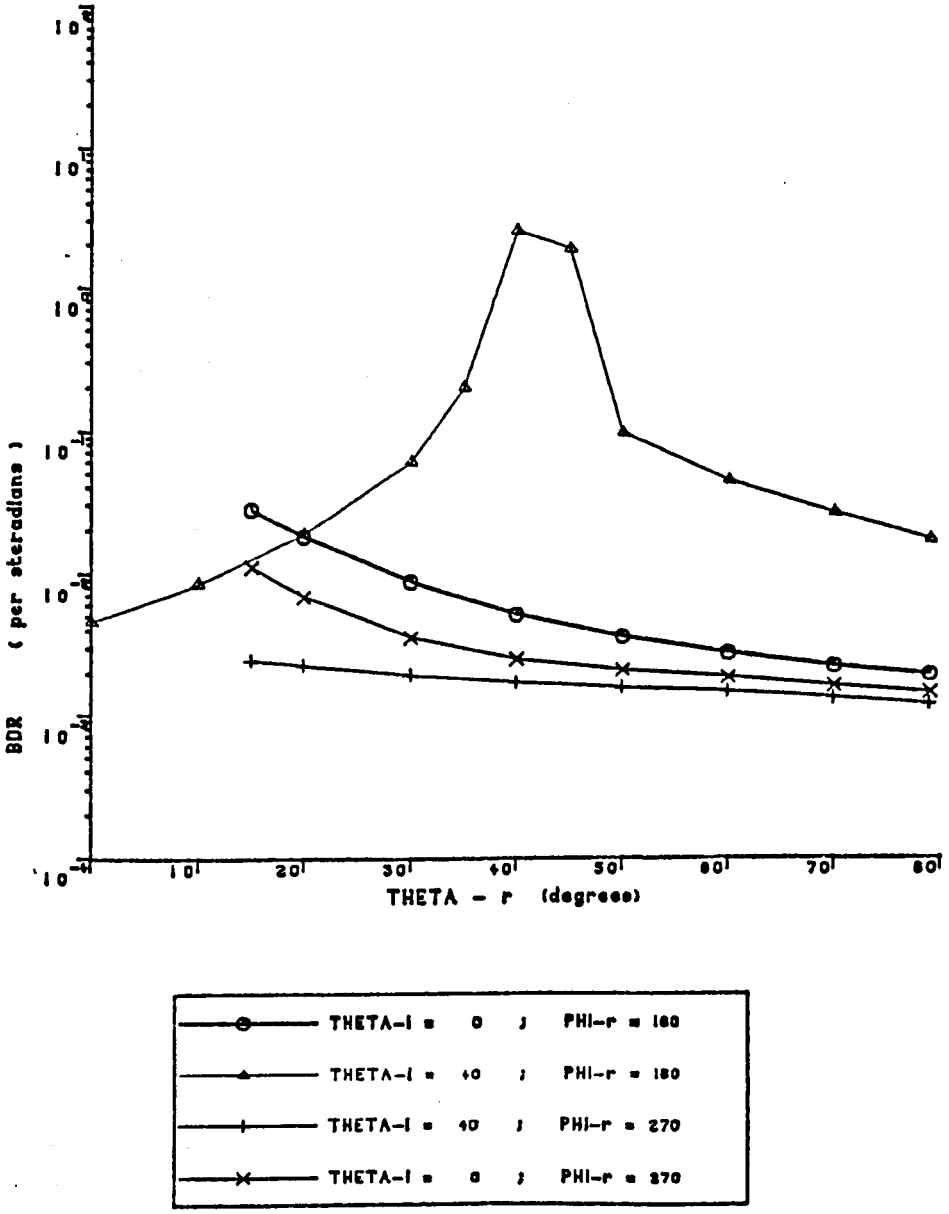

Figure 4.22

spectral BDR of SKYSORB sample
632.8 nm
NARROW beam incident on L.H.S. position

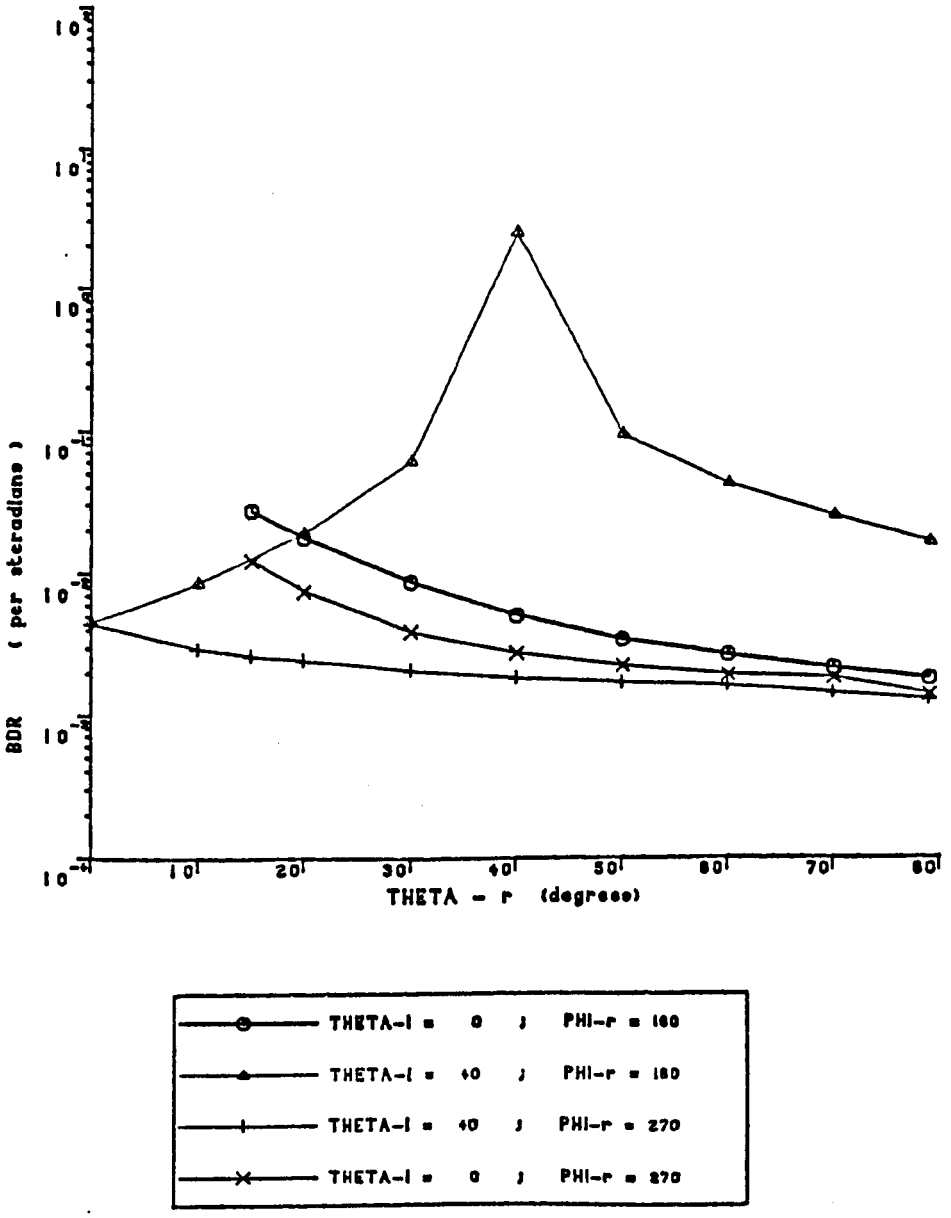

Figure 4.23

spectral BDR of SKYSORB sample
632.8 nm
NARROW beam incident on R.H.S. position

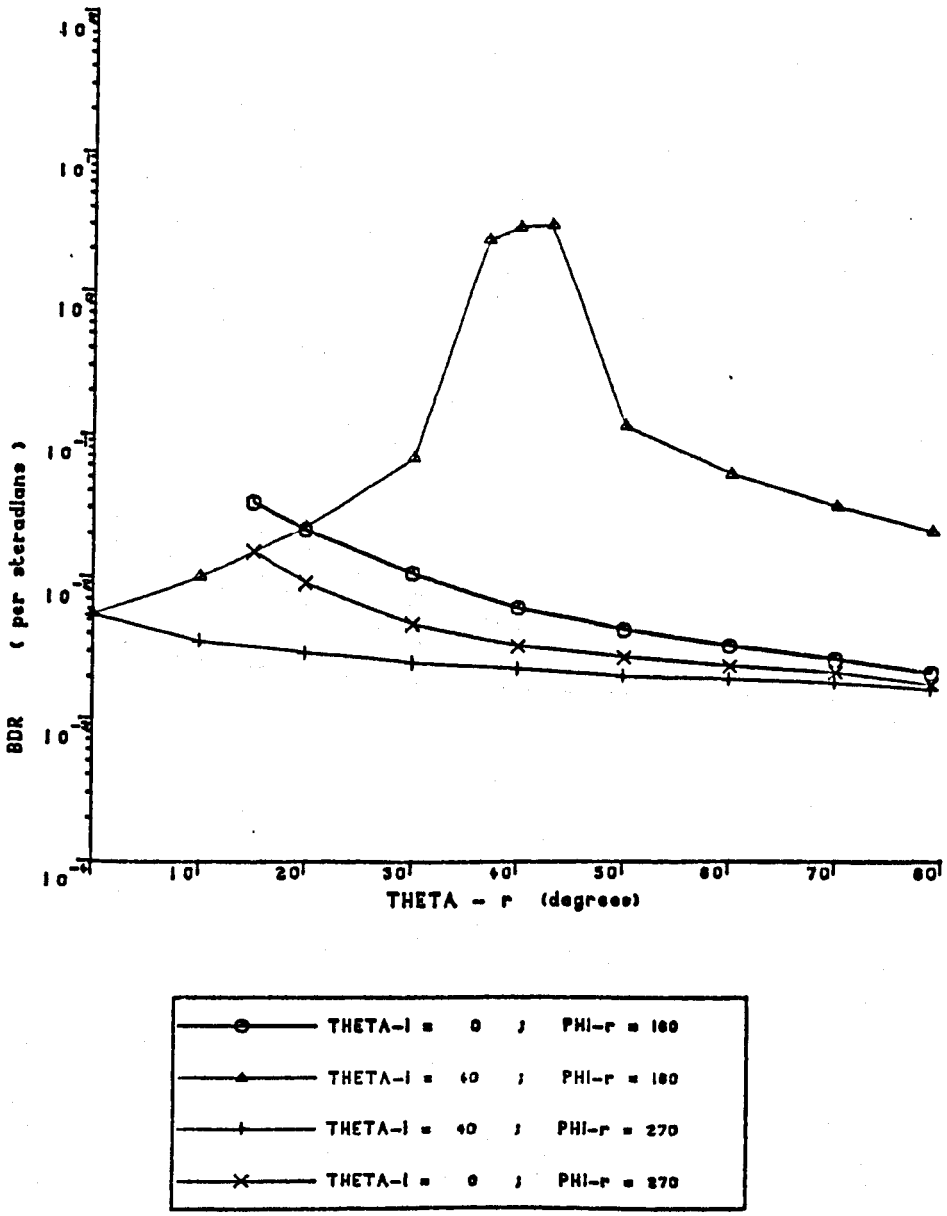

Figure 4.24

spectral BDR of SKYSORB sample
632.8 nm
WIDE beam incident on CENTRE position

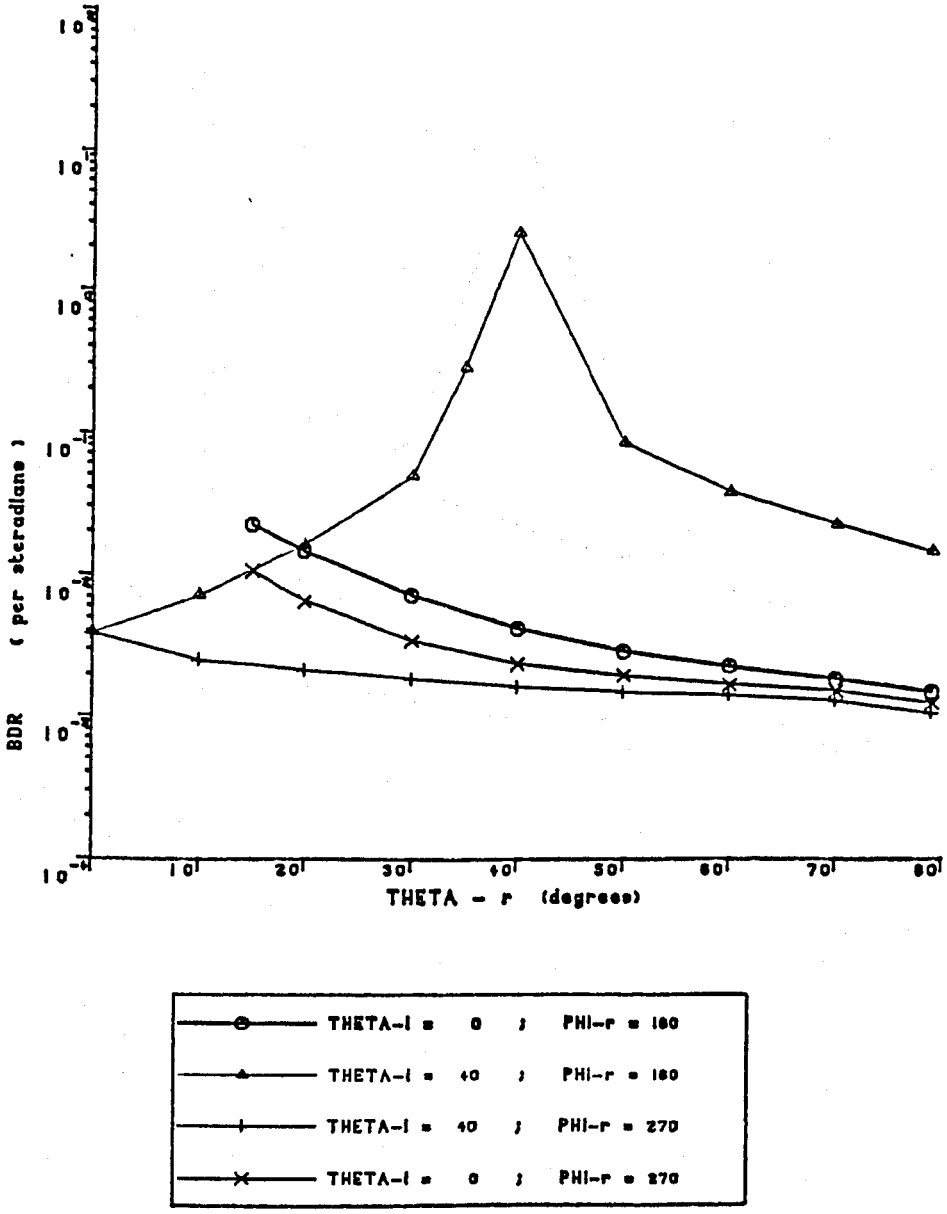

Figure 4.25

spectral BDR of SKYSORB sample
1152.3 nm
WIDE beam incident on CENTRE position

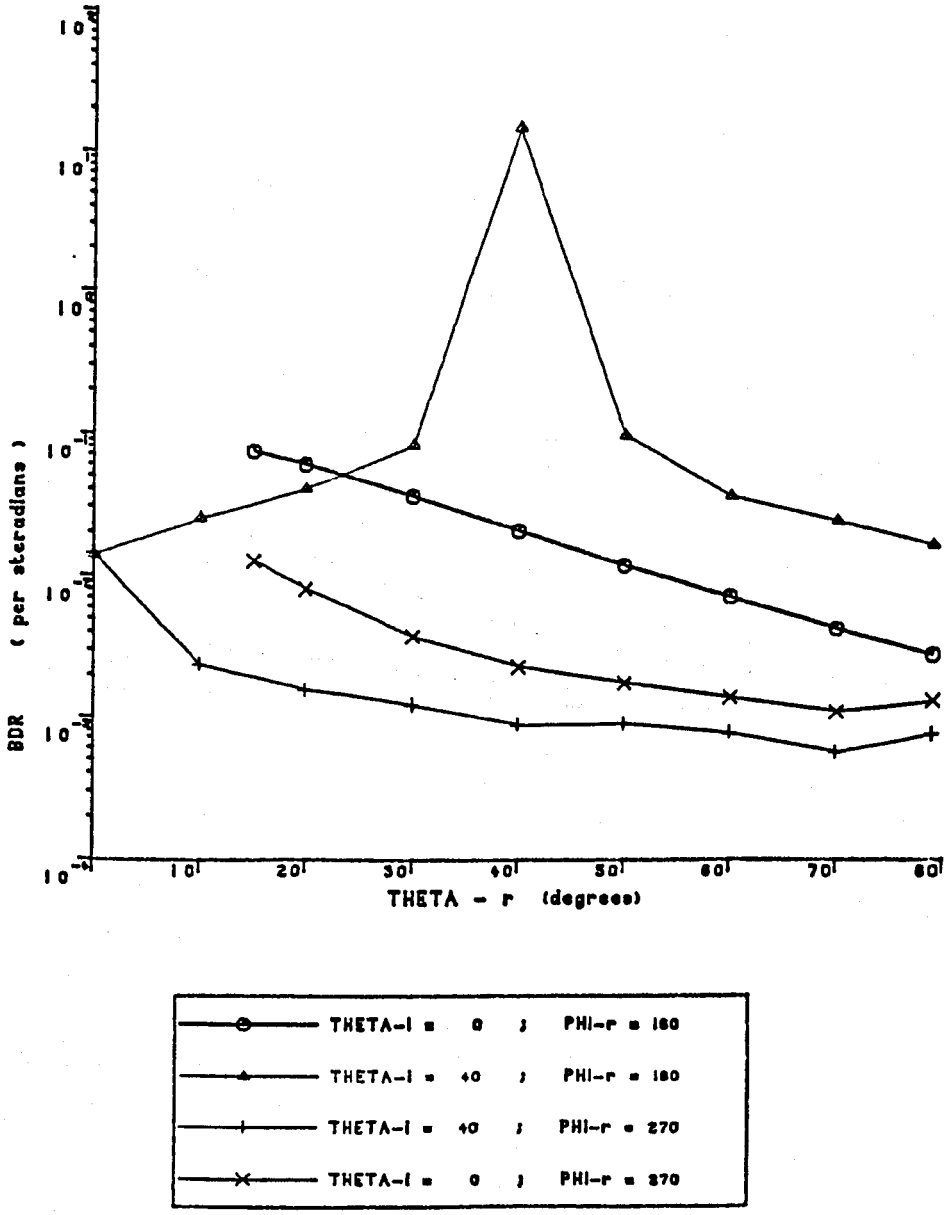

Figure 4.26

spectral BDR of MAXORB sample
632.8 nm
NARROW beam incident on CENTRE position

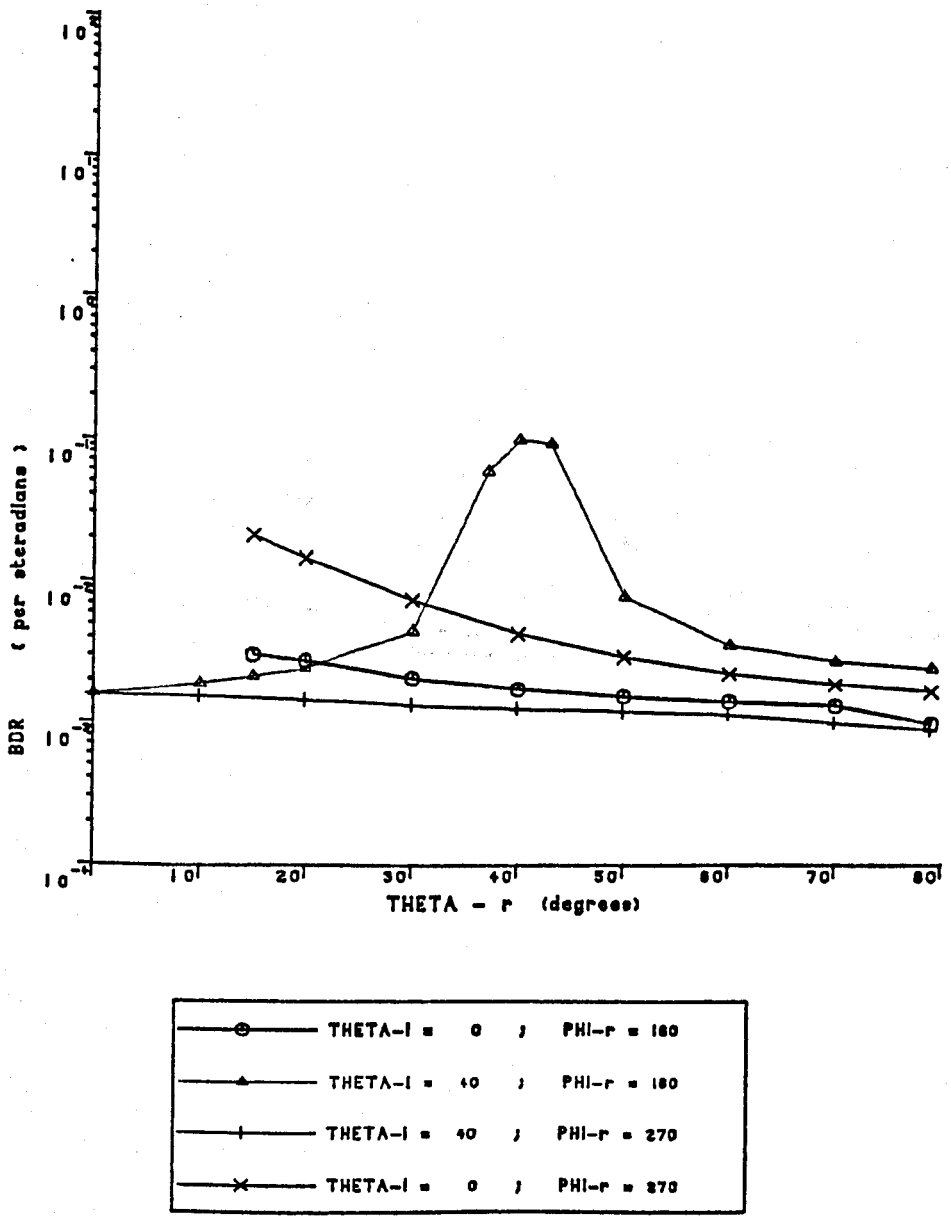

Figure 4.27

spectral BDR of MAXORB sample
632.8 nm
NARROW beam incident on L.H.S. position

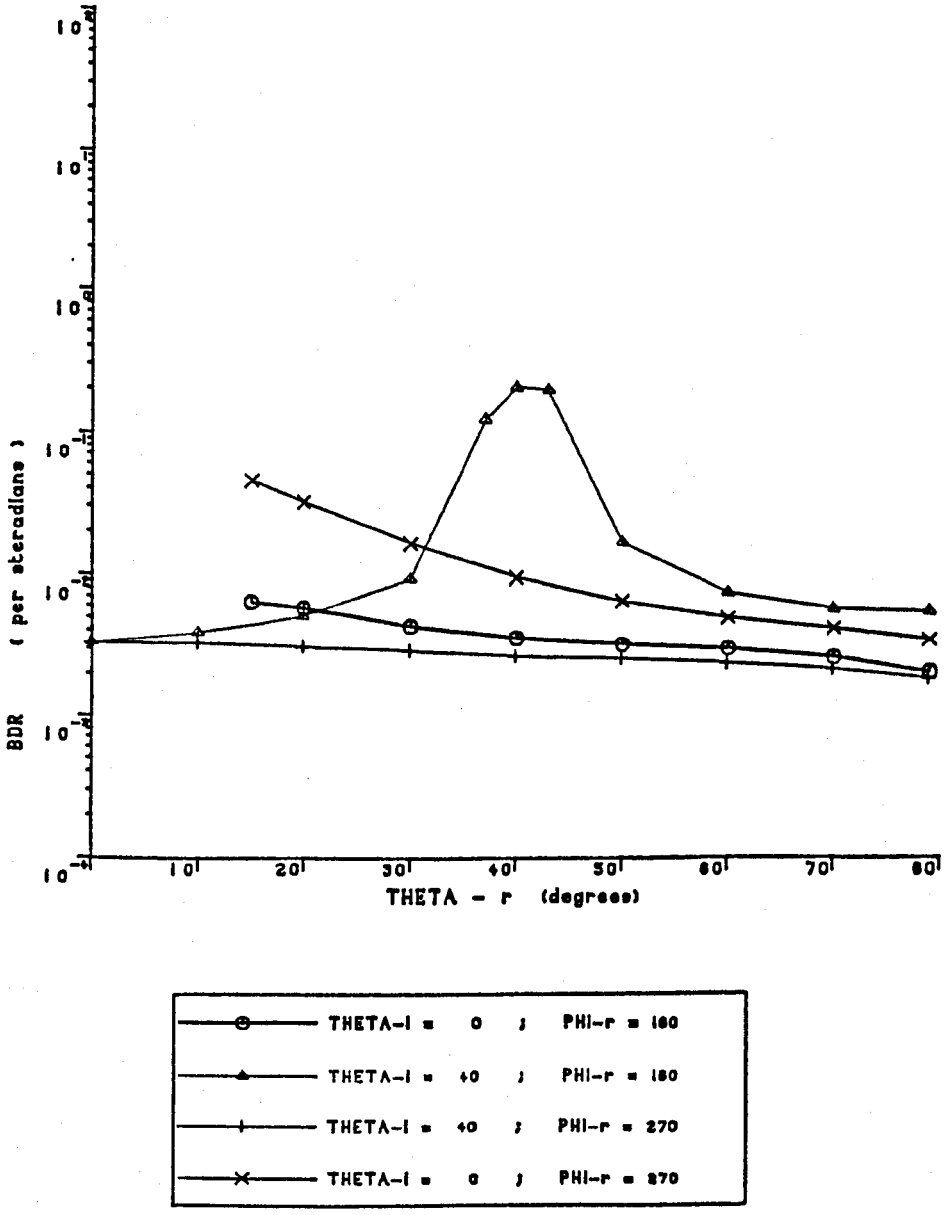

Figure 4.28

spectral BDR of MAXORB sample
632.8 nm
NARROW beam incident on R.H.S. position

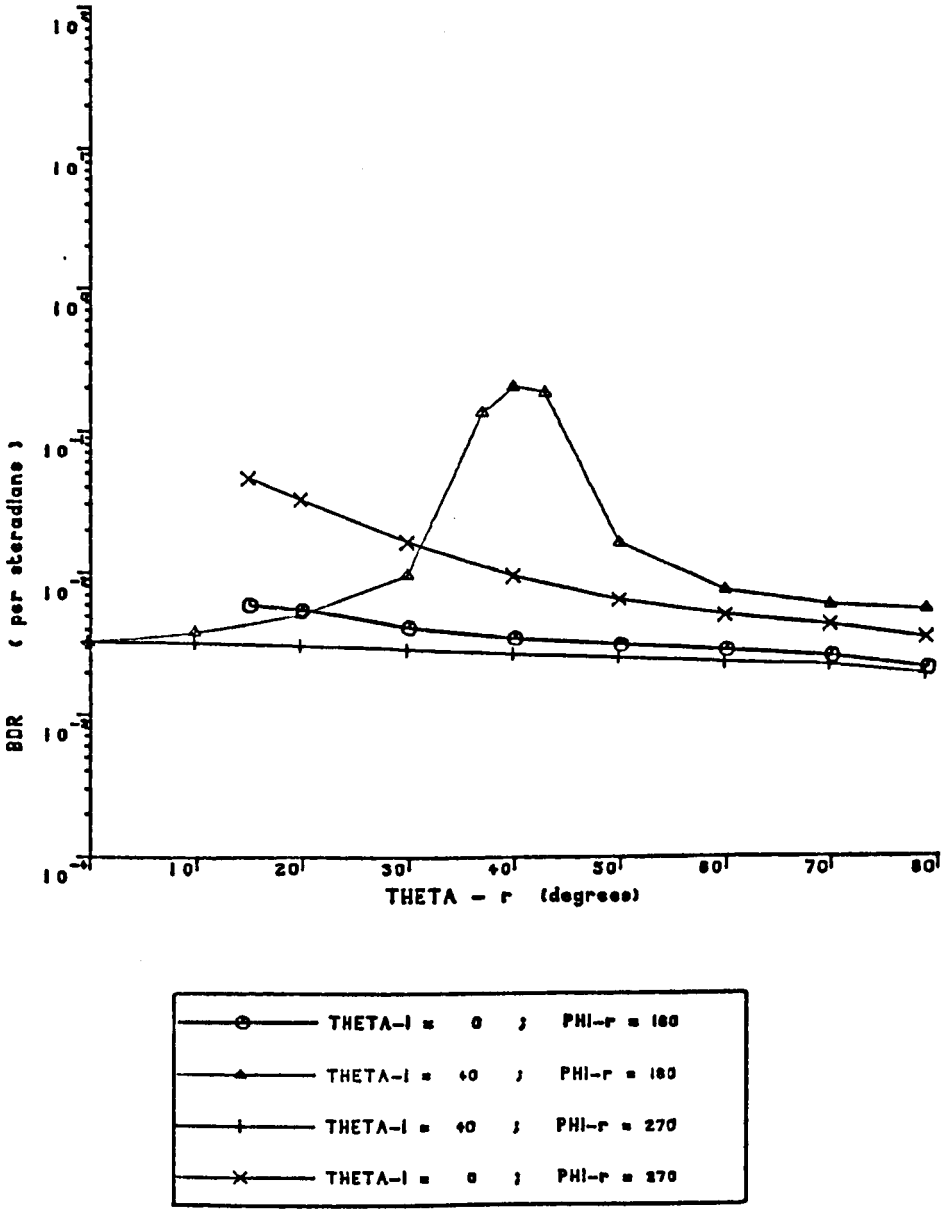

Figure 4.29

spectral BDR of MAXORB sample
632.8 nm
WIDE beam incident on CENTRE position

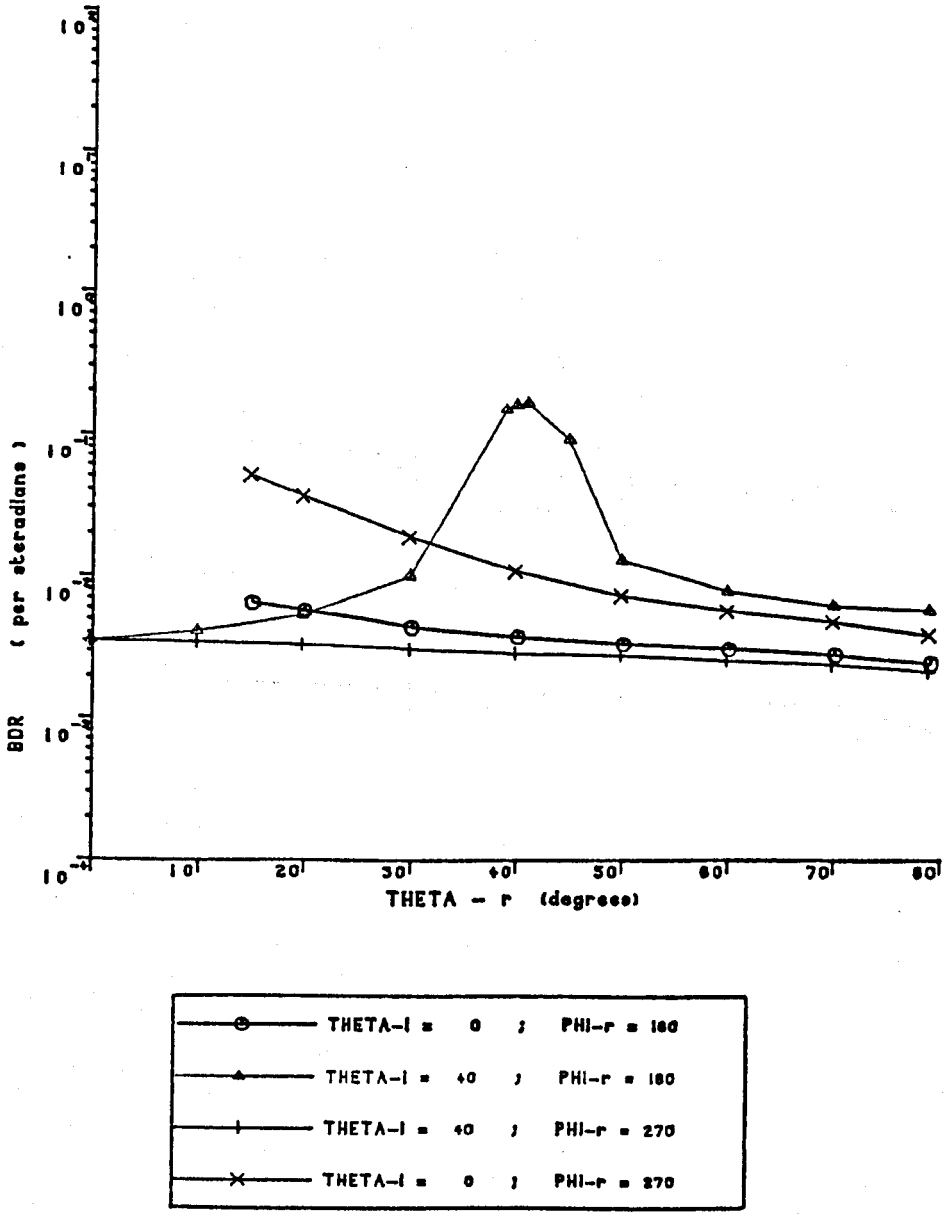

Figure 4.30

spectral BDR of MAXORB sample
1152.3 nm
WIDE beam incident on CENTRE position

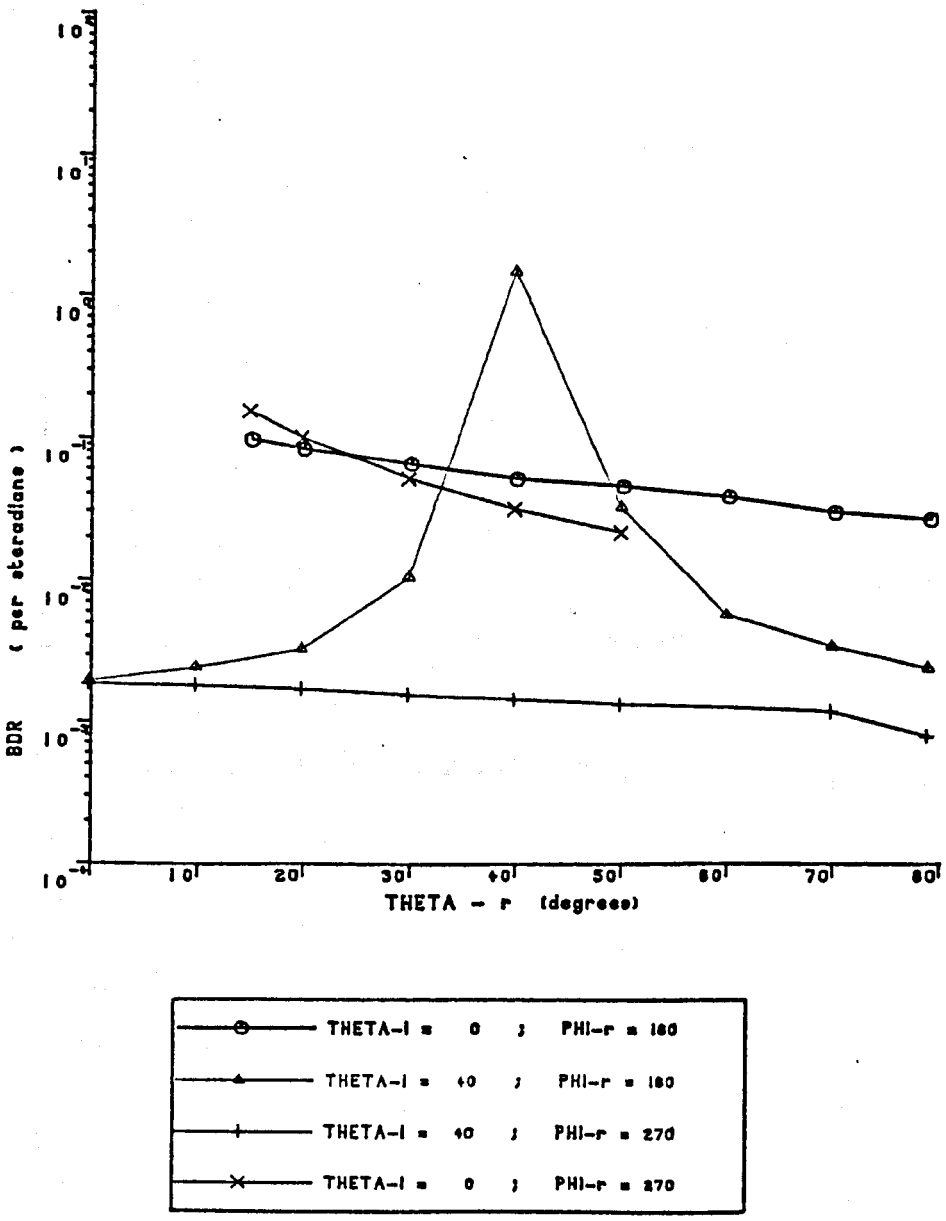

Figure 4.31

spectral BDR of CUSORB sample
632.8 nm
NARROW beam incident on CENTRE position

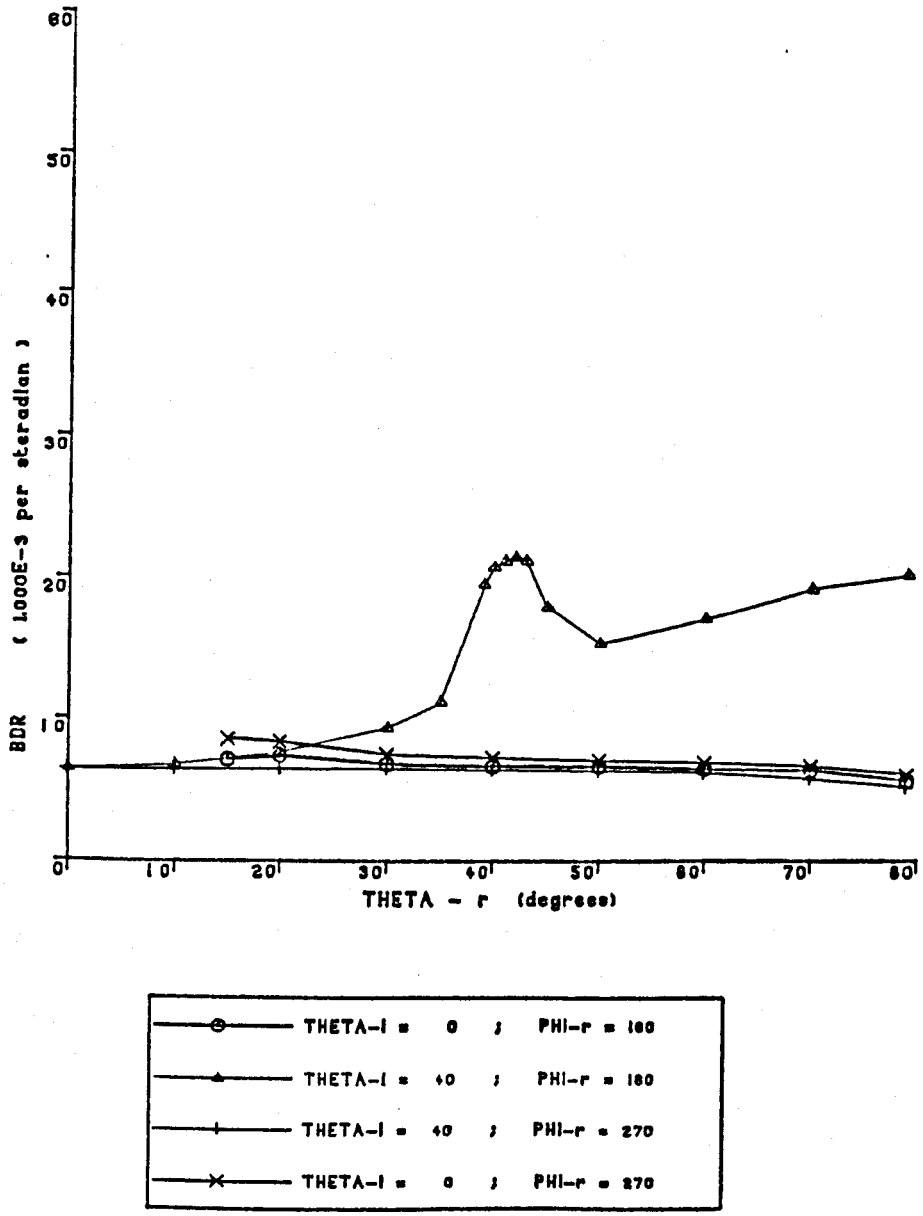

Figure 4.32

spectral BDR of CUSORB sample
632.8 nm
NARROW beam incident on L.H.S. position

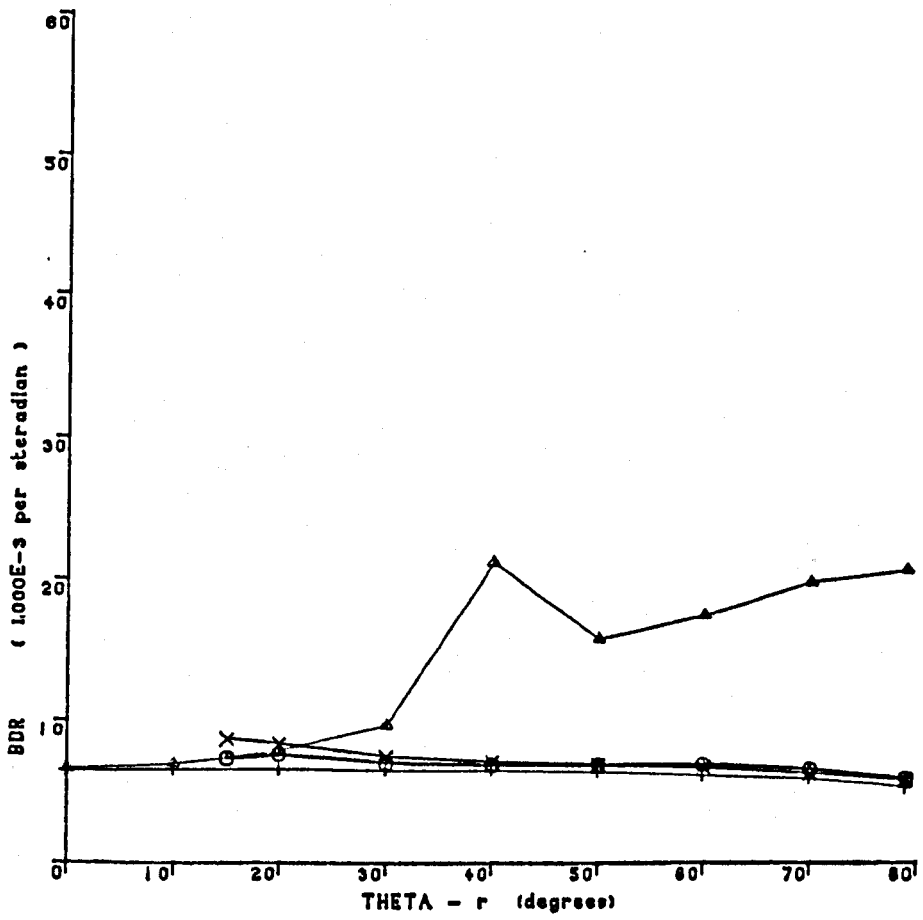

Figure 4.33

spectral BDR of CUSORB sample
632.8 nm
NARROW beam incident on R.H.S. position

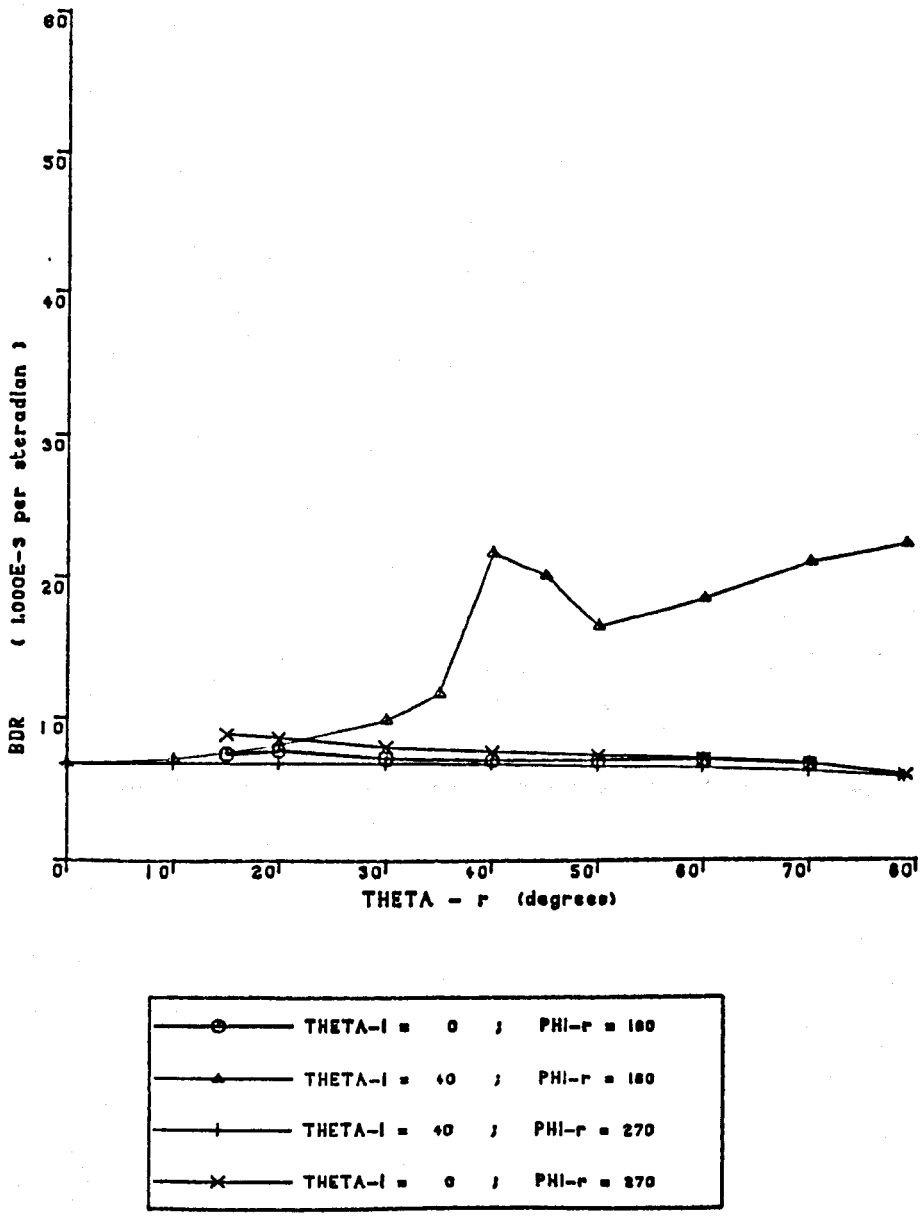

Figure 4.34

spectral BDR of CUSORB sample
632.8 nm
WIDE beam incident on CENTRE position

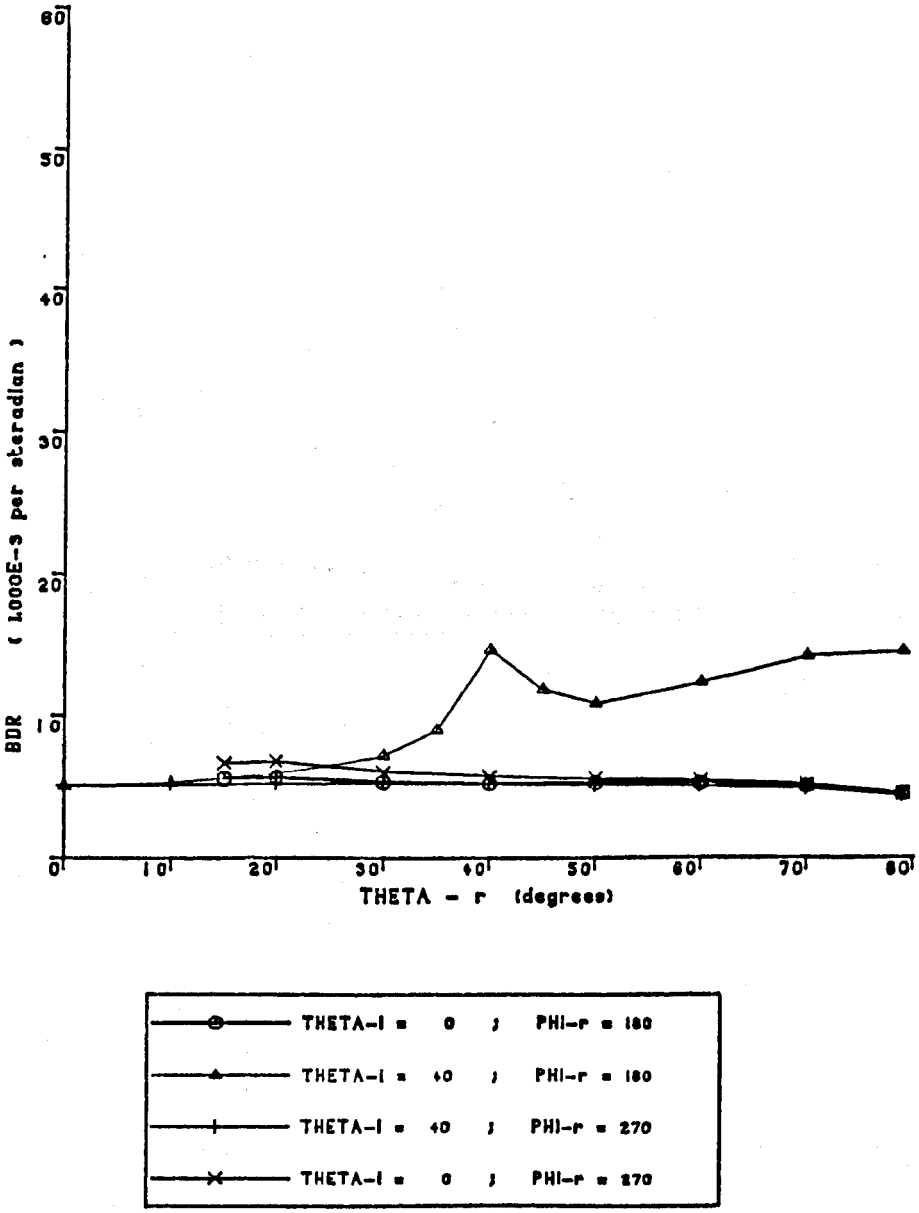

Figure 4.35

spectral BDR of CUSORB sample
1152.3 nm
WIDE beam incident on CENTRE position

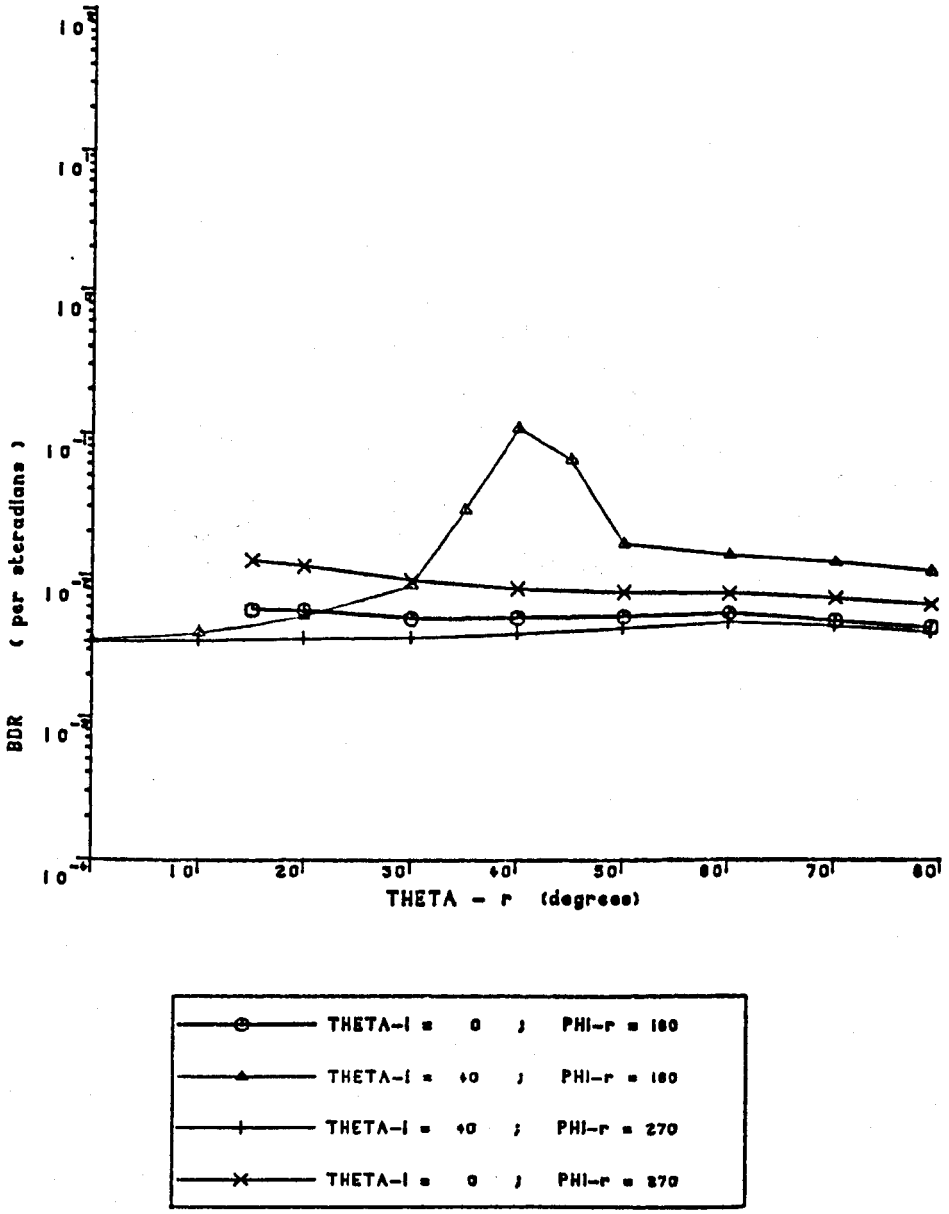

Figure 4.36

spectral BDR of S'COAT-100 sample
632.8 nm
NARROW beam incident on CENTRE position

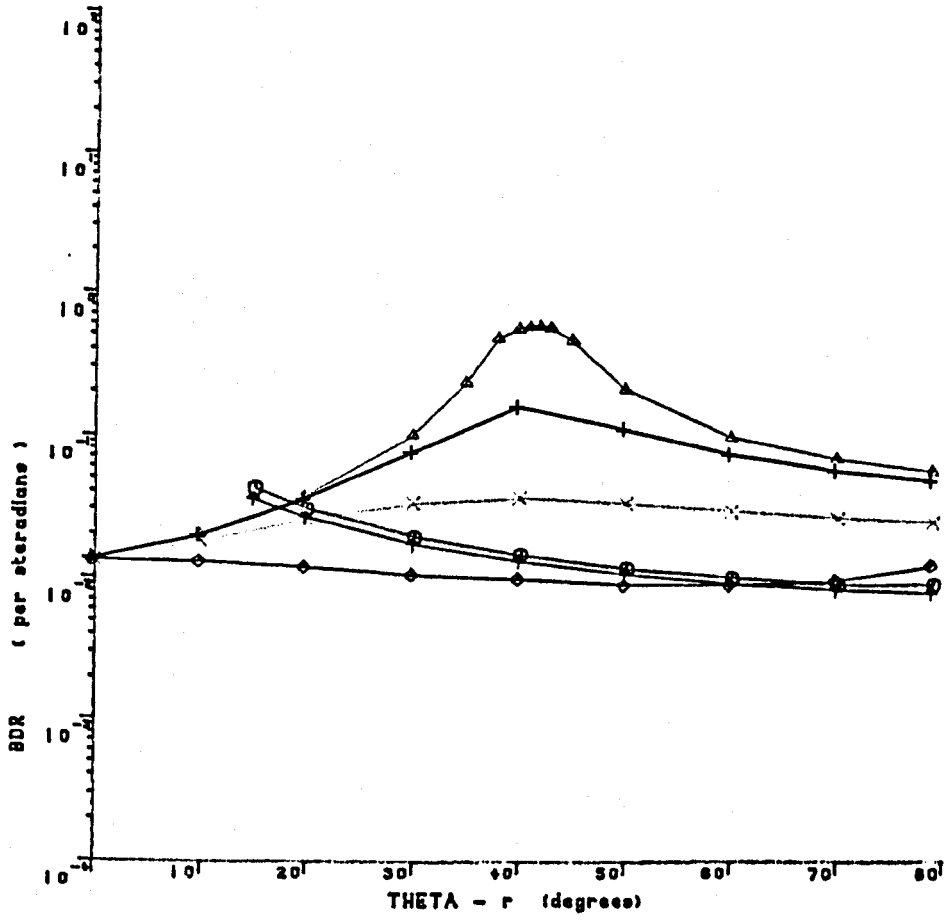

Figure 4.37

spectral BDR of S'COAT-100 sample
632.8 nm
NARROW beam incident on L.H.S. position

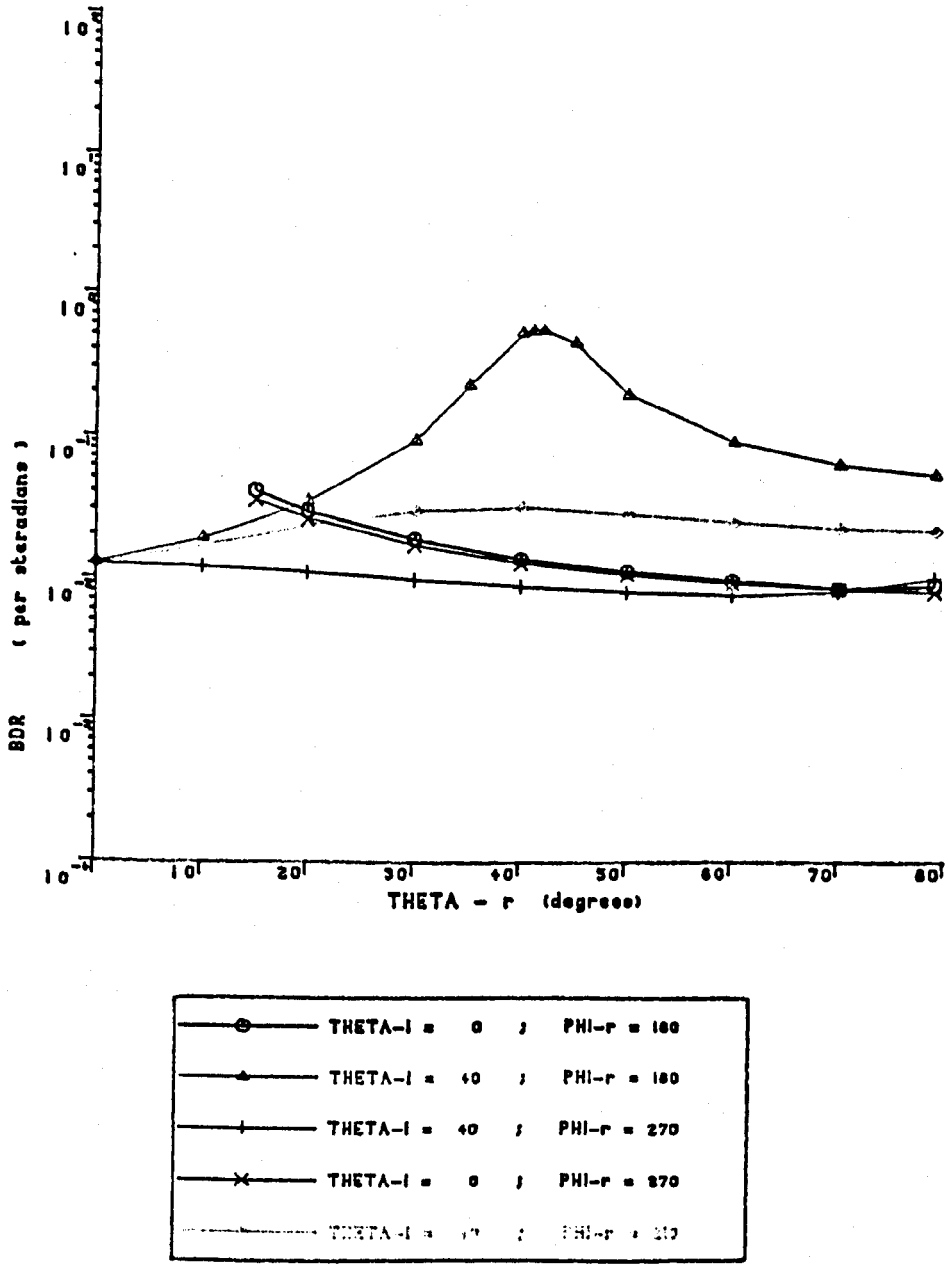

Figure 4.38

spectral BDR of S'COAT-100 sample
632.8 nm
NARROW beam incident on R.H.S. position

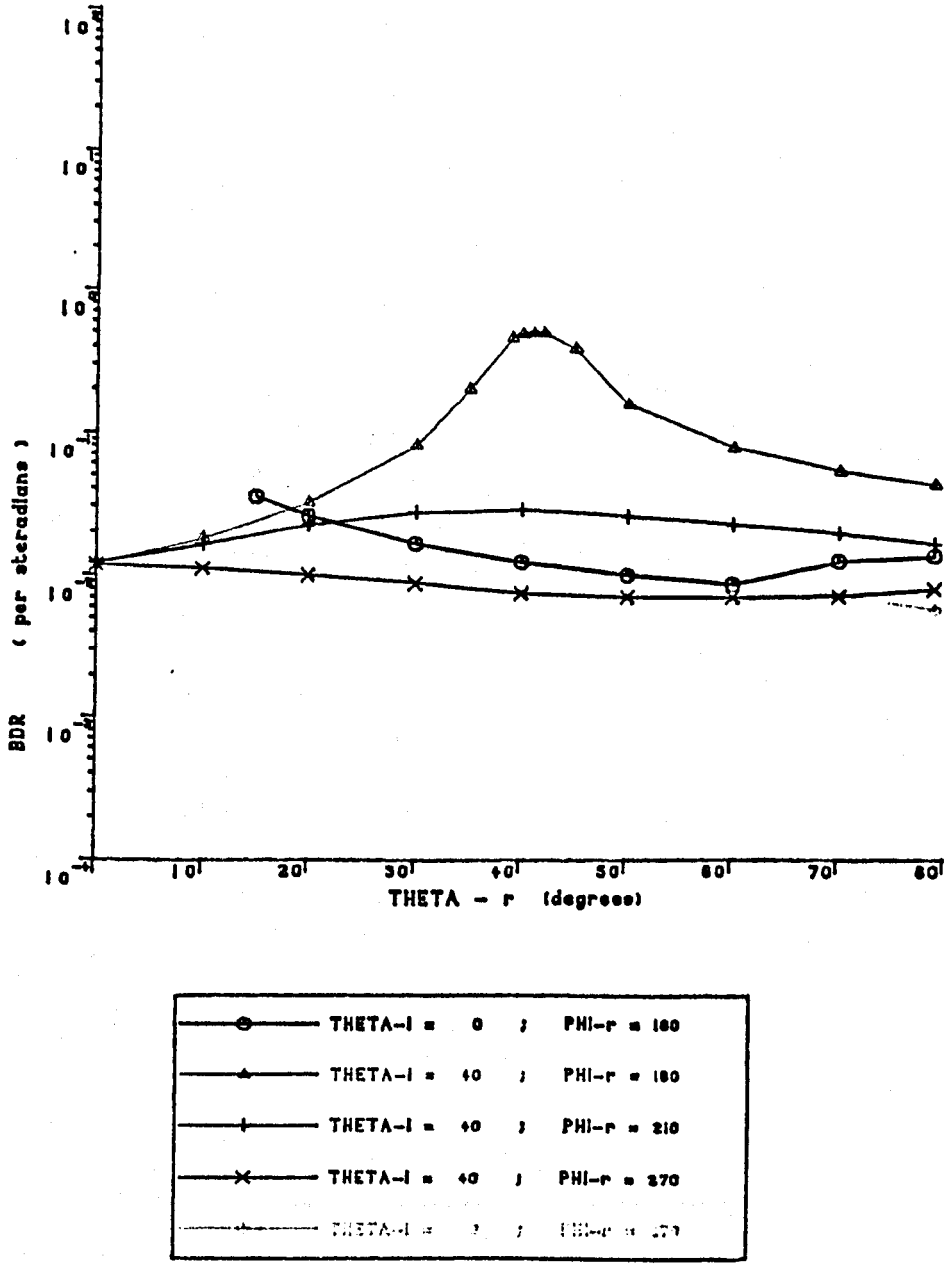

Figure 4.39

spectral BDR of S'COAT-100 sample
632.8 nm
WIDE beam incident on CENTRE position

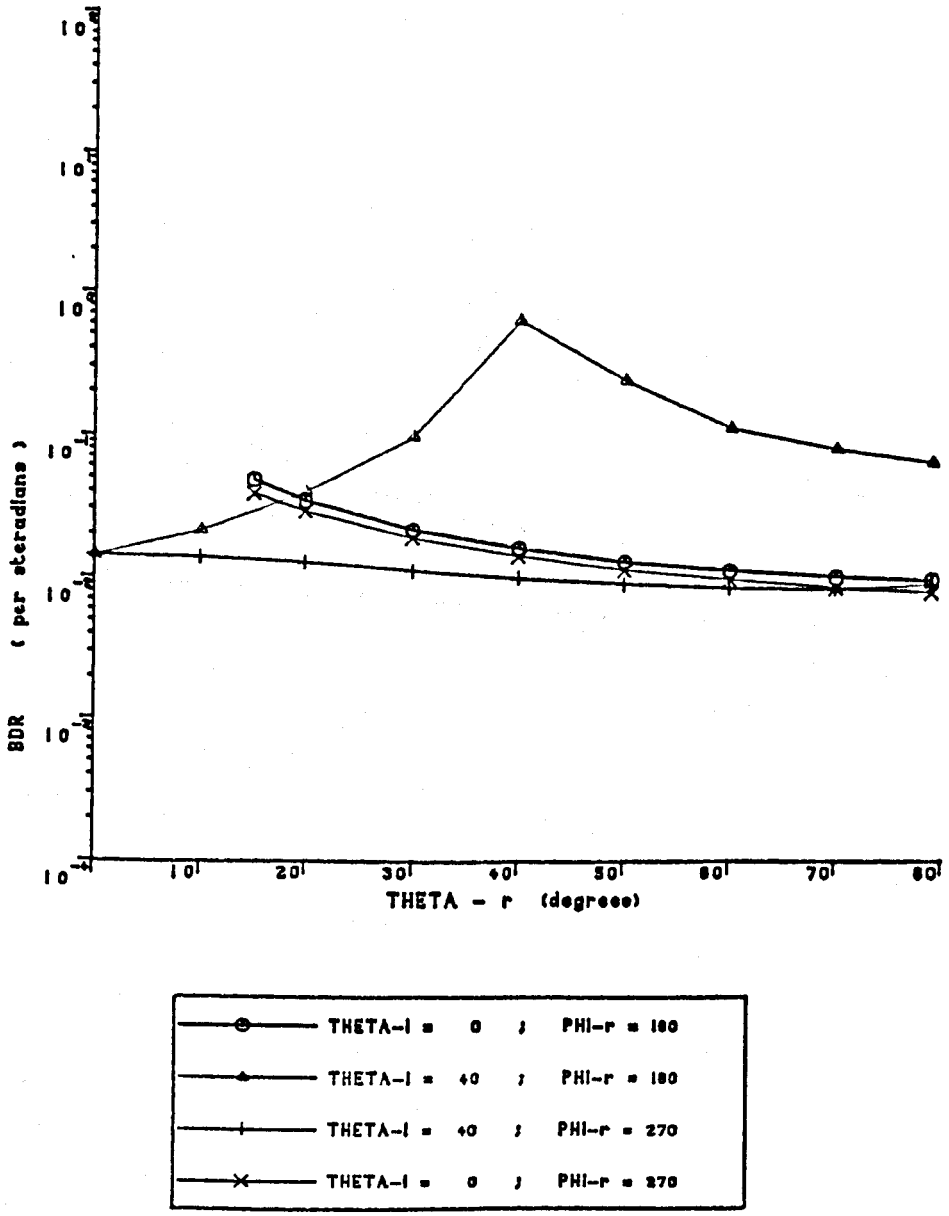

Figure 4.40

spectral BDR of S'COAT-100 sample
1152.3 nm
WIDE beam incident on CENTRE position

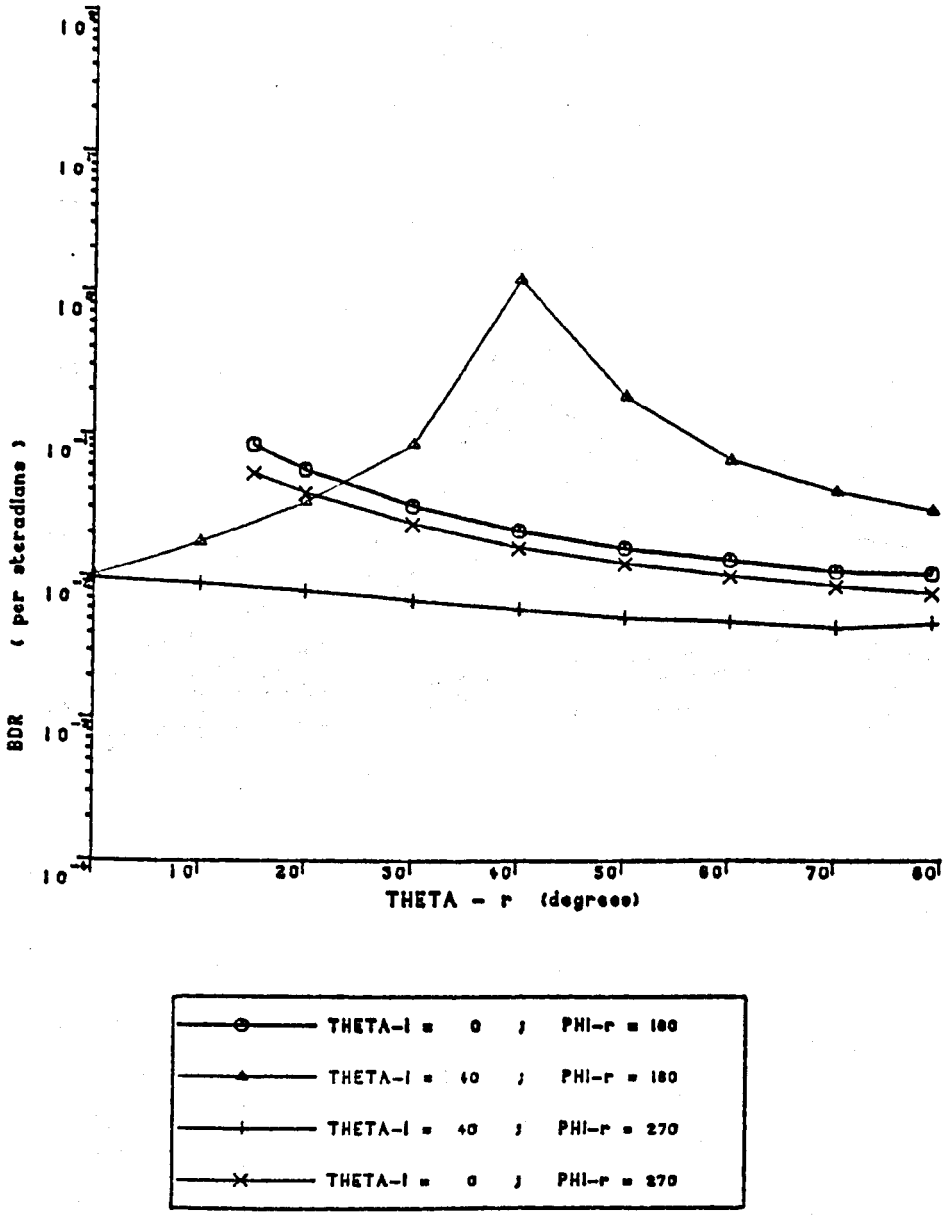

Figure 4.41

633 nm
COMPARISON OF SPECULAR REFLECTANCES
(all curves : THETA-i = 40 deg , PHI-r = 180 deg)
wide beam

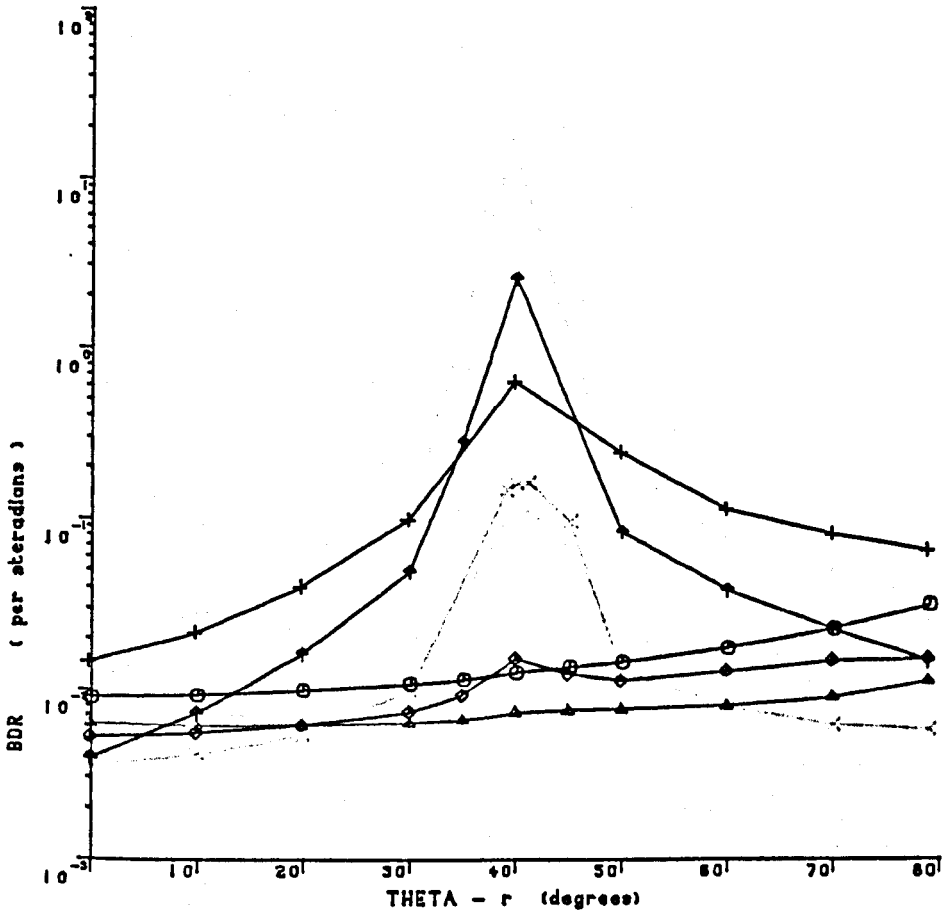

Figure 4.42

1152 nm
COMPARISON OF SPECULAR REFLECTANCES
(all curves : THETA-i = 40 deg , PHI-r = 180 deg)

wide beam

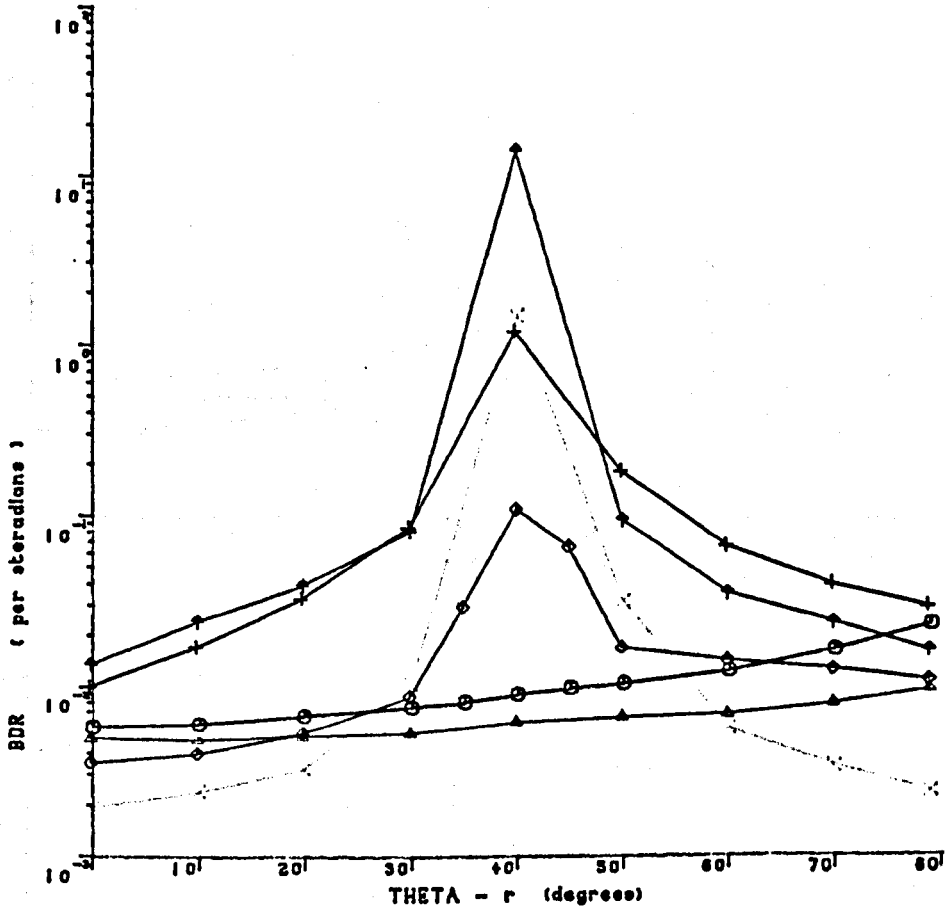

FIGURE 4.43

NEXTEL

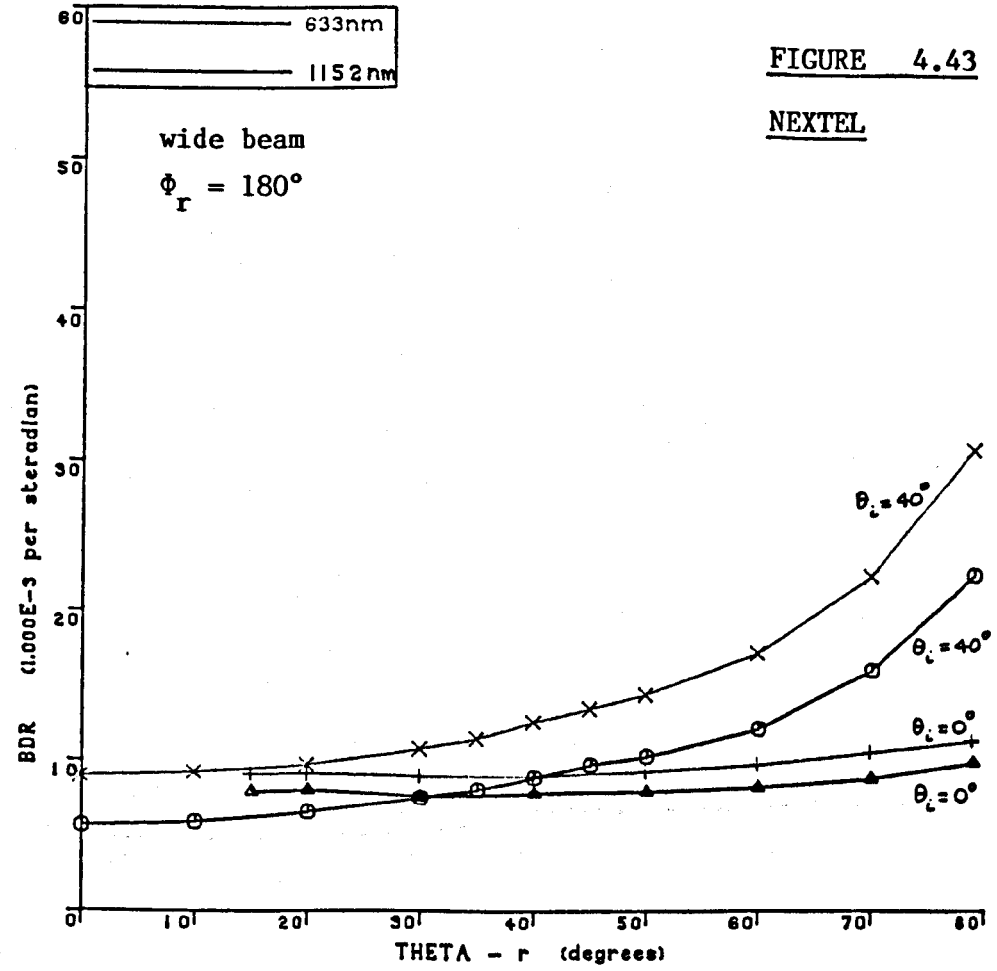

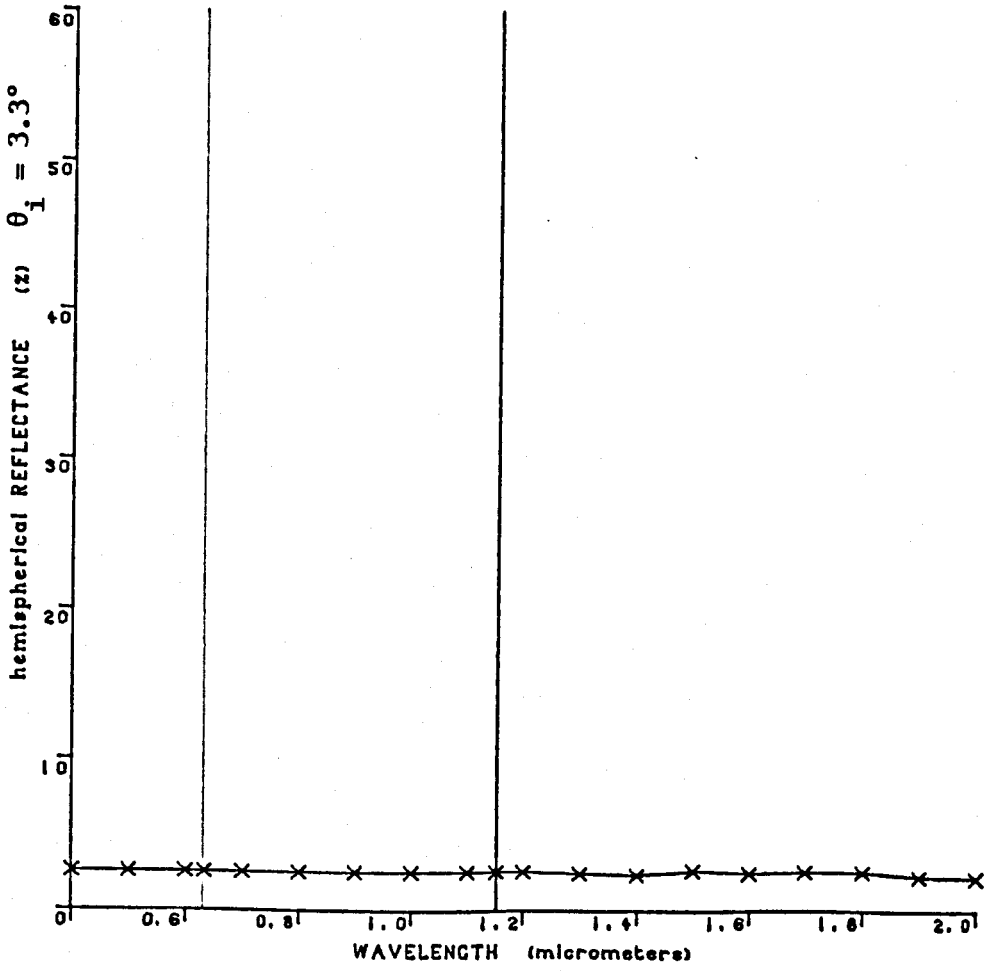

FIGURE 4.44

SOLARCOAT - 50

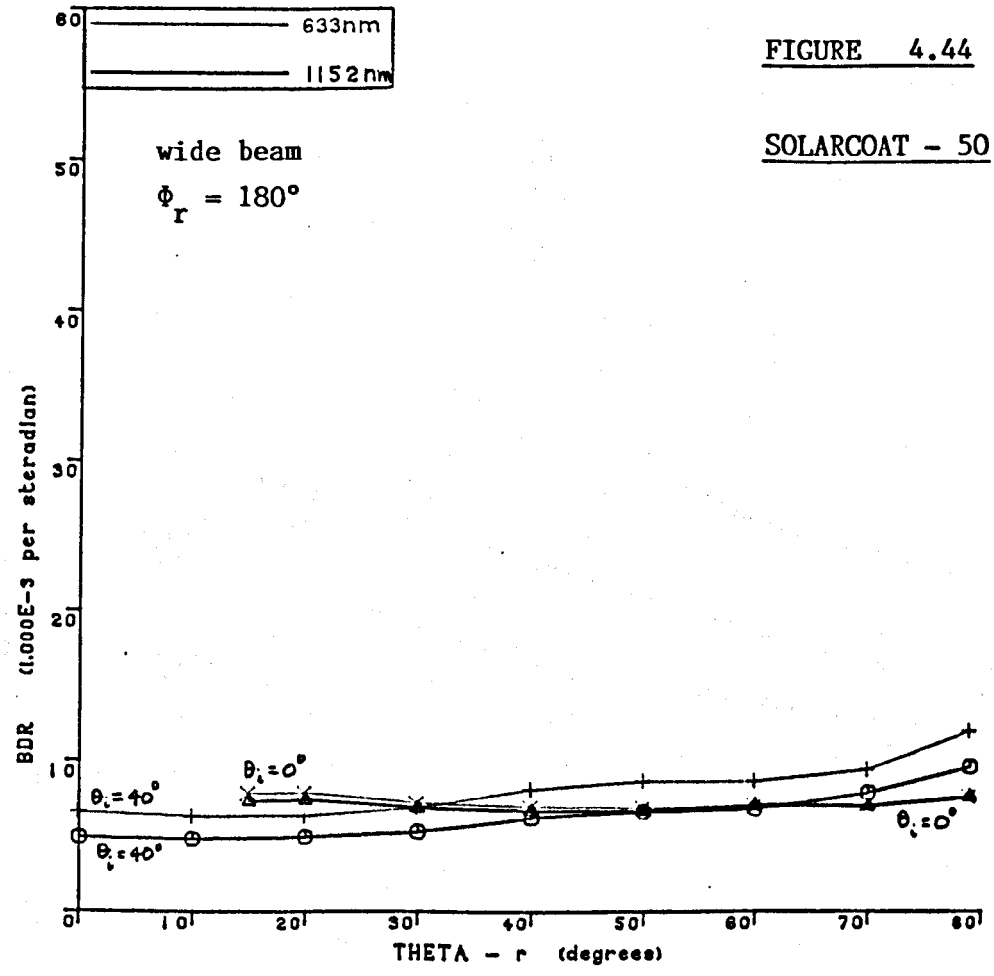

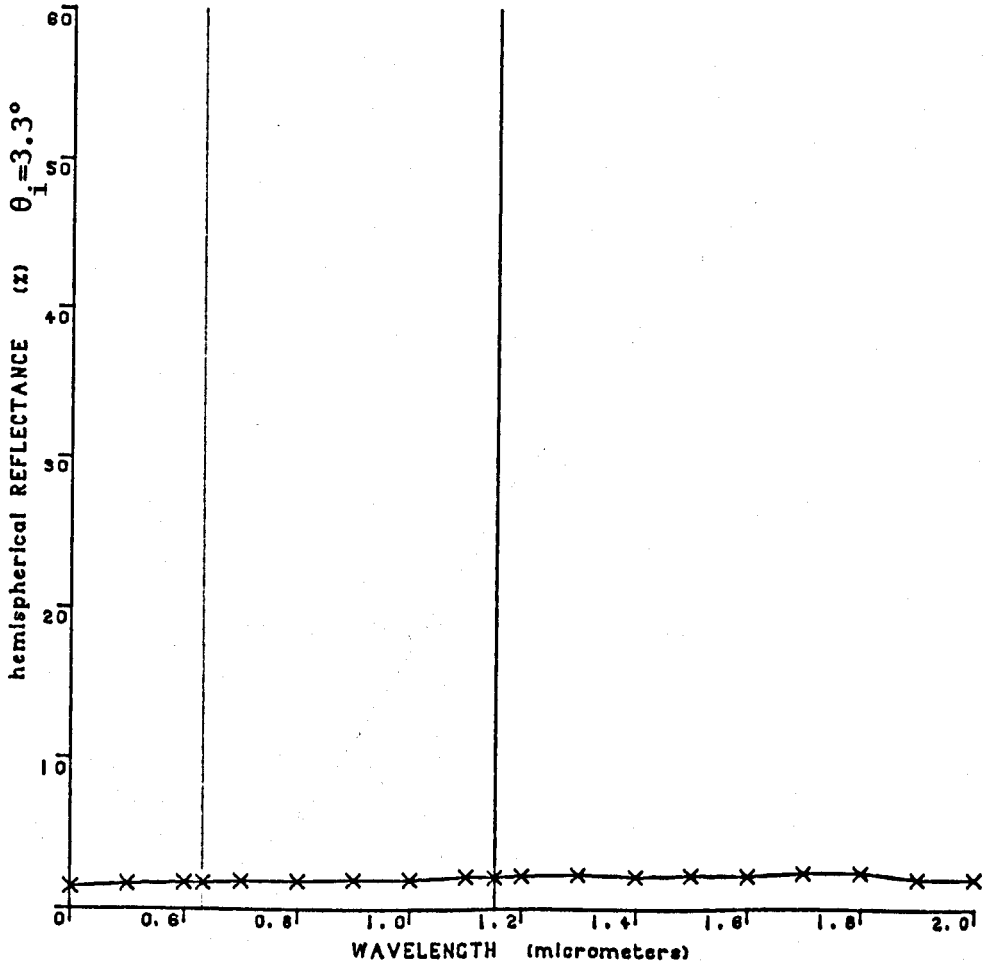

FIGURE 4.45

SKYSORB

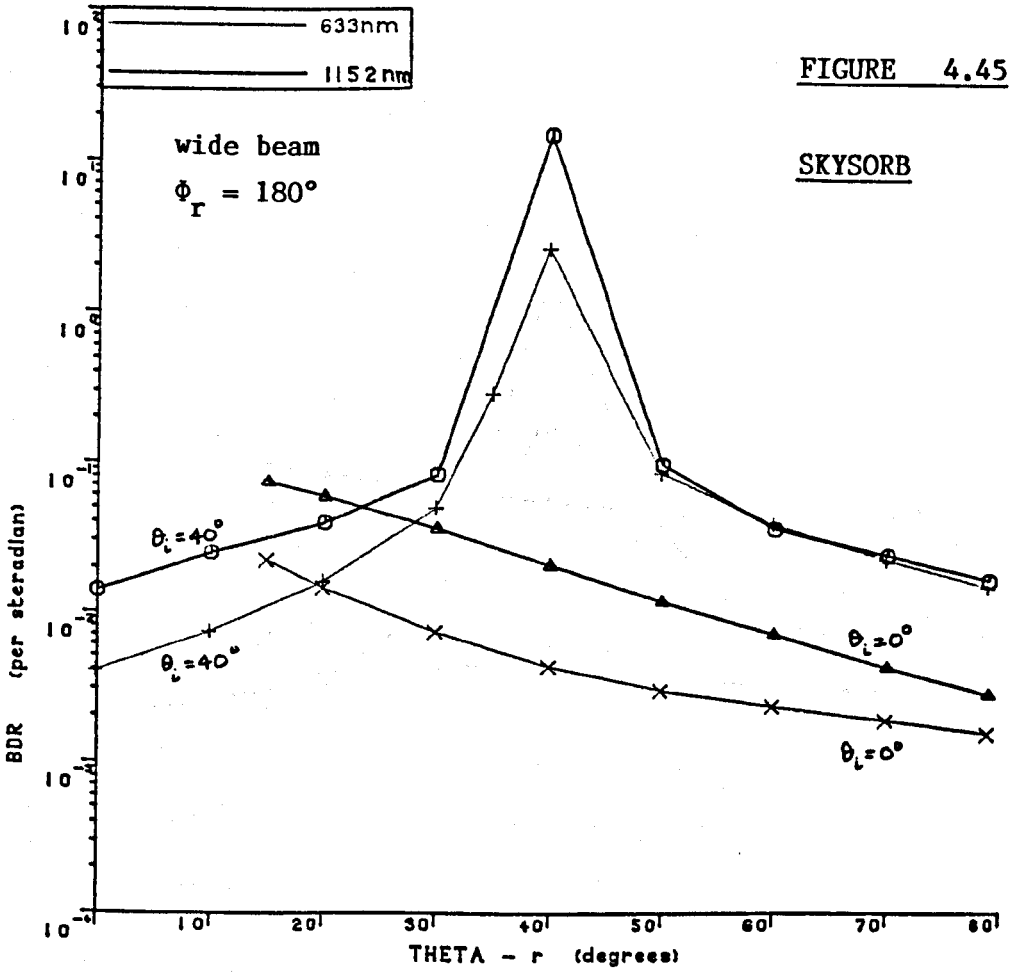

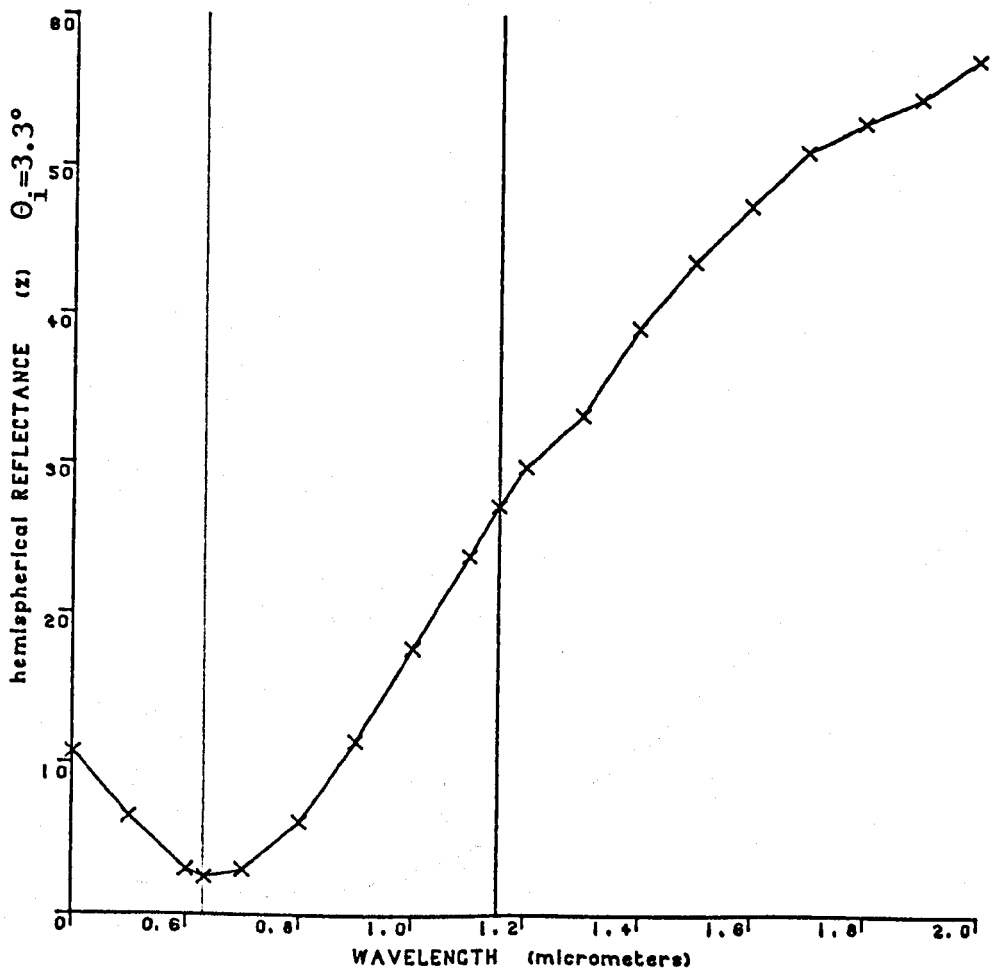

FIGURE 4.46

MAXORB

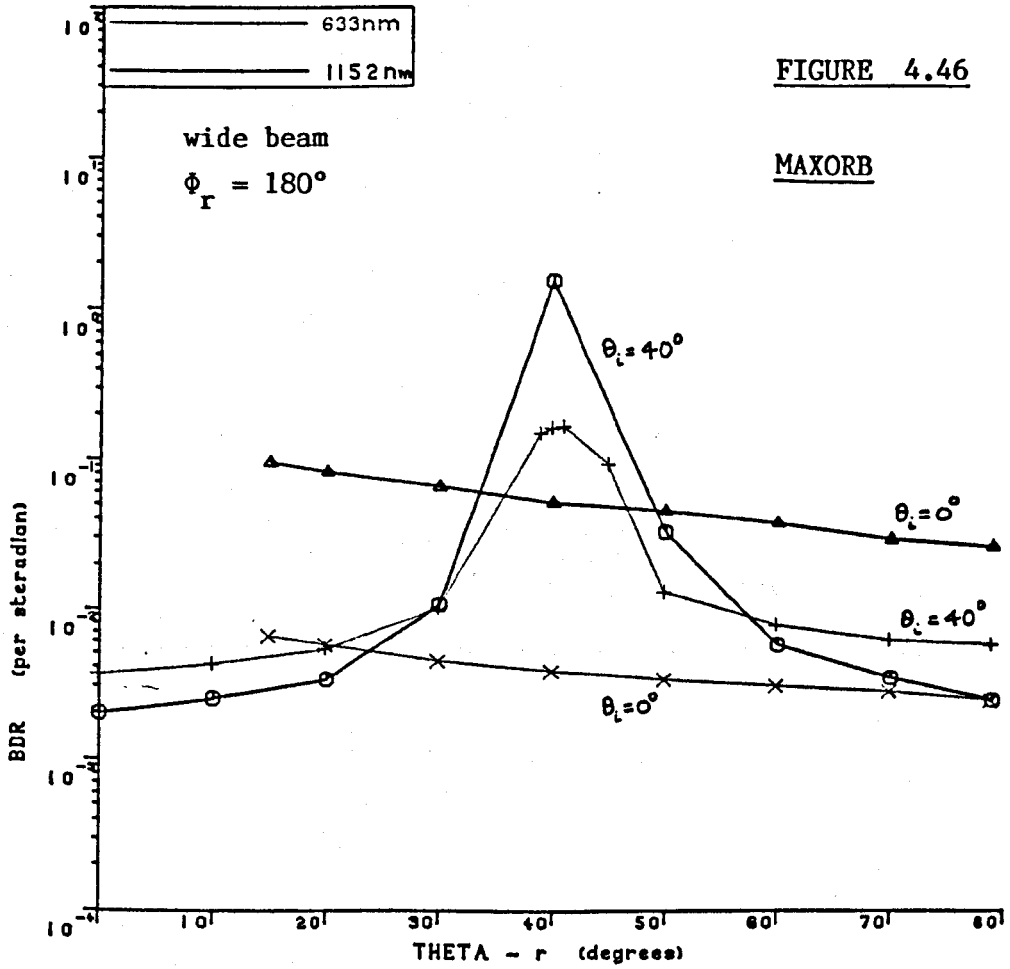

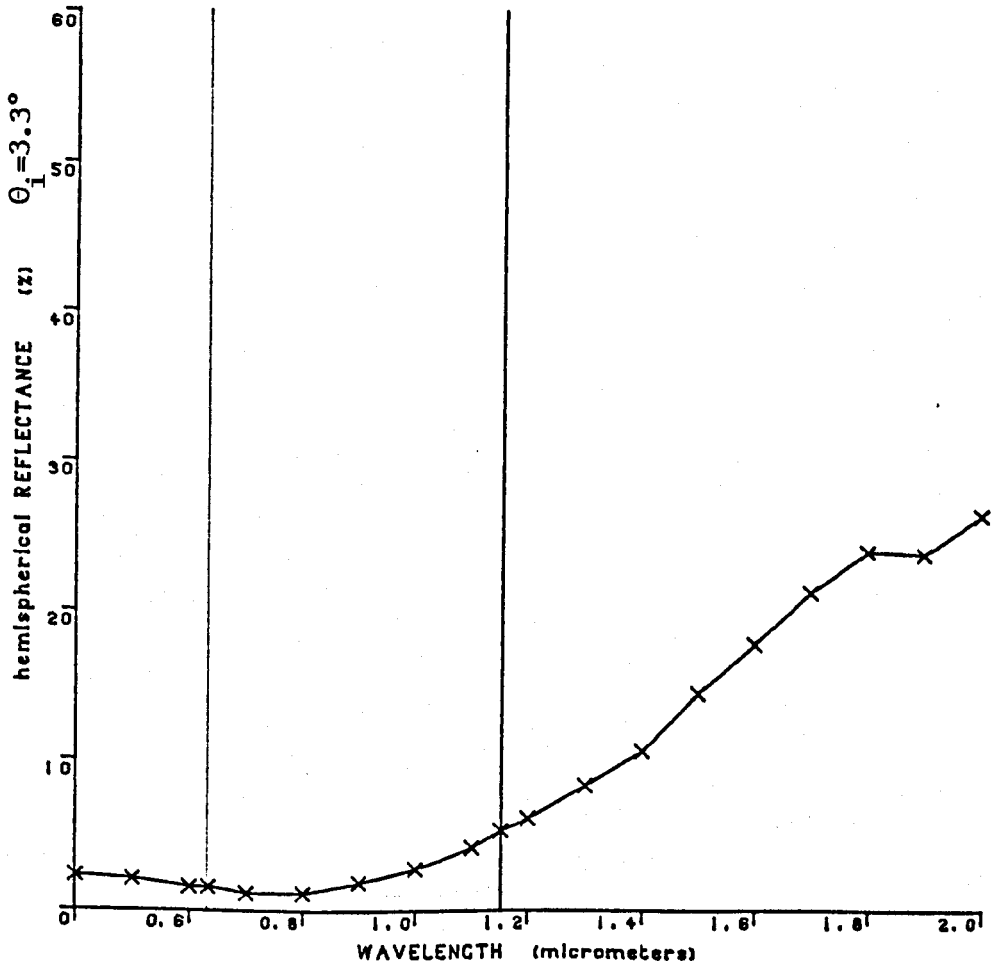

FIGURE 4.47

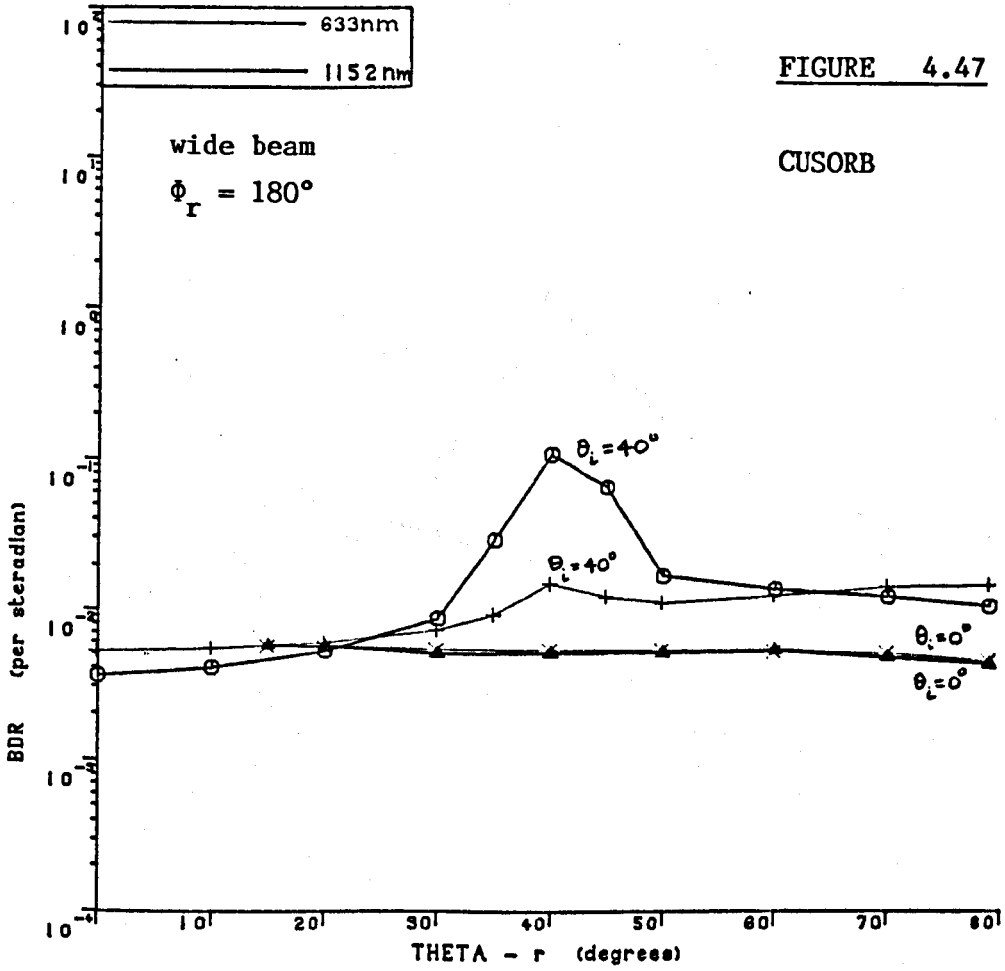
633nm
1152nm
wide beam
Φ_r = 180°
CUSORB
θ_i=40°
θ_i=40°
θ_i=0°
θ_i=0°
BDR (per steradian)
THETA - r (degrees)

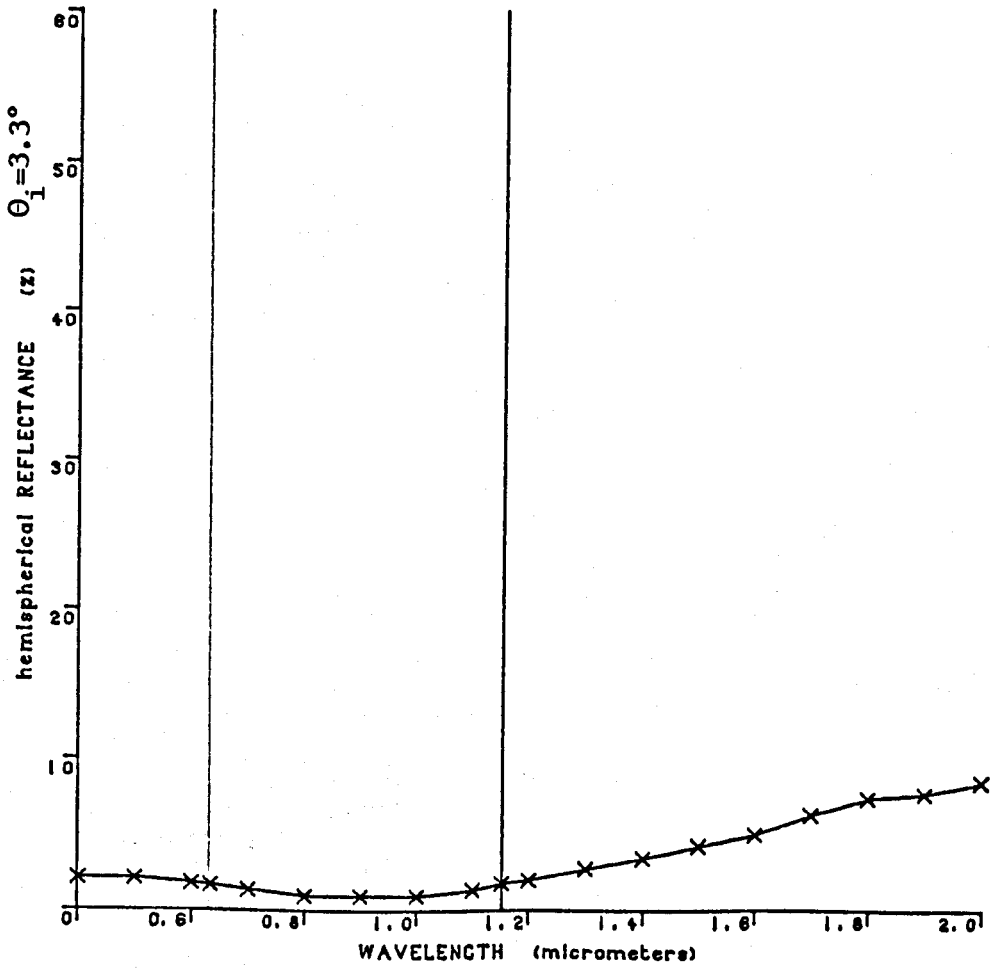
θ_i=3.3°
hemispherical REFLECTANCE (%)
WAVELENGTH (micrometers)

FIGURE 4.48

SOLARCOAT - 100

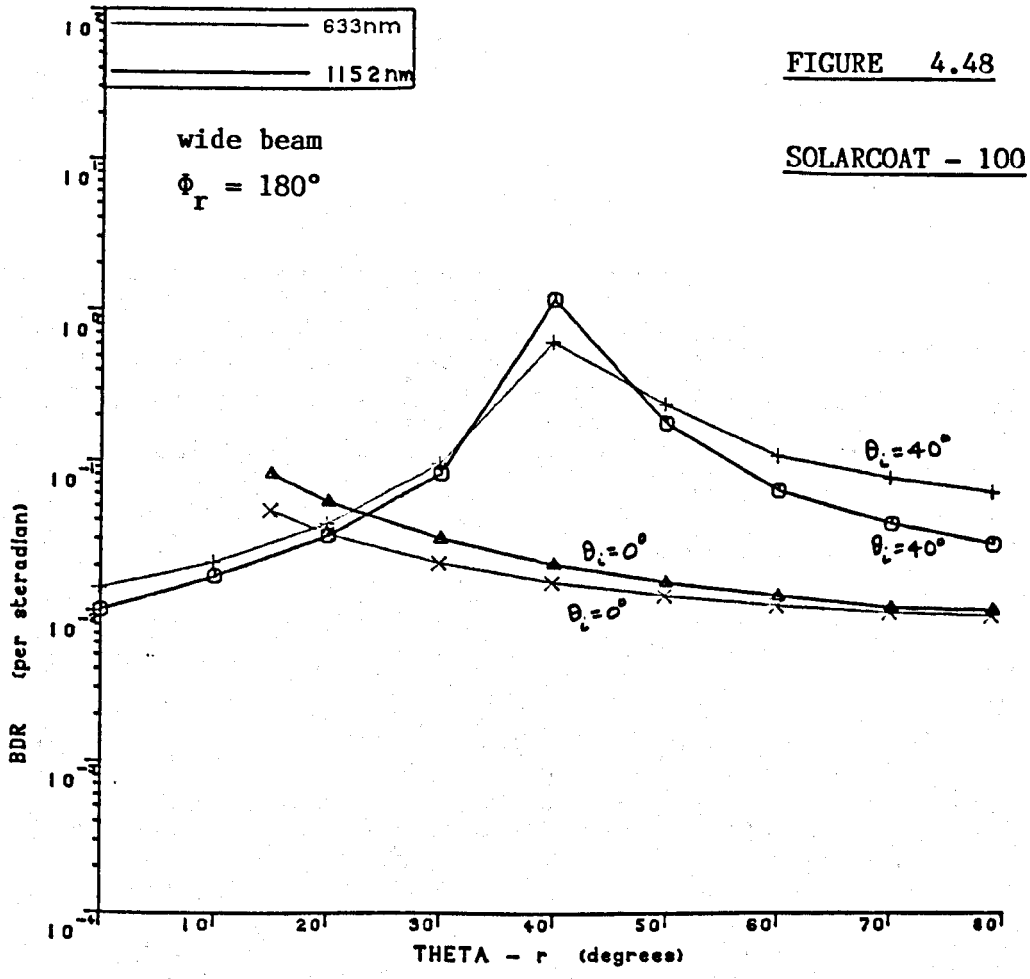

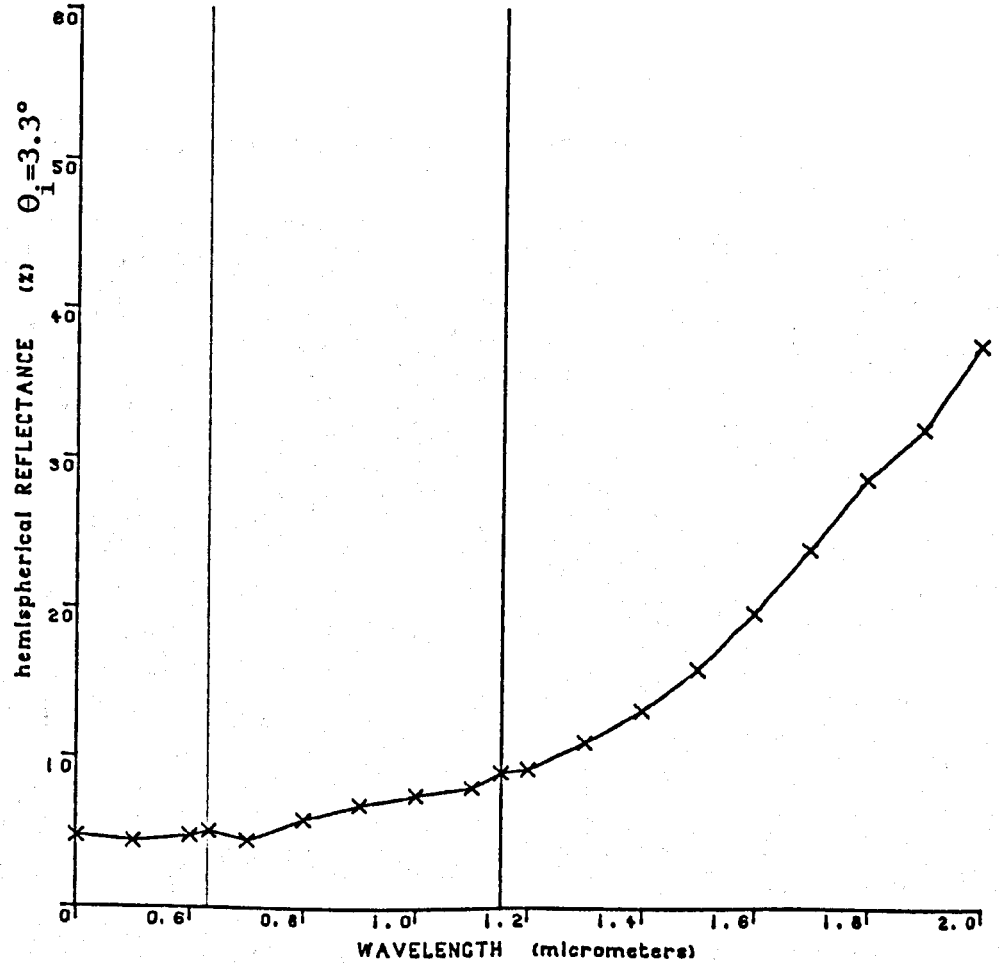

SEM'S of NEXTEL FIGURE 4.49

magnification = 320 , tilt angle = 20° scale marker = 10 μ

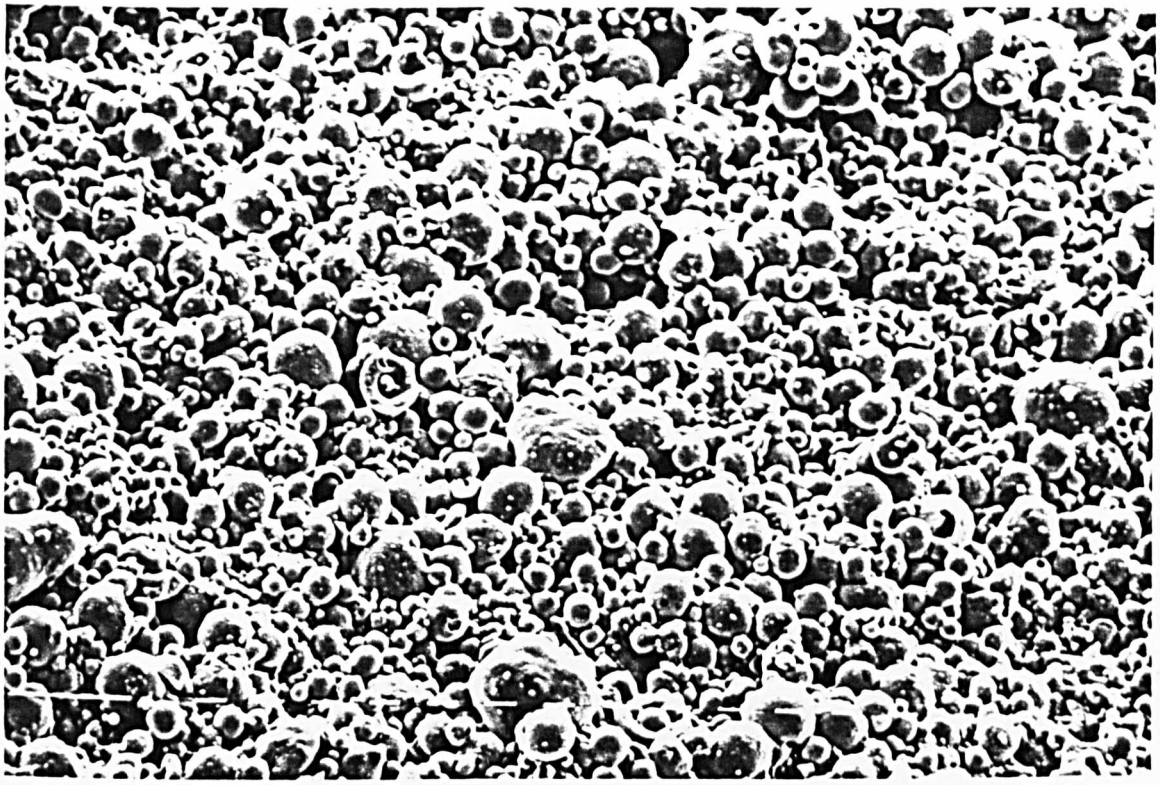

magnification = 1250 , tilt angle = 0° scale marker = 10 μ

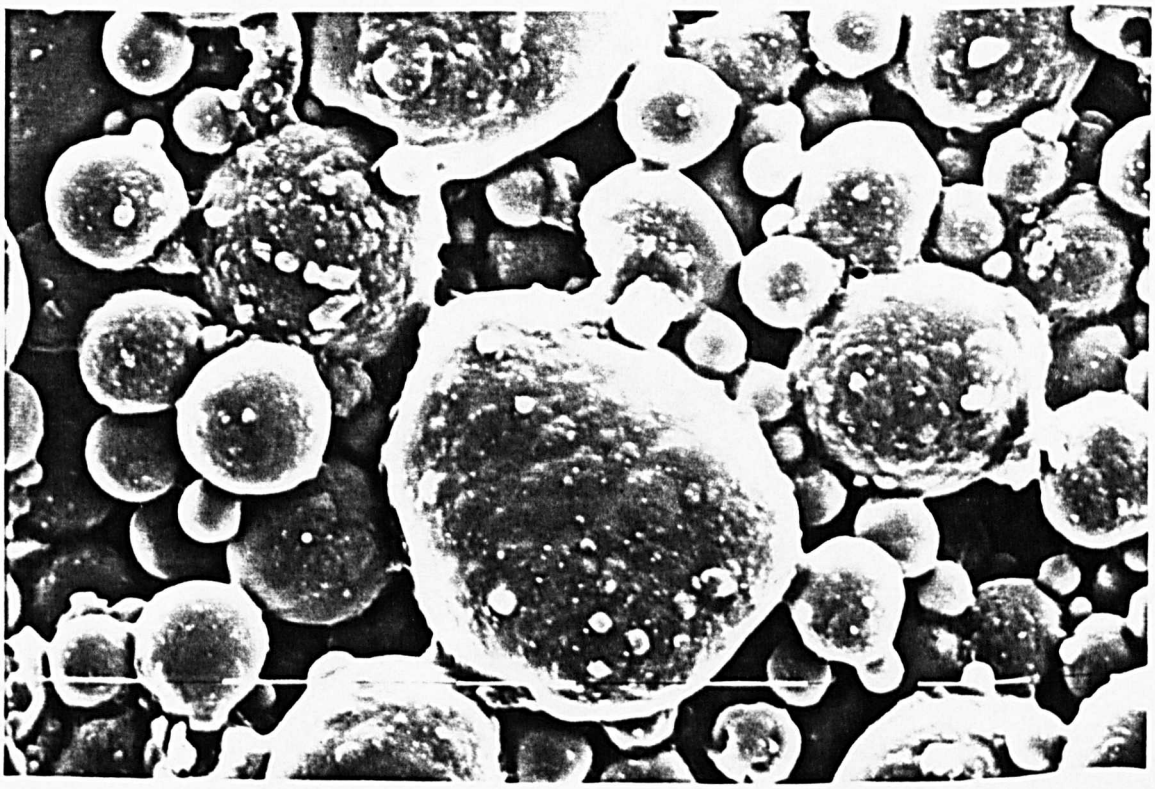

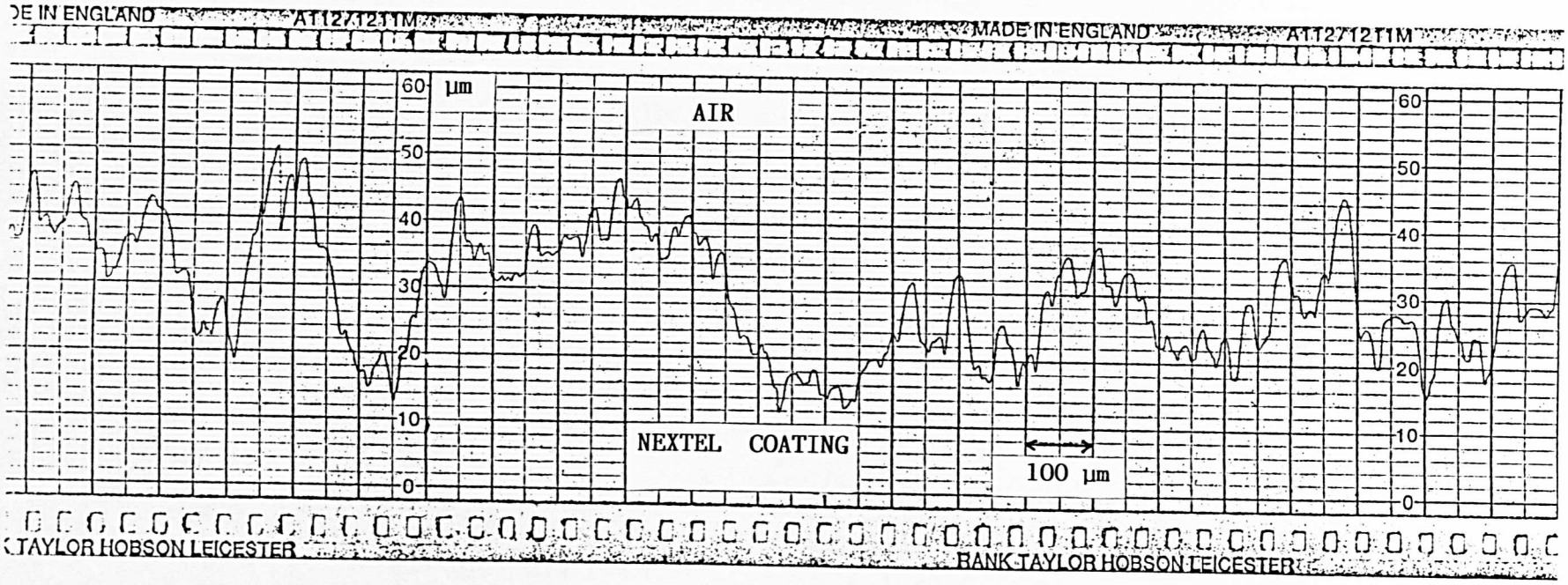

TYPICAL SURFACE ROUGHNESS OF NEXTEL SAMPLE

FIGURE 4.50

SEM'S of SOLARCOAT - 50 FIGURE 4.51

magnification = 80 , tilt angle = 40° scale marker = 100 μ

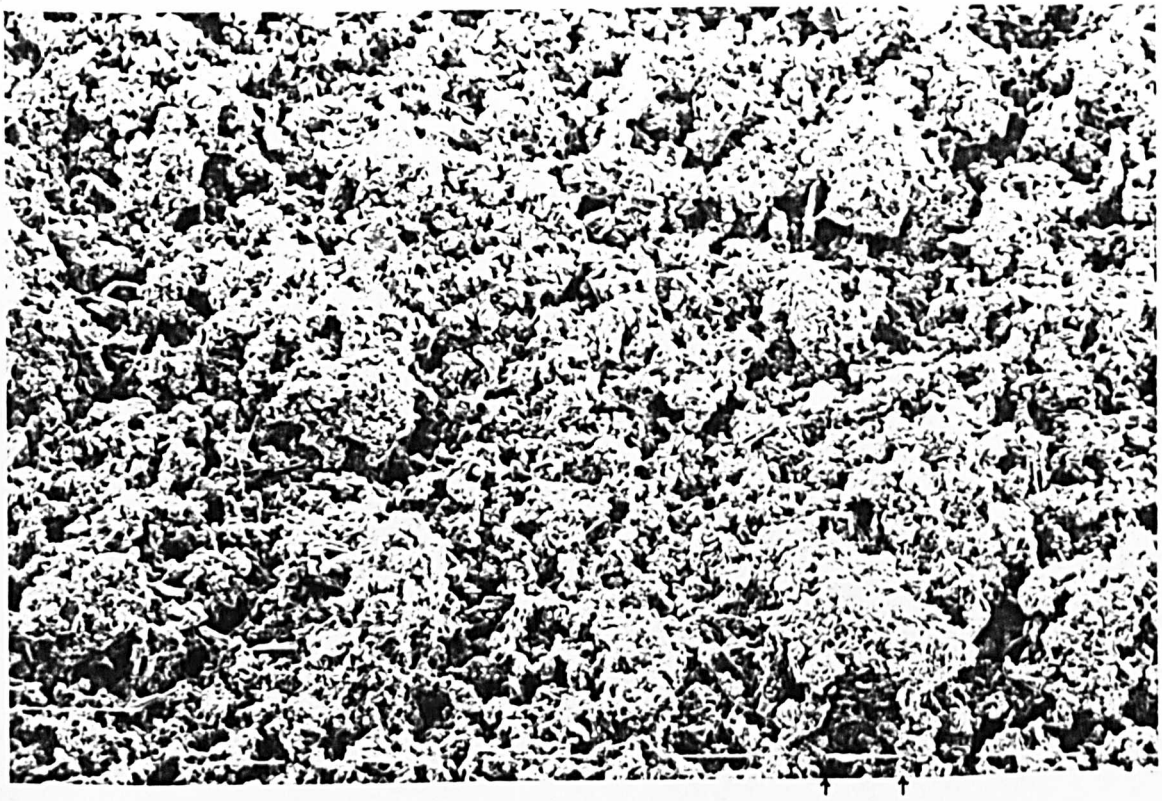

magnification = 320 , tilt angle = 40° scale marker = 10 μ

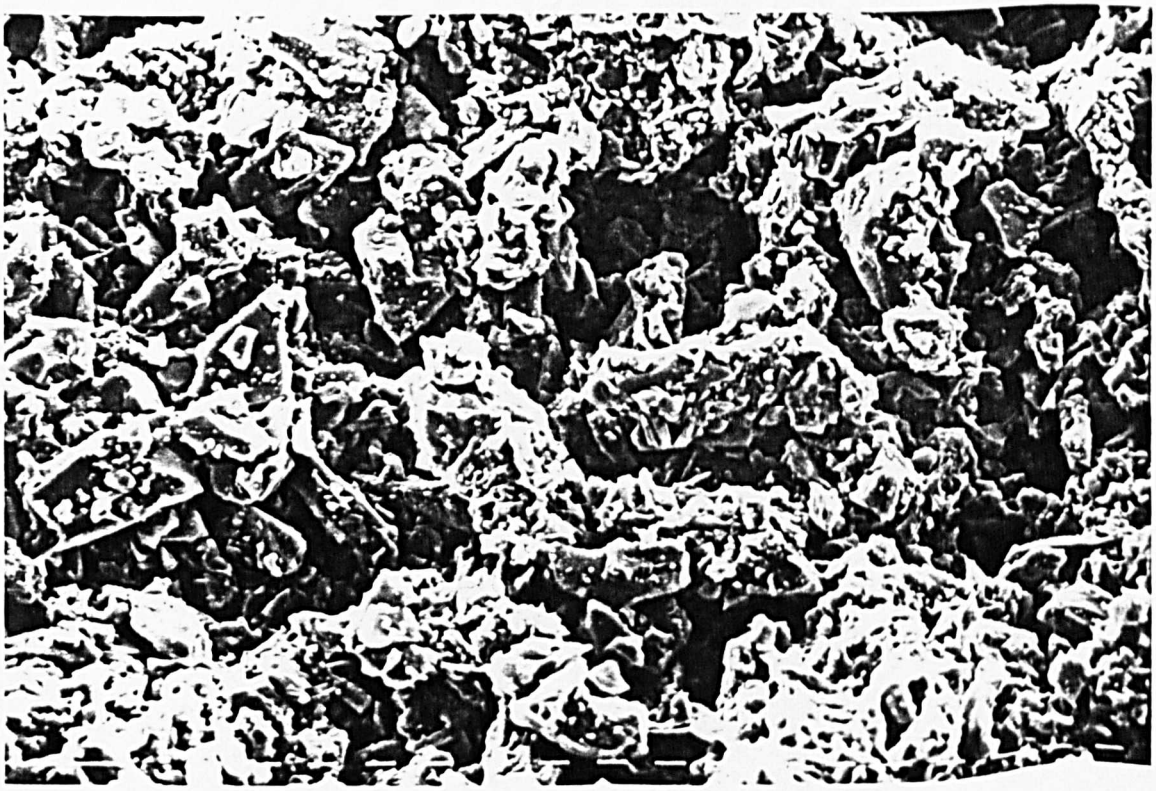

FIGURE 4.52

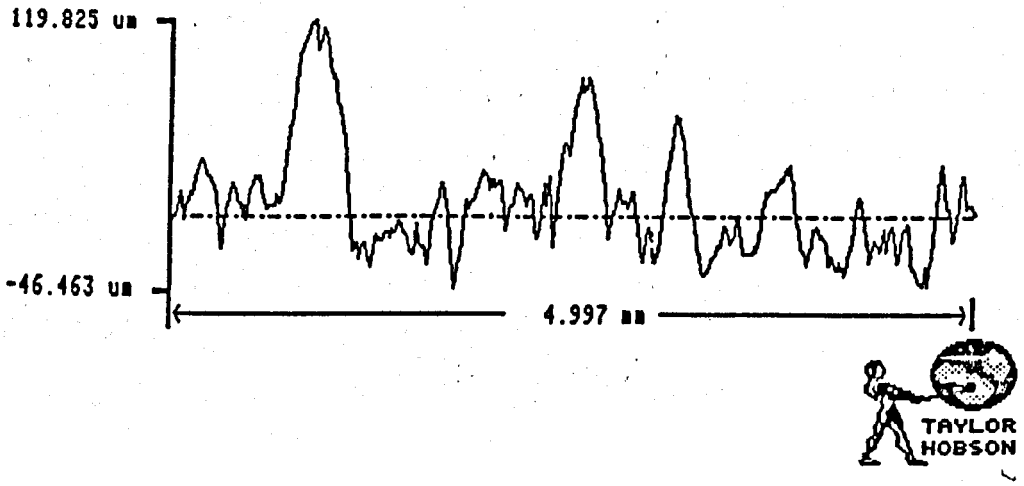

TYPICAL SURFACE ROUGHNESS OF SOLARCOAT - 50 SAMPLE

SEM'S of SKYSORB FIGURE 4.53

magnification = 2500 , tilt angle = 40° scale marker = 1 μ

magnification = 10,000 , tilt angle = 40° scale marker = 1 μ

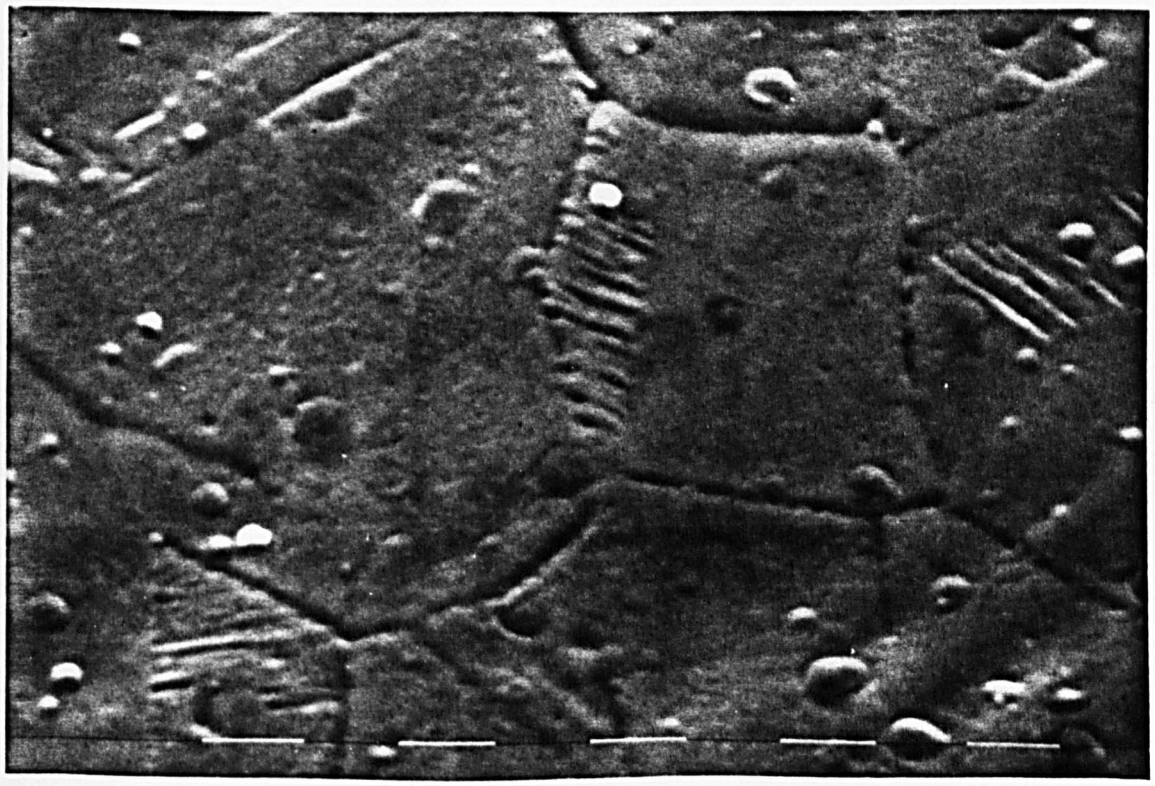

FIGURE 4.54

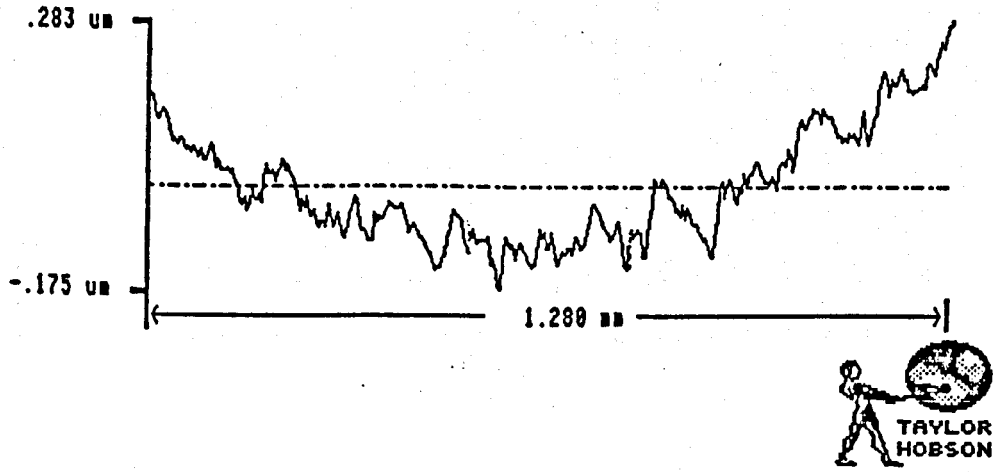

TYPICAL SURFACE ROUGHNESS OF SKYSORB SAMPLE

SEM'S of MAXORB

FIGURE 4.55

magnification = 1250 , tilt angle = 0° scale marker = 10 μ

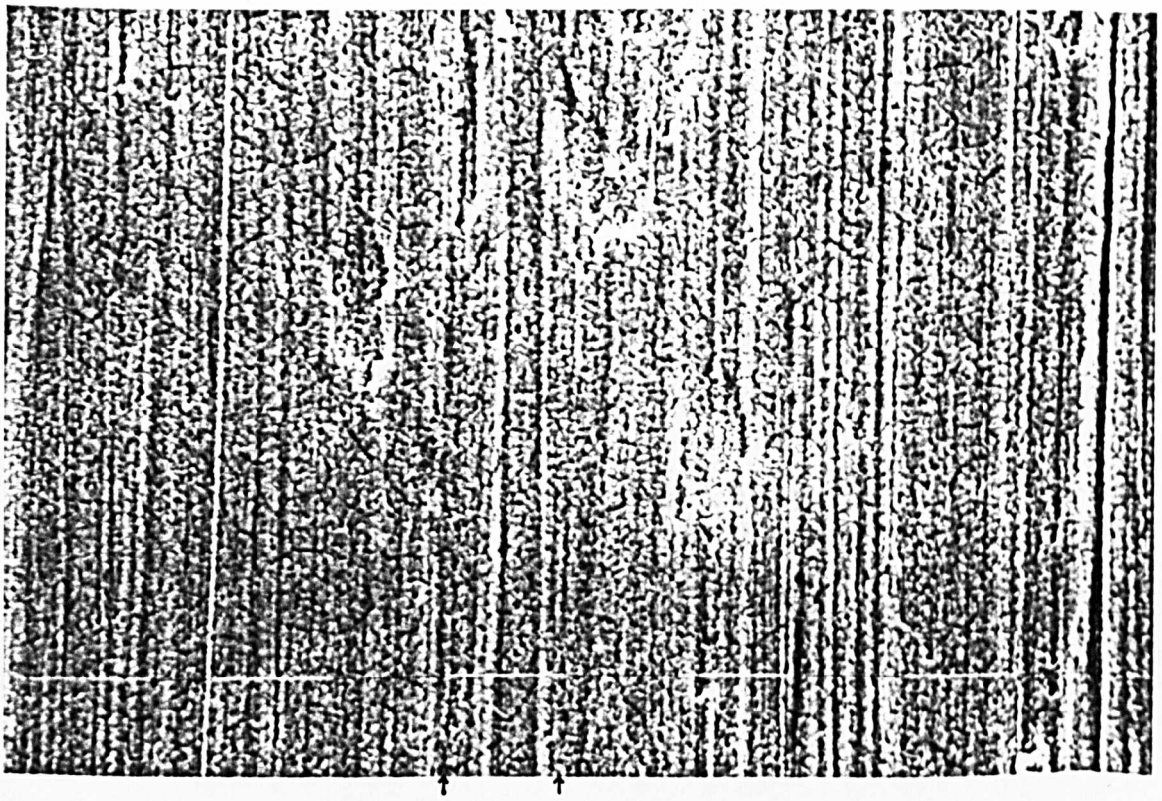

magnification = 10,000 , tilt angle = 40° scale marker = 1 μ

FIGURE 4.56

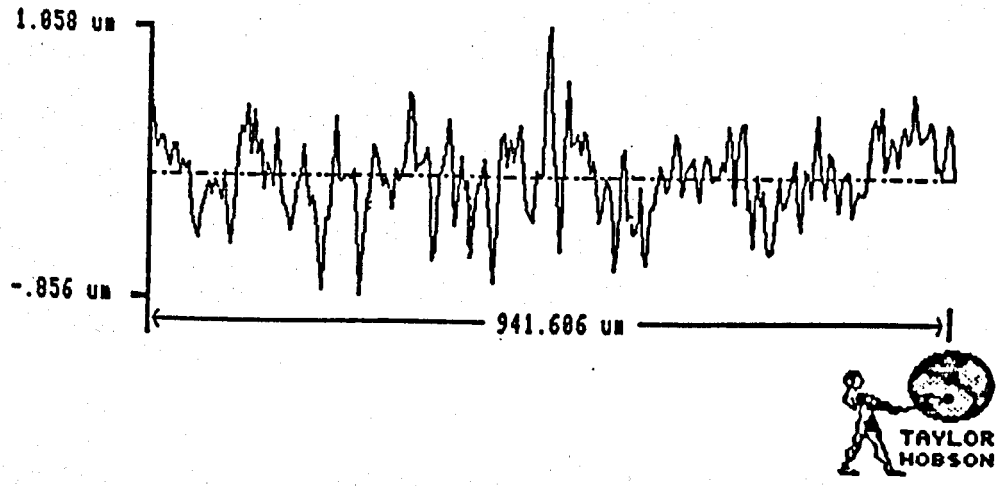

TYPICAL SURFACE ROUGHNESS OF MAXORB SAMPLE

SEM'S of CUSORB

FIGURE 4.57

magnification = 320 , tilt angle = 40° scale marker = 10 μ

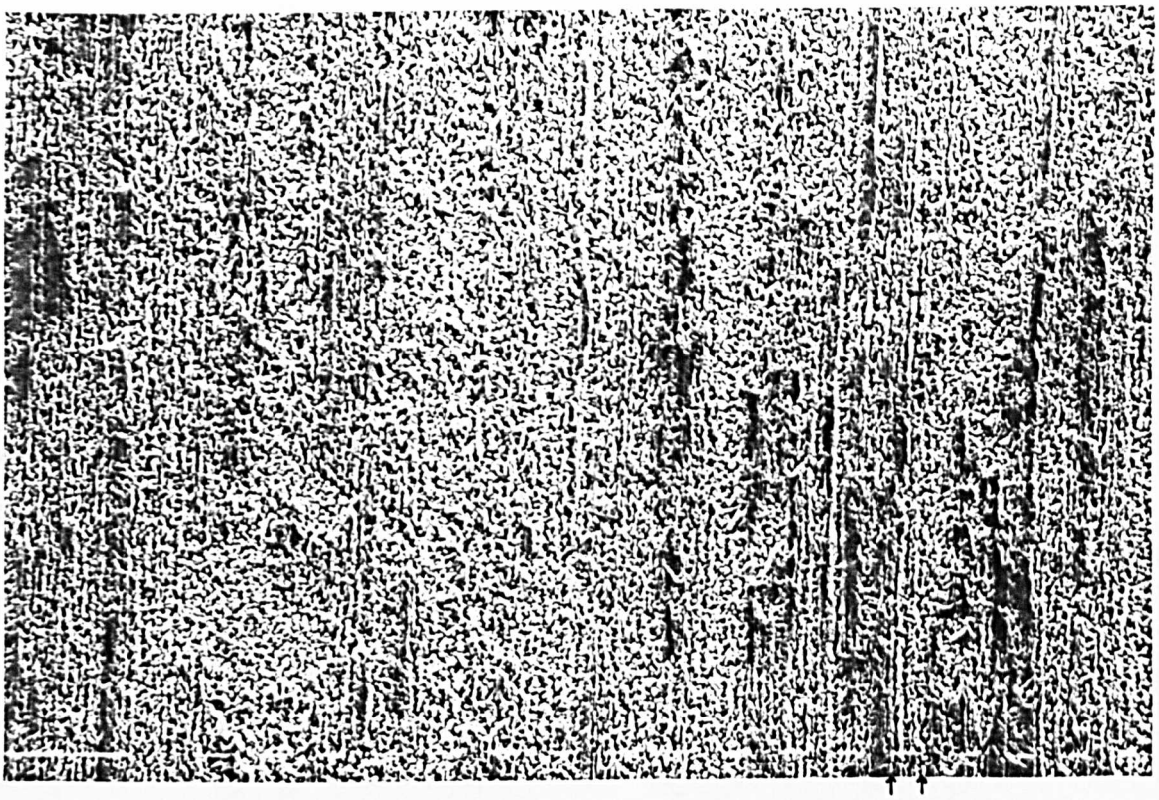

magnification = 2500 , tilt angle = 40° scale marker = 10 μ

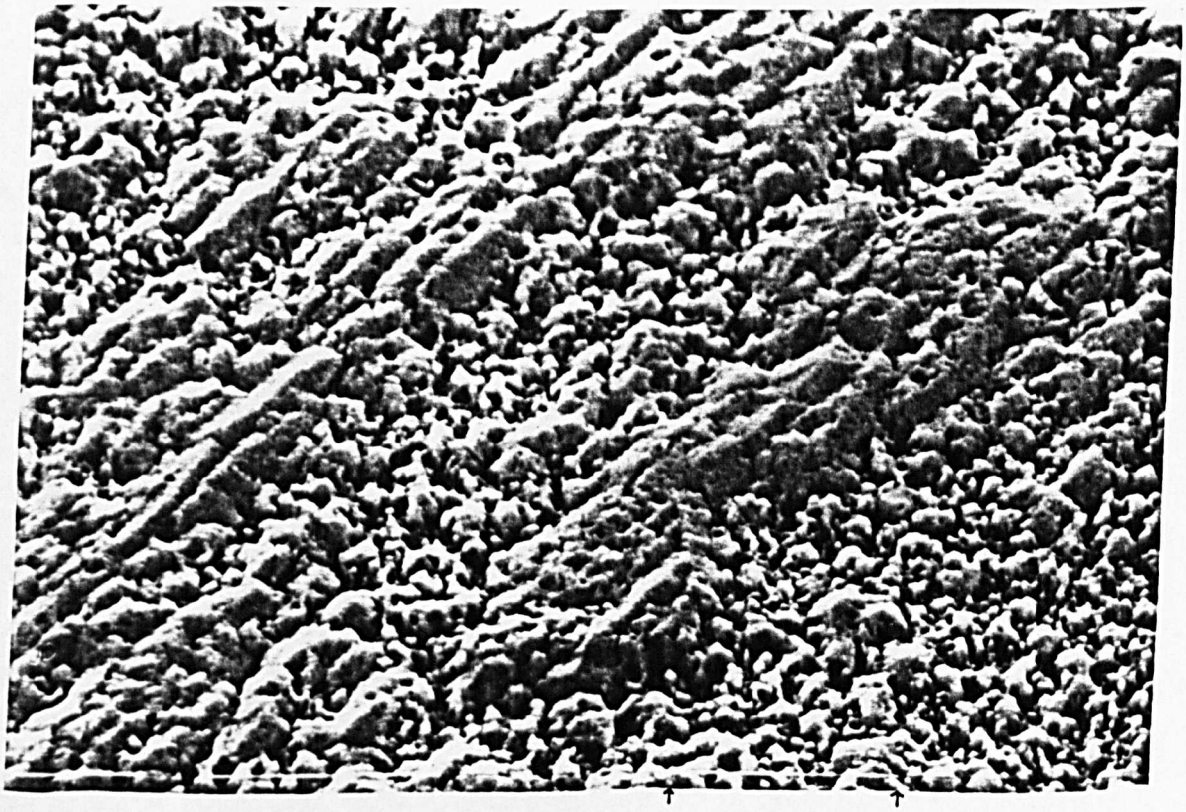

FIGURE 4.58

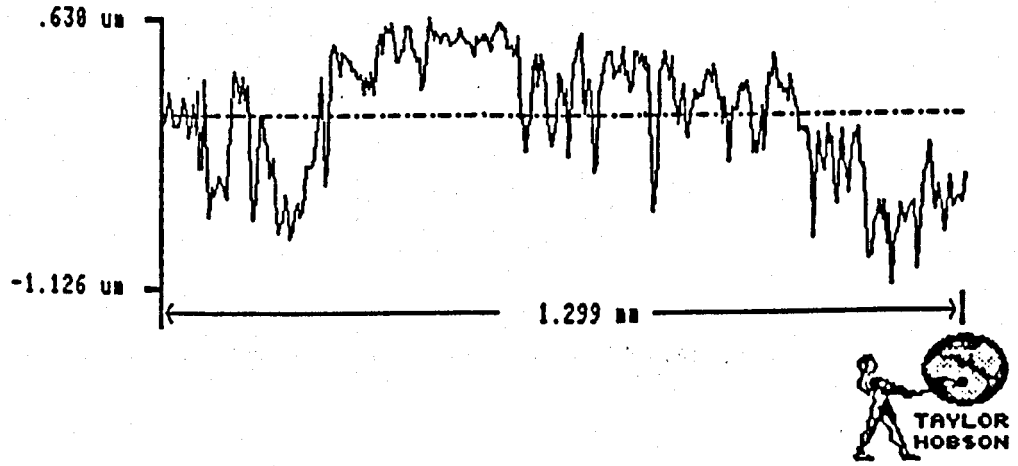

TYPICAL SURFACE ROUGHNESS OF CUSORB SAMPLE

SEM'S of SOLARCOAT - 100 FIGURE 4.59

magnification = 40 , tilt angle = 0° scale marker = 100 μ

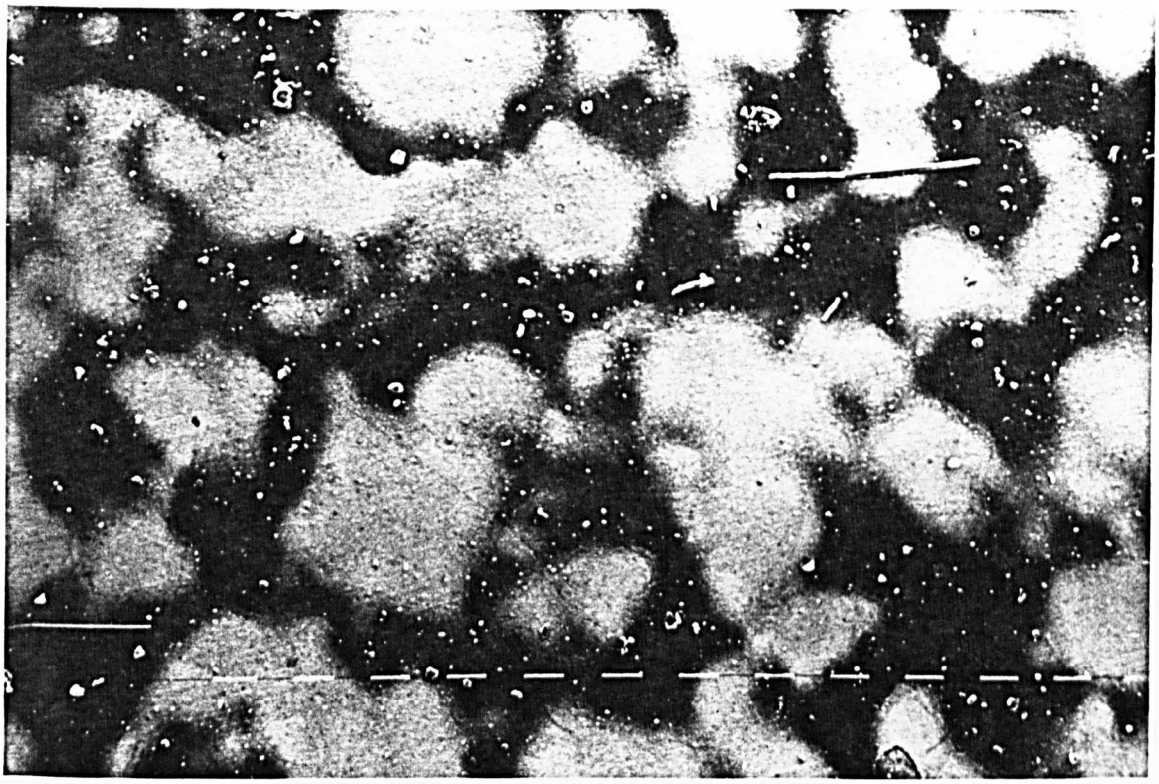

magnification = 1250 , tilt angle = 40° scale marker = 10 μ

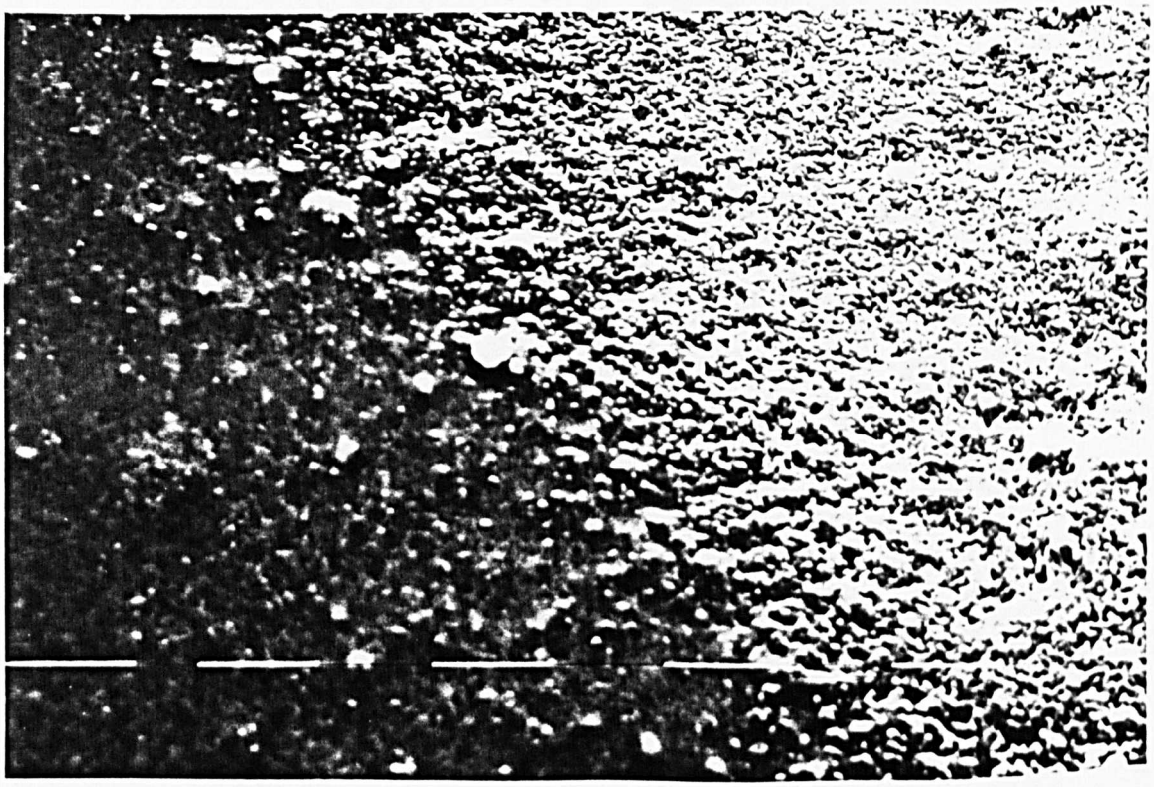

FIGURE 4.60

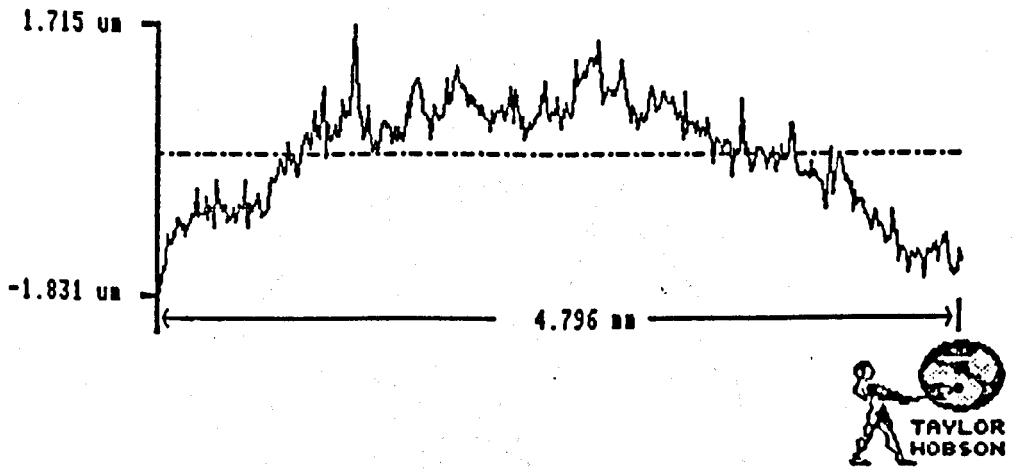

TYPICAL SURFACE ROUGHNESS OF SOLARCOAT - 100 SAMPLE

FIGURE A1.1

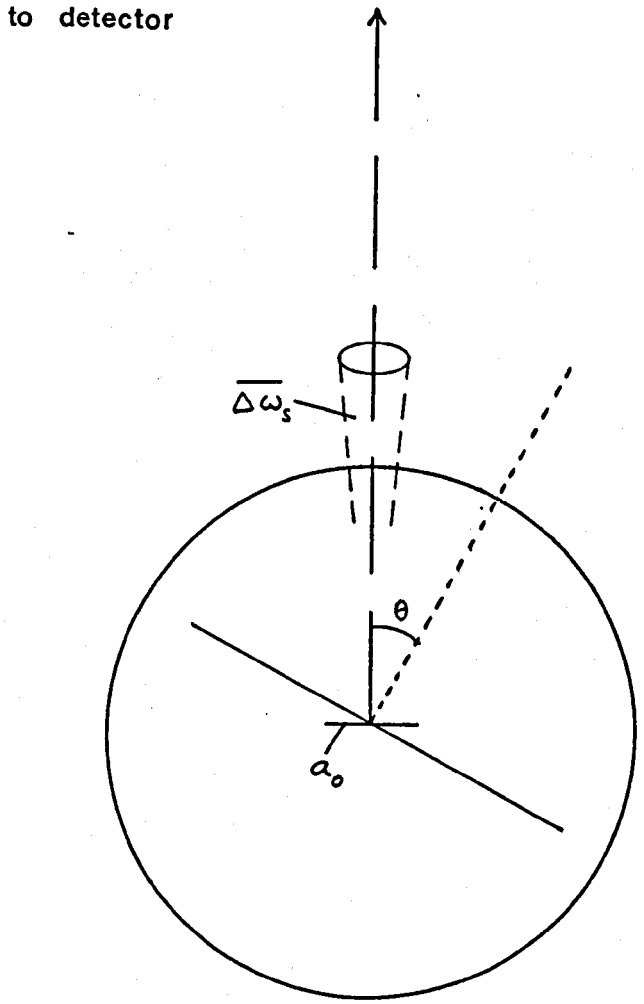

FIGURE A1.2

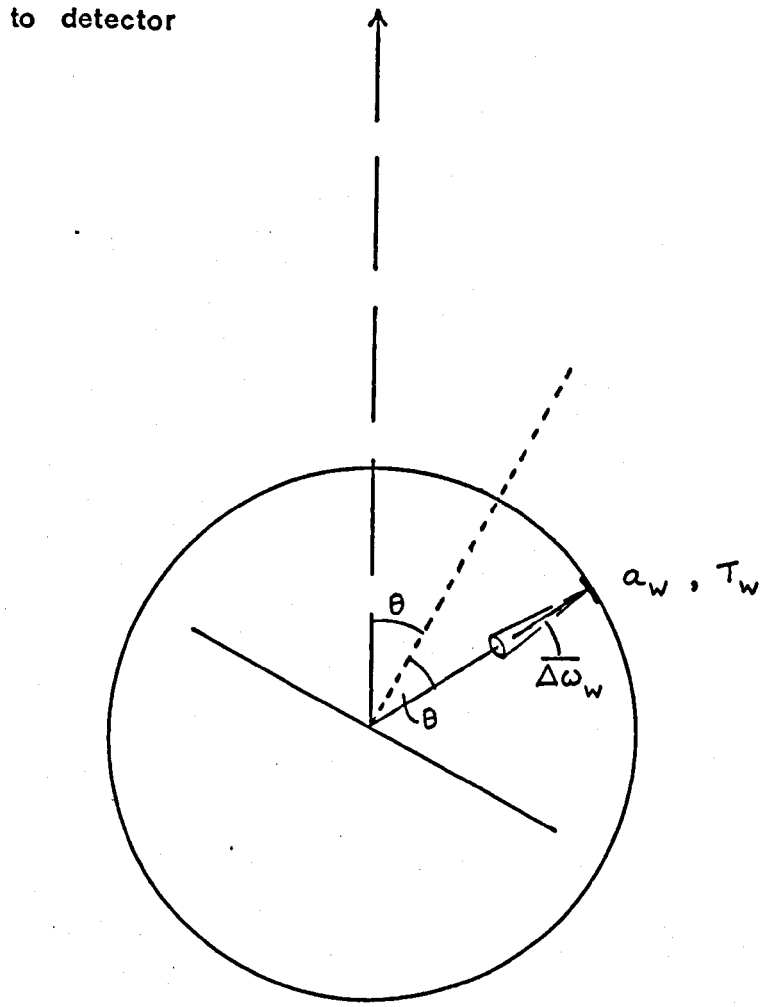

FIGURE A1.3

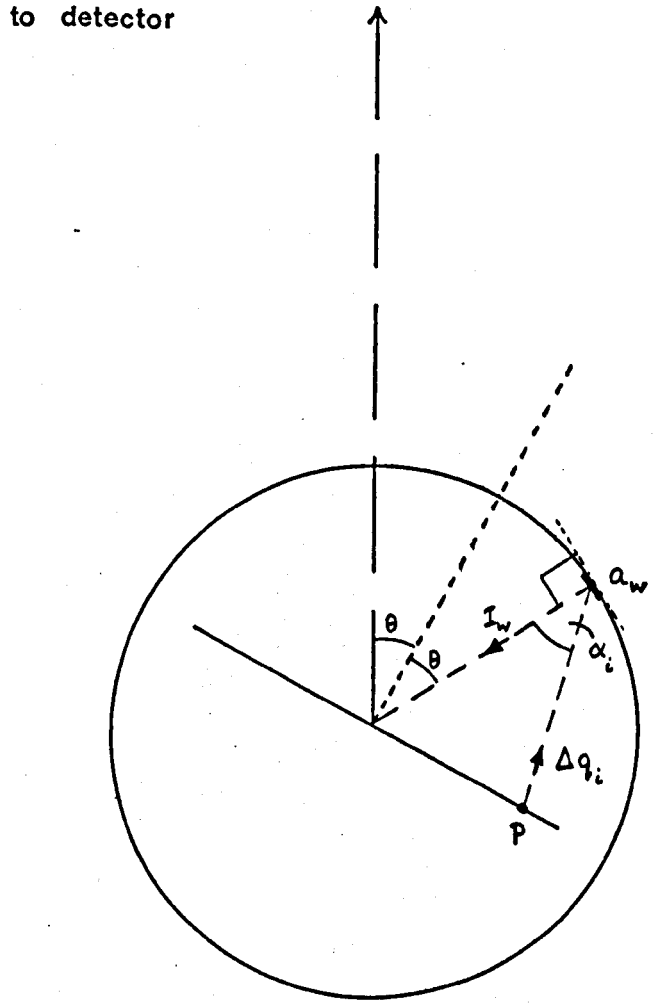

FIGURE A1.4

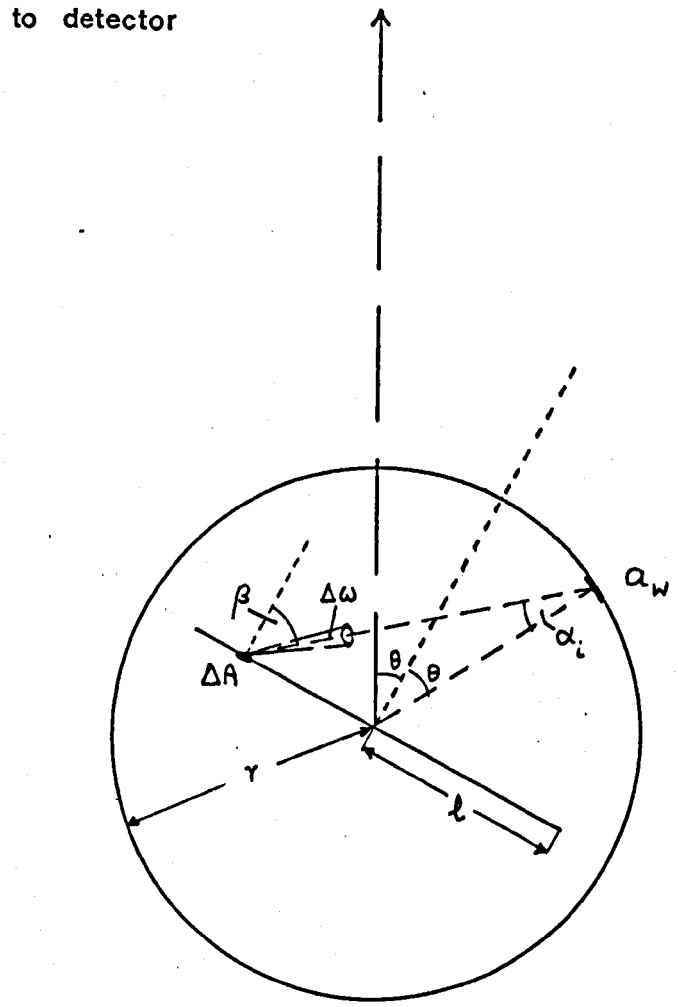

FIGURE A1.5

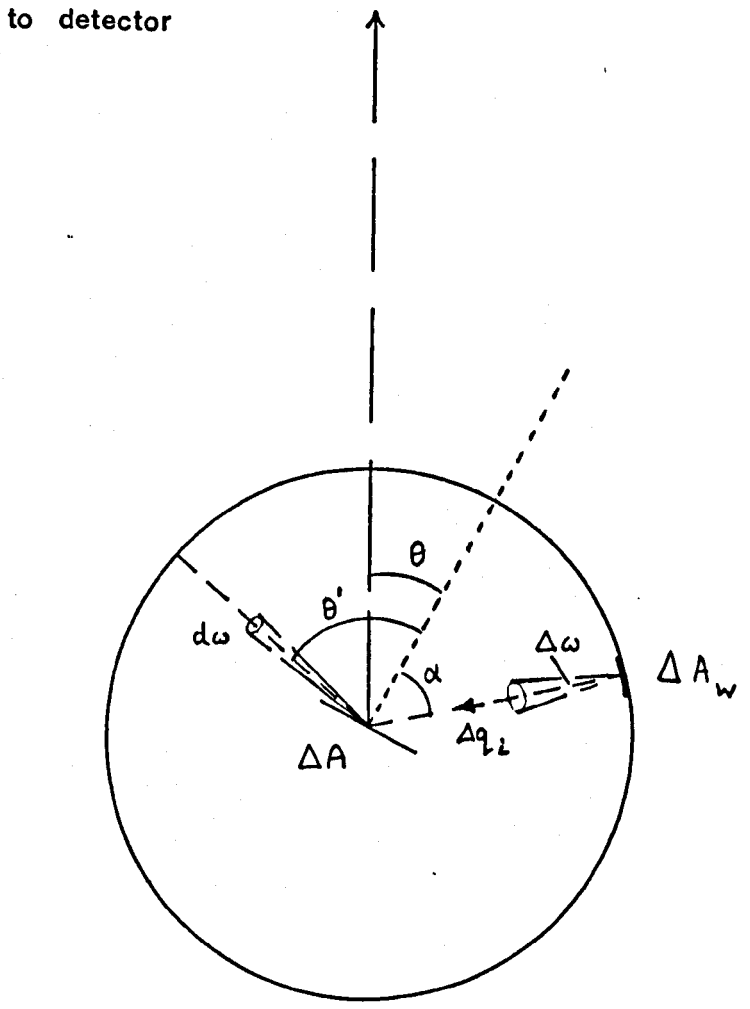

FIGURE A1.6

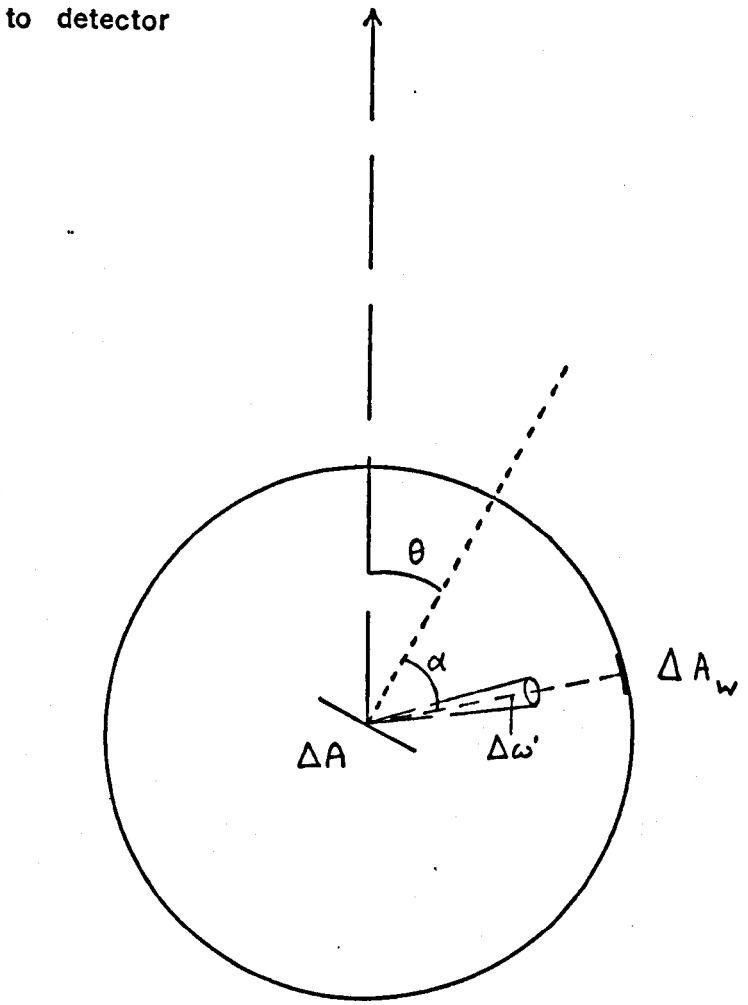

FIGURE A1.7

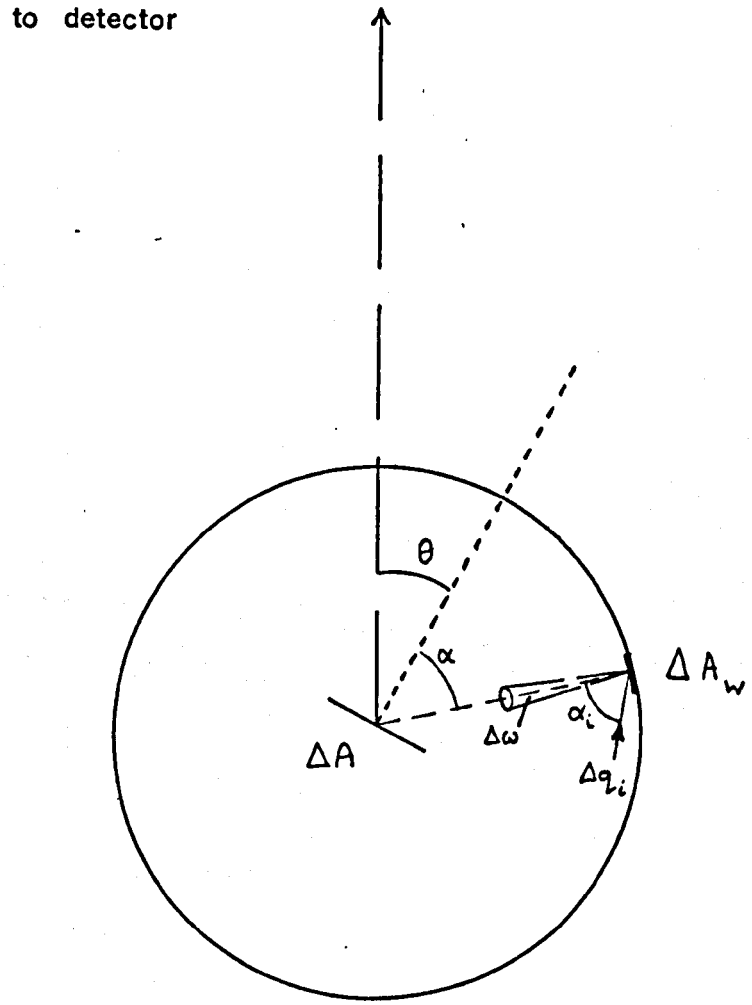

FIGURE A3.1

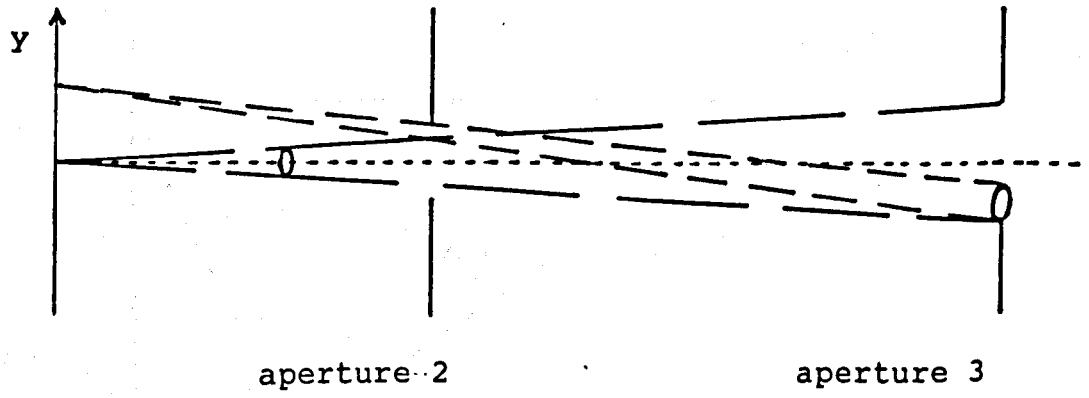

FIGURE A3.2

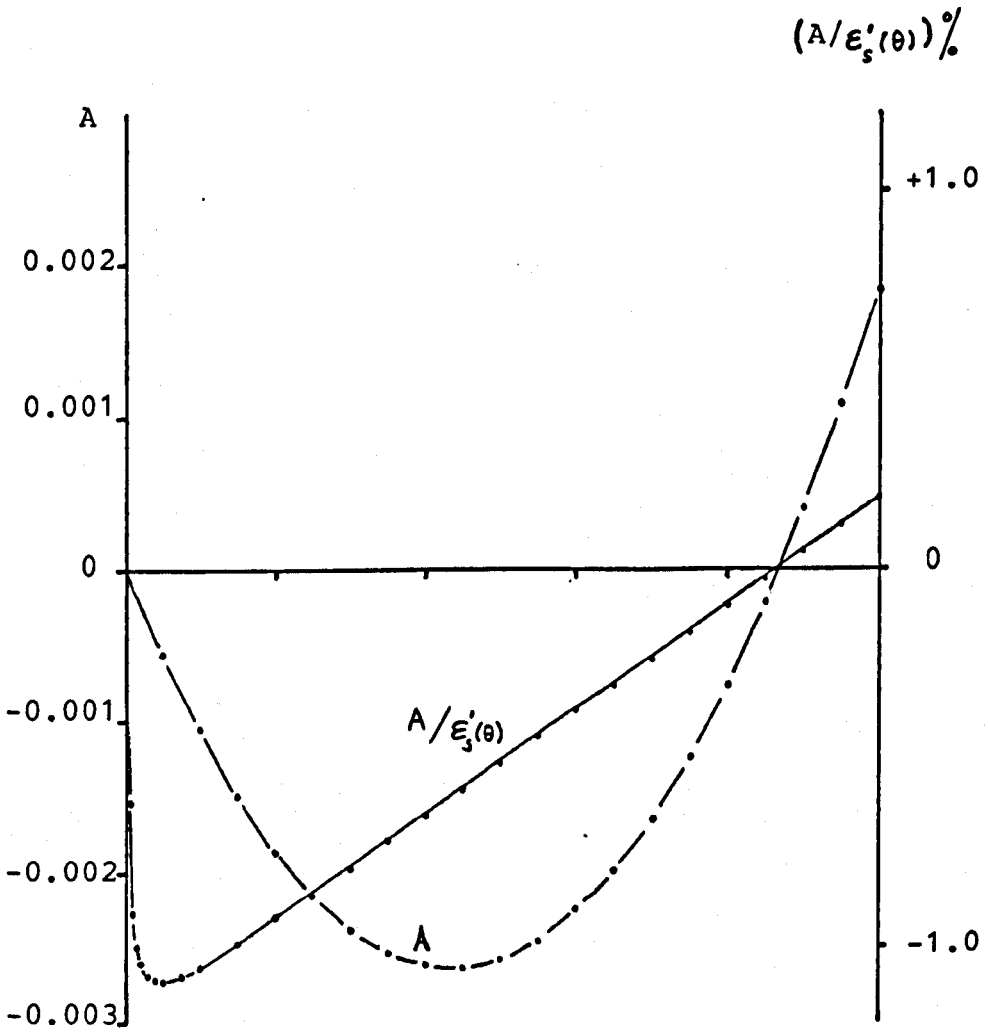
$(A/\varepsilon_s'(\theta))\%$
A
0.002
0.001
0
-0.001
-0.002
-0.003
+1.0
0
-1.0
$A/\varepsilon_s'(\theta)$
A

TABLES

TABLE 2.1 GEOMETRICAL CONFIGURATIONS OF MEASUREMENT

GEOMETRICAL CONFIGURATION DESCRIPTOR	MEASURED QUANTITIES					
	SPECTRAL	TOTAL	SPECTRAL	TOTAL	SPECTRAL	TOTAL
directional	α'_λ	α'	ε'_λ	ε'		
conical	α_λ	α	ε_λ	ε		
hemispherical	α_λ	α	ε_λ	ε		
bi-directional					ρ''_λ	ρ''_λ
directional hemispherical					ρ'_λ	ρ'
hemispherical directional					ρ'_λ	ρ'
bi-hemispherical					ρ_λ	ρ
conical hemispherical					ρ_λ	ρ
hemispherical conical					ρ_λ	ρ
bi-conical					ρ_λ	ρ
directional conical					ρ'_λ	ρ'
conical directional					ρ'_λ	ρ'

Table 2-2 Summary of Kirchhoff's-law relations between absorptivity and emissivity

Type of quantity	Equality	Restrictions
Directional spectral	$\alpha'_\lambda(\lambda,\theta,\varphi,T_A) = \epsilon'_\lambda(\lambda,\theta,\varphi,T_A)$	None
Directional total	$\alpha'(\theta,\varphi,T_A) = \epsilon'(\theta,\varphi,T_A)$	Incident radiation must have a spectral distribution proportional to that of a blackbody at T_A, $i'_{\lambda,i}(\lambda,\theta,\varphi) = C(\theta,\varphi)i'_{\lambda b}(\lambda,T_A)$; or $\alpha'_\lambda(\theta,\varphi,T_A) = \epsilon'_\lambda(\theta,\varphi,T_A)$ are independent of wavelength (directional-gray surface)
Hemispherical spectral	$\alpha_\lambda(\lambda,T_A) = \epsilon_\lambda(\lambda,T_A)$	Incident radiation must be independent of angle, $i'_{\lambda,i}(\lambda) = C(\lambda)$; or $\alpha'_\lambda(\lambda,T_A) = \epsilon'_\lambda(\lambda,T_A)$ do not depend on angle (diffuse-spectral surface)
Hemispherical total	$\alpha(T_A) = \epsilon(T_A)$	Incident radiation must be independent of angle and have a spectral distribution proportional to that of a blackbody at T_A, $i'_{\lambda,i}(\lambda) = Ci'_{\lambda b}(\lambda,T_A)$; or incident radiation independent of angle and $\alpha'_\lambda(\theta,\varphi,T_A) = \epsilon'_\lambda(\theta,\varphi,T_A)$ are independent of λ (directional-gray surface); or incident radiation from each direction has spectral distribution proportional to that of a blackbody at T_A and $\alpha'_\lambda(\lambda,T_A) = \epsilon'_\lambda(\lambda,T_A)$ are independent of angle (diffuse-spectral surface); or $\alpha'_\lambda(T_A) = \epsilon'_\lambda(T_A)$ are independent of wavelength and angle (diffuse-gray surface)

Table 2-3 Summary of reciprocity relations between reflectivities

Type of quantity	Equality	Restrictions
A. Bidirectional spectral	$\rho''_\lambda(\lambda,\theta,\varphi,\theta_r,\varphi_r) = \rho''_\lambda(\lambda,\theta_r,\varphi_r,\theta,\varphi)$	None
B. Directional spectral	$\rho'_\lambda(\lambda,\theta,\varphi) = \rho'_\lambda(\lambda,\theta_r,\varphi_r)$ where $\theta = \theta_r$, $\varphi = \varphi_r$	$\rho'_\lambda(\lambda,\theta_r,\varphi_r)$ is for uniform incident intensity or $\rho''_\lambda(\lambda)$ independent of θ, φ, θ_r, and φ_r
C. Bidirectional total	$\rho''(\theta,\varphi,\theta_r,\varphi_r) = \rho''(\theta_r,\varphi_r,\theta,\varphi)$	$i'_{\lambda,i}(\lambda,\theta,\varphi) = Ci'_{\lambda,i}(\lambda,\theta_r,\varphi_r)$ or $\rho''_\lambda(\theta,\varphi,\theta_r,\varphi_r)$ independent of wavelength
D. Directional total	$\rho'(\theta,\varphi) = \rho'(\theta_r,\varphi_r)$ where $\theta = \theta_r$, $\varphi = \varphi_r$	One restriction from both *B* and *C*

TABLE 3.1 THERMOCOUPLE CALIBRATION

	Sample T/C	Reference T/C	Ambient Temp. T/C	Sample Chamber Wall Temp. T/C
BOILING WATER BATH	100.8	100.9	100.8	100.8
	100.3	100.3	100.2	100.4
ICE-SLURRY BATH	-0.3	-0.3	-0.3	-0.2
	-0.3	-0.3	-0.2	-0.2

TABLE 3.2 ADDITIVE CORRECTION TERM IN EQ.3.12

$\epsilon_s'(\theta)$	A	$A/\epsilon_s'(\theta)$
0.0	$+3.00 \times 10^{-5}$	-
0.005	-3.07×10^{-5}	-6.13×10^{-3}
0.05	-5.45×10^{-4}	-1.09×10^{-2}
0.10	-1.05×10^{-3}	-1.05×10^{-2}
0.15	-1.49×10^{-3}	-9.90×10^{-3}
0.20	-1.85×10^{-3}	-9.25×10^{-3}
0.25	-2.15×10^{-3}	-8.58×10^{-3}
0.30	-2.37×10^{-3}	-7.90×10^{-3}
0.35	-2.53×10^{-3}	-7.21×10^{-3}
0.40	-2.61×10^{-3}	-6.53×10^{-3}
0.45	-2.63×10^{-3}	-5.83×10^{-3}
0.50	-2.57×10^{-3}	-5.14×10^{-3}
0.55	-2.45×10^{-3}	-4.45×10^{-3}
0.60	-2.25×10^{-3}	-3.75×10^{-3}
0.65	-1.99×10^{-3}	-3.05×10^{-3}
0.70	-1.65×10^{-3}	-2.36×10^{-3}
0.75	-1.25×10^{-3}	-1.66×10^{-3}
0.80	-7.70×10^{-4}	-9.63×10^{-4}
0.85	-2.25×10^{-4}	-2.65×10^{-4}
0.90	$+3.90 \times 10^{-4}$	$+4.33 \times 10^{-4}$
0.95	$+1.08 \times 10^{-3}$	$+1.13 \times 10^{-3}$
1.00	$+1.83 \times 10^{-3}$	$+1.83 \times 10^{-3}$

TABLE 3.3 MATERIALS STUDIED IN THE PRESENT WORK

MATERIAL/ TRADE NAME	TYPE	ABSORBER DESCRIPTION	SUBSTRATE	MANUFACTURER	MAX.TEMP. (^{o}C)
MAXORB	selective absorber	oxide of Ni	Ni	INCO-SS - UK	200
CUSORB	" "	"	Cu	"	350
SKYSORB	" "	oxidized stainless steel	Stainless steel	"	200
SOLARCOAT-100	" "	black paint	Cu	ZUEL - USA	538 (1000^{o}F)
SOLARCOAT-50	non-selective "	"	Brass	ZUEL - USA	260 (500^{o}F)
NEXTEL	" "	"	Al	3M - UK/USA	150
GLASS	dielectric		-		
ALUMINIUM	metal		-		
COPPER	"		-		
BRASS	"		-		

TABLE 3.4 DIRECTIONAL VARIATION OF EMITTANCE AND EMISSIVE POWER OF METALS

θ^{o}	POLISHED Al		POLISHED Cu		POLISHED BRASS	
	$\varepsilon'(\theta)$	$e'(\theta)$ $[Wm^{-2} sr^{-1}]$	$\varepsilon'(\theta)$	$e'(\theta)$ $[Wm^{-2} sr^{-1}]$	$\varepsilon'(\theta)$	$e'(\theta)$ $[Wm^{-2} sr^{-1}]$
10	0.042	13.7	0.020	6.7	0.032	10.4
20	0.042	13.0	0.020	6.4	0.032	10.0
30	0.043	12.4	0.020	5.7	0.032	9.0
40	0.045	11.4	0.020	5.0	0.032	8.0
50	0.048	10.4	0.021	4.3	0.033	7.0
60	0.054	9.0	0.023	3.7	0.037	6.0
65	0.061	8.7	0.025	3.3	0.041	5.7
70	0.071	8.0	0.029	3.3	0.045	5.4
75	0.086	7.4	0.034	3.0	0.055	4.7
80	0.111	6.4	0.046	2.7	0.080	4.7

sample temperature 368K

TABLE 3.5 DIRECTIONAL VARIATION OF EMITTANCE AND EMISSIVE POWER OF SOLAR SELECTIVE ABSORBERS

θ^{o}	SOLARCOAT 100		SKYSORB		CUSORB		MAXORB	
	$\varepsilon'(\theta)$	$e'(\theta)$ $[Wm^{-2} sr^{-1}]$	$\varepsilon'(\theta)$	$e'(\theta)$ $[Wm^{-2} sr^{-1}]$	$\varepsilon'(\theta)$	$e'(\theta)$ $[Wm^{-2} sr^{-1}]$	$\varepsilon'(\theta)$	$e'(\theta)$ $[Wm^{-2} sr^{-1}]$
10	0.173	57.2	0.109	35.8	0.085	28.1	0.081	26.8
20	0.175	55.2	0.111	34.8	0.085	26.8	0.081	25.4
30	0.180	52.2	0.113	32.8	0.086	25.1	0.082	23.8
40	0.185	47.5	0.117	29.8	0.090	23.1	0.088	22.4
50	0.191	41.1	0.123	26.4	0.095	20.4	0.099	21.4
60	0.196	32.8	0.137	22.7	0.104	17.4	0.110	18.4
65	0.198	28.1	-	-	0.108	15.4	-	-
70	0.198	22.7	0.165	19.1	0.115	13.0	0.127	14.4
75	0.192	16.7	0.190	16.4	0.121	10.4	0.135	11.7
80	0.168	9.7	0.224	13.0	0.119	7.0	0.145	8.4

sample temperature 368K

TABLE 3.6 DIRECTIONAL VARIATION OF EMITTANCE AND EMISSIVE POWER OF NON-SELECTIVE ABSORBERS

θ^{o}	NEXTEL-VELVET		SOLARCOAT-50		GLASS	
	$\varepsilon'(\theta)$	$e'(\theta)$ $[Wm^{-2} sr^{-1}]$	$\varepsilon'(\theta)$	$e'(\theta)$ $[Wm^{-2} sr^{-1}]$	$\varepsilon'(\theta)$	$e'(\theta)$ $[Wm^{-2} sr^{-1}]$
10	0.976	322	0.833	274	0.890	293
20	0.976	307	0.832	261	0.890	280
30	0.976	233	0.832	241	0.890	258
40	0.976	250	0.831	213	0.884	226
50	0.961	207	0.830	178	0.869	187
60	0.941	157	0.819	137	0.833	139
65	0.921	130	0.814	115	-	-
70	0.900	103	0.806	92.3	0.748	85.6
75	0.850	73.6	0.786	67.9	0.668	57.9
80	0.799	46.5	0.734	42.5	0.593	34.5

sample temperature 368K

TABLE 3.7 COMPARISON OF ε

ε			
MATERIAL	PRESENT WORK (computed from $\varepsilon'(\theta)$ values measured at 368K).	MANUFACTURERS SPECIFICATION	OTHER WORK
MAXORB	0.100 ± 0.003	0.08-0.11 (373K)	0.14 (373K) MUSA,1980
CUSORB	0.095 ± 0.002	0.08-0.15	
SKYSORB	0.133 ± 0.004	0.10-0.14	0.11 (373K) MUSA,1980
SOLARCOAT-100	0.184 ± 0.004	0.15-0.25	
SOLARCOAT-50	0.810 ± 0.02	0.93	
NEXTEL	0.940 ± 0.02	0.93 (422K)	0.96 (373K) MUSA,1980
GLASS	0.840 ± 0.02		0.85 (373K) VAN DER LEIJ 1979.
ALUMINIUM	0.053 ± 0.002		0.09 HOTTEL & SERAFIM, 1967
COPPER	0.023 ± 0.001		0.02 HOTTEL & SERAFIM, 1967
BRASS	0.038 ± 0.002		0.03 HOTTEL & SERAFIM, 1967

TABLE 3.8 CALCULATED VALUES OF ε AND $\varepsilon/\varepsilon'(0°)$

MATERIAL	ε	$\varepsilon'(0°)$	$\varepsilon/\varepsilon'(0°)$
MAXORB	0.100	0.081	1.235
CUSORB	0.095	0.085	1.118
SKYSORB	0.133	0.109	1.220
SOLARCOAT-100	0.184	0.173	1.064
SOLARCOAT-50	0.813	0.833	0.976
NEXTEL	0.939	0.976	0.962
GLASS	0.835	0.890	0.938
ALUMINIUM	0.053	0.042	1.262
COPPER	0.023	0.020	1.150
BRASS	0.038	0.032	1.188

TABLE 4.1 BDR MEASUREMENT ERROR

θ_r	% error in ρ''_λ
0	3.02
10	3.03
20	3.03
30	3.03
40	3.03
50	3.04
60	3.05
70	3.07
75	3.10
80	3.18

TABLE 4.2 COMPARISON OF COMPUTED ρ'_λ WITH NPL MEASUREMENTS

SAMPLE	WAVELENGTH [nm]	computed ρ'_λ	NPL measurement of ρ'_λ
NEXTEL	633	0.028	0.026
	1152	0.024	0.026
SOLARCOAT - 50	633	0.020	0.018
	1152	0.020	0.021

TABLE 4.3 SOME ρ''_λ RATIOS RELATING TO FIGURES 4.41 AND 4.42

SAMPLE	WAVELENGTH [nm]	$\rho''_\lambda(\theta_r=0°)$ [10^{-3} sr^{-1}]	$\frac{\rho''_\lambda(\theta_r=40°)}{\rho''_\lambda(\theta_r=0°)}$	$\frac{\rho''_\lambda(\theta_r=80°)}{\rho''_\lambda(\theta_r=0°)}$	$\rho'(\theta_r\simeq3°)$ (NPL)
NEXTEL	633	8.91	1.40	3.45	0.026
	1152	5.64	1.56	3.96	0.026
SOLARCOAT - 50	633	6.14	1.18	1.78	0.018
	1152	4.92	1.26	1.93	0.021
SKYSORB	633	3.91	633.3	3.66	0.025
	1152	13.87	1013.2	1.16	0.027
MAXORB	633	3.59	44.4	1.60	0.016
	1152	1.98	741.8	1.21	0.053
CUSORB	633	5.09	2.90	2.87	0.017
	1152	3.54	30.3	2.99	0.018
SOLARCOAT - 100	633	14.20	42.7	4.39	0.051
	1152	10.05	115.5	2.81	0.090

TABLE 4.4 POLARIZATION OF THE INCIDENT BEAM

WAVELENGTH (nm)	n	k	ρ'_p	ρ'_n	polarized fraction using Eq.A2.3	polarized fraction using Eq.A2.4
633	0.066	4.020	0.980	0.989	0.005	0.005
950	0.11	6.56	0.986	0.993	0.004	0.004
1250	0.370	7.700	0.966	0.983	0.008	0.009